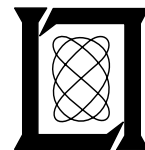# MLS Multipath Studies
Volume I: Mathematical Models and Validation

J. E. Evans
J. Capon
D. A. Shnidman
R. B. Burchsted
R. S. Orr
S. M. Sussman

25 February 1976

Lincoln Laboratory
MASSACHUSETTS INSTITUTE OF TECHNOLOGY
LEXINGTON, MASSACHUSETTS

1. Report No.	2. Government Accession No.	3. Recipient's Catalog No.
FAA-RD-76-3, I		

4. Title and Subtitle	5. Report Date
MLS Multipath Studies Volume I: Mathematical Models and Validation	25 February 1976
	6. Performing Organization Code

7. Author(s)	8. Performing Organization Report No.
J.E. Evans J. Capon D.A. Shnidman R.B. Burchsted R.S. Orr S.M. Sussman	ATC-63

9. Performing Organization Name and Address	10. Work Unit No. (TRAIS)
Massachusetts Institute of Technology Lincoln Laboratory P.O. Box 73 Lexington, MA 02173	
	11. Contract or Grant No.
	DOT-FA74WAI-461

12. Sponsoring Agency Name and Address	13. Type of Report and Period Covered
Department of Transportation Federal Aviation Administration Systems Research and Development Service Washington, DC 20591	Project Report
	14. Sponsoring Agency Code

15. Supplementary Notes

16. Abstract

This report summarizes MLS multipath work carried out at Lincoln Laboratory from March 1974 to Sept. 30, 1975. The focus of the program is the development of realistic models for 1) the multipath in representative real world environments and 2) the multipath characteristic of candidate MLS techniques. These multipath and system models are used in a comprehensive computer simulation to predict the strengths and weaknesses of major MLS systems when subjected to representative real world environments. The report is organized into two volumes. Volume I describes the algorithms and validation of various portions of the program. In Volume II, the simulation (or selected portions thereof) is applied to key multipath related MLS issues.

Mathematical models are given for the major MLS multipath sources (ground reflections, building and aircraft reflections, and shadowing by objects and humped runways), and it is shown that they agree well with field data (including the Lincoln measurements at Logan Airport). Models for the techniques (Doppler and scanning beam) considered in phase II of the U.S. MLS program are presented together with validation by comparison with theory and bench tests. Also presented are the results of a general study in motion averaging.

The (validated) computer simulation (and portions thereof) is then applied to studying 1) the critical areas required by the TRSB system to avoid excessive reflection effects, 2) the expected TRSB performance with vertical polarization and benefits that might be derived with an alternative polarization and 3) siting of a specific TRSB system at Friendship International Airport (MD).

17. Key Words	18. Distribution Statement
Microwave landing system L-band multipath C-band multipath	Document is available to the public through the National Technical Information Service, Springfield, Virginia 22151.

19. Security Classif. (of this report)	20. Security Classif. (of this page)	21. No. of Pages	
Unclassified	Unclassified		

VOLUME I

TABLE OF CONTENTS

iv

VOLUME II

TABLE OF CONTENTS

VOLUME I

LIST OF ILLUSTRATIONS

x

I. INTRODUCTION

The US national Microwave Landing System (MLS) program has as its goal the development of the system which is to become the common civil/military international standard for the remainder of this century. The extensive deliberations of the RTCA Special Committee SC-117 led to the selection of two air derived concepts (scanning beam and Doppler scan) which were developed in a joint DOT DOD/NASA program, with the time reference scanning beam emerging as the winner of the U.S. MLS phase II assessment. In addition, several alternative systems (both air derived and ground derived) are under consideration by the International Civil Aviation Organization (ICAO) for adoption as the new international standard.

The resistance to coherent interference, i.e., multipath has proved to be a key technical issue in assessing the relative and absolute capabilities of the various systems. Although all the proposed MLS techniques are generally more resistant to multipath than is the ILS, MLS is expected to provide guidance over much wider coverage in an environment characterized by continuing construction of buildings near the approach and landing zone and the increased use of wide bodied aircraft (both potentially significant multipath sources). There has been considerable operational experience with MLS equipment, especially scanning beam systems [1-15], but it has not been practically possible to address the many issues involved in multipath performance solely by field tests.

This report summarizes the multipath studies performed by MIT Lincoln Laboratory for the FAA MLS office during the MLS phase II effort. The cornerstone of this Lincoln effort has been the development of realistic models

for 1) the multipath in representative real world airport environments, and 2) the multipath characteristics of candidate MLS techniques. These multipath and system models are used in a comprehensive simulation to assess the potential strengths and weaknesses of the various systems as well as to optimize the performance of a given system.

Referring to Fig. 1-1, the user-specified program input (denoted by trapezoids) consists of the desired flight profile, location and description of the MLS equipment and scatterers (e.g., buildings, aircraft, runway humps), and the aircraft flight control system. The program then "flies" the aircraft down the desired path making computations at discrete "evaluation points" which correspond to a desired data rate, e.g., the ICAO 5 Hz rate.

At each evaluation point, the multipath signals from all of the various scattering and shadowing objects are computed for each of the MLS functions (azimuth, elevation, DME). These multipath results are then used as an input to a second computer program which is a mathematical model for the particular MLS technique under study. The resulting raw errors can then be plotted immediately and/or input to a mathematical model of an aircraft flight control system model so as to examine the impact of the multipath on the path following performance and control surface activity. The program output includes comprehensive multipath diagnostics, permitting the user to ascertain the causes of the computed errors. In addition, we have developed various support packages which allow detailed study of the multipath reflections from individual scatterers and their effect upon specific receiver implementations.

SIMPLIFIED BLOCK DIAGRAM
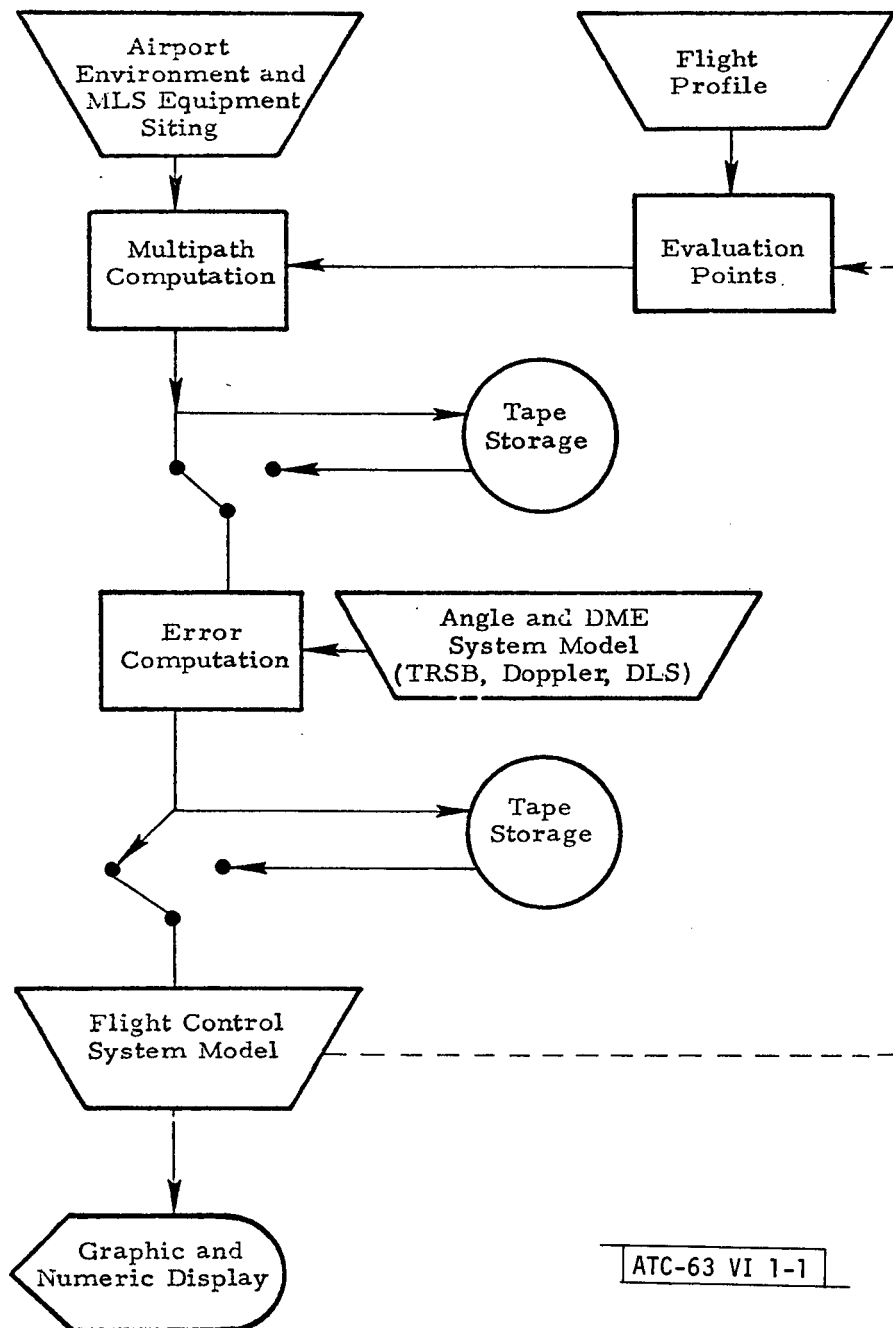
Fig. 1-1. Simplified block diagram of MLS computer simulation.

The remainder of the report is organized in chapters which 1) describe the algorithms and validation of various portions of the program, and 2) applications of the simulation (or selected portions thereof) to addressing various key multipath-related MLS issues. Chapter II describes the multipath scattering model and some of the validation by comparison with theoretical calculations and field data. Specific algorithms are presented for:

1. Specular ground reflection
2. Scattering from obstacles such as aircraft, buildings, hangars, trucks
3. Diffuse scattering from ground
4. Runway hump shadowing
5. Shadowing due to aircraft approaching line of sight

An important part of the multipath model development involved critically analyzing the work that had been accomplished in the multipath area in the US and other countries. Table 1-1 summarizes the major data sources used in the model development.

After reviewing the multipath data available at the commencement of the Lincoln MLS activity, it was determined that insufficient field data existed to definitively address many important modeling issues. For example, little data existed to suggest appropriate C-band models for complicated buildings (e.g., as at terminals), or which objects at an airport would yield significant MLS multipath. Therefore, a series of channel characterization experiments were carried out at Logan International Airport (Boston, Mass.) under the technical direction of Lincoln Laboratory to address these key issues.

	Reflections from:			Shadowing by:		
	Buildings	Aircraft	Other Sources	Aircraft	Runway Humps	Buildings
Qualitative Characteristics	1 - 16 A 10 14 15 E	6 16 A 8 10 A E	6 8 A 5 10 E	6 9 10 11 12 16 A 2 7 9 12 13 E	1 6 8 10 11 13 } A 11 13E }	6 10 A 10 E
Quantitative Characteristics Reflection coefficient	8 10 14 16 A 8 10 13 14 15 E	14 A E 10 A E	---	---	---	---
Spatial extent	1 - 16 A 10 15 E	6 8 10 14 16 A 10 E 8 10 15 E		6 10 13 16 A 2 7 9 12 13 E	10 11 13 A 11 13 E	6 10 A E
Size, distance factors	3 6 8 10 16 A 10 E	6 8 10 14 16 A 8 10 E	---	6 10 13 16 A 13 E	10 11 13 A 11 13 E	10 A E
Secondary paths	10 A E 2 15 E	10 A E	---	10 A 13 A E	10 A 13 A E	10 A
Spatial coherence	1 - 16 A 2 4 7 9 12 } E 13 15 }	1 - 16 A	---	10 16 A	10 A	10 A E

1. Bendix TACD (ref. 34)
2. Bendix MLS Phase II (ref. 22)
3. Calspan (refs. 23-25)
4. FAA tests at NAFEC (refs. 1-8)
5. FAA civilian airport meas.(ref. 9)
6. Hazeltine TACD (ref. 33)
7. Hazeltine MLS Phase II (ref. 30)
8. ITT/GIlfillan TACD (ref. 18)

9. ITT/GIlfillan MLS Phase II (ref. 31)
10. MIT Lincoln Laboratory (refs. 36,66)
11. Texas Inst./Thompson CSF TACD (ref. 26)
12. Texas Inst./Thompson CSF MLS Phase II (ref. 32)
13. United Kingdom (ref. 27)
14. U.S. Army (ref. 37)
15. USAF/IITRI (ref. 28)
16. ELAB (ref. 40)

A = analytical studies
B = experimental studies (field measurements)

TABLE 1-1

MAJOR SOURCES OF MULTIPATH ENVIRONMENT DATA FOR MULTIPATH MODEL DEVELOPMENT

Chapter III describes these Logan measurements in the context of validation of the multipath model. Also described in Chapter III are the results of comparing the multipath model predictions with US MLS phase II field results from NAFEC and Wallops Island as well as with experiments at Wright Patterson Air Force Base (Ohio).

In Chapter IV, we describe the mathematical models developed for the scanning beam (frequency and time reference), Doppler scan (commutated and beam port), and DME systems developed by the US MLS phase II contractors. Also described are models for several variants on these systems, such as the scanning beam multipath control technique (MCT) and the thinned Doppler array.

An important feature of the dynamic MLS performance is the possibility of reducing errors by choosing a signal format with measurement rate > desired data rate so that a number of individual measurements can be averaged together to yield a single output data point. Since the individual measurement errors typically oscillate in sign along the flight path, there arises the possibility of significant improvement by this "motion averaging" process. This motion averaging improvement is a particularly important factor in reducing elevation system errors due to reflections from vertical structures. Chapter V presents a general analysis of expected benefits from motion averaging which is applicable to all MLS techniques which have been proposed to ICAO.

Chapter VI describes the validation of the computer programs for the various MLS techniques. The validation process for the angle receivers is shown in Fig. 1-2. For the DME systems, bench test data is not available, so the validation has consisted of comparison of the receiver simulation with

1-6

ATC-63 VI 1-2
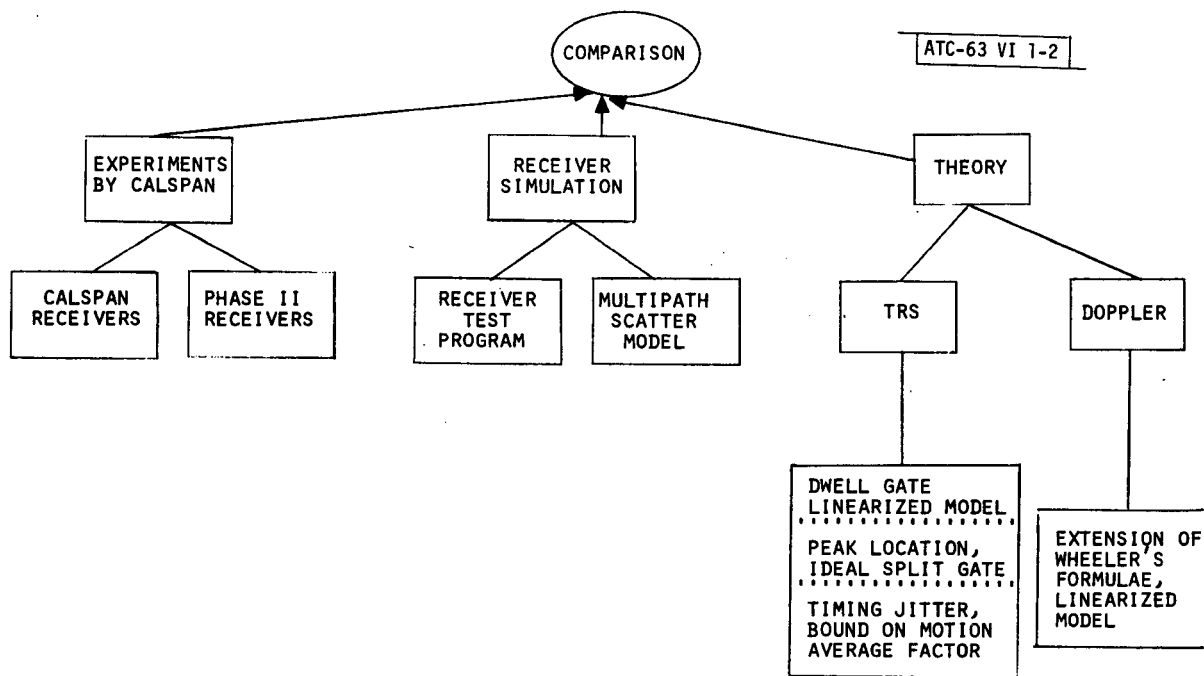
Fig. 1-2. Validation process for MLS system models.

theoretical results. Also discussed in Chapter VI are the results of full simulations based on runways at Logan and JFK airports. It is shown that there is a good correspondence between the observed results and the system theory from Chapters IV, V and VI.

An important goal in the computer simulation development has been to yield a final product which can be used by interested parties (e.g., the FAA, DOD, international civil aviation authorities, contractors, etc.) as an aid in site selection, system optimization, etc. Thus, the program has been written in a generally available computer language (Fortran) and structured to facilitate transition to other computer facilities. Chapter VII briefly describes the computer program organization as well as the support programs which augment the ability to address various aspects of the total multipath performance (a more detailed description of the use of the full simulation will appear separately).

The last three chapters demonstrate the applicability of the multipath and system models to several multipath related MLS issues. Chapter VIII summarizes the preliminary results on the critical areas needed for the TRSB system so as to avoid excessive reflection effects. In the next phase, these estimates will be combined with estimates of the areas required to avoid shadowing effects and summarized in a separate ATC report.

Considerable controversy has arisen in the U.S. MLS program over the choice of polarization for the TRSB system. The Lincoln contributions in this area are summarized in Chapter IX, which presents some systems calculations together with the results of an airport survey to better assess the expected building multipath levels in the real world with the various polarization choices.

Chapter X provides an example of the use of the MLS simulation program for an actual siting problem at Baltimore runway 15. Whereas the full simulations presented in Chapter VI are primarily concerned with aircraft and building reflections, Chapter X considers the case where irregular up-sloping terrain is the chief threat for the proposed TRSB system.

PAGE PURPOSELY
LEFT BLANK

PAGE PURPOSELY
LEFT BLANK

II. DESCRIPTION OF MULTIPATH SCATTERING MODELS

The purpose of this chapter is to present a brief description of the algorithms which have been used to determine the multipath components which occur due to obstacles which are found in typical airport environments. A more detailed description of these subroutines will be given in a subsequent report.

Descriptions are presented of the models employed to compute the effects due to specular reflection, as well as diffuse scattering, from the ground located near the transmitter antenna. In addition, a description is given of the algorithms used to determine the effect due to scattering from buildings, or hangars, and aircraft. The methods for treating the shadowing effect due to runway humps, and aircraft or buildings which are near the line of sight between transmitter and receiver, are also discussed.

It should be noted that these models involve two rather distinct steps:

1. the very complicated real world objects are represented by certain simpler objects which more readily lend themselves to practical computation routines. As an example, aircraft fuselages are modeled as metallic cylinders

2. a feasible computation algorithm is used to give a quantitative expression of the scattered signal. Here, the tradeoff is between accuracy and the computational speed. To achieve this, we typically have used a mixture of physical optics and geometric optics algorithms as opposed to full solutions of the boundary value problem

In this chapter, a limited amount of validation data will be presented to provide some perspective on the magnitude of the various scattered signals.

The next chapter will provide much more extensive validation data drawing heavily on the measurements accomplished at Logan International Airport (Boston, MA) as a part of the Lincoln Laboratory phase II MLS activity.

2.1 Specular Ground Reflection

The magnitude and phase of the multipath component due to specular reflection from the ground is computed by using the Fresnel-Kirchoff diffraction formula[48, 49, 51]. An illustration of the geometry required for determining the effects due to specular reflection from the ground is given in Fig. 2-1. The terrain in the vicinity of the transmitter antenna is physically modeled as a series of rectangular and triangular plates. These plates can be oriented in arbitrary directions, and each has its own characteristic dielectric and roughness properties.

The complex reflection coefficient due to specular reflection from the ground is obtained by means of a numerical integration of the Fresnel-Kirchoff diffraction integral, over the rectangular and triangular plates, as follows

$$\rho_s = \frac{j\,r_o}{\lambda} \int\limits_{\substack{\text{first two} \\ \text{and one-third} \\ \text{Fresnel zones}}} \int \frac{1}{R_r R_t}\, e^{-jk(R_r+R_t-r_o)} \cdot e^{-\frac{1}{2}\left(\frac{4\pi}{\lambda}\sigma_h \cos\theta_t\right)^2}$$

$$\cdot\ R_{eq} \frac{\cos\theta_t + \cos\theta_r}{2}\, dS \ , \tag{2-1}$$

where λ is the wavelength of the incident radiation, k is the wavenumber ($= 2\pi/\lambda$), σ_h is the root-mean-square roughness height of an appropriate surface element, and R_{eq} is the equivalent Fresnel reflection coefficient

2-2
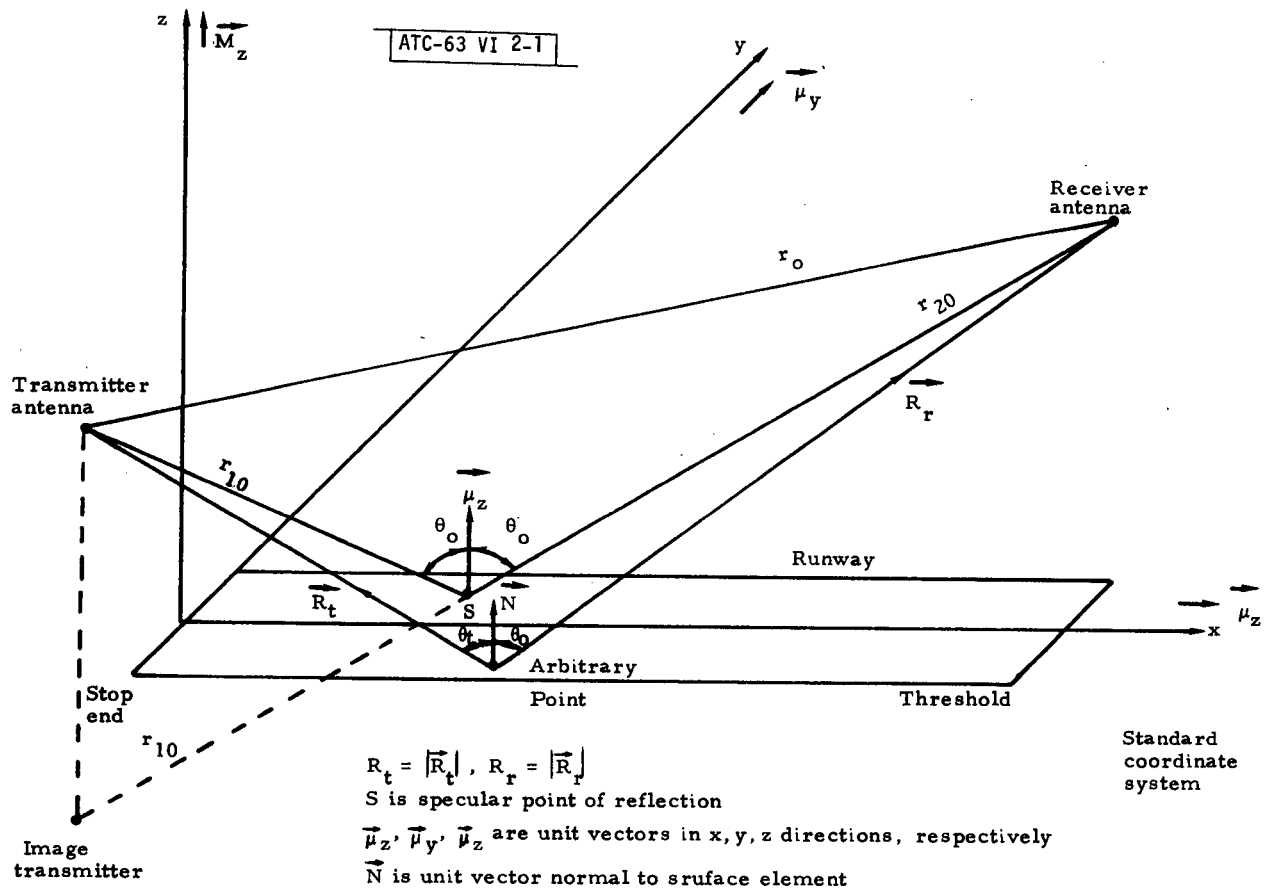
Fig. 2-1. Geometry for specular reflection from the ground.

which takes into account the finite dielectric and conductivity properties of an appropriate surface element, as well as its arbitrary orientation.

The amplitude and phase of the multipath component due to specular reflection from the ground can be obtained as

$$V_s = |\rho_s| \qquad , \qquad (2\text{-}2)$$

$$\psi_s = ARG\{\rho_s\} + k(r_{10} + r_{20} - r_0) \quad . \qquad (2\text{-}3)$$

In addition to these quantities, computations are also performed for the planar azimuth and elevation angles for the direction of propagation of a multipath component relative to the transmitter, the relative time delay, and the Doppler frequency, cf. Fig. 2-2. These planar angles are computed according to the vector direction between the transmitter and the specular point on the ground, as shown in Fig. 2-2, i.e.,

$$\alpha_s = \tan^{-1}(R_{ty}/R_{tx}) \qquad , \qquad (2\text{-}4)$$

$$\beta_s = \tan^{-1}(R_{tz}/R_{tx}) \qquad . \qquad (2\text{-}5)$$

The receiver Doppler frequency is given as the dot product of the receiver velocity vector with the unit vector from receiver position to the specular point, as shown in Fig. 2-2, i.e.,

$$\omega_{sD} = k \vec{V}_A \cdot \vec{R}_r / |\vec{R}_r| = k V_A \cos \gamma \qquad , \qquad (2\text{-}6)$$

where $\vec{V}_A$ is the vector aircraft velocity, and $V_A = |\vec{V}_A|$. The time delay of the specular ground reflection relative to the direct wave is obtained by
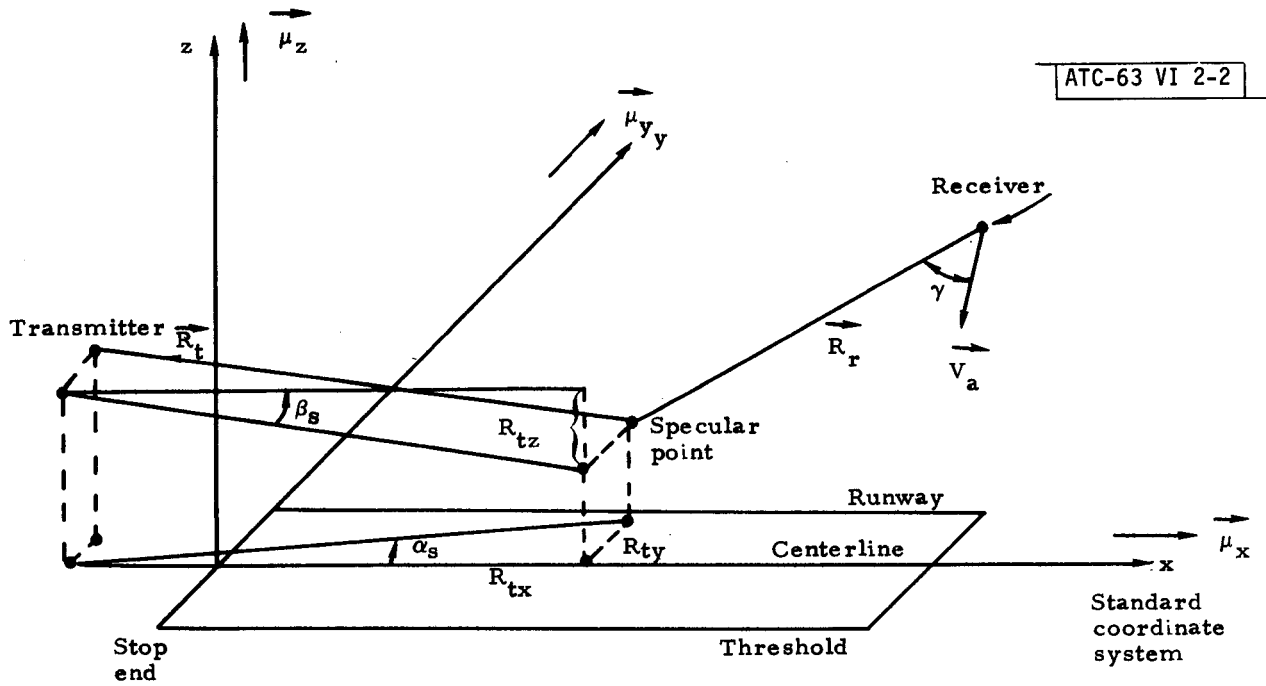
$\vec{V}_A$ is aircraft velocity vector

$\vec{\mu}_x, \vec{\mu}_y, \vec{\mu}_z$ are unit vectors in x, y, z directions, respective

$$\vec{R}_t = R_{tx} \vec{\mu}_x + R_{ty} \vec{\mu}_y + R_{tz} \vec{\mu}_z$$

Fig. 2-2. Method for computing planar angles and Doppler frequency.

assuming that this multipath component arrives at the receiver along the direction defined by the specular point of reflection, so that

$$t_{sD} = (r_{10} + r_{20} - r_0)/c \quad . \tag{2-7}$$

A number of computer validation results have been obtained for the sub-routine which computes the characteristics of the multipath component due to the specular reflection from the ground. One such result is shown in Fig. 2-3. This figure depicts the computed and theoretical[63] values of the magnitude of the Fresnel-Kirchoff diffraction integral vs the number of Fresnel zones used in the integration region, for a flat, smooth, perfectly conducting surface. It is seen that there is a relatively good agreement between the results of the computation and the theoretical curve.

2.2 Scattering From Buildings

In order to compute the effects due to scattering from buildings, a building wall is physically modeled by one, or more, vertical rectangular surfaces as shown in Fig. 2-4. Each surface is characterized by a relative complex dielectric constant and root-mean-square roughness height. Thus, for example, a building with a long glass window which is framed by brick on the bottom and metal on the top could be represented by three plates.

The amplitude and phase of the multipath components due to scattering from a single surface are computed by making use of Babinet's principle[5,63], so that we may consider the equivalent problem of diffraction by a rectangular opening in an opaque screen. Thus, the complex reflection coefficient of the multipath component due to scattering from a single rectangular surface is given by
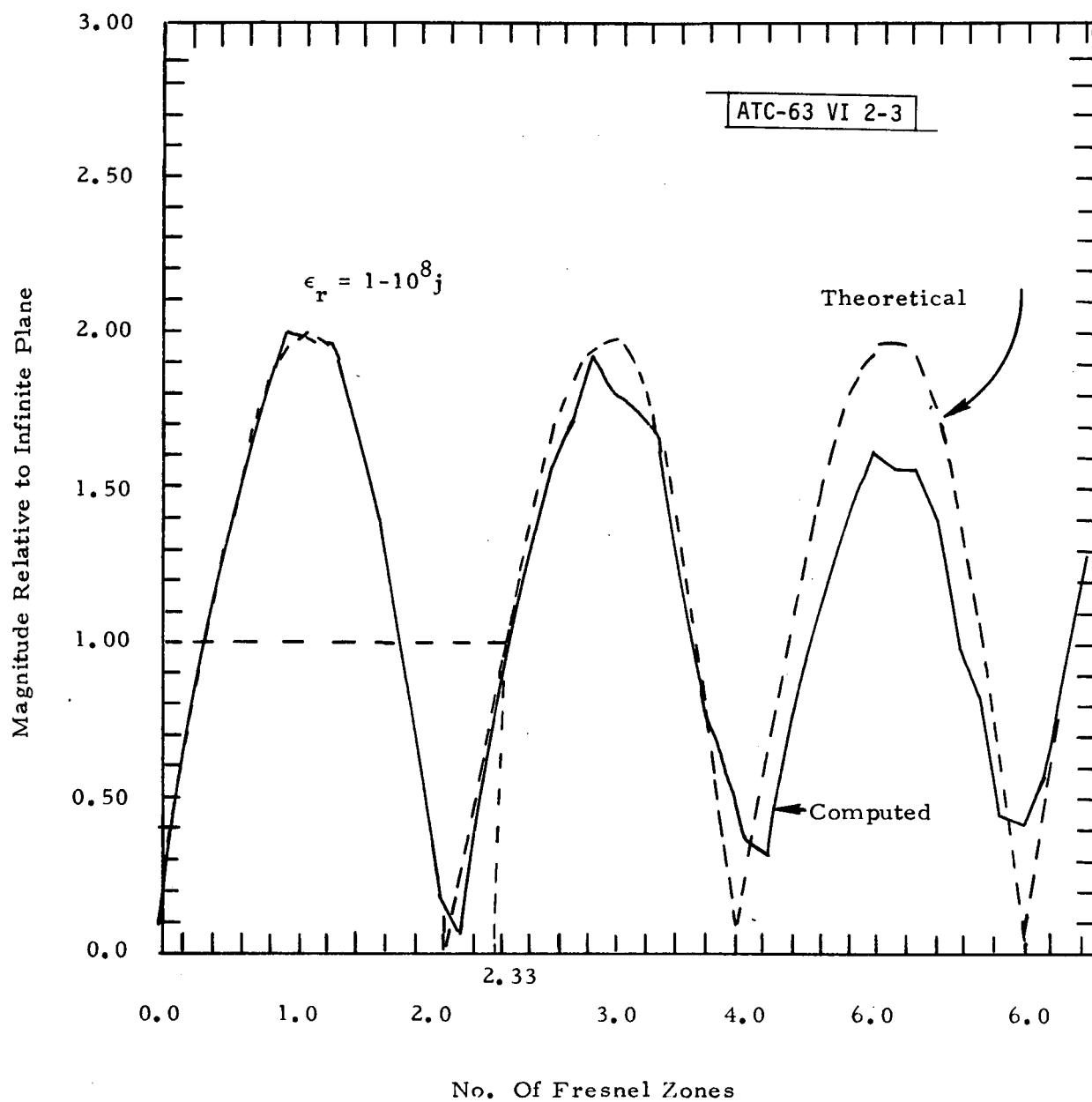
Fig. 2-3. Comparison of computed and theoretical values of magnitude of Fresnel-Kirchoff diffraction integral vs number of Fresnel zones used in integration region, for a flat, smooth, perfectly-conducting surface.
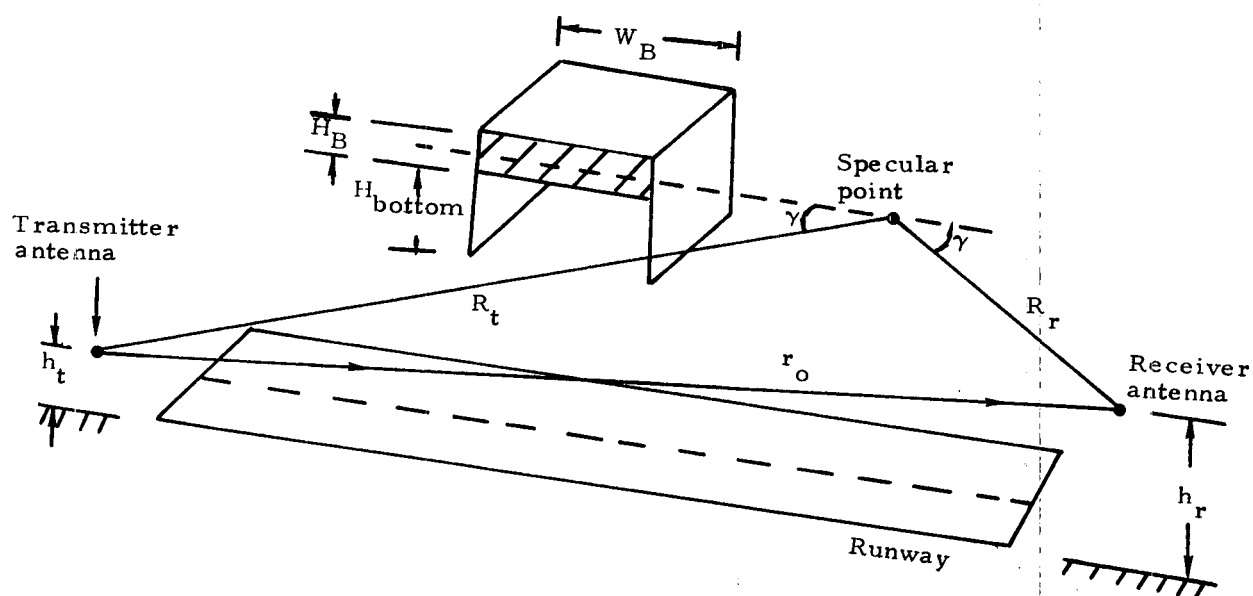
Fig. 2-4. Geometry employed for obtaining characteristics of multipath components due to scattering from buildings.

$$\rho_B = \rho_{Ba}\, \rho_{Be}\, \rho_R\, \rho_r\, R_{eq} \quad , \tag{2-8}$$

where R_{eq} is the equivalent Fresnel reflection coefficient which takes into account the finite dielectric and conductivity properties of the building surface as well as its arbitrary orientation, ρ_r is the attenuation factor due to the building surface roughness, given by

$$\rho_r = e^{-\frac{1}{2}\left(\frac{4\pi}{\lambda}\sigma_h \cos \theta_t\right)^2} \quad , \tag{2-9}$$

ρ_R is a distance factor which takes into account the fact that a power loss occurs due to the greater path distance of the multipath signal, and is given by

$$\rho_R = \frac{r_o}{R_t + R_r} \quad , \tag{2-10}$$

ρ_{Be} is the elevation factor computed as

$$\rho_{Be} = \varepsilon^{j\pi/4}\, (F(u_{top}) - F(u_{bot}))/\sqrt{2} \quad , \tag{2-11}$$

where

$$u_{top} = (H_{bottom} + H_B - h_s)\sqrt{2}\,/R_f \quad , \tag{2-12}$$

$$u_{bot} = (H_B - h_s)\sqrt{2}\,/R_f \quad , \tag{2-13}$$

$$F(u) = \int_o^u e^{-j\pi x^2/2}\, dx \quad , \tag{2-14}$$

$$R_f = \sqrt{\lambda \cdot \frac{R_t R_r}{R_t + R_r}} \quad , \tag{2-15}$$

h_s is the height of the specular point above the ground, and ρ_{Ba} is the azimuthal factor computed as

$$\rho_{Ba} = \varepsilon^{j\pi/4} (F(u_{right}) - F(u_{left}))/\sqrt{2} \; , \tag{2-16}$$

where

$$u_{right} = (W_B - W_s)\sqrt{2} \sin \gamma/R_f \; , \tag{2-17}$$

$$u_{left} = -W_s \sqrt{2} \sin \gamma/R_f \; , \tag{2-18}$$

and W_s is the directed distance between the specular point and the left-hand edge of the building.

The amplitude and phase of the multipath component due to scattering from each building surface can be obtained as

$$V_B = |\rho_B| \; , \tag{2-19}$$

$$\psi_B = ARG\{\rho_B\} + k(R'_t + R'_r - R_t - R_f) \; , \tag{2-20}$$

In this case the computations for the planar azimuth and elevation angles, relative time delay and Doppler frequency are similar to those presented for the multipath component due to specular reflection from the ground.

The computations presented previously refer to a ray path which extends from the transmitter to the obstacle, and then to the receiver. This path may be denoted as X-O-R. In addition to this ray path, computations are performed for three other ray paths which involve ground reflections. One of these ray paths includes a ground reflection between transmitter and obstacle, denoted as X-G-O-R, the second ray path involves a ground reflection between obstacle and receiver, denoted as X-O-G-R, and the third ray path

includes ground reflections between transmitter and obstacle and between obstacle and receiver, denoted as X-G-O-G-R. These other paths are computed in much the same manner as the X-O-R path by using appropriate combinations of transmitter, image transmitter, receiver, or image receiver positions.

Various computer validation results have been obtained for the subroutine which computes the characteristics of the multipath component due to scattering from buildings. One particular example geometry is shown in Fig. 2-5a. In Fig. 2-5b, we compare the results using the computational methods above with computations by ITT Gilfillan[18], who employed the geometric theory of diffraction[62]. It is observed that there is reasonably good agreement between the data given in Fig. 2-5b. In addition, we mention that the present computational technique requires much less computer time than that based on the geometrical theory of diffraction.

2.3 Scattering From Aircraft

A discussion is now presented of the algorithms used to compute the characteristics of the multipath components due to scattering from the aircraft. It has been assumed[†] that the major contribution to the scattered energy is due to the fuselage and tail fin of the aircraft. In addition, it is assumed that the fuselage can be physically modeled as a horizontal cylinder, and the tail fin as a section of a cylinder, as depicted in Fig. 2-6. These cylindrical surfaces are considered to be perfect conductors with zero roughness.

[†]There is also considerable physical evidence to support this assumption. Measurements of the radar cross section of aircraft[59] show the largest returns are from the fuselage and tail fin. These monostatic results can be directly related to the bistatic case of interest for MLS [60].

BUILDING

H_B = 60'

H_{bottom} = 0

(1 200, 1 200)   (1 400, 1 200)

XMTR
ANTENNA
(0, 0, 9)

RUNWAY

AIRCRAFT
RCVR
h_r = 50'

FREQUENCY IS 5 GHZ
BUILDING IS PERFECT CONDUCTOR,
    0   ROUGHNESS

ATC-63 VI 2-5b

COMPUTATIONS BY
ITT/GILFILLAN USING
GEOMETRIC THEORY
OF DIFFRACTION

COMPUTATIONS USING MODEL
DESCRIBED IN THIS CHAPTER

MULTIPATH AMPL. REL. DIRECT (DB)

XMTR-RCVR DISTANCE (FT)
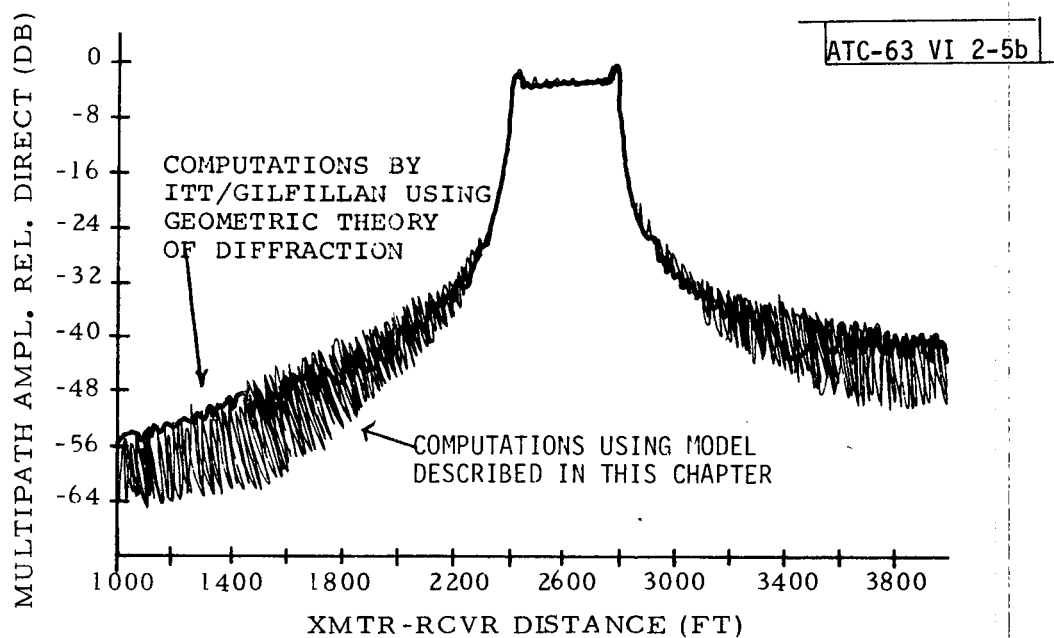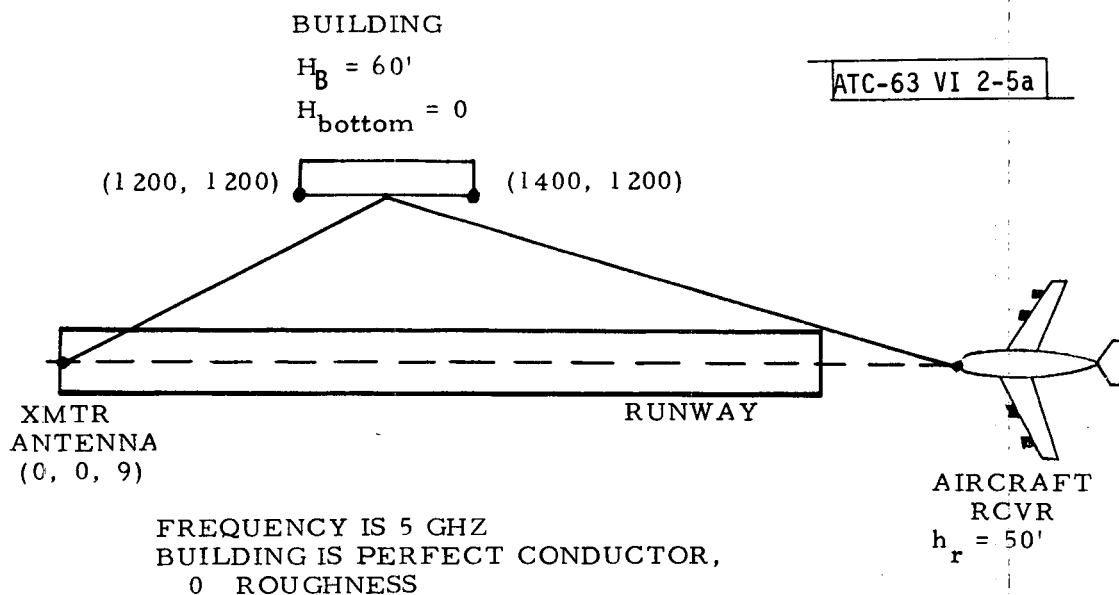
Fig. 2-5.   Illustration of multipath reflections from large
building.
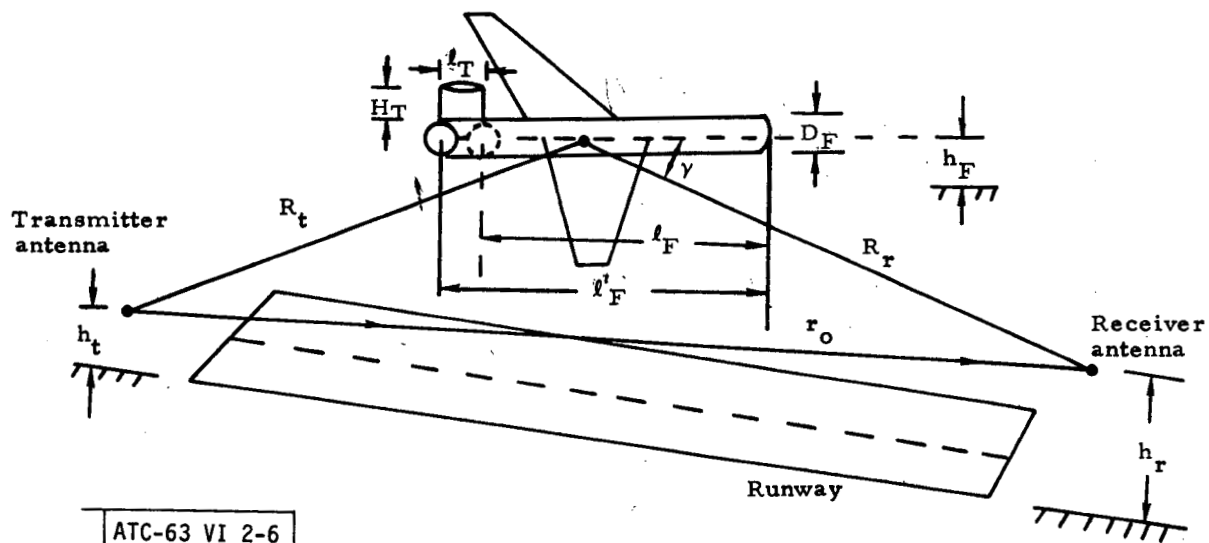
ℓ'_F = fuselage length entered in computer table

ℓ_F (= ℓ'_F - ℓ_T) = fuselage length used in computations

Fig. 2-6. Geometry used for obtaining characteristics of multipath components due to scattering from aircraft.

The amplitude and phase of the multipath components due to scattering from aircraft are computed by employing Babinet's principle, so that we may consider the equivalent problem of diffraction by a rectangular opening in an opaque screen. This procedure is similar to that described previously for the corresponding problem involving buildings. However, in the present case, when dealing with aircraft, a correction factor[52] is applied to take into account the divergence of rays from the cylindrical surfaces used to model the fuselage and tail fin.

The complex reflection coefficient of the multipath component due to scattering from aircraft is computed as

$$\rho_A = \rho_{Aa} \, \rho_{Ae} \, \rho_R \, R_{eq} \quad , \tag{2-21}$$

where R_{eq} is the equivalent Fresnel reflection coefficient which takes into account the depolarization loss due to near-specular reflection from the curved surface of the cylinder, ρ_R is the distance factor given previously in Eq. (2-10), and ρ_{Aa}, ρ_{Ae} are the azimuthal and elevation factors, respectively. We first consider the case of the fuselage, so that the factor ρ_{Aa} corresponds to the azimuthal factor for a building. In this computation the length of the fuselage, ℓ_F, plays the role of W_B, which was defined previously as the width of the building. Thus, the computation of ρ_{Aa} is done in a manner similar to that for ρ_{Ba} given previously in Eqs. (2-16)-(2-18). The factor ρ_{Ae} accounts for the divergence of rays due to the curved surface of the fuselage. Since the factor ρ_{Aa} accounts for the finite length of the fuselage, ρ_{Ae} is computed as if the fuselage were a cylinder which is infinite in extent.

In the case of the tail fin, the factor ρ_{Ae} is computed in a manner similar to that given previously for the elevation factor for a building in Eqs. (2-11)-(2-15). The factor ρ_{Aa}, in this case, accounts for the divergence of rays due to the curved surface of the tail fin.

The amplitude and phase of the multipath component due to scattering from aircraft can be obtained as

$$V_A = |\rho_A| \qquad , \qquad (2-22)$$

$$\psi_A = \text{ARG}\{\rho_A\} + k(R_t + R_r - r_o) \quad . \qquad (2-23)$$

The calculations for the planar azimuth and elevation angles, relative time delay, and Doppler frequency are similar to those presented previously for the multipath component due to specular reflection from the ground. The computations for both the fuselage and tail fin take into account the four ray paths X-0-R, X-G-0-R, X-0-G-R, X-G-0-G-R, discussed previously in connection with the calculations for buildings.

A number of computer validation results have been obtained for the subroutine which computes the characteristics of the multipath component due to scattering from aircraft. An example geometry is shown in Fig. 2-7a. In Fig. 2-7b, we compare the results using the algorithms above with experimental data and calculations by ITT Gilfillan[18]. The ITT calculations are based on modeling the fuselage and wing engine pod by many small plates, and then using the geometric theory of diffraction. It is seen that there is reasonably good agreement between these two sets of data. Also, the algorithm used here is many times faster in computational speed.

McDONNELL DOUGLAS DC-10

ATC-63 VI 2-7a

275'

REFERENCE
LINE

XMTR
ANTENNA
(-44, 0, 7)

RUNWAY

AIRCRAFT
RCVR
$h_r = 10'$

FREQUENCY IS 5 GHz
LENGTH OF FUSELAGE (ℓ_F) IS 107'
RADIUS OF FUSELAGE (R_{fus}) IS 9.8'
HEIGHT OF FUSELAGE (h_F) IS 15'
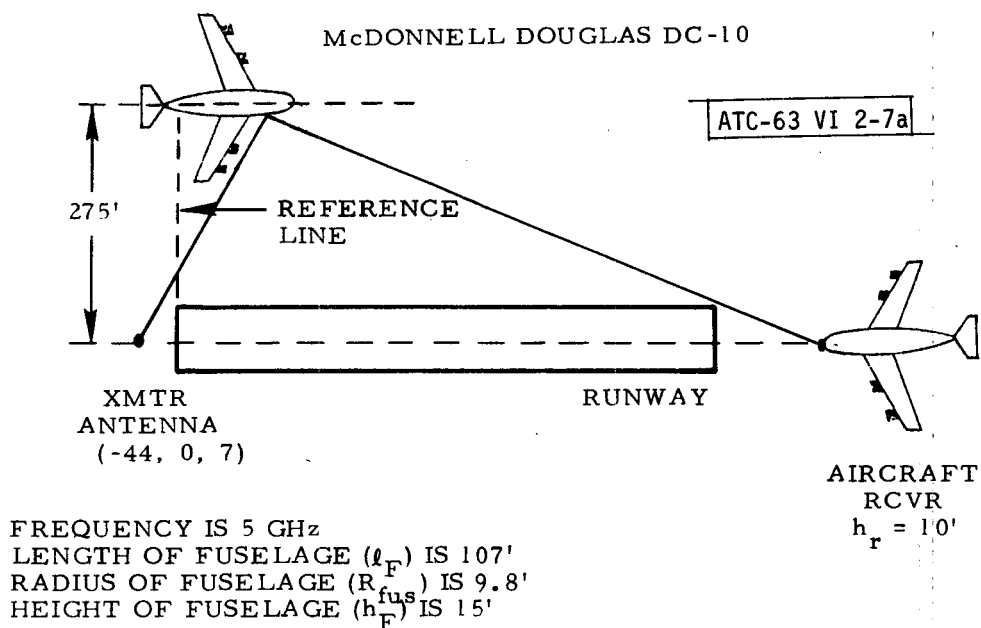
Fig. 2-7a. Geometry for ITT measurements[18] on DC-10 aircraft fuselage.

MEASURED VALUES BY ITT

ITT computations

Lincoln computer
model

ATC-63 VI 2-7b

REFERENCE-RCVR DISTANCE (FT)

MULTIPATH AMPL. REL. DIRECT (Db)
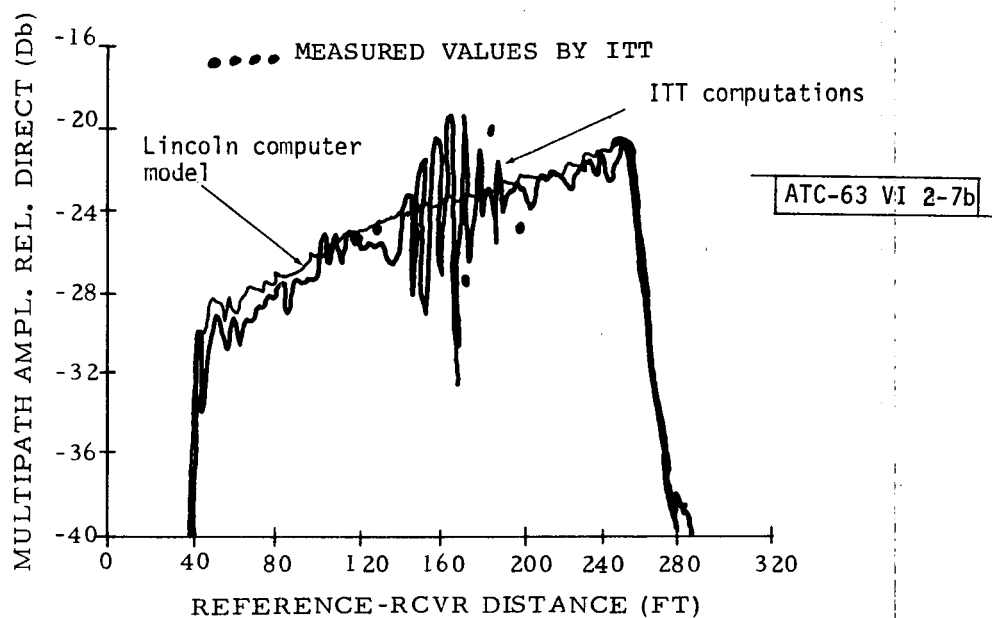
Fig. 2-7b. Comparison of computer simulation results with ITT
computations and field data.

2-16

2.4 Diffuse Scattering From Ground

A description is now given of the computations which were used to obtain the multipath components due to diffuse scattering from the ground. These diffusely scattered waves arrive at the aircraft receiver antenna from a wide range of angles in both azimuth and elevation, due to radiation from a large surface area on the ground known as the glistening surface[48]. In addition, the phase angles and amplitudes of these waves cannot be predicted, from a practical computational point of view, for any rough surface which is a sample function from the ensemble of such rough surfaces. It is only possible to obtain average functionals for these values, where, as usual, the averages are taken with respect to the ensemble of rough surfaces.

It is assumed that the ground can be modeled as a rough surface with a Gaussian height distribution, with root-mean-square roughness height, σ_h, and a Gaussian correlation coefficient with correlation length, σ_ℓ. In order to obtain tractable computations, we have followed Kodis[54], Barrick[55] and McGarty[56], in assuming that the surface is very rough, and that it is perfectly conducting.

The following assumptions are also required in the analysis:

(1) The radius of curvature everywhere on the scattering surface must be much greater than the wavelength of the incident radiation.

(2) Multiple scattering effects can be neglected.

(3) The root-mean-square surface height is much greater than the wavelength.

The condition given in assumption (3) implies that the surface is very rough.

The geometry assumed for diffuse scattering is shown in Fig. 2-8. The mean-square value of the scattered field at the receiver, relative to the directly transmitted field, is

$$\frac{<|E_S|^2>}{|E_o|^2} = \frac{1}{4\pi} \int\limits_{\substack{\text{ground} \\ \text{surface}}} \int \left(\frac{r_o}{R_t R_r}\right) \sigma \, ds \quad , \tag{2-24}$$

where σ is the bistatic radar cross section for the rough surface. It can be shown that

$$\sigma(\theta_S, \phi_S, \phi_i) = \frac{\sec^4 \gamma}{s^2} \exp\left[-\frac{\tan^2 \gamma}{s^2}\right] |R(\xi)|^2 \quad , \tag{2-25}$$

where θ_S, ϕ_S are the scattering angles, ϕ_i is the incidence angle, all depicted in Fig. 2-8, and

$$\tan \gamma = \frac{(\sin^2\phi_i - 2 \sin\phi_i \sin\phi_S \cos\theta_S + \sin^2\phi_S)^{1/2}}{\cos\phi_i + \cos\phi_S}, \tag{2-26}$$

$$s = 2 \sigma_h/\sigma_\ell \quad , \tag{2-27}$$

$$R(\xi) = \frac{-\sin\phi_i \sin\phi_S \sin^2\theta_S + a_2 a_3}{4 \sin^2\xi \cos^2\xi} \quad , \tag{2-28}$$

$\phi_i = \beta$

$\phi_s = \phi$

$\theta_s = \varphi$

$\rho = \phi\, h_r\, \tan\phi$
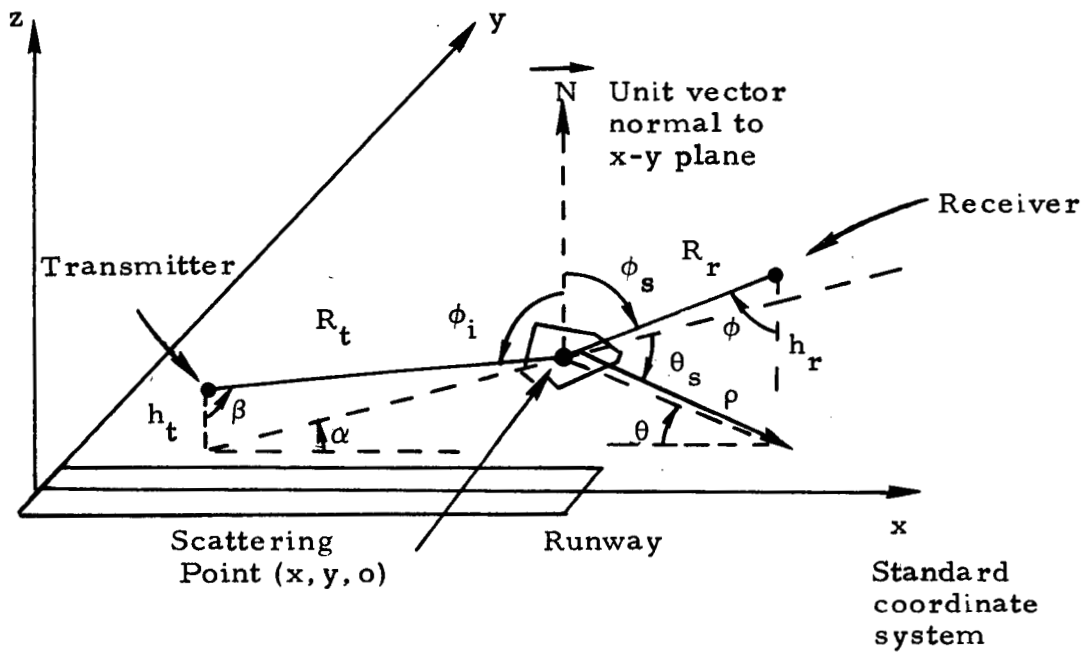
Fig. 2-8. Geometry for diffuse scattering from ground.

$$a_2 = \cos\phi_i \sin\phi_S + \sin\phi_i \cos\phi_S \cos\theta_S \quad , \tag{2-29}$$

$$a_3 = \sin\phi_i \cos\phi_S + \cos\phi_i \sin\phi_S \cos\theta_S \quad , \tag{2-30}$$

$$\cos\xi = \sqrt{\frac{1}{2}} \sqrt{(1 - \sin\phi_i \sin\phi_S \cos\theta_S + \cos\phi_i \cos\phi_S)} \quad . \tag{2-31}$$

We now define the channel spread function, $K(\theta,\phi)$, as the power per square radian incident at the receiver, relative to the directly transmitted power, coming from directions θ in azimuth and ϕ in elevation, cf. Fig. 2-8. This function may be obtained from Eq. (2-24) as

$$K(\theta,\phi) = \frac{1}{\Delta\theta\Delta\phi} \frac{< |E_S|^2 >}{|E_o|^2}$$

$$= \frac{1}{4\pi\Delta\theta\Delta\phi} \int\int_S \left(\frac{r_o}{R_t R_r}\right)^2 \sigma \, dxdy \quad , \tag{2-32}$$

where S is the incremental area defined in the xy-plane by the increments $\Delta\theta$, $\Delta\phi$. It is straightforward to evaluate $K(\theta,\phi)$ from Eqs. (2-25) and (2-32) by noting that $dxdy = \rho d\rho d\theta$, $\rho = h_r \tan\phi$, $\frac{d\rho}{d\phi} = h_r \sec^2\phi = R_f^2(\theta,\phi)$, so that

$$K(\theta,\phi) = \frac{r_o^2}{4\pi} \frac{\sigma(\theta + \alpha(\theta,\phi), \phi; \beta(\theta,\phi))\tan\phi}{R_t^2(\theta,\phi)} \quad , \tag{2-33}$$

where it has been assumed that $\Delta\theta$, $\Delta\phi \to 0$, and where the dependence of the various quantities in Eq. (2-33) on θ,ϕ has been taken into account and use has been made of the fact that $\theta_S = \theta + \alpha$, $\phi_S = \phi$, $\phi_i = \beta$, cf. Fig. 2-8.

The relative magnitude of the scattered wave coming from the direction θ to θ + Δθ, in azimuth, and φ to φ + Δφ, in elevation, is

$$V_D(\theta,\phi) = K^{1/2}(\theta,\phi) \cdot (\Delta\theta\Delta\phi)^{1/2} \quad , \qquad (2-34)$$

while the relative phase shift, $\psi_D(\theta,\phi)$, is randomly selected from the interval (-π,π) for each different pair of angles (θ,φ). The planar angles, Doppler frequency, and time delay for each multipath component is computed in a manner similar to that given previously for the multipath component due to specular reflection from the ground.

We now present some of the computer results for the subroutine which performs the computations for diffuse scattering from the ground. In Fig. 2-9 we have plotted max $V_D(\theta,\phi)$ for -π ≤ θ, φ ≤ π for a typical linear 3° flight path. The fluctuation of the amplitude of this multipath component is seen from this figure to be quite rapid along the flight path. In addition, the level of this multipath component is quite small, on the order of -35 dB, and less. This behavior appears to be quite typical for the diffuse ground scattered multipath component. It should be observed that the low level of this multipath component tends to make it relatively unimportant as far as MLS performance is concerned.

2.5 Shadowing Due To Runway Humps

A discussion is now presented of the shadowing, or attenuation, of the directly transmitted signal due to the convex runway surfaces, or humps, which occur in a typical airport environment. The diffraction geometry for this
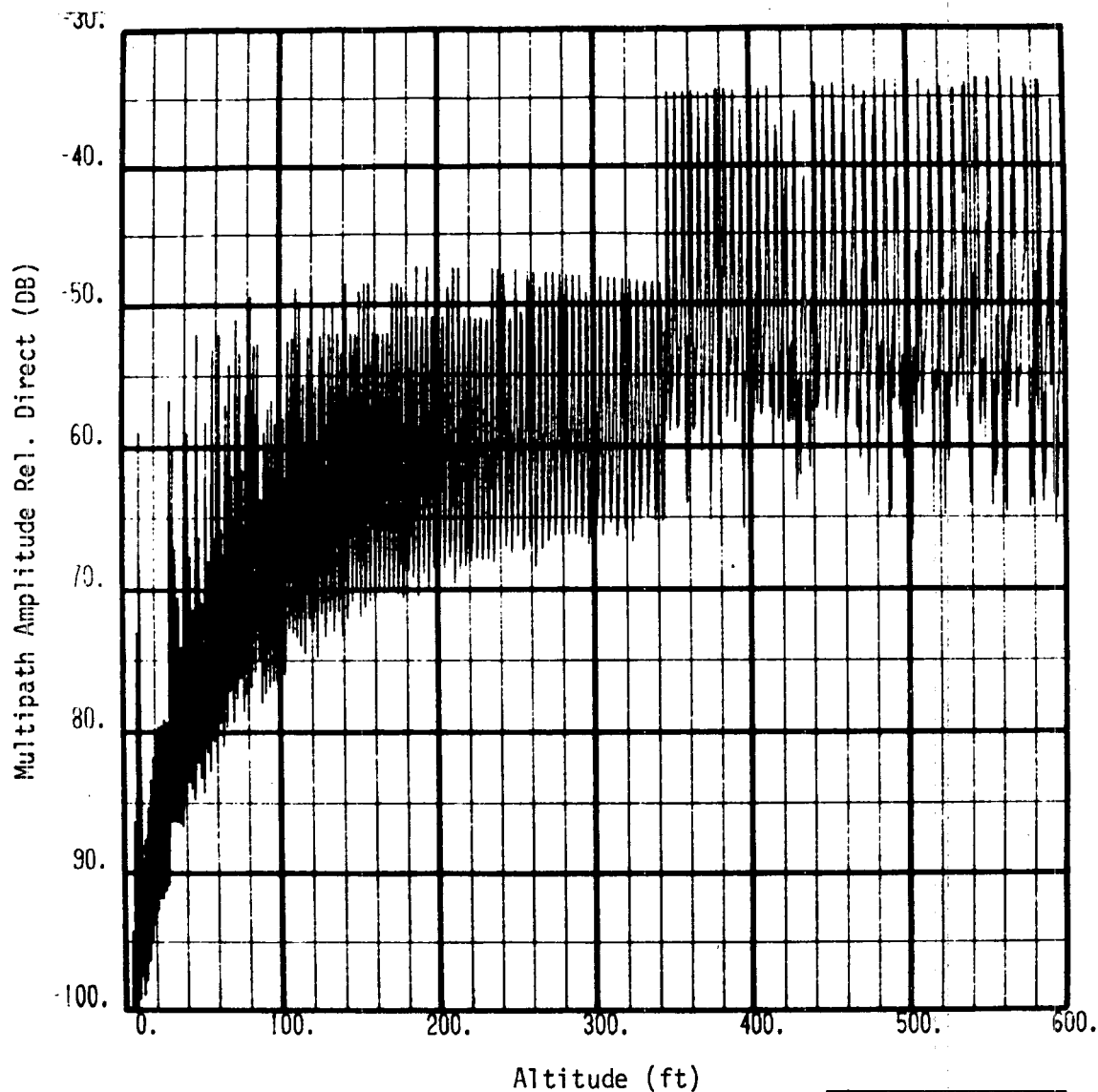
Fig. 2-9. Plot of amplitude, in dB, of diffuse ground scattering multipath component, with largest amplitude, vs altitude, for transmitter at (-500, 0, 8), receiver on linear 3° flight path between (9000, 0, 0) and (21000, 0, 600), σ_h = 0.5', σ_ℓ = 1.0'.

problem is assumed to be that shown in Fig. 2-10, and corresponds to that employed by the United Kingdom Royal Aircraft Establishment[27] to describe their experimental data on shadowing due to runway humps. The physical model for the runway is that of a triangle which coincides with the surfaces leading up to the hump. This model involves the treatment of four ray paths as shown in Fig. 2-10. The first ray path from transmitter to receiver corresponds to that of classical knife edge diffraction theory. The other three ray paths from image transmitter to receiver, transmitter to image receiver, and image transmitter to image receiver, are required in order to have a model which yields results that are somewhat in agreement with experimental data.

The ratio of the diffracted wave to free-space signal is given by

$$\frac{E_D}{E_o} = \sum_{i=1}^{4} \rho_i \, A_i \, G(\alpha_i, \beta_i) e^{j(\psi_i + k(D_i - D_1) + \phi_i)} \quad , \tag{2-35}$$

where the index i = 1,4 corresponds to the four ray paths shown in Fig. 2-10 and

$$A_i = \left[\frac{(\frac{1}{2} - s_i)^2 + (\frac{1}{2} - c_i)^2}{2} \right]^{1/2} \quad , \tag{2-36}$$

$$c_i = \int_0^{u_i} \cos(\frac{\pi}{2} x^2) \, dx \quad , \tag{2-37}$$
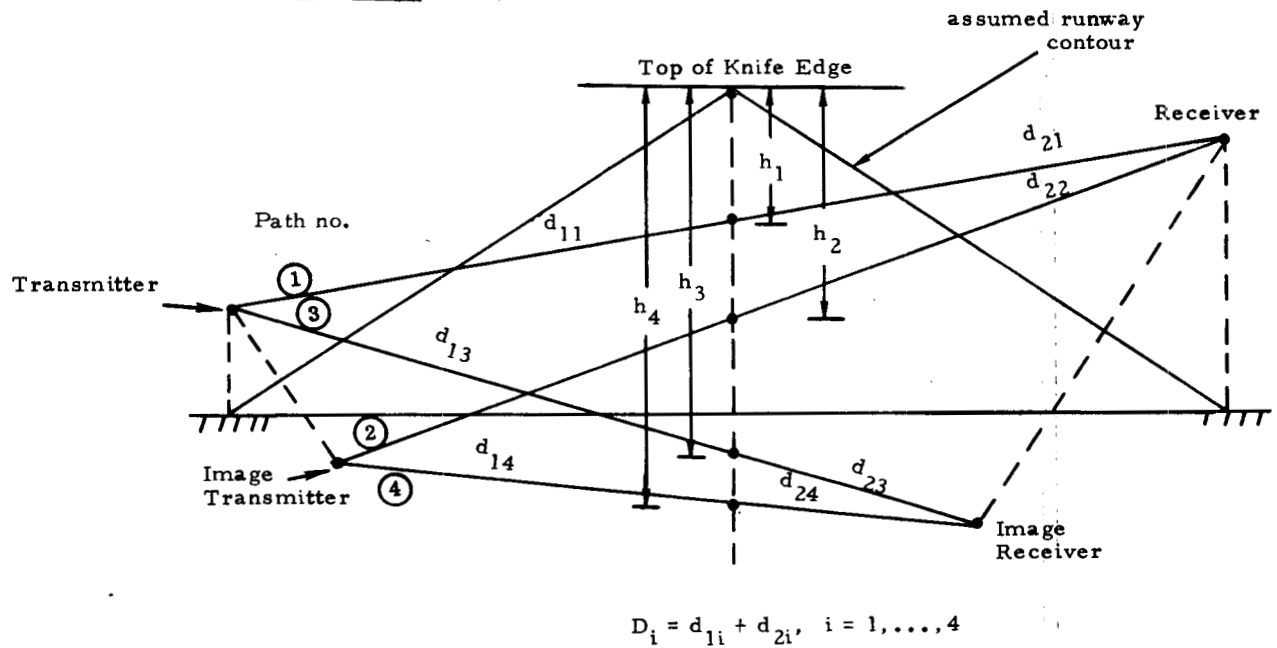
Fig. 2-10.   Diffraction geometry used for runway hump shadowing problem.

$$D_i = d_{1i} + d_{2i}, \quad i = 1, \ldots, 4$$

$$S_i = \int_0^{u_i} \sin\left(\frac{\pi}{2} x^2\right) dx \qquad , \qquad (2\text{-}38)$$

$$u_i = h_i \left(\frac{2 D_i}{\lambda \, d_{1i} \, d_{2i}}\right)^{1/2} \qquad , \qquad (2\text{-}39)$$

$$\psi_i = \frac{\pi}{4} - \tan^{-1}\left[\frac{\frac{1}{2} - S_i}{\frac{1}{2} - C_i}\right] \qquad , \qquad (2\text{-}40)$$

and the quantities k, λ are the wavenumber and wavelength of the free-space signal defined previously. The factor $\rho_i e^{j\phi_i}$ is the complex reflection coefficient due to reflection from the ground for the i-th ray path, i = 1,4, cf. Fig. 2-10. We have $\rho_1 = 1$ and $\phi_1 = 0$, and it is assumed that $\rho_2 = \rho_3 = \rho, \rho_4 = \rho^2$, $\rho = 1$, and $\phi_2 = \phi_3 = \pi, \phi_4 = 2\pi = 0$ (mod 2π). The quantity ρ can be set to a value other than unity in the computer program, if so desired.

The amplitude and phase of the direct wave, after the effect of shadowing is taken into account, are obtained from Eq. (2-35) as

$$V_{SH} = |E_D/E_O| \qquad , \qquad (2\text{-}41)$$

$$\phi_{SH} = \text{ARG}\{E_D/E_O\} \qquad . \qquad (2\text{-}42)$$

In actuality, the amplitude and phase of the direct wave, in the MLS computer simulation program, are fixed at unity and zero, respectively. Therefore, the multipath amplitudes are multiplied by $1/V_{SH}$, and the phase angle ϕ_{SH} is subtracted from the multipath phase angle. It should be noted that this computation is performed in the receiver signal processing subroutines,

since the transmitter radiation pattern, $G(\alpha_i, \beta_i)$ is system-dependent. That is, the runway hump computational subroutine obtains the quantities $T_i(=A_i e^{j(\psi_i + k(D_i - D_1) + \phi_i)}$, α_i, β_i, $i = 1,4$, and passes these 12 values to the receiver subroutines, which then combine them appropriately, according to the system being considered, to determine the shadowing effect.

A comparison is now given of the computational results obtained for the signal loss due to runway hump shadowing, as outlined in this section, with some experimental data due to the U.K.R.A.E. These data are shown in Fig. 2-11, which depicts the C-band signal loss measured by the UK along the Bedford main runway and the corresponding computational results for a transmitter antenna height of 1.0 feet.

The agreement between the experimental data and predictions is regarded as fair. For other transmitter heights, the computer model shows sizable oscillation in V_{SH} as the LOS is almost blocked which do not appear in the field data. We will attempt to resolve these differences in two ways during the next phase of activity. Discussions are to be held with RAE to better ascertain the amount of smoothing used in their data plots as well as experimental procedures, fine grain runway contour, etc.

Secondly, we will investigate an alternative computational approach based on physically modeling the hump as a paraboloid[26,58]. It is our hypothesis that the discontinuity at the apex of the triangle accounts for much of the differences between computed fields and field results. Since runway construction standards[61] call for a smooth transition between runway sections of differing slope, this alternative physical model should be more realistic.
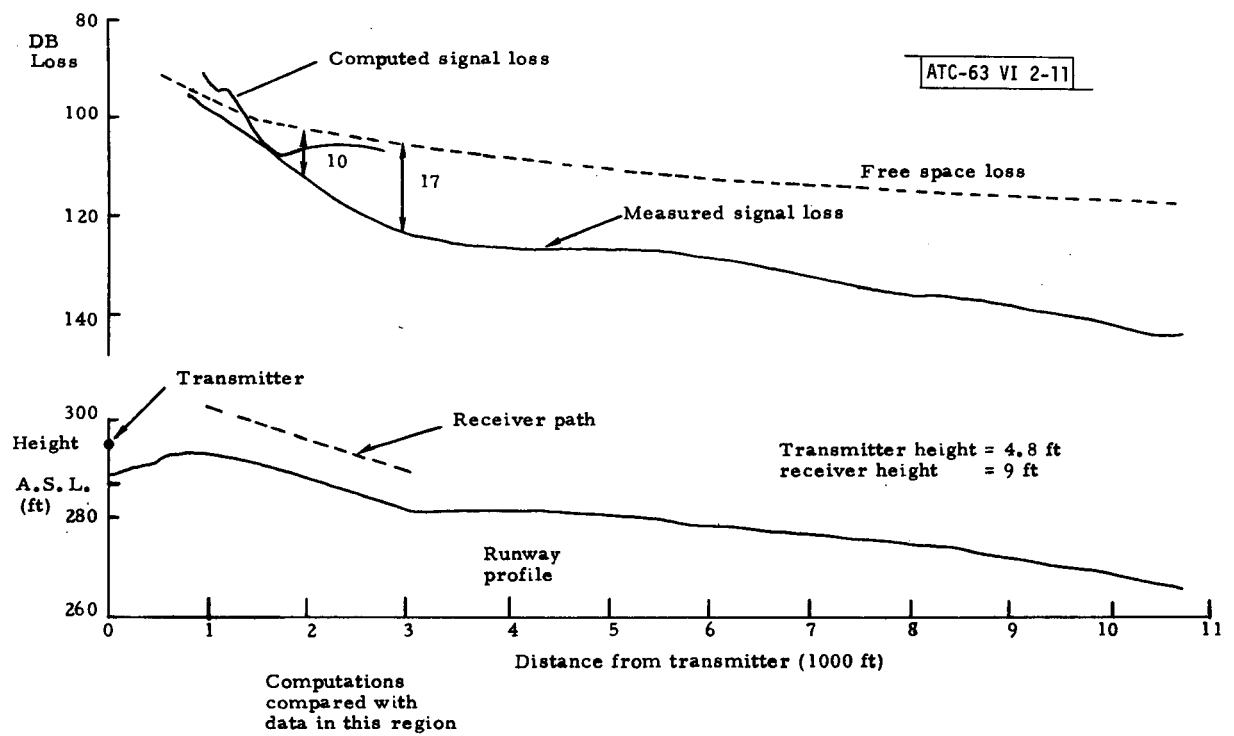
Fig. 2-11. Comparison of multipath model with UK measurements of C-band signal loss, due to runway hump shadowing, at R.H.E. Bedford (U.K.) main runway.

2.6 Shadowing Due To Aircraft Approaching Line of Sight

We now consider the shadowing effect, due to forward scattering, when an aircraft approaches the line of sight between the transmitting and receiving antennas. In this case, diffraction phenomena occur, rather than reflections. The magnitude of the forward-scattered wave depends, in general, on the shape of the aircraft projected onto the plane perpendicular to the line of sight. For simplicity, this projected area is taken to be a circular disk of the same area. The diffraction effects are then assumed to be due to this circular disk. It is assumed that this diffraction signal can be treated as a multipath signal with parameters which will be be specified.

The geometry assumed for the forward scattering due to the aircraft is shown in Fig. 2-12a. An estimate of the projected area may be obtained from this figure as

$$A_p = \pi r_F^2 \cos \theta_1 + (A_W + 2r_F \ell_F) \sin \theta_1 \quad . \tag{2-43}$$

The forward-scattering cross section is taken as

$$\sigma_F = \frac{4\pi A_p^2}{\lambda^2} \left[\frac{2J_1(u)}{u} \right]^2 \quad , \tag{2-44}$$

where $u = D_{DISK} \sin \psi / \lambda$, ψ is the angle between the line from blocking aircraft to receiver and the line of sight to blocking aircraft, as illustrated in Fig. 2-15b, and

$$D_{DISK} = \left(\frac{4}{\pi} A_p \right)^{1/2} \tag{2-45}$$

The ratio of the scattered energy to that of the direct signal is then

$$\frac{|E_s|^2}{|E_o|^2} = \frac{r_o^2}{4\pi R_t^2 R_r^2} \sigma_F$$

$$= \left(\frac{r_o A_p}{R_t R_r \lambda}\right)^2 \left[\frac{2J_1(u)}{u}\right]^2 \quad . \qquad (2\text{-}46)$$

Hence, using Eq. (2-44), the relative magnitude of the forward-scattered wave at the receiver is

$$V_F = |E_s|/|E_o|$$

$$= \frac{A_p r_o}{\lambda R_t R_r} \left|\frac{2J_1(u)}{u}\right| \cdot G(\alpha,\beta) \quad . \qquad (2\text{-}47)$$

The relative phase-shift, ψ_F, of the forward-scattered wave is taken as π radians if $J_1(u)/u$ is positive and 0 if $J_1(u)$ is negative. The relative time delay is assumed to be

$$\tau = (R_t + R_r - r_o)/c \quad , \qquad (2\text{-}48)$$

with a zero relative Doppler frequency. The values of α and β used in the transmitter antenna pattern $G(\alpha,\beta)$ are taken to be those corresponding to the direction from the transmitter to the center of the blocking aircraft.

If for a given geometry V_f is too large (e.g., $V_F > 0.5$), then the assumption of Fraunhofer diffraction which is implicit in the use of a
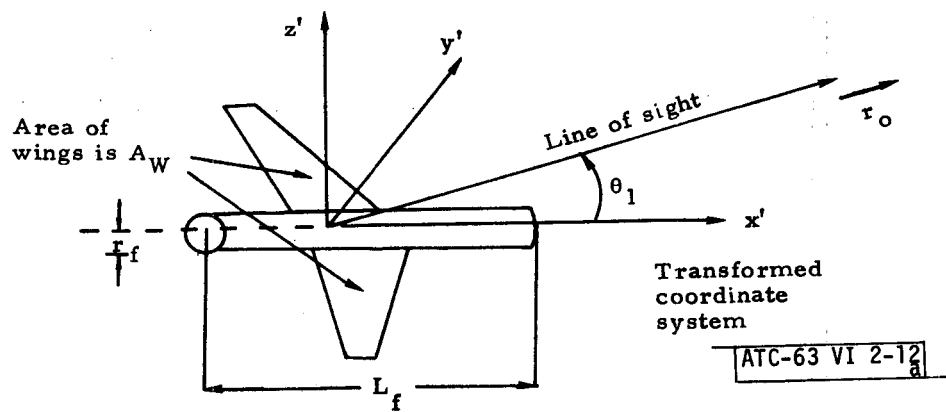
$$r_O = r_o = \text{Distance between x MTR and RCVR}$$

Fig. 2-12a. Geometry for forward scattering due to aircraft approaching the line of sight.
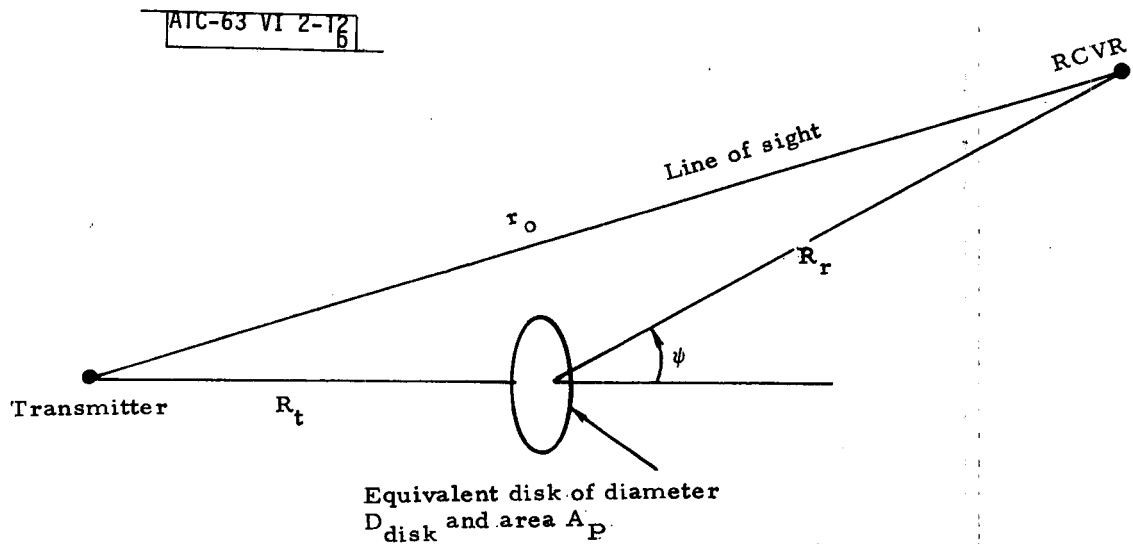
Fig. 2-12b. Disk model for obtaining shadowing effect due to aircraft approaching the line of sight.

2-30

forward scattering cross section is no longer valid. The phase II version
of the computer simulation program will flag such an occurrence as total
blockage and attempt no further signal processing at that particular eval-
uation point.

A more refined Fresnel diffraction model which takes better account
of the projected aircraft shape is under active development and should be
operational shortly. The computational algorithms for this model are based
on the notion of edge rays and obstacle rays somewhat analogous to the rays
used in the geometric theory of diffraction[62]. This edge ray theory (which
will be described in a subsequent report) has been applied successfully to
explain some of the shadowing test data obtained in the Discrete Address
Beacon System (DABS) program[64]. Thus, this more refined approach is felt
to be highly desirable for determining the shadowing effect due to aircraft,
and also buildings, approaching the line of sight between transmitter and
receiver.

III. SCATTERING MODEL VALIDATION

A key feature of the MLS multipath model development is validation of the model by comparison with appropriate field data.[†] During the first phase of the study, the principal focus has been on data at a carrier frequency of 5.1 GHz, although some comparisons have been made at 15 GHz and 1090 MHz. The key points to be addressed in the validation were:

(1) Does the physical model assumed for the scatterers at the airport make sense? This involves issues such as whether buildings scatter much like a flat plate coplanar with the vertical walls and whether aircraft tail fins yield specular reflections over a range of angles corresponding to a section of a cylinder. Another issue of the same type is the number of scatterers which need to be modeled in a given environment.

(2) With appropriate specification of parameters such as dielectric constant and surface roughness, do the quantitative predictions of the model agree well with the field data?

To answer these questions, Lincoln made an indepth analysis of field measurements sponsored by the FAA and various other organizations. Although field measurements involving multipath effects on MLS date back to the late

---

[†]Validation of the computational algorithms by comparison with more exact theoretical calculations was presented in Chapter II.

1950's[1-15], it was found that only the later data was obtained carefully enough to address the issues above. This later data included:

(a) MLS contractor TACD measurements as well as the MLS phase II measurements at NAFEC and Wallops Island[18, 22, 26, 30-34].

(b) United Kingdom measurements at RAE Farnborough and Bedford[27].

(c) USAF measurements at Wright-Patterson AFB (WPAFB)[28].

It was soon realized that there was actually little data to address point (1) above in the context of large civilian airports. Consequently, Lincoln acted as technical director for an extensive set of multipath experiments at Logan Airport, the results of which are discussed in section 3.1. The UK and MLS contractor TACD data of principal interest for validation was presented in the previous chapter. In section 3.2, we describe some of the relevant re-sults of the WPAFB data. Section 3.3 considers the data obtained by the MLS Phase II contractors at NAFEC and Wallops Island.

3.1 The Logan MLS Multipath Experiment

The Logan MLS multipath experiment was performed at the Logan Interna-tional Airport with the cooperation of its owner, the Massachusetts Port Authority. It was a joint effort (sponsored by the FAA) of Lincoln Laboratory and the Institute of Telecommunication Sciences (ITS), Boulder, Colorado. ITS provided the means of taking and processing the C-band data and Lincoln super-vised the experiment and analyzed the processed data. The data were taken during two periods, from 17 October 1974 to 26 October 1974 and from 8 December 1974 to 13 December 1974. Since this data has been described elsewhere[29], our objective here will be to briefly discuss some of the highlights.

3-2

Carrier wave data was taken, but the dominant signal waveform used for the experiments was short pulses (6.67 nsec) so that delays due to transmission path differentials as small as 7 ft could be detected. Pulse compression and incoherent integration were used to achieve the necessary levels of signal-to-noise ratio. Because of this fine resolution, one multipath reflection can be distinguished from another and each compared to the model predictions. Any reflections unaccounted for by the model would be recognized as such (none, however, were found).

The choice of a six-foot parabolic dish as the transmittting antenna provided a narrow pencil beam (2° between 3 dB points) so that usually only one object at a time was illuminated. Also, by tilting the dish upwards by approximately 1.6°, the ground reflections could be reduced to a level similar to that which would be encountered by a well designed MLS. This greatly helped to establish the integrity of the measured levels and allowed for direct comparisons with the model results.

The locations of the transmitter and receiver were both known to within approximately 15 ft. Locations were generally determined by noting positions relative to some marking on the runway or some object which could be located on the area photograph of the airport map. In a few cases where the data provided estimates of the separation between transmitter and receiver, a comparison was made with the estimation provided by the photograph/map technique and this resulted in excellent.agreement.

One major purpose of the experiment was to test a key hypothesis of the Lincoln multipath model; namely, that a building could be reasonably modeled

by a few flat plates, each with a suitable reflection coefficient. This was, in fact, borne out by the data.

For the purposes of multipath reflections, buildings could generally be classified into one of two categories: (1) buildings with complex surfaces (broken by columns, jetways, etc.) and low reflections, and (2) buildings with simple surfaces. For both, the model is a plate that concurs (in size) with the dimensions of the building. For the latter case, the reflection coefficient is determined from the dielectric property of the building surface material, while for the former case the reflection coefficient is chosen to be commensurate with peak measured M/D levels and not related to the construction material. This was due to the fact that the complicated surfaces generally broke up the reflected signal, thereby reducing the M/D levels significantly below that which would be expected for a homogeneous plate, while not producing measurable reflections elsewhere.

Both simple and complicated faced buildings were used during the experiment. Typical for a complicated faced building was Pier C, shown in Fig. 3-1. A series of measurements were made on Pier C from runways 4R-22L and 4L-22R as shown in Fig. 3-2. No reflections that did not correspond to a specular reflection or diffraction from the building were observed.

For example, from transmitter site T1, geometric optics suggests that no appreciable multipath would be observed from Pier C for receiver positions anywhere along runway 4-22L. No reflections as large as -32 dB with respect to the direct signal were observed. From transmitter site T2, geometric

Fig. 3-1. Pier C (building 33) at Logan airport.
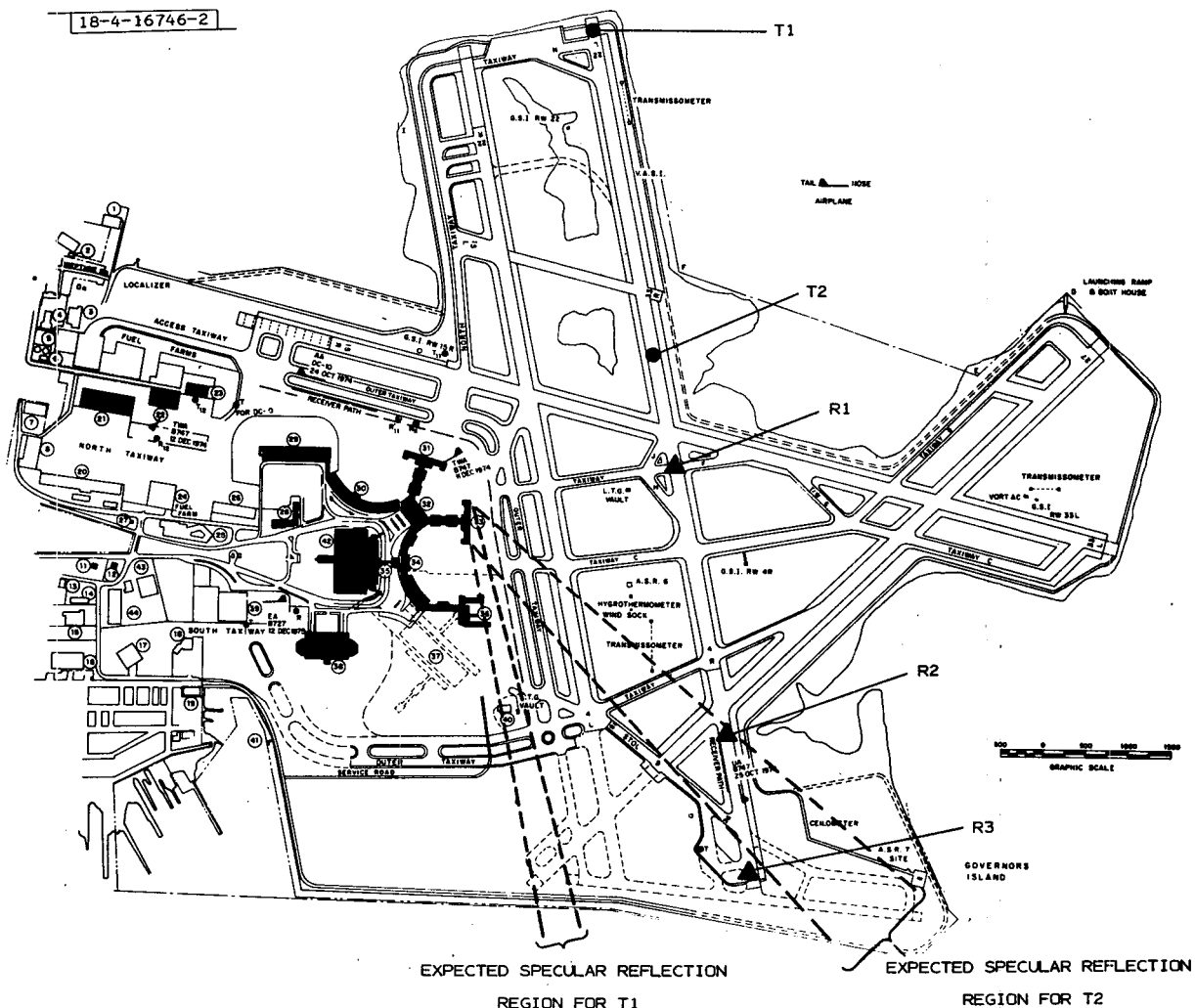
Fig. 3-2. Location of aircraft, transmitters, and receivers for airplane and terminal building multipath experiments at Logan International Airport.

optics suggests that reflections would only be encountered between receiver points R2 and R3. And indeed, this was the case with the field data. The measured levels of multipath often varied rapidly with the specular point. This behavior is not represented by the model, but it is not important since the largest reflections were small and the model reflection coefficient can be chosen to correspond to the peak level observed.

It should be emphasized that the terminal area was quite active at the time the measurements were made. However, the only measurable reflections for the measurements of Fig. 3-2 were from Pier C and from what is believed to be an aircraft on the taxiway between runway 4-22R and Pier C. This is an important experimental finding since it suggests that many of the complicated features (delivery trucks, luggage carts, etc.) in a terminal area may be ignored as far as modeling significant multipath is concerned.

Similar measurements were performed on the other major buildings bordering the runway, in particular, Pier D and the International Building. In all cases, the results were essentially identical to those of Pier C above.

The Delta hangar, pictured in Fig. 3-3, is a simple faced building. The section to the left is metal clad and reflections from it can be compared quantitatively to the model's. The transmitter and receiver were positioned so that as the receiver antenna height was changed (referred to as a mast run), the specular point moved vertically along the face of this left-hand section. As the specular point moved across the lower edge of the large, metal part at

Fig. 3-3. The Delta hangar.

the top of the building, edge diffraction was observed. The results are compared to that of the model in Fig. 3-4. We see that there is good agreement.

Reflections from airplanes were also studied and utilized to improve and verify the aircraft models used for multipath computations. During the experiment it was found that the tail was the main source of airplane multipath reflection for the geometries used. The wings are not suitably oriented to cause reflections for MLS, and the fuselage is doubly curved in the front and rear and is shadowed by wings and engines in the center. The tail is large, oriented for reflections, relatively flat, and because it is angled slightly upward and is slightly curved, it generates reflections over large angles in space. The original model overestimated in both level and extent the reflections from the fuselage and underestimated the vertical extent of the tail reflections. By exaggerating the tail height, by choosing the largest tail fin length, and by decreasing slightly the fuselage length, better agreement between measurement and model are achieved. Alternatively, one could tilt the tail of the model instead of exaggerating its height. Model fuselage M/D levels were generally higher than those observed, but this is acceptable because: (1) the measurements were at geometries[*] at which more wing blockage occurs than would occur in more realistic scenarios, (2) it was felt that a cylinder model for fuselages is very reasonable physically, and (3) it is better for the model to overestimate multipath levels rather than underestimate them.

---

[*]In particular, the restricted range of receiver heights.

DELTA
HANGAR

ATC-63 VI 3-4

52°   53°

680 FT

675 FT

1025 FT
1025 FT
1100 FT

52°
R'₆   47°
16.5°   14°   R₆

1075 FT
33°
37.5°
1250 FT

$R_o = 420.2$ FT
$R_f = 9.0$ FT

$R_o = 407$ FT
$R_f = 8.9$ FT

T₆

SCALE (ft)
0   100   200   300   400   500
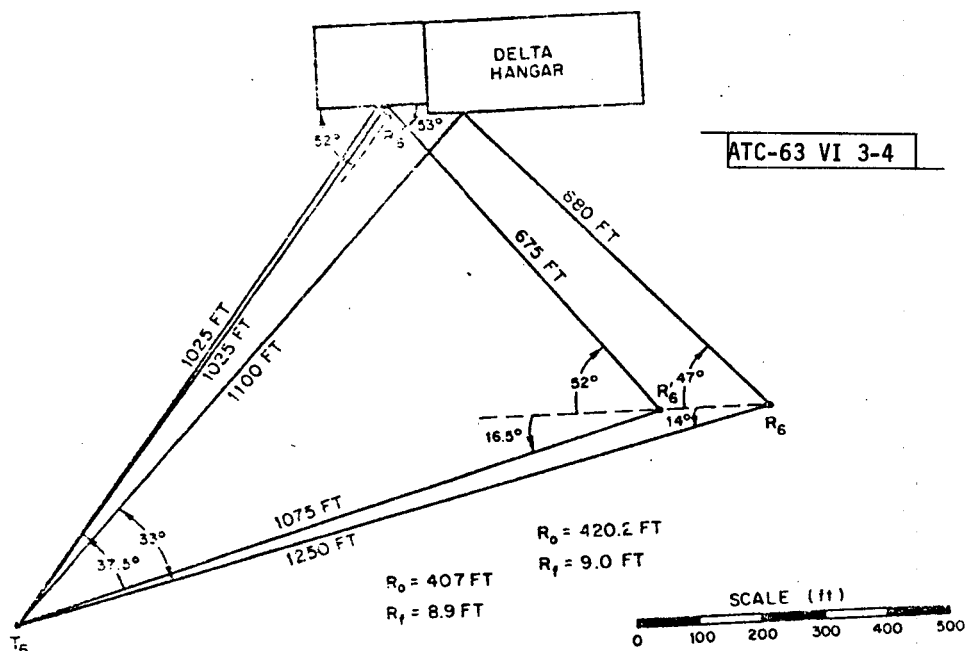
(a) Geometry for 8 December 1974.
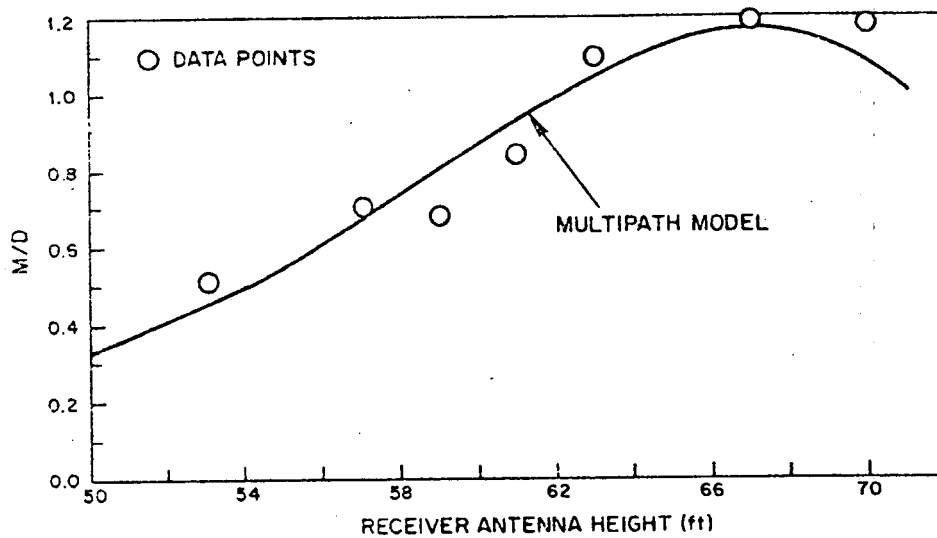
(b) Comparison of 8 December 1974 data with multipath model M/D results.

Fig. 3-4. Results of Delta hangar multipath measurements.

Figure 3-5a illustrates the geometry of the transmitter and receiver relative to a Boeing 747. Note that the angle of the incoming ray, referenced to the centerline of the plane, is 20°, while that of the outgoing ray is 35°. The curvature of the tail is responsible for this result. A receiver mast run was performed and the measured levels are superimposed on top of the model results in Fig. 3-5b. We see that the data follows the overall shape of the model curve as well as agreeing in level. Similar measurements and results were also obtained for DC-10 and B 727 aircraft.

In summary, it was established that the location of all important building reflections could be determined by modeling the buildings by simple, flat plates and using geometrical optics and diffraction theory. Although other refelctions occur, they apparently are so far below the direct levels that they can be readily ignored and, in fact, were not large enough to be measured in our experiment. Buildings, therefore, could be classified into two categories, complicated and simple. Complicated buildings, such as most terminal buildings, appear to be modelable by a single plate with a reflection coefficient commensurate with peak measured levels. Simple buildings, such as hangars, can be modeled by one or two plates whose reflection coefficients are determined by the dielectric and roughness properties of the surface construction material.

Aircraft reflections are more complicated because of the multitude of curved surfaces involved. The result is that there is no single number which tends to characterize reflections as is the case with many buildings. In addition, it is more difficult to judge the angular extent of the reflections
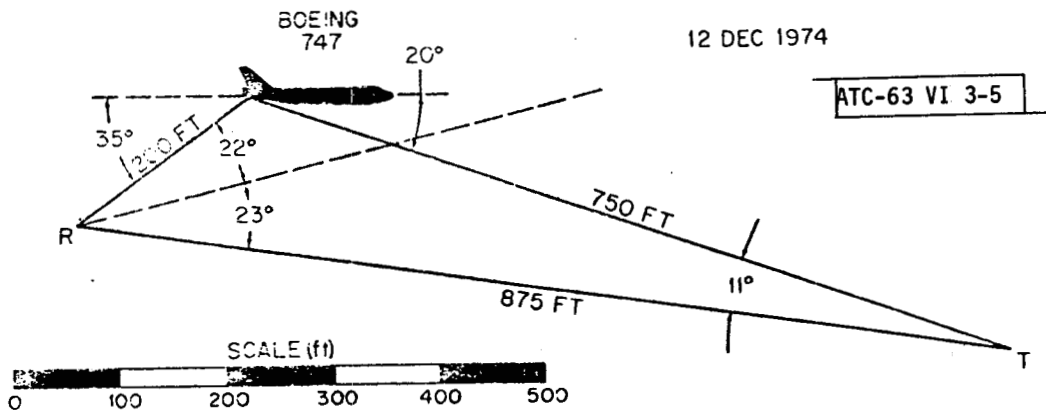
(a)   Geometry for 12 December 1974 Boeing 747 mast run.
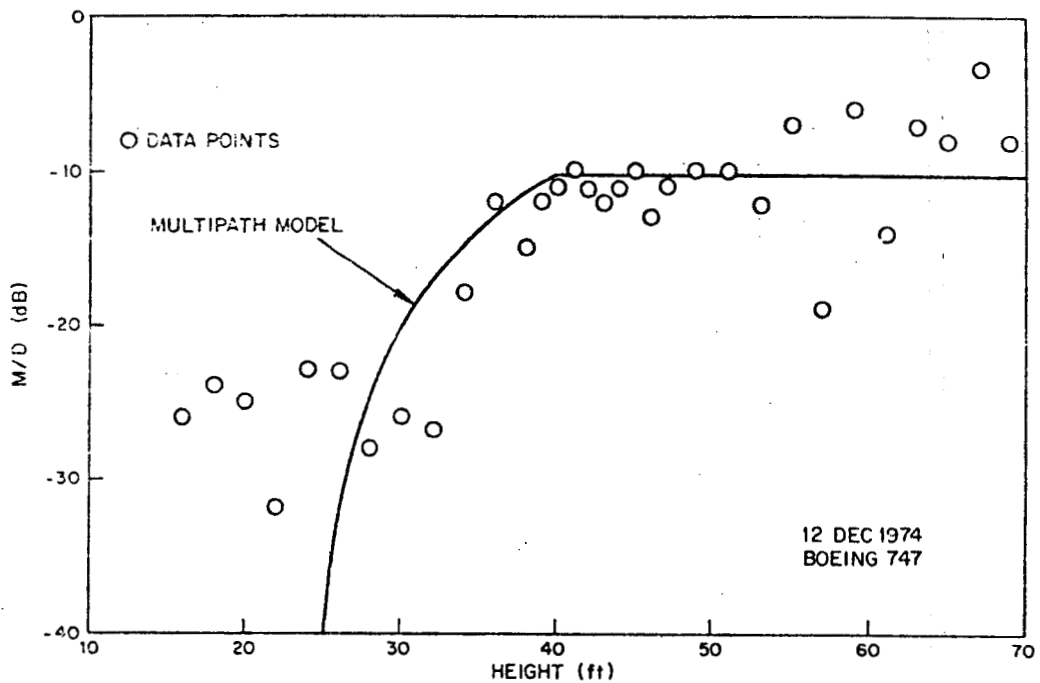
(b)   Comparison of 12 December 1974 data with multipath M/D results.

Fig. 3-5.   Results of B747 tail fin measurements at Logan airport.

and one is more dependent on the model for determination of the range of the reflection and the level for any particular geometry. There remains one principle which we can state. For airplanes on the ground, their tail reflections tend to dominate over other reflections for a couple of reasons. First, for the geometries that are likely to be found between the transmitter, airplane and receiver, the tail is curved and oriented for reflections over a wider variety of situations. Second, fuselage reflections are often shadowed by the wings.

Good agreement between the model and experiment results was noted. There are some deficiencies in the airplane model due to the necessary simplicity of the model, but the resulting discrepancies should not be important. The utility of the model in helping to categorize and understand data from experiments and in extrapolating to new situations is obvious.

3.2   The Wright-Patterson Air Force Base Experiment

In the spring of 1974, an experimental program to measure multipath at Wright-Patterson Air Force Base (WPAFB), using a 5.130 GHz carrier signal, was undertaken by the Illinois Institute of Technology Research Institute (IITRI). Broad antenna patterns, unlike those proposed for MLS, were used through the experiment so that it is difficult to make a direct comparison between the measured multipath levels and MLS multipath. In addition, the broad beams cause ground reflections which contribute significantly to the measured M/D level as illustrated in Fig. 3-6. Unfortunately, IITRI made no attempt to account for them or to characterize the ground so that others
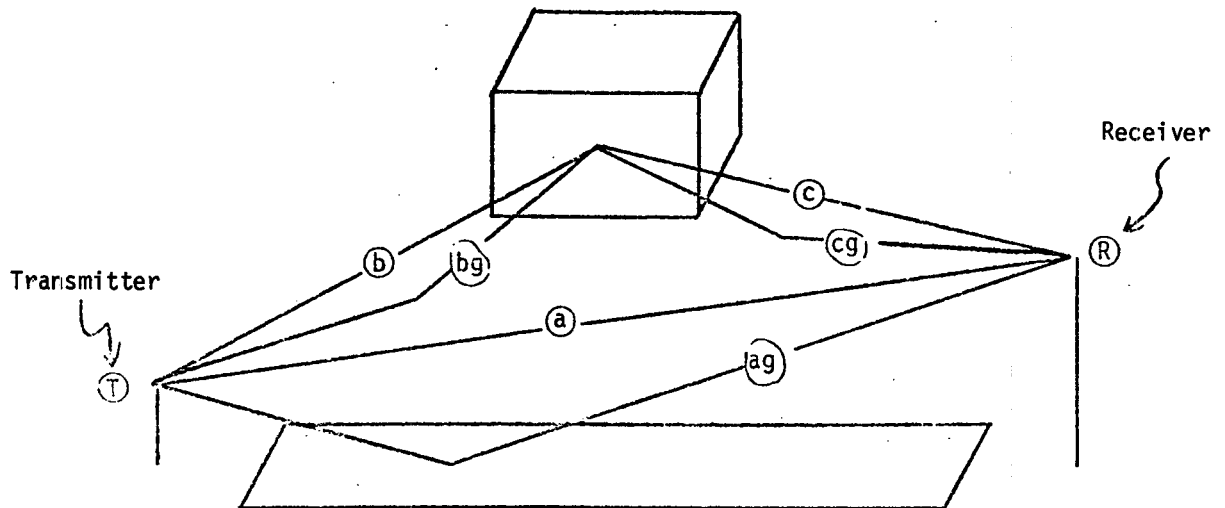
Measured "DIRECT" signal level depends on paths a and ag

Measured "MULTIPATH" signal level depends on paths b, bg, c, cg

Fig. 3-6.   Role of ground reflections in determining multipath/direct amplitude ratio.

might attempt to do so. As a result, the levels of the multipath could not be conclusively interpreted. Only the extent over which the multipath is observed has any real validity. The results applicable to the computer model validation are, therefore, limited. They are: (1) the scalloping patterns due to interaction between direct and reflected signals as a function of receiving position, (2) the extent of reflections as compared to predictions from ray geometry, and (3) the importance of ground reflections in determining the M/D level.

Figure 3-7 shows the section of WPAFB used for the multipath measurements. Unlike Logan Airport, where the building visible from the runways were primarily terminal buildings with jet ports, etc., at WPAFB, the buildings were primarily hangars which opened towards the runway. The surfaces typically were glass in a metal framework or corrugated asbestos with the exception of building 485 which was smooth concrete. The screens were the same as those used in the FAA tests at Wallops Island. Since these walls were typically quite homogeneous, one would expect them to reflect much like flat plates. And indeed, it was observed that in all cases the building and screen reflection regions were highly predictable as means of ray geometry.

The degree of coherence between the direct signal and reflected signals is of particular importance for assessing motion averaging[*] improvement in a given situation. It was not possible to investigate this with the measurement equipment at Logan; however, at WPAFB measurements were made of the scalloping in received signal power between a direct signal and a building

---

*See Chapter V for a discussion of motion averaging.
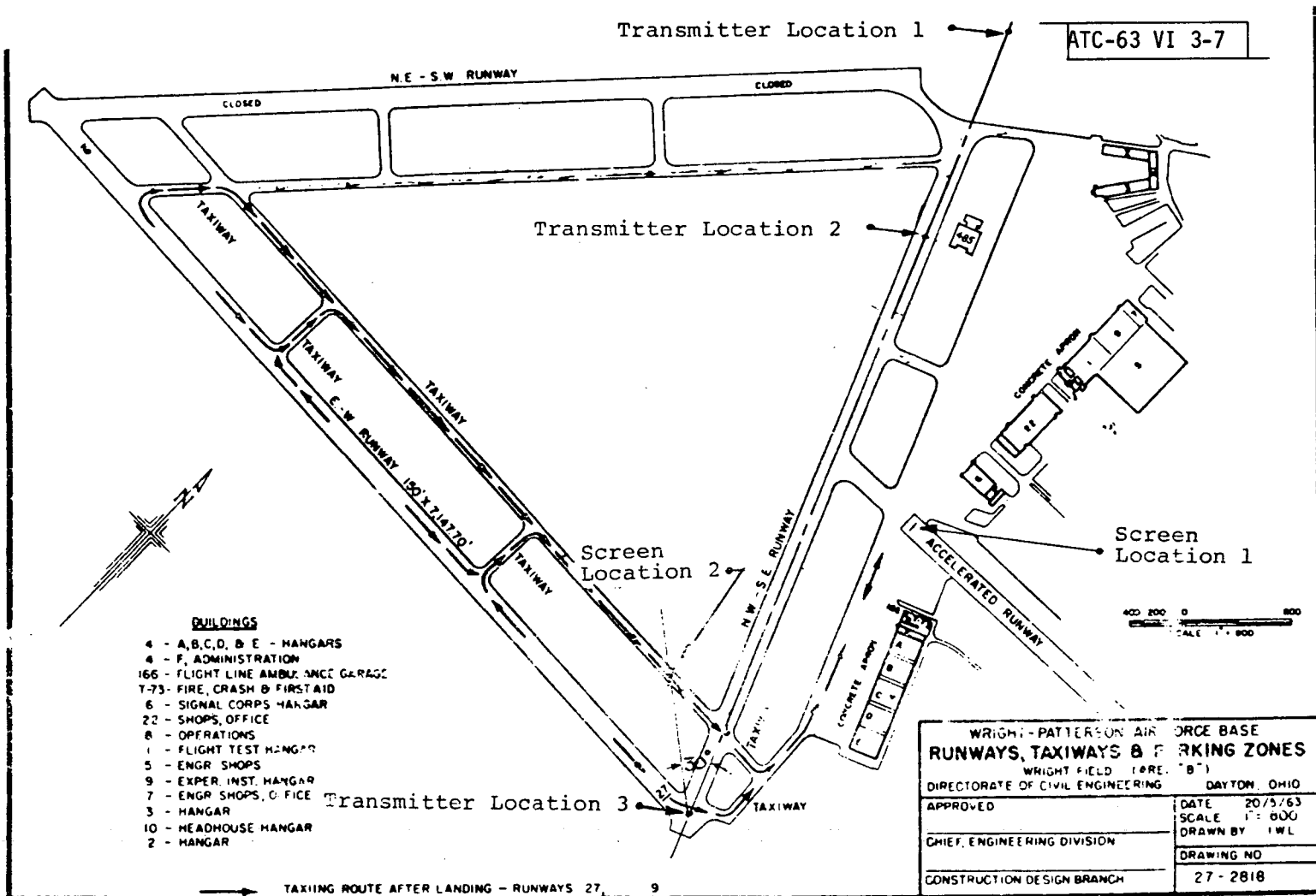
Fig. 3-7. Runway layout and principal test locations in Area B, Wright Patterson AFB.

reflection, as illustrated in Fig. 3-8. The multipath model described in Chapter II assumes that this interaction can be represented as interference between the true transmitter and an image transmitter located as indicated in Fig. 3-8a. In Fig. 3-8b, we see that the model prediction agrees quite well with the observed fluctuations.

Good agreement between predicted and measured scalloping was obtained for most of the other buildings. The report does bring into question the cause of the scalloping behavior observed from building 22 reflections. When the receiver was moved along the runway, the scalloping of approximately 3/ft is consistent with interference between reflections from building 22 and the direct signal and/or reflections from building 485. However, when the receiver was moved towards building 22 the scalloping was very different. This latter result could be due to the receiver being or moving into the shadow region of building 485, but the information provided in the report is insufficient to draw any definite conclusions.

Some of the screen data at WPAFB demonstrates the necessity of incorporating the secondary ground reflection paths* of Fig. 3-6 in determining multipath levels. In section 3.3.2 of the IITRI report[28], data is presented on screen multipath for three different receive antenna heights with the geometry shown in Fig. 3-9. The data indicated that at the 20-foot receiver height the received multipath signal is near a null. This particular phenomena was attributed to inhomogeneities in the screen by IITRI since over flat ground the first null would appear at 64 ft. However, further investigation by

---

*In the parlance of Chapter II, these are the X-O-G-R, X-G-O-R, X-G-O-G-R and X-G-R paths.

image transmitter

160'

Bldg 485

200'

T-1
SITE

1600'

1600'

160'

750'

RUNWAY
ZERO
REFERENCE PT

2450'
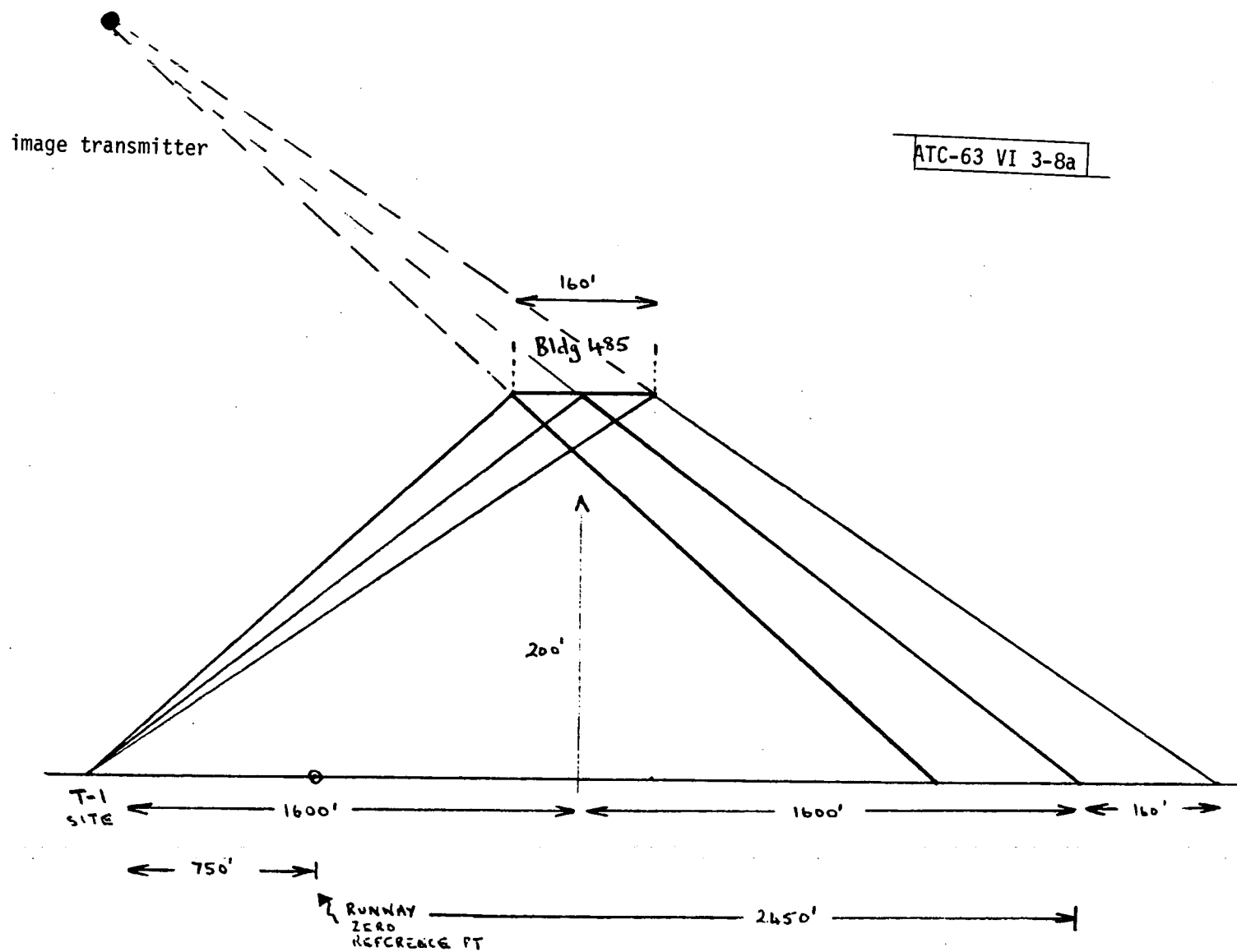
Fig. 3-8a.   Building 485 reflection geometry.
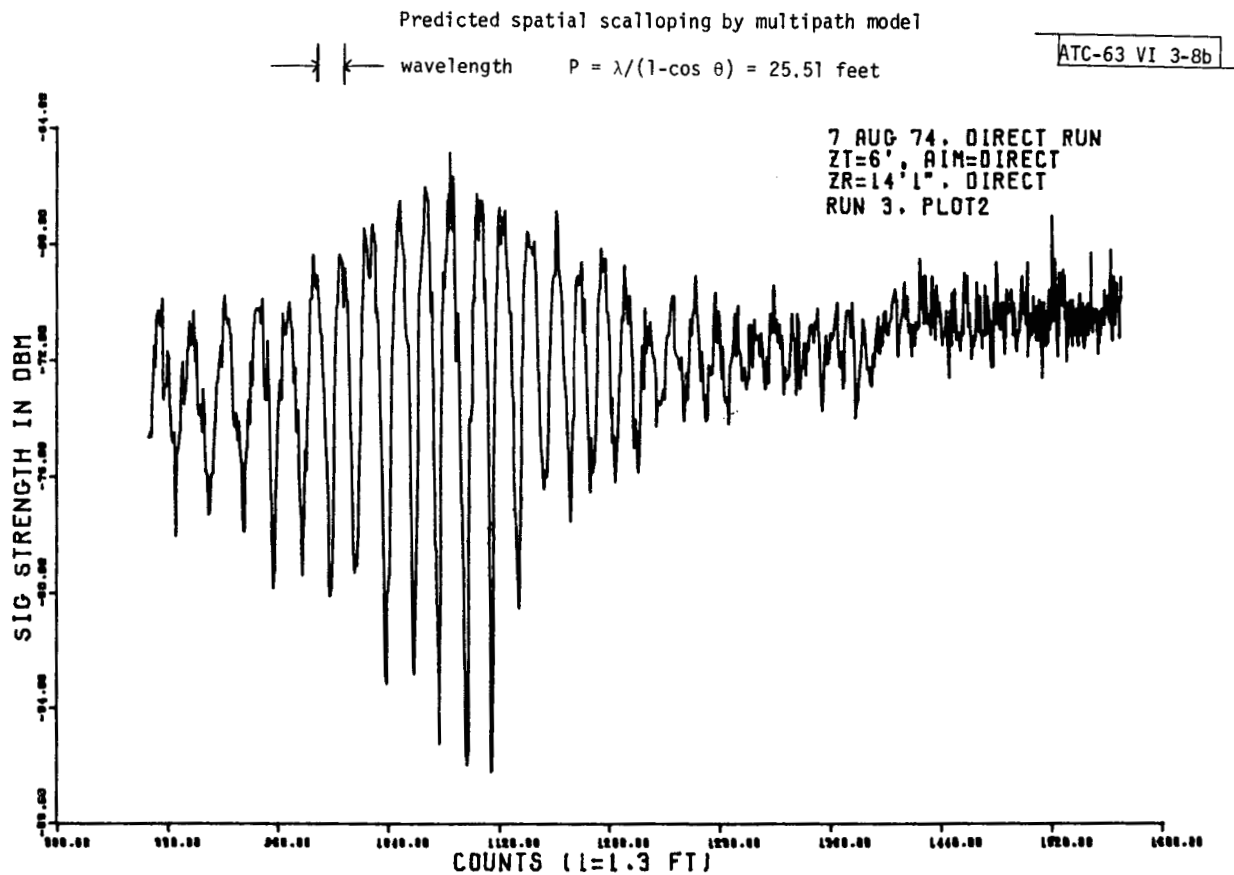
Fig. 3-8b. Scalloping in received signal amplitude for WPAFB Bldg. 485 measurements.

Fig. 3-9. Test geometry for screen on east-west taxiway.

Lincoln determined that the ground between the transmitter and the screen was shaped like a bowl, as shown in Fig. 3-10. By considering the transmitter, screen, and receiver location, and the contour of the ground, one finds that the signal reflected directly from the screen to the receiver and the signal reflected from the screen to the receiver via a ground bounce arrive essentially out of phase for a receiver height of approximately 20 ft. Therefore, the observed data is consistent with the model predictions for a flat screen.

To summarize, we conclude that in the limited areas for which the data in the report can be used to test the validity of the multipath model, the data is consistent with the model.

3.3 Analysis of MLS Phase II Static Test Data

The main purpose of the effort reported here was to validate the computer simulation model for multipath reflectors. The simulation scenarios duplicated the multipath screen and parked aircraft tests that are required by the Phase II MLS test plan[63]. The ratio of multipath signal to direct (M/D), obtained from the simulation, was compared with the measured data from the static tests reported by the MLS contractors. Primary emphasis was placed on the Bendix data for two reasons: (1) the Bendix reports contained the most complete documentation of the tests, and (2) the ICAO tests will be conducted at the Bendix sites at NAFEC.

A list of the tests and pertinent reflector geometry are presented in Table 3-1. The available data on multipath-to-direct (M/D) signal ratio was
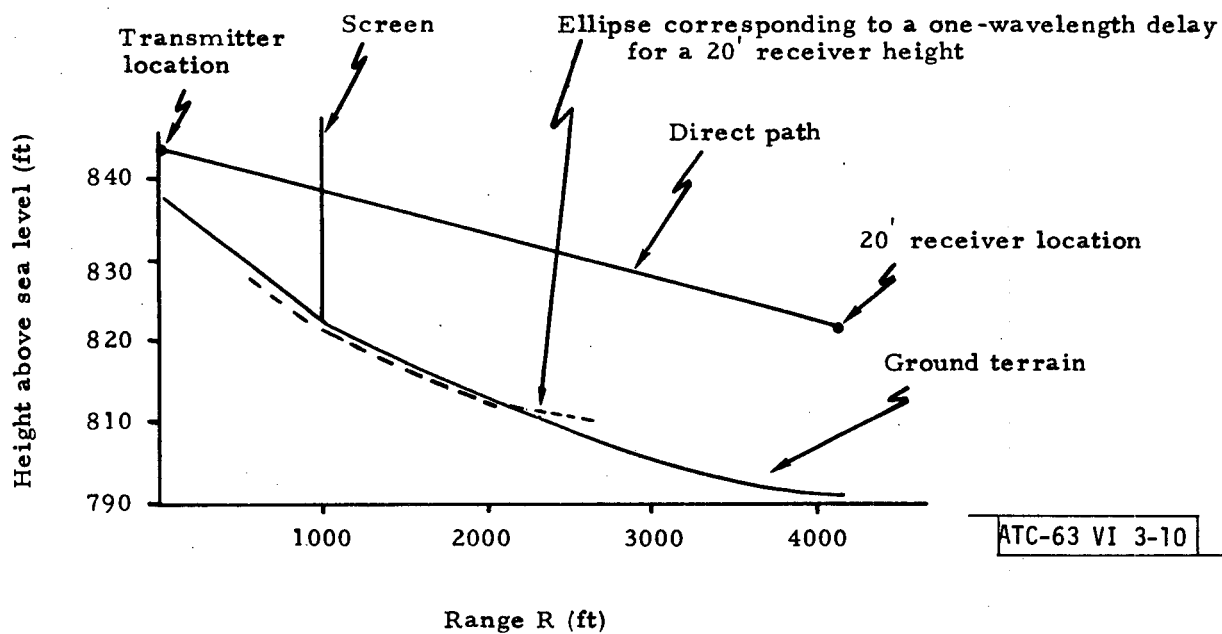
Fig. 3-10. Comparison of ground contour and ellipse for a one-wavelength delay.

TABLE 3-1

MULTIPATH TEST CONFIGURATIONS (BENDIX SITES)

Test No.	Function	Transmitter Location x_T, y_T, z_T[†] (ft)	Reflector[*] Location x_S, y_S (ft)	Reflector Angle (deg)	Multipath Region	Vertical Probe Test Point x_R, y_R (ft)
1	AZ	0, 0, 17	x_T + 433, y_T + 250	-13.58	Rollout	5465, 0
2	AZ	0, 0, 18	x_T + 433, y_T + 250	-13.98	Threshold	7465, 0
3	AZ	0, 0, 22	x_T + 433, y_T + 250	-14.29	Glide slope	2465, 223
5	EL-1	7547, 255, 13	x_T + 200, y_T + 50	+ 3.3	Threshold	8555, 0
6	EL-1	7547, 255, 18	x_T + 200, y_T + 50	-5.7	Glide slope	8455, 270
7	EL-2	5547, 255, 13	x_T + 600, y_T + 150	-1.1	Threshold	8065, 0
8	EL-2	5547, 255, 13	x_T + 600, y_T + 150	+15.5	Flare	6465, 0
14	AZ	0, 0, 19	8146, -211	+15.1	Threshold	8565, 0
14	EL-1	7547, 255, 14	8416, -211	+15.1	Threshold	8426, 0
14	EL-2	5547, 255, 14	8146, -211	+15.1	Threshold	8565, 0

[*]Screen reflector is 52 ft long, 25 ft high, 2.0 ft off ground.

[†]Transmitter height is referred to test point ground level.

obtained from the contractor Phase II reports. The most extensive material, which included the direct and reflected signal levels measured separately, was published by Bendix. This type of data was very beneficial in analyzing the experiments for effects that would have been masked in the combined M/D ratio.

In setting up the geometry for the computer simulations, the surveyed positions at NAFEC from the Bendix report were utilized. Because of undulations in ground level, there is some uncertainty as to the effective ground height. The ground level at the test van location usually established the effective ground plane, and the transmitter height was referred to this plane. In cases where the results seemed to be very sensitive to the choice of ground level, a more precise estimate was obtained to represent the effective height of the terrain between transmitter and receiver.

Besides the geometric configuration, the computer simulation requires as input certain parameters describing the properties of the scattering surfaces. One parameter is the surface roughness height which strongly influences the reflected signal level. Screen roughness was estimated by FAA personnel to be as high as $\pm$ 2 inches. By comparing simulation results with the measured data, it was found that an rms roughness height of 0.75 inch produced good agreement with azimuth data taken of NAFEC. This value was used for all simulations at C-band.

For the Ku-band (λ = 0.8 in.) data at EL-2, the apparent surface roughness height is smaller because the scale of the "waviness" of the screen is comparable to the Ku-band Fresnel radius. The screen surface is locally smooth

over small regions. Within these regions the roughness height, applicable at Ku-band, is considerably smaller than the value used for C-band. Although the local roughness is less, the reflected Ku-band signal is scattered over a larger angular sector as a result of the different orientations of the different reflecting regions. This divergence phenomenon is not incorporated in the simulation model, and hence, correspondence between simulation and experimentation at Ku-band is not to be expected.

In general, the azimuth test data for both screens and parked aircraft could be quantitatively reconciled with simulation results. The reconciliation involved taking into account the ground bounce component on both the direct and reflected paths and the tilt of the screen from true vertical. A small deviation from vertical causes wide fluctuations in M/D when the ground bounce is a significant factor. This was the case with the Bendix azimuth system as a result of a slow horizon cutoff in the elevation pattern of the azimuth antenna.

An illustration of this is provided by the data for test 1, azimuth multipath at rollout. The screen is oriented to produce maximum multipath at 5500 ft from the azimuth site. The multipath is out of beam by 30° in the azimuth plane and is, therefore, easily resolved from the direct signal by the directivity of the scanning function. Figures 3-11(a) and 3-11(b) indicate M/D ratios from computer simulation, and three contractors' data for the two required tests. The simulation concurs with the Bendix data from the original Phase II tests. In the supplemental TRS tests, the screen was apparently misaligned horizontally and vertically.

ATC-63 VI 3-11

M/D (dB)

x - Distance (kft)

Bendix Initial — Phase II
Bendix Supplemental
ITT/G
Simulation
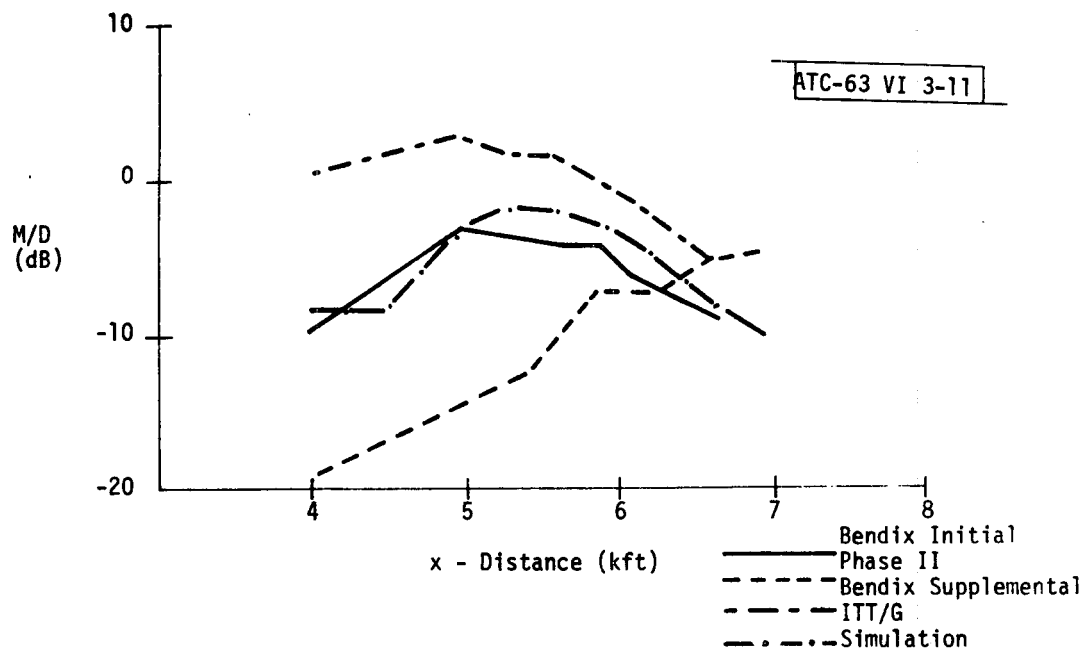
a) Horizontal cut at h = 15 ft

M/D (dB)

Height (ft)
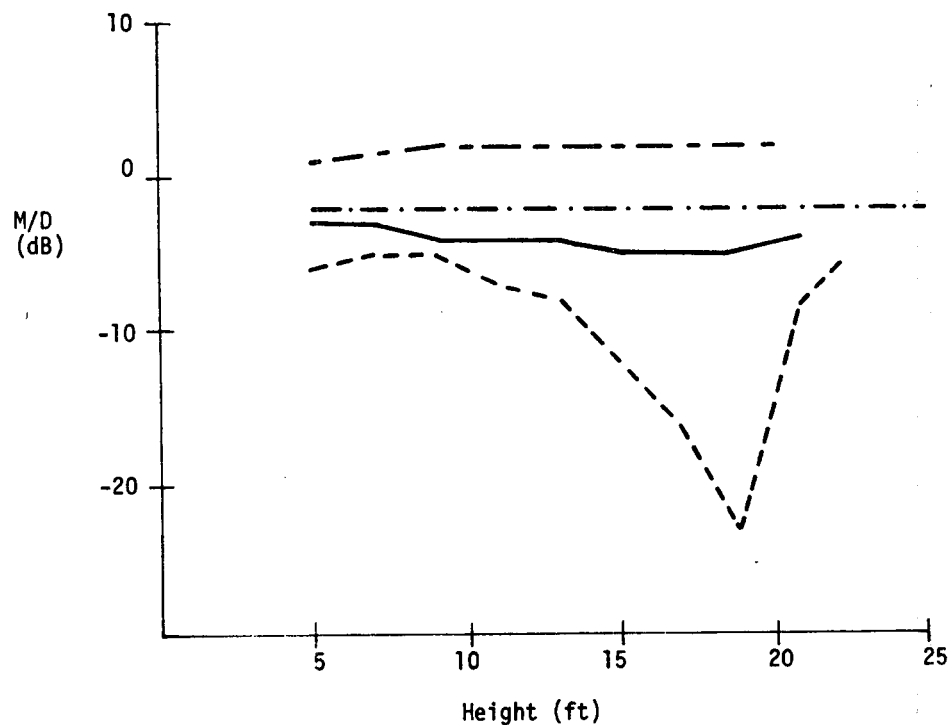
b) Vertical cut at x = 5500 ft

Fig. 3-11. Test 1. Azimuth at rollout; horizontal and vertical cuts.

Horizontal misalignment causes the multipath region in Fig. 3-11(a) to fall further from the transmitter. A slight vertical misalignment is evident from Fig. 3-12 wherein direct and multipath signal levels are plotted separately. Analysis places the first null produced by ground bounce interference with the direct signal at a height of 32.9 ft. The data seems to be tending in that direction. The reflected signal null at 18.5 ft for the supplemental tests can be accounted for by a screen deviation from vertical of only 1°.

Similar behavior also occurred in test 2, azimuth multipath at threshold. The screen is oriented for a multipath maximum at 7500 ft from the azimuth transmitter. The M/D ratios for two horizontal and one vertical cuts are illustrated in Figs. 3-13 and 3-14. The simulation, with parameters selected to fit the Bendix configuration, concurs with the original Bendix tests on the horizontal cuts. The vertical cut demands more detailed investigation through the separate plots of direct and screen reflected signal levels.

The sharp and deep nulls in Fig. 3-14(b) are indicative of ground bounce on both paths.[*] The predicted location of the first null is at a height of 40.5 ft as compared to 38 ft for the direct path data. The measured distance (20 ft) from peak to null is almost exactly as predicted. On the reflected path, a deviation of 0.8° in screen tilt from true vertical accounts for the null position as well as for the peak-to-null spacing.

_____

[*]The amplitude calibration was altered during this run at a point coinciding with a discontinuity in file sequence numbers for data recording.
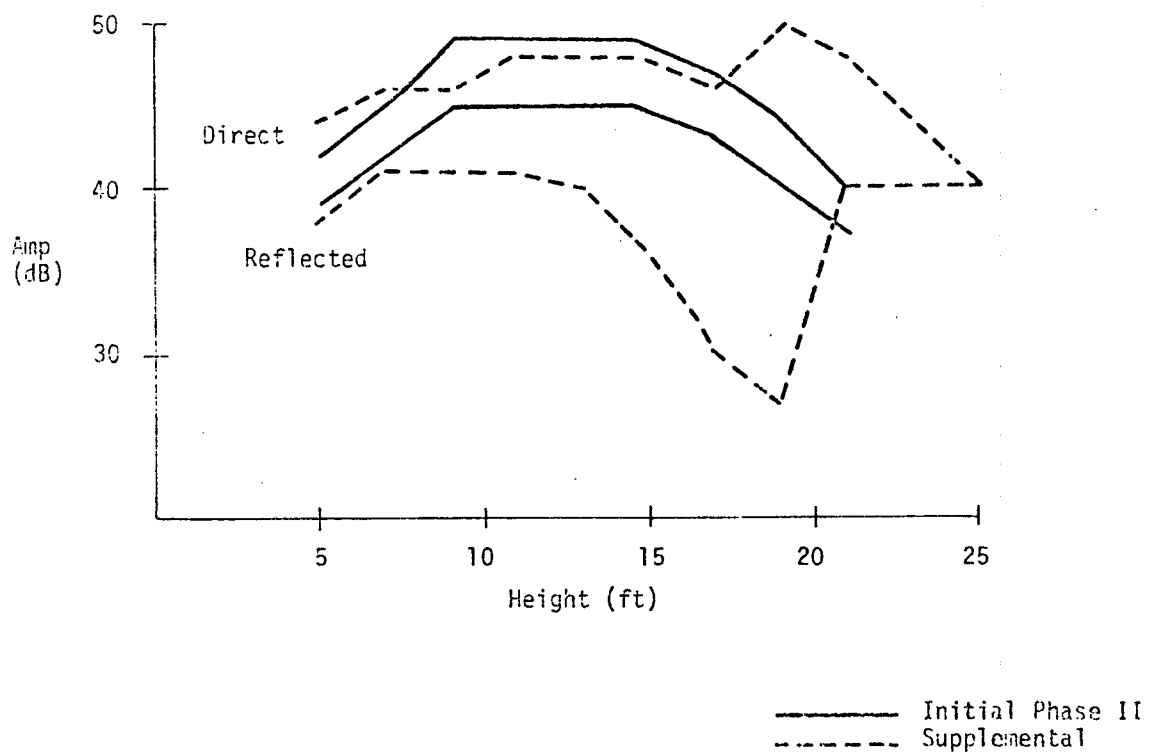
Fig. 3-12. Test 1. Azimuth at rollout; Bendix vertical cut at x = 5465 ft.

a) h = 50 ft

b) h = 16 ft
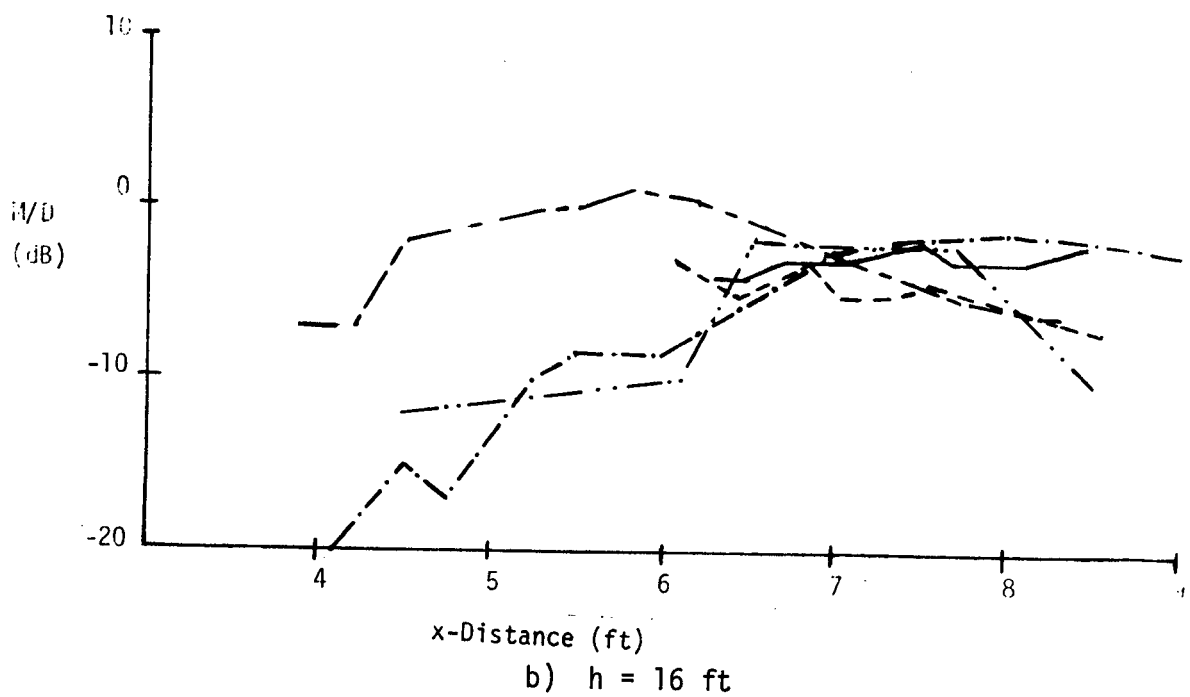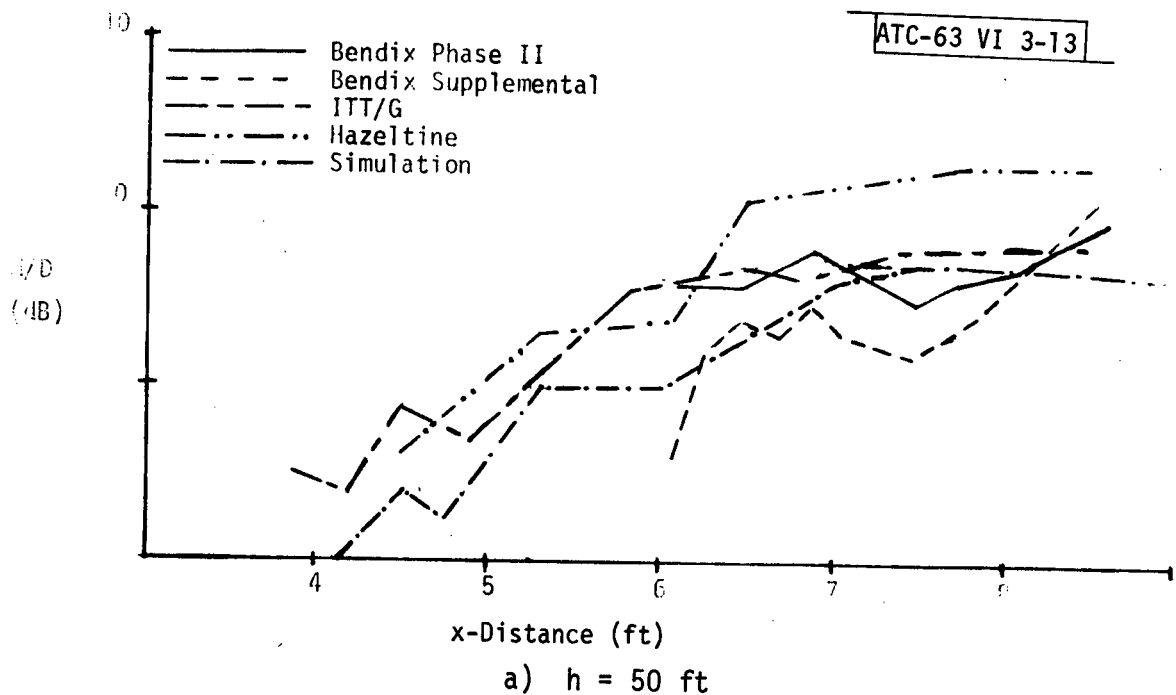
Fig. 3-13. Test 2. Azimuth at threshold; horizontal cuts.

ATC-63 VI 3-14

Bendix
ITT/G
Hazeltine
Simulation

M/D (dB)

Height (ft)

a) M/D ratio

Amp. (dB)

Direct

Reflected

Height (ft)
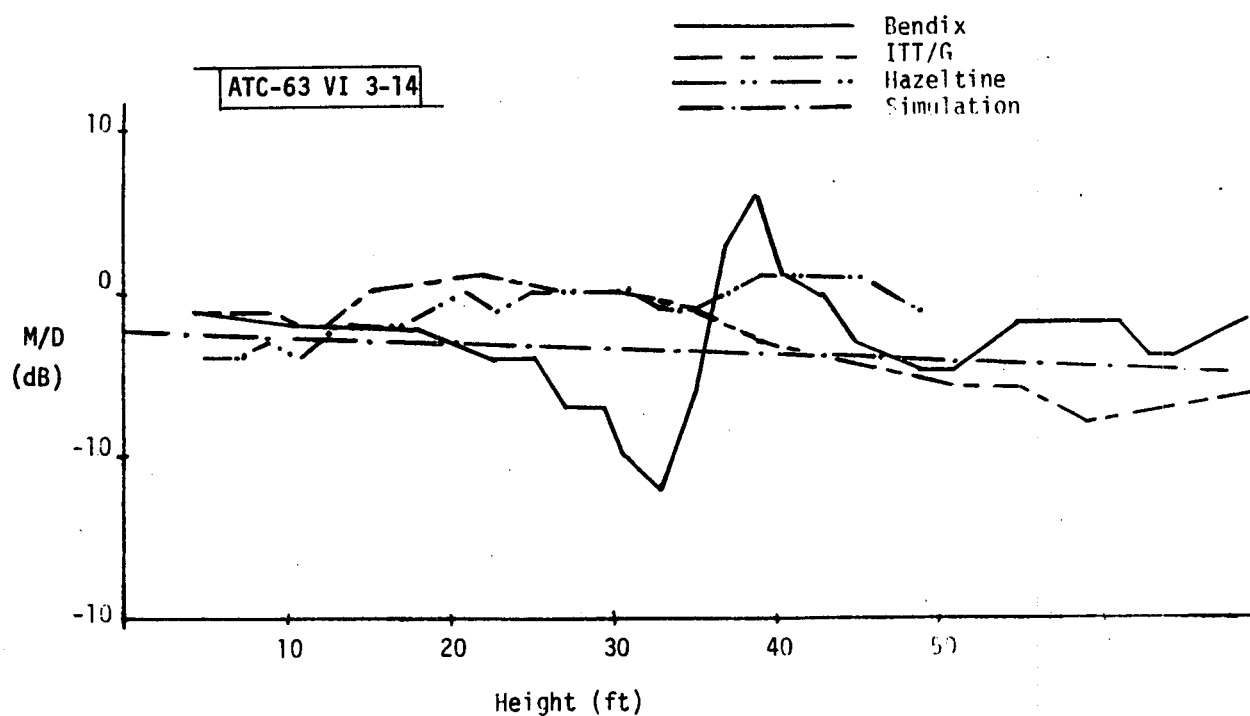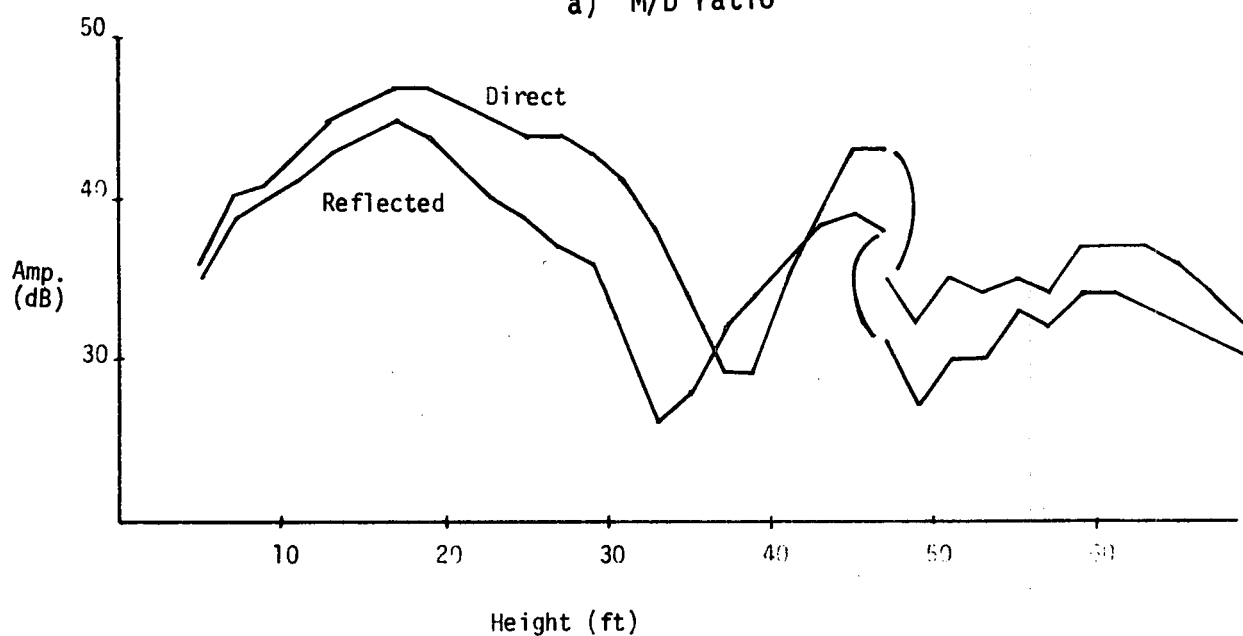
b) Separate signal levels; Bendix data

Fig. 3-14. Test 2. Azimuth at threshold; vertical cut at x = 7500 ft.

At the peak near 17 ft when both paths are reinforced by ground bounce, the M/D ratio is -2 dB compared to -3 dB for the simulation. At the next overlap of peaks at approximately 51 ft, the M/D is -5 dB compared to slightly less than -4 dB for the simulation. The relative level of the ground bounce can be determined from the ratio of peak to notch in the lobing pattern. The notch depth is approximately 19 dB for both curves in Fig. 3-14(b). By solving for ρ in $20 \log [(1+\rho)/(1-\rho)] = 19$ dB, the ground bounce signal level is found to be -2 dB.

In contrast to the azimuth tests, the measured data for elevation did not concur satisfactorily with the simulation. Most of the disagreement can be attributed to one of the following reasons. First, the measurement of M/D ratio requires adequate resolution between direct and multipath signals. In the azimuth tests, the multipath was sufficiently out of beam to permit separation of direct and multipath in the scan dimension. In the elevation tests, the multipath is in beam, and separation could be accomplished in only the orthogonal azimuth direction. For this purpose, a directional receiving antenna was used to record the direct and multipath signals separately. This approach was not entirely successful.

Figure 3-15 shows data from test 5, elevation 1 at threshold. Detailed examination of the directional antenna pattern and the test geometry indicated that the lack of angular resolution could account for the observed data.

The intended M/D ratio on a horizontal cut, as given by the simulation for the Bendix site, is indicated in addition to data from four experiments.
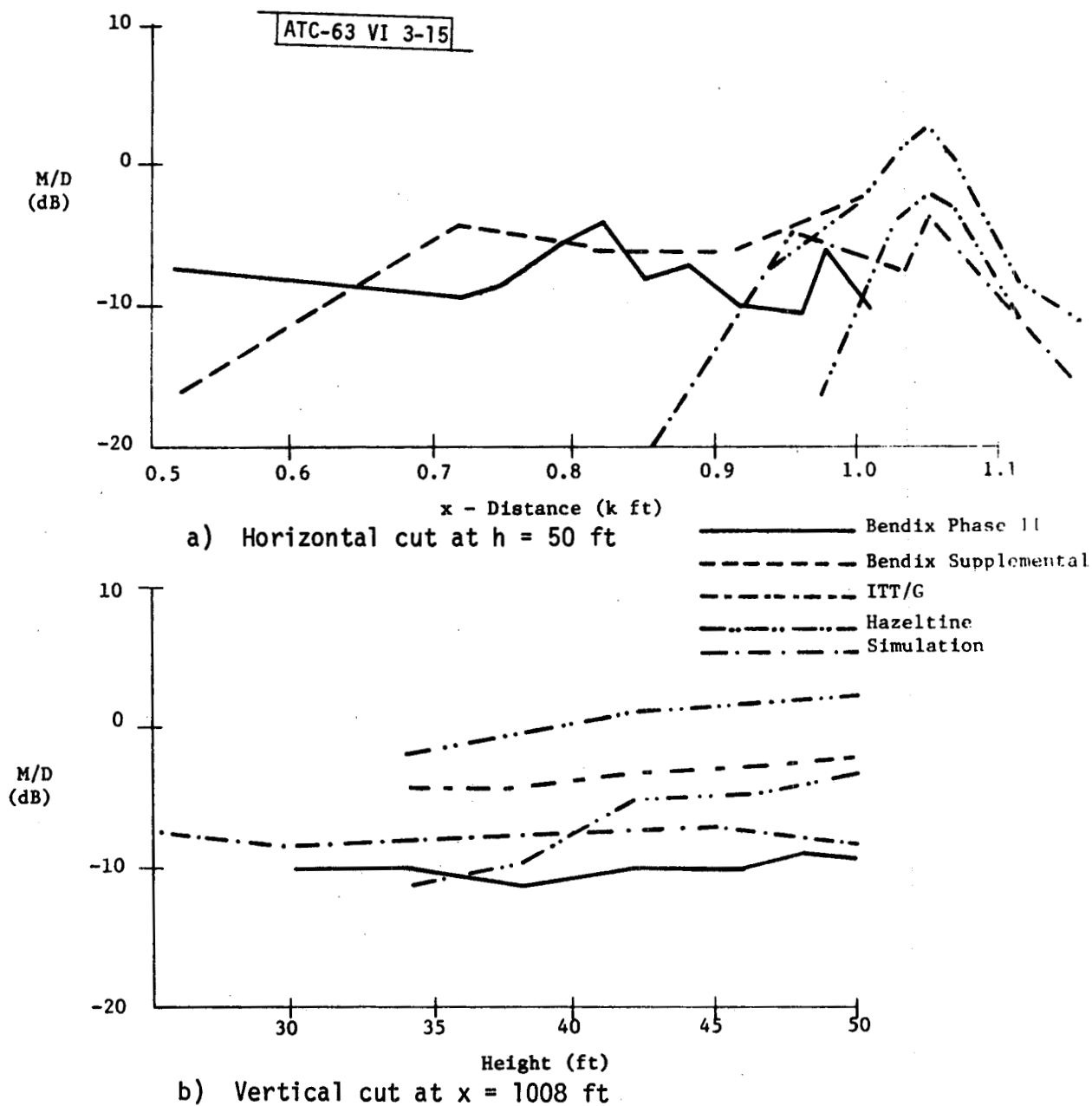
Fig. 3-15. Test 5. Elevation -1 at threshold; horizontal and vertical cuts.

None of the tests agrees sufficiently with the simulation, although Hazeltine's data more closely resemble the desired shape.*

The data from the vertical cuts are indicated in Fig. 3-15(b) including also ITT. The Bendix multipath appears to have missed the mark. At the test point for the vertical probe (1007 ft forward of EL-1), the multipath is well below its peak. In an effort to reconcile the observations with a model, the direct and multipath signals, measured separately, were scrutinized in more detail. Figure 3-16 illustrates the data for the Phase II original and supplemental Bendix tests.

Note the pronounced lack of repeatability between the two sets of experiments. Ignoring the absolute level shift, there is only a slight similarity in the fluctuations for the two tests. The later test has a lower density of experimental points and less consistency between adjacent points; consequently, attention was concentrated on the earlier data. Analysis suggests that the ripple in signal levels represents reflections (or direct signal) passing through the skirts of the directional receiving antenna.

The second source of disagreement for the elevation tests is caused by screen surface irregularities. The simulation model treats the screen as, on the average, a perfectly plane surface with some small-scale roughness. The roughness is taken into account by a reduction in the reflection coefficient, but in other respects the simulation utilizes a plane surface specular reflection model. The real screen has irregularities that cause the multipath to

---

*The two Hazeltine curves are before and after (A) antenna modifications to reduce multipath levels.
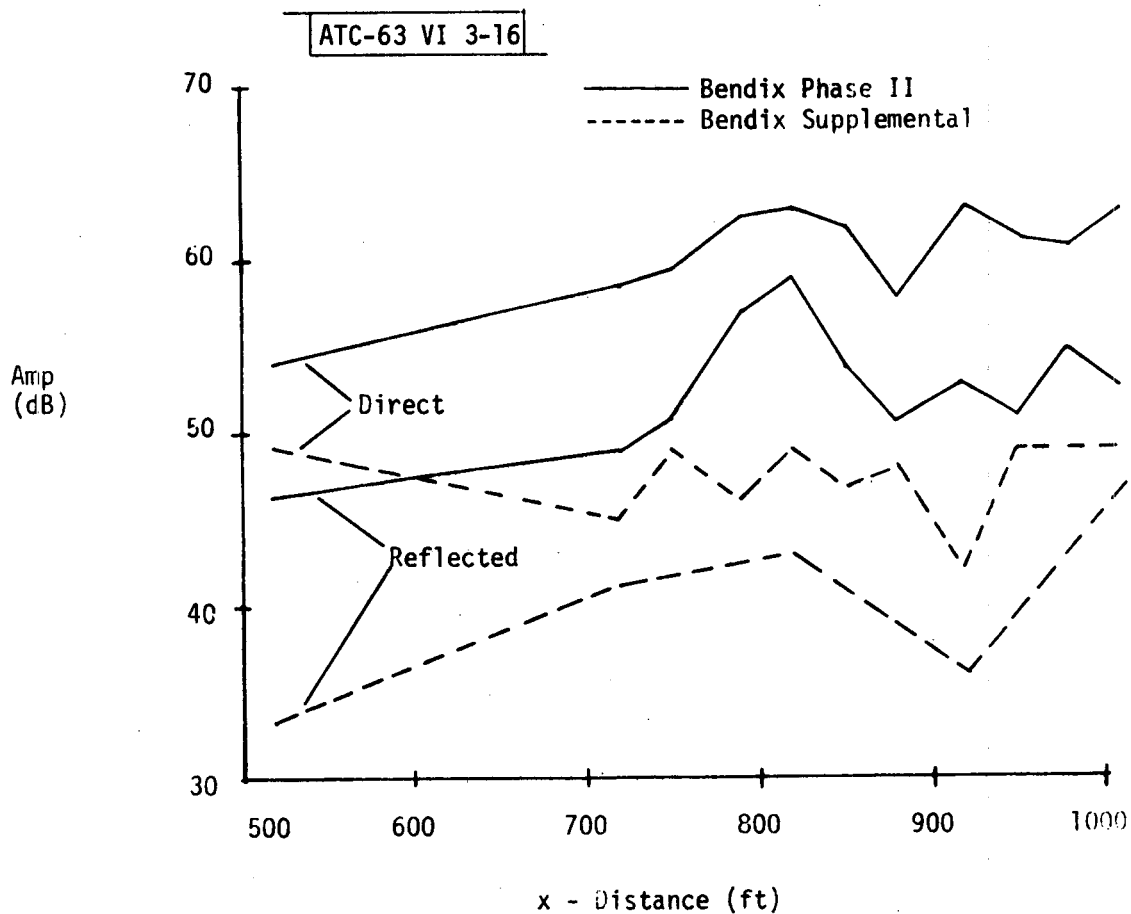
Fig. 3-16. Test 5. Elevation -1 at threshold; Bendix horizontal cut at h = 50 ft.

scatter in directions other than the angle defined by specular reflection. As a consequence, the multipath appears over a wider angular spread and at lower amplitude than predicted. The EL-2 tests of Ku-band are more subject to this effect than the EL-1 tests at C-band, as illustrated in Fig. 3-17 which shows horizontal and vertical cuts for test 7, EL-2 multipath at threshold.

To summarize, with the exception of test 5 (Elevation-1 at threshold), a reasonable explanation of the measurements was established. The computer simulation model has been clearly validated from azimuth test data. For EL-1 tests, the lack of agreement between experiment and simulation is probably attributable to shortcomings in the test methods. For EL-2 tests, screen imperfections apparently introduce effects not incorporated in the model. Although model validation was the primary objective, merely understanding the experimental data was a difficult task. For a specific test configuration, there is substantial variability from contractor to contractor and between tests conducted at different times by the same contractor.

In future multipath experiments, static tests should serve their intended purpose of assuring that the multipath signal distribution in space is as expected and that all significant parameters are determined. One such parameter that was not controlled or measured with sufficient accuracy is the screen tilt, an important factor in the elevation error.[*] The experience in Phase II should be a warning that tests conducted for nominally the same configuration cannot be compared without carefully verifying that the conditions are actually the same.

---

[*]In the ICAO test, measurement of multipath separation (coding) angle will permit indirect determination of screen tilt.

ATC-63 VI 3-17

M/D
(dB)

a) Horizontal cut at h = 50 ft

x - Distance (kft)

Bendix Phase II
———— ITT/G
—··—··— Hazeltine
—·—·—· Simulation

M/D
(dB)

Height (ft)

b) Vertical cut at x = 2518 ft
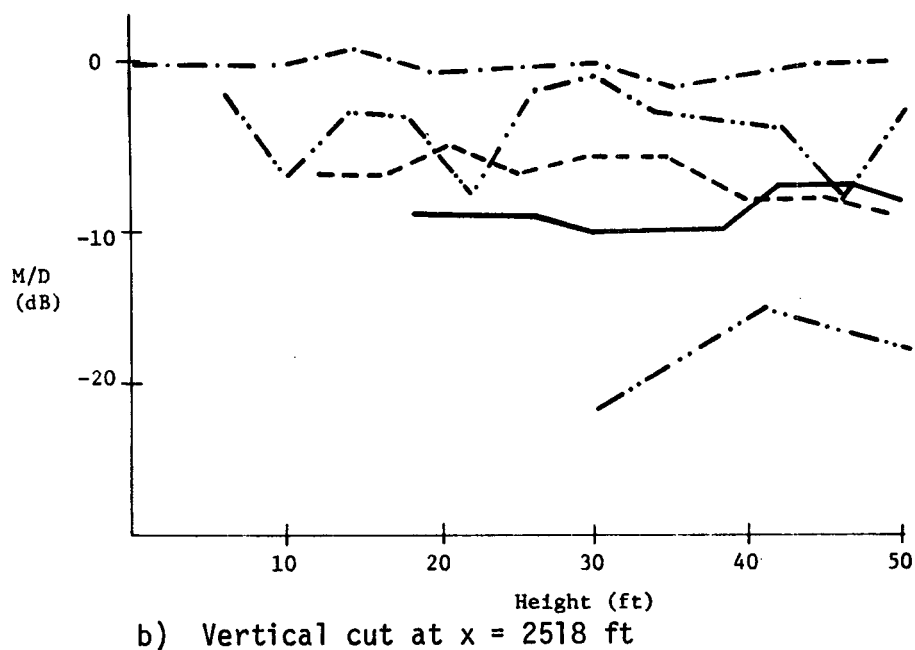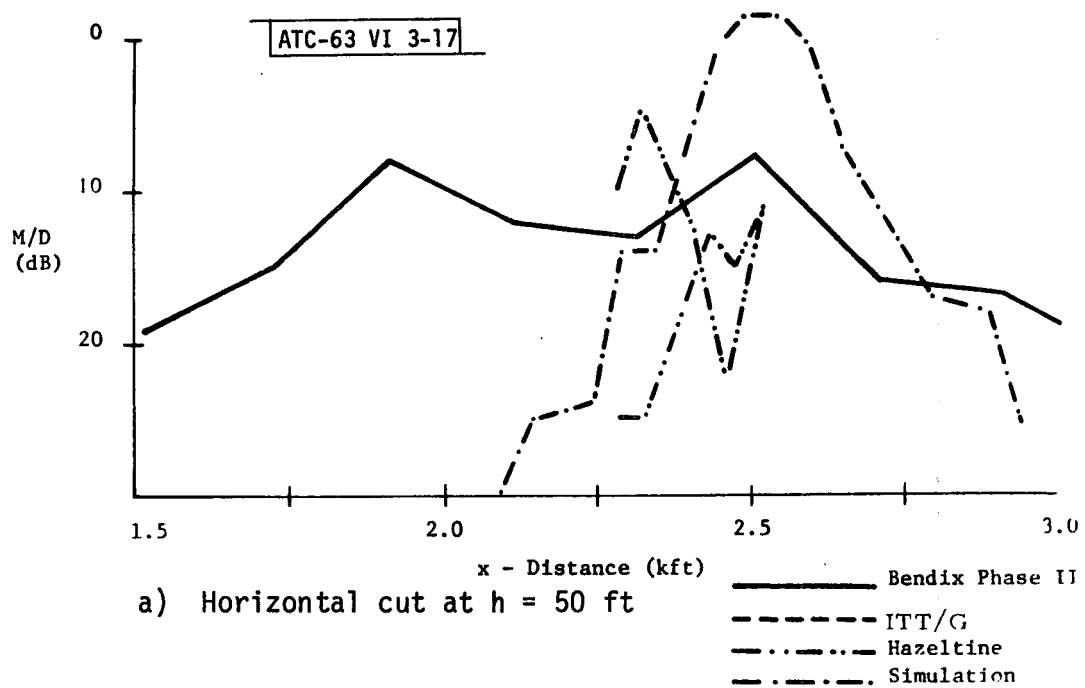
Fig. 3-17. Test 7. Elevation -2 at threshold; horizontal and vertical cuts.

3-36

IV. SYSTEM MODELS

The system models constitute the set of mathematical specifications, algorithms, and associated software which define the simulation of the MLS transmitters and receivers for both the angle and range functions. A receiver model takes as input a parametric description of the current multipath environment and supplies as output the error in the associated angle or range measurement. A functional signal processing approach has been taken in developing these models -- that is, the emphasis has been placed on modeling the principal multipath-induced error factors. This is done at a level which avoids detailed component characterization, and it thereby gains the advantage of simplicity and the necessary computational speed which permits the receiver programs to execute in reasonable amounts of time in full system runs containing flight paths with hundreds of evaluation points.

Figure 4-1 indicates the scope of the receiver models developed during the Lincoln Laboratory Phase II effort. Initially, a model for each U.S. contractor system was devised: the scanning beam FRS[*] of Bendix and TI and the Doppler scan systems of Hazeltine and ITT/Gilfillan. When it became evident that TRS[†] was to be a strong candidate within the Scanning Beam Working Group, the Bendix FRS model was modified to simulate the to-fro TRS. A number of TRS beam processors other than the basic dwell gate technique were simulated, among them split-gate trackers, peak detector, and MCT[‡] processors.

---

[*] Frequency Reference System
[†] Time Reference System
[‡] Multipath Control Technique

ATC-63 VI 4-1

ANGLE

SCANNING BEAM

DOPPLER

ITT/G
HAZELTINE

FRS

TRS

BENDIX
TI

BENDIX

DWELL
GATE

SPLIT
GATE

PEAK
DETECTOR

DME

CONVENTIONAL
PULSE

CHIRP

TI

THRESHOLD
RECEIVER

COMPARATOR
RECEIVER

BENDIX
HAZELTINE

ITT/G
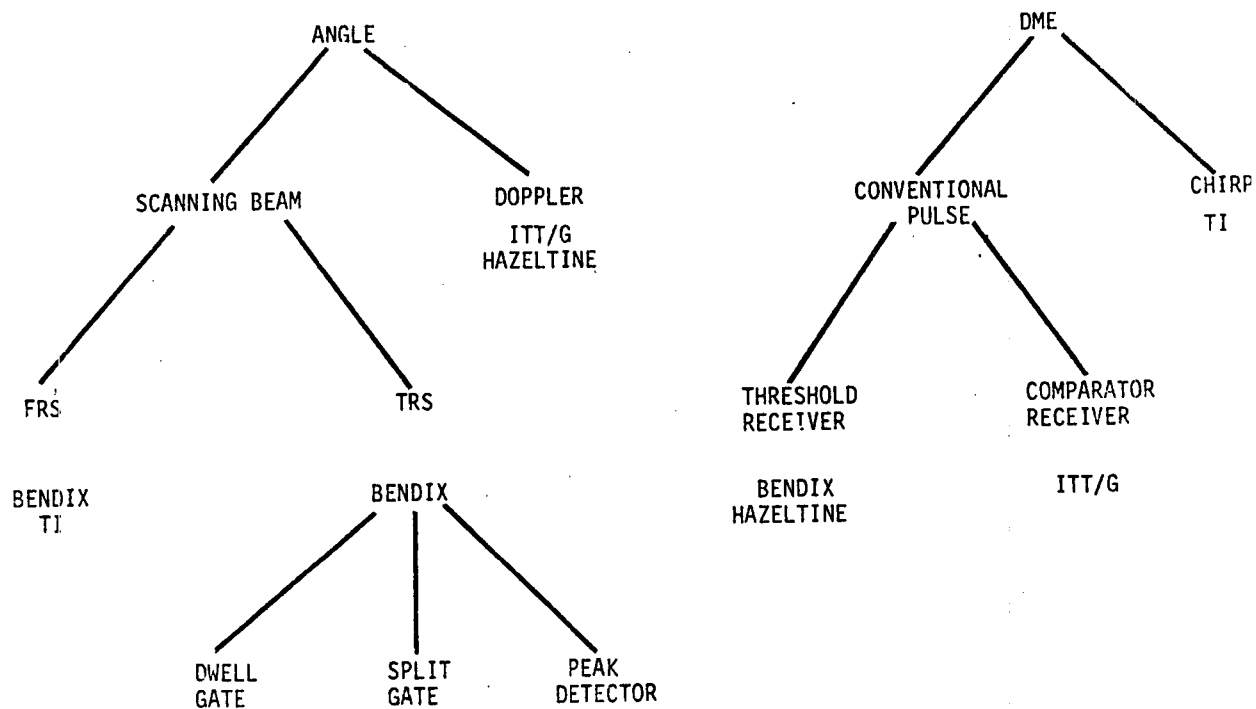
Fig. 4-1. MLS receiver models developed during first phase of Lincoln MLS program.

At the outset, each contractor system model included a two-way link DME representative of its particular design. Further downstream in the program, it became clear that a set of canonical one-way link models which could be combined in arbitrary manner to form a downlink-uplink pair would be a far more useful tool, and the DME subroutines were reconfigured accordingly. The breakdown in Fig. 4-1 reflects this latter situation. The conventional pulse DME has a trapezoidal or Gaussian waveform and can use either of two leading edge detectors: threshold or delay-and-compare. Texas Instruments breadboarded a pulse compression ("chirp") DME for which a computer model also exists.

4.1 General Receiver Responsibilities

Further explanation of the overall function of the receiver subroutines and the specific tasks which they perform is given in this section. The following sections discuss the mathematical models for each receiver class in some detail.

The receiver program is called following the calculation of the multi-path parameters for the (nominal) receiver position and the pertinent function (AZ, EL1, EL2, DME). Although the multipath has been edited in a function-specific manner prior to the receiver call, further editing can be done within the receiver routine itself. For example, a particular DME processor may eliminate all components whose relative path delay exceeds some threshold delay. Each receiver program also applies the transmitter elevation and azimuth beam patterns to the input multipath amplitudes, and further editing could be done on the basis of weighted multipath.

Having completed the multipath calculation, the receiver then generates some representation of the total received signal from which the angle or range error can be extracted. In multiple scan systems -- this class now includes virtually all the angle and DME systems of present interest -- each scan signal is represented separately. Ultimately, error outputs are produced at the MLS data rate (e.g., 5 Hz) by combining data obtained from the individual scans (generally by multiscan weighting). For scanning beam angle systems and DME, the signal representation consists of a set of samples of an envelope waveform (plus the angle subcarrier for FRS). For Doppler scan, the errors can be computed from a knowledge of the dominant (in amplitude) received component and the phase function of the IF signal.

The input multipath data is provided at a selectable rate, usually the MLS data rate, and the multiscan data is generated by extrapolation on that single input. It is assumed that the multipath components are stationary over the data frame in amplitude and angles of arrival but that the relative phase and delay change as a function of the transmitter-specular point-aircraft locations. The aircraft velocity vector is assumed constant over the frame.

A number of effects which are of real importance in hardware receivers have been intentionally neglected or minimized in the receiver models. Receiver noise is excluded from the models because (i) the link budgets and avionics specifications indicate that nominal operation occurs at high SNR, and (ii) the principal object of the current study has been the effect of multipath upon the operation of various MLS systems. Non-ideal component behavior and instrumentation errors are excluded as well on the grounds that

these are not fundamental to the objective. The signal models are simplified somewhat by neglecting certain intermodulation products which occur in, for example, the detector which mixes the Doppler reference and angle signal or the FRS angle subcarrier demodulator. No detailed models of acquisition and tracking have been implemented. At the initial point on the flight path, the system is placed in track (i.e., scan gates or multipath rejection filters are centered on the direct path coordinate); with each successive evaluation point, the gates and filters are recentered on the MLS indicated position (not the true signal coordinate). No track smoothing or reacquisition is implemented. This level of modeling has proved to be sufficient to detect "bright flash" anomalies in scanning beam and pulling of the Doppler rejection filters without making performance strongly dependent upon specific acquisition/tracking algorithms. Subsequent versions of the full simulation model will be equipped to handle higher order dynamic search and track functions.

4.2 Scanning Beam Angle System Models

The essential concepts of the basic FRS model upon which the Phase II Bendix and TI simulations were based are presented first. Those areas in which the two differ are noted in passing. Following that, the modifications required to convert to a TRSB model are given.

4.2.1 Frequency Reference System

The FRS angle subsystems operate according to the scanning beam principle. A narrow fan beam is swept periodically and unidirectionally through the coverage volume. The angle coordinate is encoded on an FM subcarrier

whose instantaneous frequency is a monotone function of time. The airborne receiver determines the dwell period of the scanning beam envelope (dwell gate) and measures the average frequency of the subcarrier over the dwell gate in order to estimate the angular coordinate.

During Phase II, Bendix/Bell[22,34] employed ground system antennas (electronically scanned line arrays) which yield angle encoding that is linear in time and sinusoidal in coordinate angle. The natural coordinates of the resulting angle subsystems are conical. By contrast, the TI model uses planar coordinates and a uniform scan in angle (mechanically rotating antennas).

Two sources of measurement error attributable to multipath phenomena are modeled. The first is dwell gate displacement resulting from errors in the leading and trailing edge threshold crossing times of the beam envelope. This error source is illustrated in Fig. 4-2. The second source of error, often dismissed in earlier simulations, arises in the frequency measurement itself. The average angle subcarrier frequency is estimated by counting both the number of subcarrier zero crossings within the dwell gate and the elapsed time from the first to last zero crossing. Sufficiently small multipath levels will permit the zero crossing counter to be "captured" by the direct path signal; that is, the average rate of crossings will be that of the direct path subcarrier frequency. The multipath will slightly perturb the location, but not the total number, of zero crossings within the dwell gate. On the other hand, a multipath component which has strength greater than the direct component at certain instants within the dwell gate may capture the

T_o, C_o = no multipath thresholds and centroid estimate

T_s, C_s = with multipath threshold and centroid estimate

ϵ = error

ATC-63 VI 4-2

$\theta_s \triangleq$ separation angle
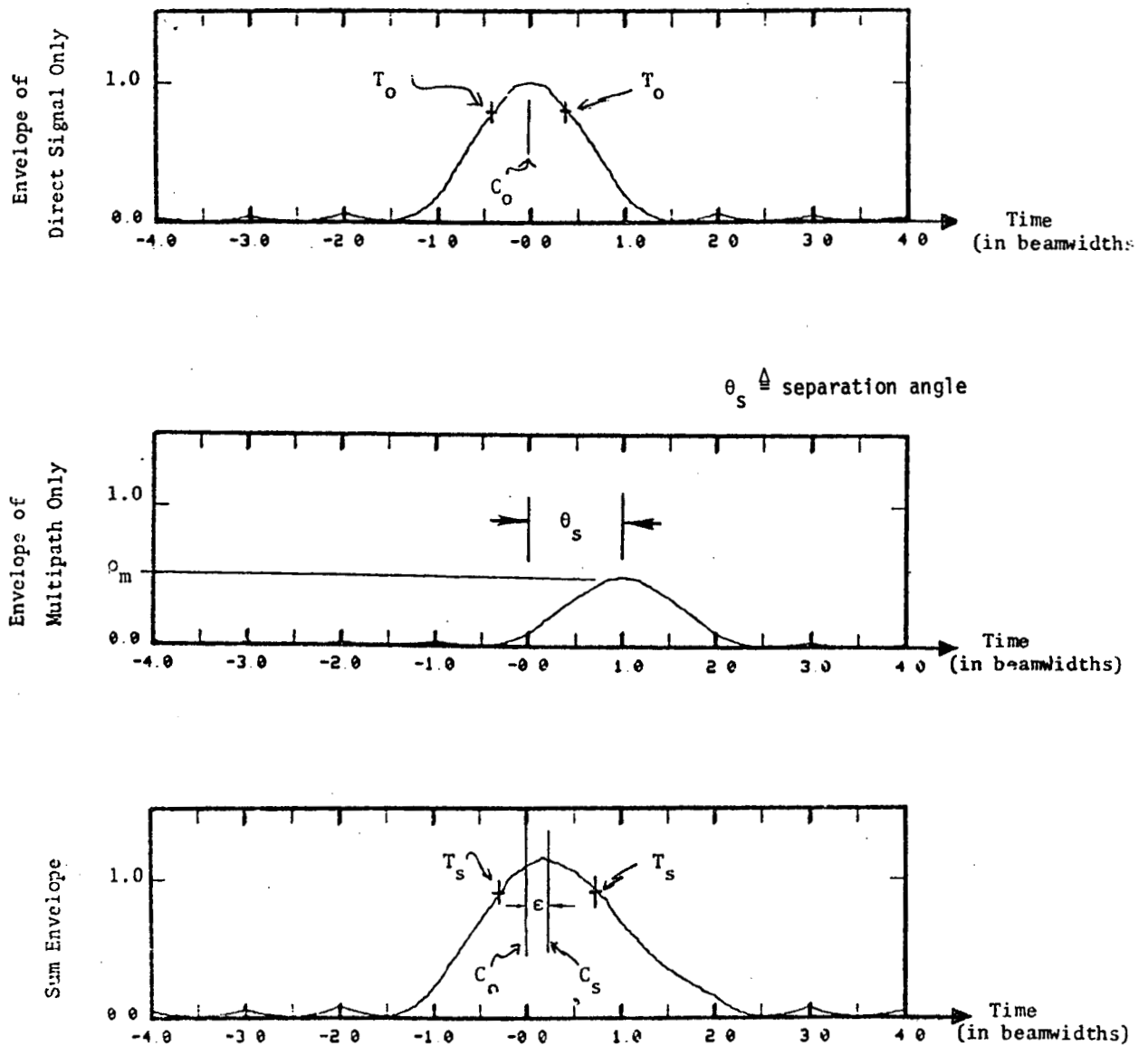
Fig. 4-2. Illustration of scanning beam dwell gate error mechanism.

counter, resulting in a frequency estimate which corresponds to a highly erroneous angle measurement. Since large angle errors can be caused by either dwell gate displacement or frequency measurement error, both are included in the simulation.

4.2.1.1 Transmitter Signal

The angle signal is generated as an FM subcarrier whose frequency changes linearly in time. The instantaneous subcarrier frequency is

$$\omega_{sub}(t) = \omega_s + \dot{\omega}t \tag{4-1}$$

and the corresponding complex transmitted waveform is*

$$s(t) = \exp j\{\omega_c t + \phi_c + m\ \exp j[\omega_s t + \tfrac{1}{2}\dot{\omega}t^2 + \phi_s]\} \tag{4-2}$$

where

ω_c = carrier frequency

ϕ_c = carrier phase angle

m = subcarrier modulation index

ω_s = subcarrier center frequency

$\dot{\omega}$ = subcarrier sweep rate

ϕ_s = subcarrier phase angle

The phase modulated wave is amplitude modulated by the scanning antenna pattern, $P(\theta,\phi,t)$, where θ is the measured coordinate and ϕ is the orthogonal coordinate. $P(\theta,\phi,t)$ is narrow ($\approx 1°$) in θ and wide (anywhere from 8° to 120°) in θ. $P(\theta,\phi,t)$ is written as product of two factors

---

*The notation expj($\cdot$) will be used to denote the complex exponential $e^{j(\cdot)}$.

$$P(\theta,\Phi,t) = P_1(\dot\theta t - \theta) \, P_2(\Phi,\dot\theta t) \qquad\qquad (4\text{-}3)$$

The first of these (P_1) describes the scan modulation or beam envelope, as observed in direction θ. The implied angle scanning is linear in time, as in the TI model. For Bendix θ is replaced by sin θ. For simplicity, the linear scan notation is retained throughout. The parameter $\dot\theta$ is the antenna angular velocity (scan rate). The second term (P_2) gives the pattern in the orthogonal coordinate; note that the orthogonal pattern is independent of the measured coordinate in all but the TI azimuth system, in which a special feature called "hopover" is employed for centerline emphasis at low elevation angles[26,32]. The time dependence of P_2 will be dropped henceforth. The time origin has been selected to be the instant at which the peak of the scanning pattern points in the direction $\theta = 0°$ (centerline for AZ, runway plane in EL). Thus, the complex signal transmitted in direction (θ_o, ϕ_o) is proportional to

$$f(t) = P_1(\dot\theta - \theta_o) P_2(\theta_o)\exp j\{\omega_c t + \phi_c + m \exp j[\omega_s t + \tfrac{1}{2}\dot\omega t^2 + \phi_s]\} \qquad (4\text{-}4)$$

4.2.1.2 Received Signal

The received signal model consists of a superposition of terms. One of these represents the direct path component, and the other (M in number) represents the multipath propagation components. Each component of the received signal is characterized by six parameters; specifically, the i-th component is described by

ρ_i = amplitude

ω_i = carrier frequency

τ_i = path delay

ϕ_i = change in phase angle due to i-th path reflection

θ_i = transmission angle to the specular point on the i-th reflector in the measured coordinate

Φ_i = transmission angle to the specular point on the i-th reflector in the orthogonal coordinate   (4-5)

The values of the six parameters are calculated for each reflector in the scattering portion of the program (see Chapter 2).

The amplitude is computed by the scattering routines as though the transmitting antenna had an omnidirectional pattern over the coverage volume. In the receiver routines, the amplitude (A_i) is weighted by the transmitting antenna pattern in the orthogonal coordinate Φ_i and normalized to the received amplitude of the direct component:

$$\rho_i = \frac{A_i P_2(\Phi_i)}{A_o P_2(\Phi_o)}$$ (4-6)

The in-coordinate pattern is accounted for separately since it is a function of time. Omnidirectional airborne antenna patterns are assumed.[*]

The received carrier frequency is computed as

$$\omega_i = \omega_o \left(1 + \frac{v_a \cos \beta_i}{c}\right)$$ (4-7)

_____

[*]An airborne antenna factor will be incorporated in the more advanced system models under development.

where

v_a = magnitude of aircraft velocity vector

β_i = angle between aircraft velocity vector and arrival angle of i-th path signal

c = speed of light in air

Letting the zero-th component of the received signal be the direct signal and the remaining M be multipath, the total complex RF signal at the receiver is

$$r(t) = \sum_{i=0}^{M} \rho_i \; P_1(\dot{\theta}t - \dot{\theta}\tau_i - \theta_i) \; expj\{\omega_i(t - \tau_i) + \phi_i$$

$$+ \; m \; expj[\omega_s(t - \tau_i) + \frac{1}{2}\dot{\omega}(t - \tau_i)^2 + \phi_s]\} \tag{4-8}$$

4.2.1.3 Receiver Processing

Figure 4-3 shows a block diagram of an FRS angle processor. The computer model starts at the second IF output. It is split into two paths; one of these determines dwell gate within which the frequency measurement is to be made, and the other consists of the frequency measuring circuitry.

The dwell gate processor computes the envelope of the received signal. In the actual circuitry this is accomplished with a linear envelope detector followed by a lowpass filter. The lowpass filter is for rejection of both noise and spurious harmonics of the angle subcarrier. The unfiltered envelope can be computed directly from Eq. (4-8) by translating r(t) down in frequency by an amount ω_0 (the received direct component frequency) and taking the magnitude

$$e(t) = |r(t) \; e^{-j\omega_0 t}| \tag{4-9}$$
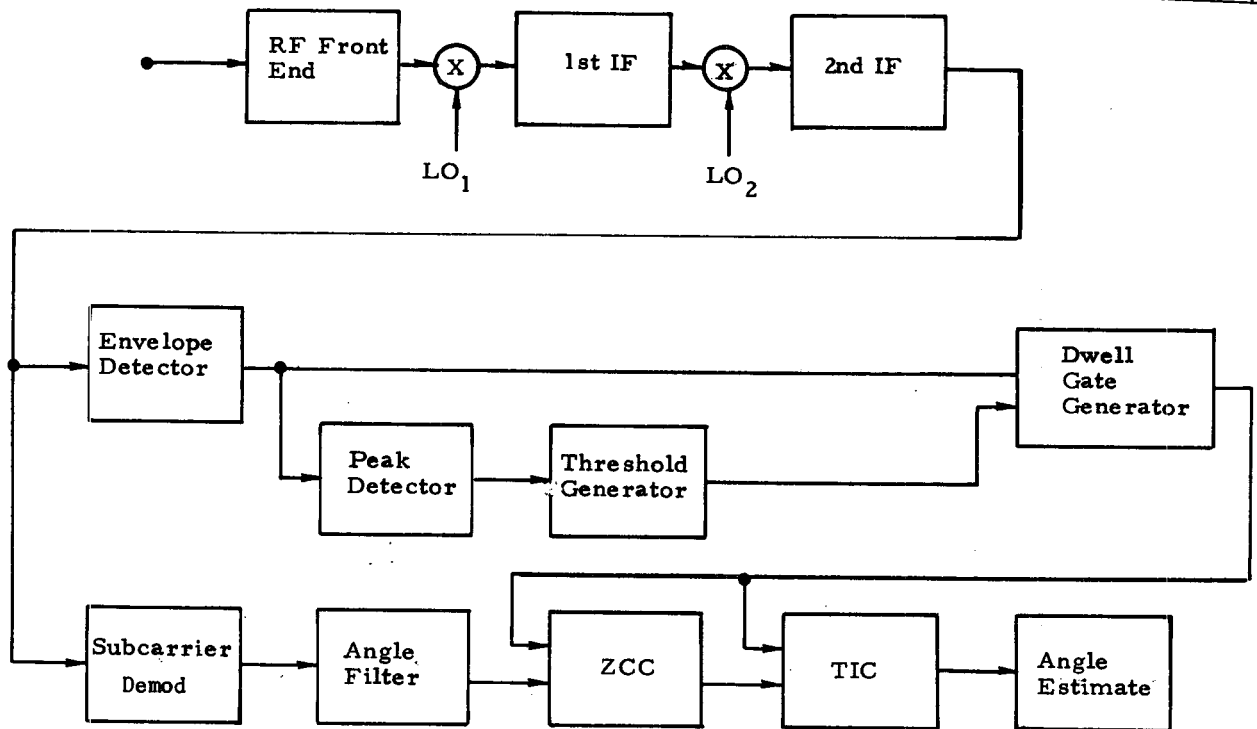
Fig. 4-3.   Bendix/Bell FRS angle processing receiver.

In the FRS simulation, a square law envelope detector is used for convenience in the filtering model, a description of which is omitted here. The filtering alters the envelope shape somewhat, but does not fundamentally change the processing which follows. The unfiltered envelope is used in the remaining discussion.

On each scan of the beam, three measurements are made on the envelope. These are: (1) the amplitude of the peak of e(t), (2) the time at which the leading edge crosses a specific threshold, and (3) the time at which the trailing edge crosses the same threshold. The threshold for the present scan can be computed from either the present peak value or the stored value of the previous peak.

The two threshold crossings are used to find the beam dwell gate. Neither the threshold crossings nor the peak can be determined from closed form expressions; instead, they must be calculated by a trial-and-error procedure which involves evaluating e(t) at a number of points. The number of points is chosen in such a way that the error in computing the threshold crossing times is small compared to the dwell gate displacement due to multipath. Since the frequency estimate uses the first and last zero crossings within the dwell gate, the crossings need only be located to within, for example, a cycle of the subcarrier.

The specifics of the dwell gate procedures differ for the two models, but the essential ingredients are:

1. A _tracker_ _scan_ _gate_ is set up. The gate is centered at the previous angle estimate. This is the extent of the tracking model in the Phase II simulation.

4-13

2. The received envelope is calculated at a number of points uniformly spaced over the scan gate. The calculated values are stored.

3. The envelope samples are searched to find the peak value, which is used to set either the present or next threshold at users' option.

4. The envelope samples are searched to find the times at which the leading and trailing edge threshold crossings occur. These times define the dwell gate. For precision in the dwell gate determination, a fine grid search between the envelope samples which straddle the threshold can be used.

Let $\tilde{t}_1$ and $\tilde{t}_2$ designate the nominal threshold crossing times in the absence of multipath, and let $\hat{t}_1$ and $\hat{t}_2$ be the times determined by the dwell gate processor. In the absence of frequency measurement error, the angle error, $\hat{\theta} - \theta_0$, due to dwell gate displacement is given in terms of the edge displacements

$$\Delta t_1 = \hat{t}_1 - \tilde{t}_1$$

$$\Delta t_2 = \hat{t}_2 - \tilde{t}_2 \tag{4-10}$$

as follows:

$$\hat{\theta} - \theta_0 = \dot{\theta}\left(\frac{\Delta t_1 + \Delta t_2}{2}\right) \tag{4-11}$$

Having determined the dwell gate, the actual receiver measures the average frequency within the dwell gate in a manner similar to the counting-

and-timing method employed in Doppler scan. That is, the angle subcarrier is demodulated, and the number of zero crossings, as well as the time interval between the first and last zero crossings within the gate, is measured. Assume that k crossings occur and that the first and last are at times t_1'' and t_2'', respectively. Then a reasonable estimate of the frequency at the dwell gate center is

$$\hat{\omega} = \frac{(k-1)\pi}{t_2'' - t_1''} \tag{4-12}$$

In the simulation model, the steps leading to (4-12) are followed quite literally. The procedure rests strongly upon the following two observations:

(1) The FM strong signal capture effect is invoked. It is assumed that when the direct component of the received signal sufficiently dominates the multipath components, the average frequency of the FM demodulator output signal is that of the direct component. In particular, the number of zero crossings of the signal is that which would have occurred in the absence of multipath. Conversely, if a multipath component is dominant in amplitude, its average frequency captures the zero crossing counter.

(2) The times at which the first and last zero crossings occur within the dwell gate are somewhat displaced by the cumulative multipath return. These times are approximated by computing the times (t_1' and t_2') at which the endpoint zero crossings would have occurred in the absence of multipath and perturbing them. The perturbation is calculated by evaluating the net phase of the demodulator output at t_1' and t_2', and linearly extrapolating time backwards (or forwards) to the nearest instant of zero phase (i.e., nearest zero crossing). The extrapolation is based upon the instantaneous frequency of the dominant component at times t_1' and t_2'.

The mathematical support for the preceding is sketched below. Without multipath, the angle signal phasor is equal to[*]

$$\exp j[\omega_s t + \frac{1}{2}\dot{\omega}t^2 + \phi_s] \tag{4-13}$$

_____

[*] The direct signal delay is set equal to zero; all multipath delays are measured relative to the direct.

times an amplitude term dependent upon the beam pattern. Neglecting any phase contribution from the beam pattern, the subcarrier zero crossings are those of the above expression. In terms of the phase argument

$$arg(t) = \omega_s t + \tfrac{1}{2} \dot{\omega} t^2 + \phi_s \qquad (4\text{-}14)$$

The net phase accumulated by the direct angle subcarrier across the dwell gate is

$$\Delta\phi_0 = arg(\hat{t}_2) - arg(\hat{t}_1)$$

$$= (\hat{t}_2 - \hat{t}_1)\,\omega_s + \dot{\omega}\left(\frac{\hat{t}_1 + \hat{t}_2}{2}\right) \qquad (4\text{-}15)$$

The greatest possible number of full half cycles of subcarrier represented by (4-15) is

$$C = \text{Integer Part} \left\lceil \frac{\Delta\phi_0}{\pi} \right\rceil \; .$$

Either C or C + 1 crossings can occur in the gate, and it is easy to determine which is the case. A zero crossing of the subcarrier phasor occurs at those times for which its argument equals 0 or π, i.e.

$$\sin[arg(t)] = 0 \qquad (4\text{-}16)$$

If $\sin[arg(\hat{t}_1)]$ and $\sin[arg(\hat{t}_2)]$ have the same algebraic sign, the number of zero crossings within the dwell gate can only be even. If their signs are opposite, an odd number of zero crossings occurs. This observation leads to a simple rule for computing the number of crossings k based on the values of A_1, A_2, and C, where

$$A_1 = \sin[arg(\hat{t}_1)]$$
$$A_2 = \sin[arg(\hat{t}_2)] \qquad (4\text{-}17)$$

The rule is summarized in Table 4-1.

C	$A_1 A_2$	k
even	+	C
odd	+	C + 1
even	-	C + 1
odd	-	C

Table 4-1. Rule for computing number of zero crossings k.

Having determined the number of subcarrier zero crossings caused by the direct wave, the instants of the first and last crossings of the direct wave within the dwell gate must be computed. The parameters q_1 and q_2, defined as follows,

$$q_1 = \arg(\hat{t}_1)(\mod \pi)$$

$$q_2 = \arg(\hat{t}_2)(\mod \pi)$$

$$(4-18)$$

represent the direct subcarrier phase excess over π at the dwell gate end-points. Thus the endpoint zero crossings of the subcarrier occur at times t_1' and t_2' given in terms of q_1, q_2, and the endpoint instantaneous frequencies $\omega_0(\hat{t}_1)$ and $\omega_0(\hat{t}_2)$:

$$t_1' = t_1 + \frac{\pi - q_1}{\omega_0(\hat{t}_1)} \tag{4-19}$$

$$t_2' = t_2 - \frac{q_2}{\omega_0(\hat{t}_2)} \tag{4-20}$$

$$\omega_0(t) = \frac{d}{dt} \arg(t) = \omega_s + \dot{\omega}t$$

By definition, the phase of the direct signal subcarrier is zero at the times t_1' and t_2' given above. However, this is not necessarily true of the

total demodulated subcarrier in the presence of multipath. That signal has nearest zero crossings at times t_1'' and t_2'' given approximately by

$$t_1'' = t_1' - \frac{\phi_{mult}(t_1')}{\omega_0(t_1')}$$

$$t_2'' = t_2' - \frac{\phi_{mult}(t_2')}{\omega_0(t_2')}$$

$$(4-21)$$

where $\phi_{mult}(t)$ represents the phase of the total demodulated subcarrier (derived below). Times t_1'' and t_2'' are substituted into (4-12) to obtain the frequency estimate $\hat{\omega}$; the corresponding angle error is found by subtracting the true center frequency $\omega_0(\theta_0/\theta)$ from $\hat{\omega}$ and multiplying by $\dot{\theta}/\dot{\omega}$:

$$error = \frac{\dot{\theta}}{\dot{\omega}}\left[\hat{\omega} - \omega_0\left(\frac{\theta_0}{\theta}\right)\right]$$

The angle subcarrier is demodulated by a limiter-discriminator. It is possible to write an expression for the phase function of the output of this circuit which includes the multipath effects, but it is cumbersome to use in the stated framework. In order to get a simple expression for the phase function used in the zero-crossing perturbation argument, it was assumed that the demodulated subcarrier is a superposition of the individual subcarriers weighted by the antenna beam pattern factor and the multipath amplitude ρ_i:

$$y(t) = \sum_{i=0}^{M} \rho_i \, P_1(\dot{\theta}t - \dot{\theta}\tau_i - \theta_i) \, expj[\omega_s(t-\tau_i) + \frac{1}{2}\dot{\omega}(t-\tau_i)^2 + \phi_s]$$

$$(4-22)$$

Equation (4-22) is not to be interpreted as a mathematical model of a limiter-discriminator output signal. It is merely a convenient artifice to carry out

the implications of the earlier assumption that the signal with the largest amplitude dominates the frequency estimate. The intention was to replace this phase function with a more exact analysis at a later date. The need never arose, however, once the FM angle code was abandoned in the U.S. scanning beam program in favor of TRSB.

Accepting (4-22) as the formula for the output yields a phase function

$$
\phi_{mult}(t) = \tan^{-1} \left\{ \frac{\sum\limits_{i=0}^{M} \rho_i P_1 (\dot{\theta}t - \dot{\theta}\tau_i - \theta_i) \sin\left\{-\tau_i \left[\omega_s + \dot{\omega}\left(t - \frac{1}{2}\tau_i\right)\right]\right\}}{\sum\limits_{i=0}^{M} \rho_i P_1 (\dot{\theta}t - \dot{\theta}\tau_i - \theta_i) \cos\left\{\tau_i \left[\omega_s + \dot{\omega}\left(t - \frac{1}{2}\tau_i\right)\right]\right\}} \right\} \tag{4-23}
$$

In the above description, it has always been assumed that the direct component dominates ($\rho_0 = 1 > \rho_i$). When this is not the case, an inverted version of the above analysis is applied. Let ρ_m, $m \neq 0$, be the dominant multipath amplitude. Then the m-th subcarrier component will dominate the frequency estimate. The number of zero crossings is computed on the basis of the phase function arg($t - \tau_m$), and the endpoint perturbation argument goes through exactly as before, except that the phase differential $\phi_{mult}(t)$ is evaluated relative to the signal y(t) expj[-arg($t - \tau_m$)]. Essentially, the analysis from (4-10) on is duplicated with τ_m and θ_m replacing $\tau_0(=0)$ and θ_0. This concludes the FRS angle receiver analysis.

4.2.2   Time Reference System

The basic scanning beam angle system model contains the essential ingredients for a time reference scanning beam (TRSB) model of the type adopted by

the FAA as the U.S. ICAO candidate. The major distinctions between TRSB and the FM angle coded system are:

1. The FM angle subcarrier is no longer transmitted;

2. An angle measurement is made from two consecutive, oppositely directed scans (the so-called to-fro). Although no synchronization signal is transmitted, the airborne receiver can determine angle by the spacing between received scans;

3. The antenna scan rates are increased to obtain several measurements within the basic 5 Hz frame, the objective being to capitalize upon multipath (or motion) averaging.

It is interesting to note that TRS is in many respects the dual of the bi-direction scan Doppler MLS (see section 4.3). Those systems similarly employ multiple scans/frame for the purpose of multipath error reduction via averaging.

Figure 4-4 shows the TRSB signal format used in the Phase II computer model. The format uses time division multiplex within a full cycle of 592 msec. The system model for EL-1 and EL-2 assumes 8 to-fro scan pairs are averaged for each data point with the time differences between scans varied in accordance with Fig. 4-4. These time differences are cycled on successive 200 msec data frames, e.g., if the first EL scan of sequence 1 is the beginning of a data frame, then the last EL scan of sequence 1 (i.e., the ninth EL scan in a "full cycle") starts the next data frame.

For simplicity, three AZ to-fro scans are assigned to each 200 msec data frame. The time differences between these are varied in accordance
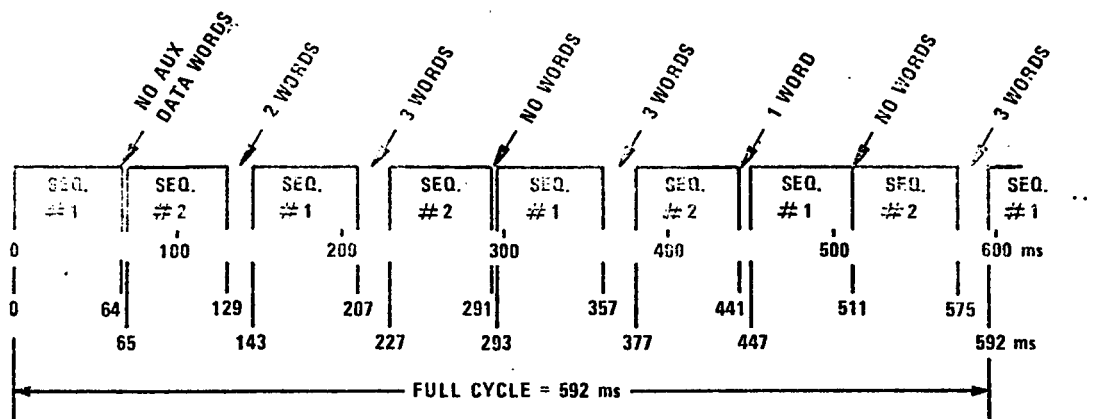
(a) Full Cycle of Functions
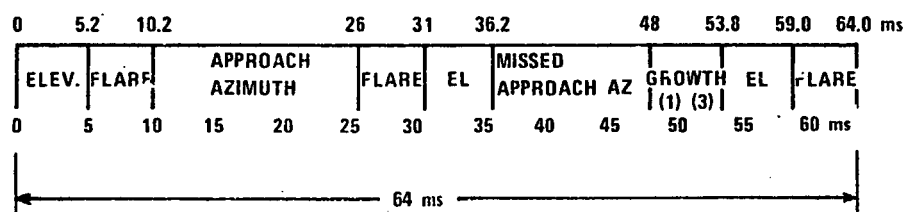
(b) Subsequence #1
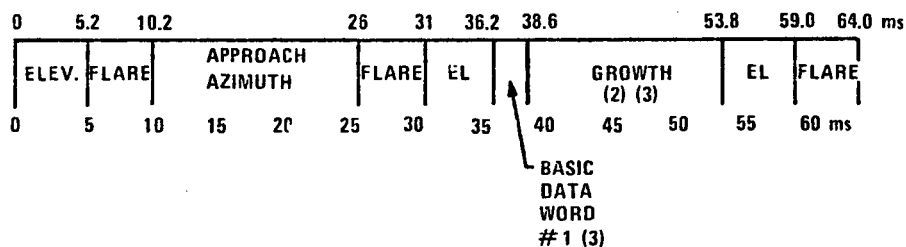
(c) Subsequence #2

NOTES: (1) AUXILIARY DATA (1 WORD) OR MISSED APPROACH ELEVATION
       (2) 360° AZIMUTH OR AUXILIARY DATA (2 WORDS)
       (3) BASIC DATA WORD #2 TRANSMITTED EITHER IN GROWTH
            OR BETWEEN SEQUENCES

ATC-63 VI 4-4

Fig. 4-4. TRSB function format.

4-21

with Fig. 4-4 and cycled between data frames as was done for the EL and flare functions.

4.2.2.1 Signal and Receiver Model

Extension of the FRS model to the TRS case involves dropping the angle code in the phase term (its effect has already been discarded in the amplitude term), and adding a phase term to account for motion averaging. In accounting for the to-fro scan pair, let the antenna scan rate be positive ($\dot{\theta} > 0$) on the to-scan, negative ($-\dot{\theta} < 0$) on the fro as illustrated in Fig. 4-5. The complex RF signal on the n-th to-scan can be written as

$$r_{1n}(t) = \left| \sum_{i=0}^{M} \rho_i P_1[\dot{\theta}(t - \tau_i(t) - (n-1)T_d)]expj\{\omega_c(t - \tau_i(t)) + \phi_i]\} \right| \tag{4-24}$$

in which the time varying delay due to A/C motion is indicated explicitly,

$$\tau_i(t) = \tau_i - \frac{v_a \cos \beta_i}{c} t \tag{4-25}$$

If the time scale is shifted so that each scan starts at t=0 (i.e., t is replaced by t + (n-1)T_d), the scan delay shows up in the phase term as a scalloping frequency. With this time scale change and multiplication by expj($-\omega_0 t$), the envelope of $r_{1n}(t)$ becomes

$$e_{1n}(t) = \left| \sum_{i=0}^{M} \rho_i P_1[\dot{\theta}(t - \tau_i) - \theta_i] \right.$$

$$\left. expj\left\{(\omega_i - \omega_0)t - \omega_c\left[\tau_i - \frac{v_a \cos \beta_i}{c}(n-1)T_d\right] + \phi_i\right\} \right| \tag{4-26}$$
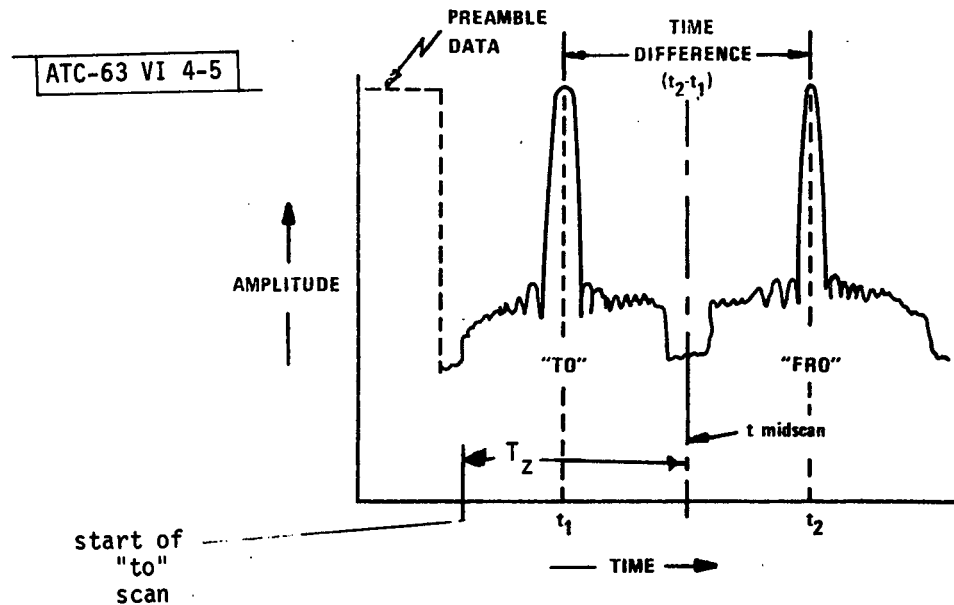
(a) Typical Pulses Received by
TRSB Receiver as Beam Scans TO and FRO
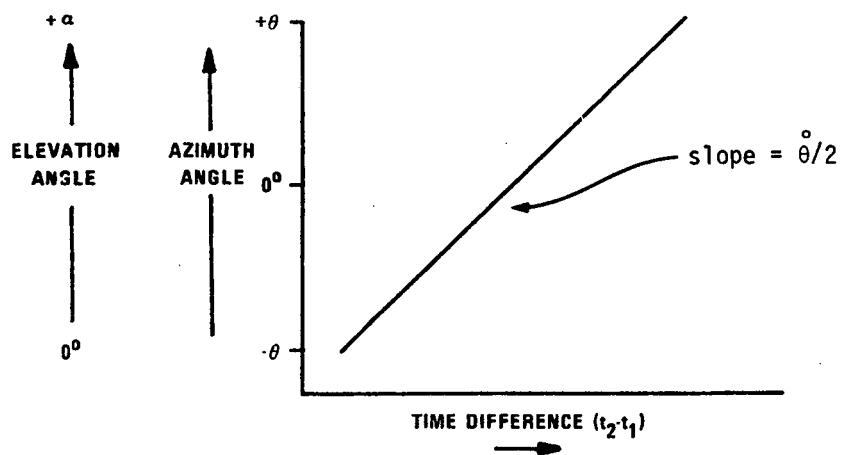
(b) Relation Between Time
Difference and Angle-in-Space

Fig. 4-5. Time reference angle measurement.

The envelope for the fro-scan is found in much the same way. In the beam envelope term, $\dot{\theta}$ is replaced by $-\dot{\theta}$ to indicate the change of scan direction, and the envelope delay is increased by an amount T_z, which is the elapsed time between $0°$ boresight on the to-scan and $0°$ boresight on the fro-scan (see Fig. 4-5). Thus, the envelope is

$$e_{2n}(t) = \left| \sum_{i=0}^{M} \rho_i P_1 [-\dot{\theta}(t - \tau_i) - \theta_i] \right.$$

$$\left. \exp j \left\{ (\omega_i - \omega_0)t - \omega_0 \left[\tau_i - \frac{v_a \cos \beta_i}{c} (n-1)T_d + T_z) \right] + \phi_i \right\} \right| \quad (4\text{-}27)$$

On each scan, the receiver generates a dwell gate for both to and fro. The thresholds for the dwell gate can be derived from either the previous scan peaks or the current peaks. Within a single slot, the threshold for the fro-pulse can be set independently or can be the same as for the to-pulse.

Let T_{11n} and t_{12n} be the dwell gate edges for the to-scan, and t_{21n} and t_{22n} be the edges for the fro-scan. The time scale has been set up so that the two dwell gates should be approximately symmetric about $t=0$. From (4-26) and (4-27) we see that the direct path envelope maximum occurs at $t = \pm \theta_0 / \dot{\theta}$ (+ for to, - for fro). The proposed angle estimator operates in a manner which is equivalent to finding the two dwell gate centers and subtracting their values to estimate $\sin \theta_0$.

The dwell gate centers are

$$T_{1n} = \frac{t_{11n} + t_{12n}}{2}$$

$$(4\text{-}28)$$

$$T_{2n} = \frac{t_{21n} + t_{22n}}{2}$$

4-24

If both gate centers occurred at the direct path envelope peak, their difference would satisfy

$$T_{1n} - T_{2n} = \frac{2\,\theta_0}{\dot{\theta}} \qquad (4\text{-}29)$$

independent of the actual scan arrival times at the aircraft. Thus, the n-th scan angle estimate is

$$\hat{\theta}_{on} = \frac{\dot{\theta}}{2}\,(T_{1n} - T_{2n}) \qquad (4\text{-}30)$$

and the frame error is found by averaging over N such estimates:

$$err = \frac{1}{N}\sum_{n=1}^{N}(\hat{\theta}_{on} - \theta_0) \qquad (4\text{-}31)$$

4.2.2.2 Multipath Control Technique

The U.S. TRSB system intends to employ a multipath control technique (MCT) to minimize the effects of ground reflection and other low elevation multipath sources in the flare system and, for some configurations, the primary elevation as well. MCT operation[21,22] consists of scanning the elevation beam down to some stop angle and subsequently decreasing the transmitted power according to a power program which will, in the absence of.multipath, yield the correct trailing edge dwell gate threshold crossing in all receivers located above the stop angle. The mirror image procedure is used on the up-scan. This section discusses the implementation of MCT in the MLS simulation.

Without MCT, the direct path signal envelope seen by a receiver at elevation θ is given in terms of the in-coordinate beam pattern as $P_1(-\dot{\theta}t - \theta)$.

With MCT the scan terminates at boresight angle θ_{stop} (equivalently, time $t_{stop} = -\theta_{stop}/ \dot{\theta}$), and an amplitude taper function $f(t)$ is applied:

$$A(t,\theta) = \begin{cases} P_1(-\dot{\theta}t - \theta) & ; \quad t \leq t_{stop} \\ f(t)\, P_1(\theta_{stop} - \theta); & t \geq t_{stop} \end{cases} \qquad (4-32)$$

The taper function is determined by the condition that the tapered waveform should cross the trailing edge dwell gate threshold at the same time as the untapered. For a fixed receiver coordinate, this is only a condition on the value of $f(t)$ at a single point. The fact that it must hold for all $\theta > \theta_{stop}$ constrains the entire function. The taper function depends upon the threshold level or, more precisely, upon the angular displacement of the beam at which the crossing occurs. Denote this displacement as v deg. Then

$$f(t) = \frac{P_1(v)}{P_1(\theta_{stop} - v + \dot{\theta}t)} \quad ; \quad t_{stop} \leq t \leq t_{stop} + \frac{v}{\dot{\theta}} \qquad (4-33)$$

The taper varies inversely with the scanning beam pattern. It has been assumed that $P_1(\cdot)$ is an even function in deriving Eq. (4-33).

The taper need only last for $v/\dot{\theta}$ sec if only receivers above stop angle are to be provided accurate guidance. After $t = t_{stop} + v/\dot{\theta}$, the beam is cut off. Without multipath, the trailing edge crossing will occur at cutoff time for receivers below θ_{stop} (see Fig. 4-6). As θ decreases, the dwell gate narrows and its center is too high (i.e., too early in time) by an amount $(\theta_{stop} - \theta)/2$. Thus if the dwell gate angle estimate $\hat{\theta}$ comes out below θ_{stop}, it is corrected upwards by an amount $(\theta_{stop} - \theta)/2$ on the assumption that the error is due to trailing edge cutoff. Thus the final estimate $\hat{\theta}$ is
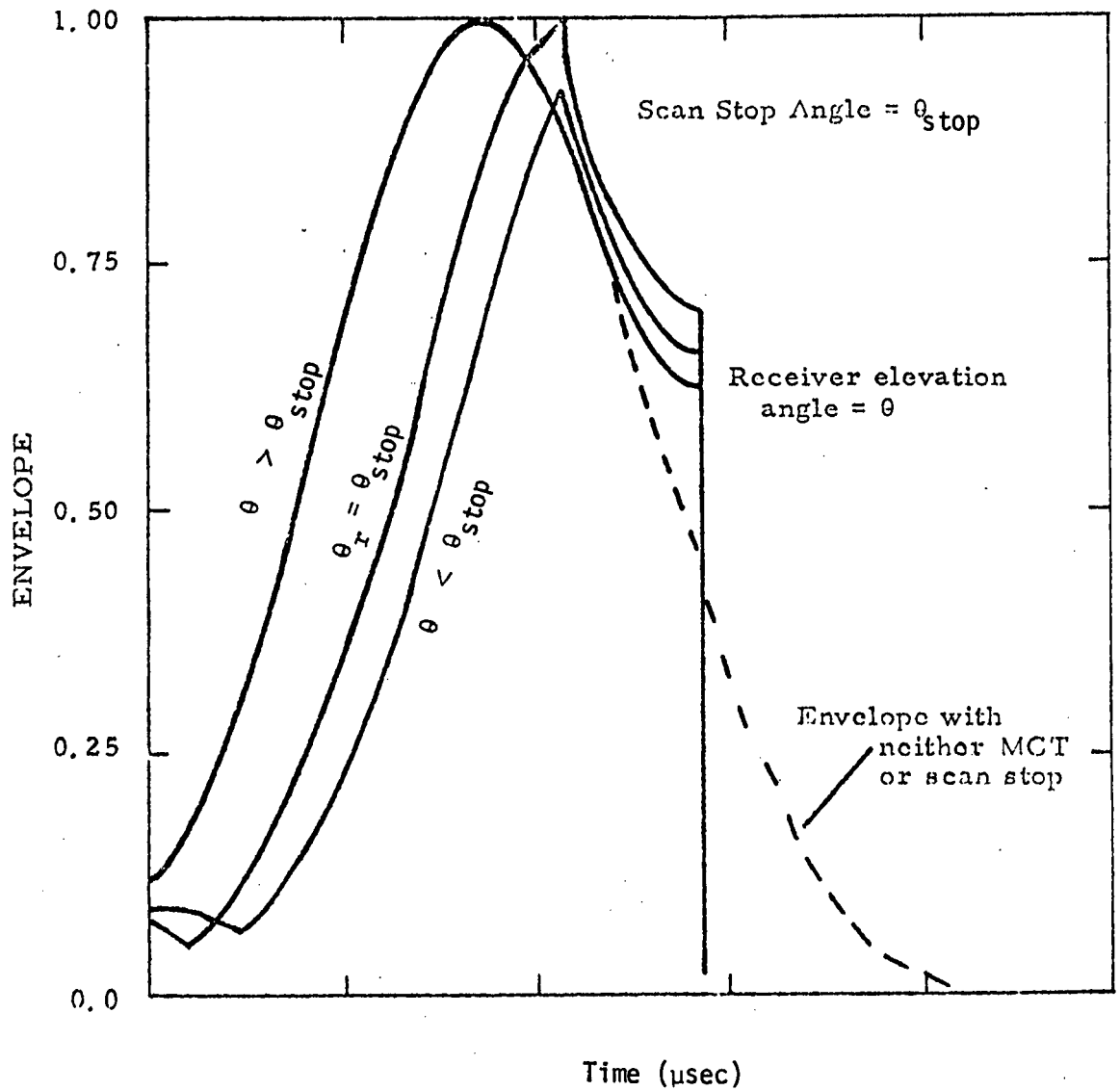
Fig. 4-6. Elevation patterns with MCT.

$$\hat{\hat{\theta}} = \begin{cases} \hat{\theta} & ; \; \hat{\theta} \geq \theta \\[2em] \dfrac{\hat{\theta} + \theta_{stop}}{2} & ; \; \hat{\theta} \leq \theta_{stop} \end{cases} \tag{4-34}$$

MCT is incorporated in the TRSB model by replacing the function $P_1[\dot{\theta}(t - \tau_i) - \theta_i]$ in Eq. (4-26) by $A(t - \tau_i, \theta_i)$, with a similar substitution being made for the fro-scan envelope. The threshold crossings are then found as before and then the MCT correction applied (if desired).

4.2.2.3 Alternative TRSB Processors

Brief consideration was given to TRSB receivers other than the dwell-gate processor discussed in Section 4.2.2.1. The work was in part motivated by the behavior of the dwell-gate processor in the presence of multipath whose amplitude exceeds the dwell-gate threshold. Early simulations of angular error vs RF phase between direct and multipath revealed the phenomenon exemplified in Fig. 4-7. The error has a nearly constant level for small phases followed by a sharp discontinuity. This behavior is explainable with reference to Fig. 4-8 which shows a multipath signal at positive separation and hence arriving later than the direct. At zero phase, the multipath adds coherently to the direct, thereby broadening the pulse and causing a large dwell-gate shift. Because of the time displacement of the two signals, the direct signal primarily determines the leading edge crossing and the multipath defines the trailing edge. Therefore, the dwell gate position is nearly independent of the phase until the phase progresses to the point where the multipath reduces the resultant so as to create a notch between the two
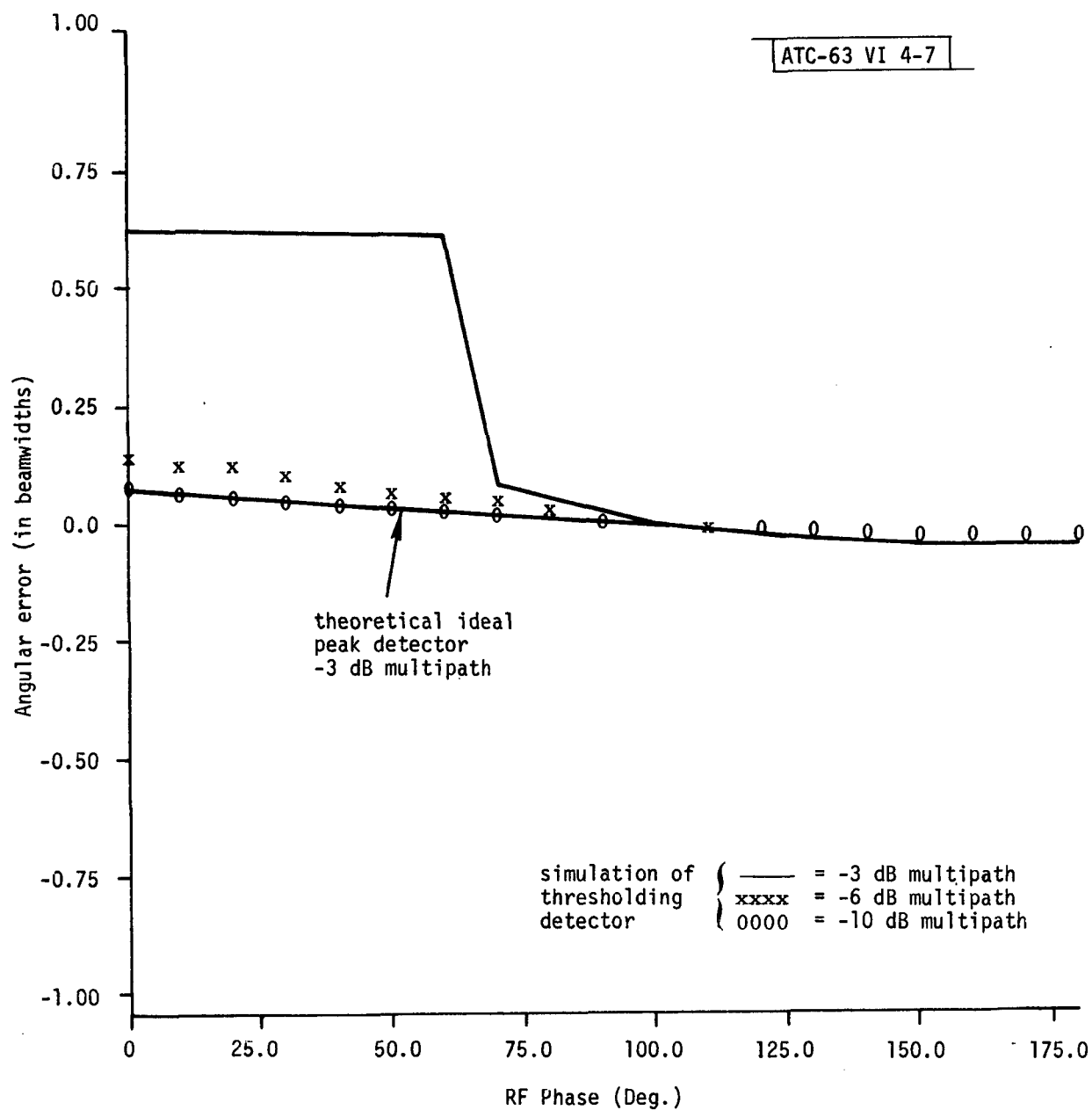
Fig. 4-7. Error vs RF phase, time-reference scanning beam system, separation angle = 1.5°.
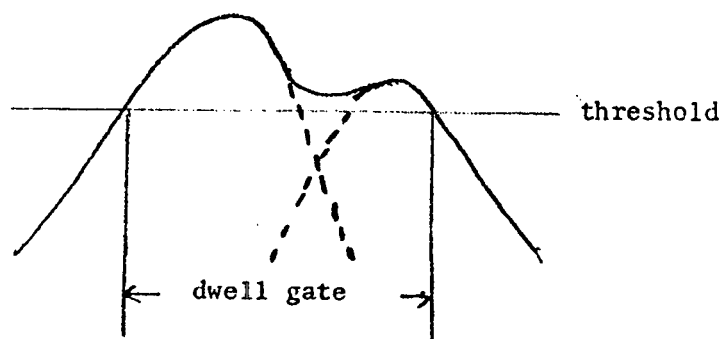
a) Multipath in phase with direct
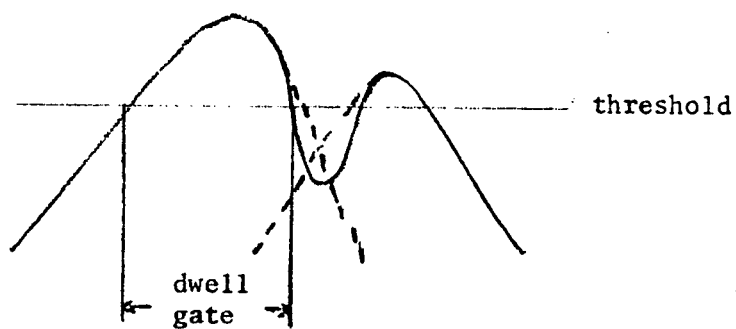
b) Multipath out of phase with direct

ATC-63 VI 4-8

Fig. 4-8. Dwell gate behavior for large multipath.

pulses. When the notch depth falls below the threshold, the dwell gate jumps to a position more nearly centered on the direct signal. The error is then correspondingly smaller and changes only slightly with phase thereafter as the pulse is narrowed due to cancellation of the direct by the multipath.

A processor that responds to pulse peak position rather than threshold crossings would be less susceptible to this type of multipath interference. A theoretical analysis of an ideal peak locator confirmed this expectation as indicated by the curve labeled "theoretical ideal peak detector -3 dB" in Fig. 4-7.

A practical approach to pulse peak location is the split-gate discriminator well known in the radar literature. Two forms of split-gate processor have been considered. In one, shown in Fig. 4-9a, the split-gate multiplies the pulse envelope and the product is integrated to yield an estimate of how far the gate is off-center from the pulse. Since the integral is proportional to pulse amplitude as well as gate offset, a correction derived from pulse peak is applied to the estimate. The off-center measurement is employed in a feedback loop to drive the gate toward the pulse peak for the next pulse period. The instantaneous pulse position is obtained by adding the off-center reading to the gate timing.

A second split-gate processor implements the operations of multiplication and integration by a convolution. The pulse is fed to a filter whose impulse response duplicates the split-gate waveform. The output of the filter which is the convolution of pulse and gate as sketched in Fig. 4-9b, passes through zero at one instant of time corresponding to the arrival of pulse peak plus a
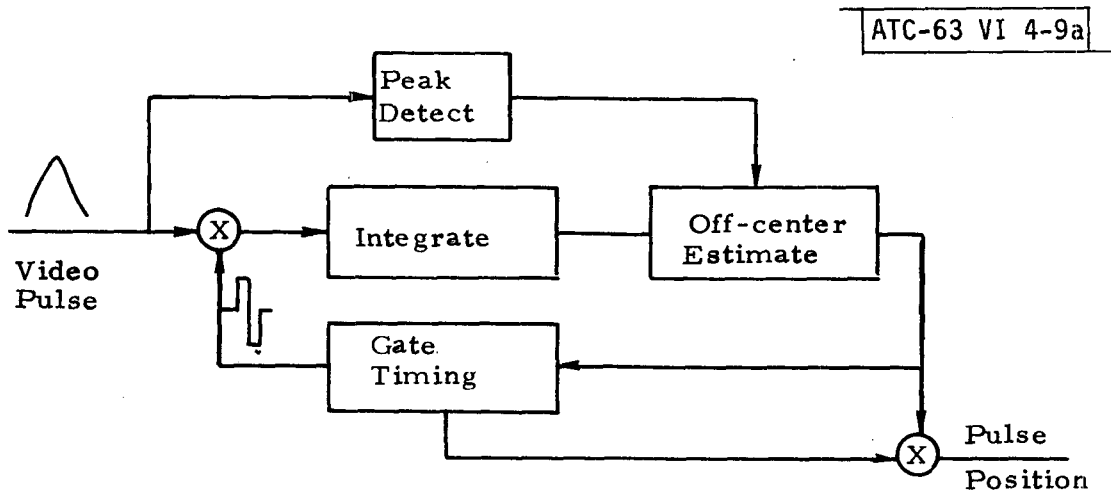
Fig. 4-9a. Split-gate multiply and integrate
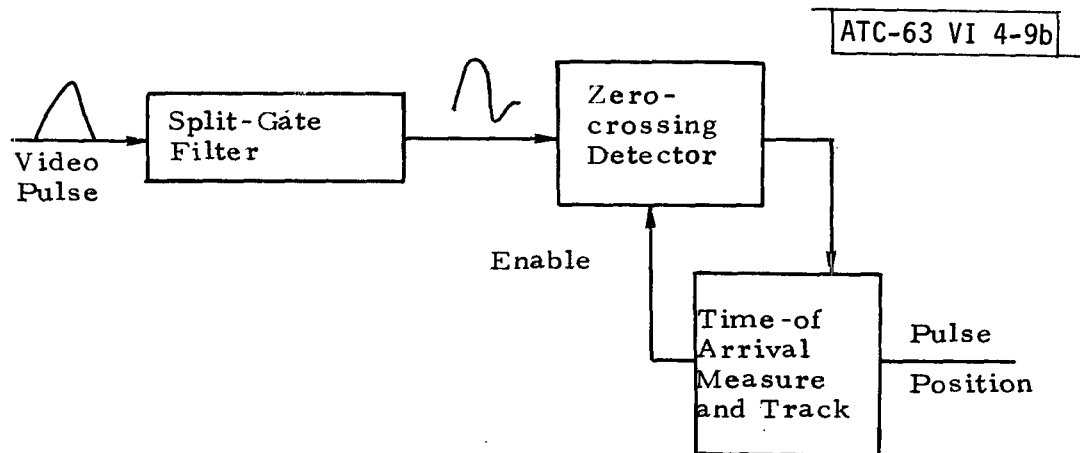
Fig. 4-9b. Split-gate convolution.

fixed delay. The zero crossing time is, therefore, a measure of pulse position. The zero-crossing processor does not require pulse amplitude correction in its estimate. However, to avoid confusion by other zero crossings, the measurement must be enabled at the proper time by a time gate or amplitude threshold crossing.

A limited number of simulation runs were carried out to compare the performance of the two split gate and dwell gate processors. These are discussed in Chapter 6.

This concludes the scanning beam system model analysis.

4.3 Doppler Scan Angle System Models

Operation of the Doppler scan MLS model is presented primarily in terms of the ITT/GIlfillan simulation. Although there is greater fundamental difference between the two Doppler models (ITT/G and Hazeltine) than between the two FRS models, the ITT/G was used as the basis for a model of the U.S. Doppler Working Group system. In Section 4.3.2, certain aspects of the Hazeltine signal generation technique are explained as an alternative Doppler antenna mechanization. Following that, a third antenna technique based upon United Kingdom work is discussed. The latter has multipath properties which differ substantially from those of the more conventional designs. To date, the U.K. Doppler system has not been simulated.

4.3.1 Basic System Model

The angle subsystems under consideration operate according to the Doppler scan principle. In a Doppler system, angle information is transmitted via a

CW signal radiated into the coverage volume. This signal is spatially modu-lated so that the frequency transmitted towards a particular point in space is a monotone function of the angular coordinate of that point. In order to counteract the effect of A/C-induced Doppler shift, a CW reference tone is transmitted simultaneously at a neighboring frequency. The airborne re-ceiver measures the difference in frequency between the two received signals (the difference frequency is essentially free of any dependence on aircraft motion) in order to estimate the angular coordinate.

During Phase II, ITT/Gilfillan employed ground system antennas (elec-tronically commutated line arrays) which generate the Doppler signal by simu-lating the motion of an RF source. The angle encoding varies sinusoidally with angle, and the array beamwidth increases in proportion to the sine of the off-boresight angle. The natural coordinates of the resulting angle sub-systems are conical.

During an angle data frame, the commutated source makes several scans across the antenna aperture. These scans are bidirectional, that is, the source motion is first in one direction, then in the opposite. The number of scans/frame varies with angle function. The angle receiver makes use of all these scans in deriving an angle estimate and in doing so it can incur the benefits of motion averaging.

The primary source of angle measurement error attributable to multipath phenomena derives from the method of frequency estimation employed by the airborne receiver. The receiver (which derives timing information from the incoming signal and thus operates synchronously with it) establishes a scan

gate over which it observes each received scan; the gate has a duration which is a fraction of the transmitted scan duration. The average angle signal frequency is estimated by counting both the number of zero crossings within the scan gate and the elapsed time from the first to last zero crossing. As in the scanning beam FRS systems, the dominant component in the received signal captures the counter and controls the average frequency. The total multipath signal perturbs the location of the endpoint crossings, causing the estimated frequency to differ from the dominant frequency.

4.3.1.1   Transmitted Signal

The reference signal is an RF tone of frequency $\omega_r (\simeq 5$ GHz). The angle signal differs from the reference by an offset $\omega_{off} (\simeq 100$ kHz) and may take on either value $\omega_r \pm \omega_{off}$, the sign of ω_{off} being governed by the scan direction. The commutation process is modeled by assuming that the source moves at a constant velocity (v_s) over the duration of a scan (T_s) and traverses the antenna aperture $L = v_s T_s$. A total of 2N scans are transmitted. On the first of these it is assumed that the carrier takes on the upper sideband value $\omega_r + \omega_{off}$ and that it alternates between lower and upper sideband on successive scans.[*] The sequence consisting of an upper followed by a lower sideband scan constitutes a bidirection scan (duration $2T_s$). At the midscan transition (or turnaround) of the commutated signal, the RF waveform is continuous as the frequency changes from $\omega_r + \omega_{off}$ to $\omega_r - \omega_{off}$. It is assumed

---

[*]This alternation of sidebands preserves the angle coding at a fixed angular direction when the scan reverses, i.e., the received frequency alternates between two values which are equidistant from ω_r. At baseband this appears as a constant frequency.

that each of the N bidirectional scan transmissions is identical.[*] By advancing the time origin an amount $2T_s$ for each scan pair, a single formula which is independent of the bidirectional scan number can be written for the signal transmitted by the moving source:

$$s(t) = \begin{cases} \exp j[(\omega_r + \omega_{off})t] & ; \ 0 \leq t \leq T_s \\ \\ \exp j[(\omega_r - \omega_{off})t + 2\omega_{off} T_s] & ; \ T_s < t < 2T_s \end{cases} \tag{4-35}$$

The reference signal is simply

$$s'(t) = \exp j(\omega_r t) \ ; \ 0 \leq t \leq 2T_s \tag{4-36}$$

A stationary observer located on the radial defined by the conical coordinates (θ, Φ), where θ is the measured coordinate angle (e.g., azimuth in the AZ system, etc.) and Φ is the orthogonal coordinate, sees a linear combination of $s'(t)$ and a Doppler shifted version of $s(t)$. Each signal is weighted by the transmitting antenna pattern in the direction (θ, Φ); these patterns are desginated as $P'(\theta, \Phi)$ and $P(\theta, \Phi)$, respectively. Each of these patterns is assumed to factor intc a product of an azimuth and an elevation pattern just as for the scanning beam case:

$$P(\theta, \Phi) = P_1(\theta) \ P_2(\Phi)$$

$$P'(\theta, \Phi) = P_1'(\theta) \ P_2'(\Phi)$$

---

[*]The process known as phase cycling (or stepping or digitization) which is employed at the angle transmitter is intentionally neglected in the model. This feature is employed to reduce granularity error in the angle estimate, but since this is an instrumentation-related, not a multipath-related problem, it need not be of concern here. Phase cycling also helps to average out filter transient effects.

In a square-law envelope detector the relative value of the angle and reference signal amplitudes is of no concern, since only the cross-product term is retained in the angle measurement. In linear envelope or other detectors, additional intermodulation (IM) products are generated. As a partial validation of the decision to employ a square-law detector, a study of the intermodulation distortion created by a multipath signal in a linear envelope detector was carried out. This is reported in Appendix B. The principal finding is that although the linear detector exhibits some small multipath suppression, the reduction is at the expense of the introduction of equally bothersome IM products. If, however, the received carrier level is at least 6 dB above the angle sideband signal, the small multipath characteristics of linear and square-law detectors nearly coincide.

The fractional Doppler shift experienced by the sideband signal $s(t)$ depends only on the conical angle θ and the commutated source velocity vector. The coordinate system is the same as for scanning beam, i.e., centerline in AZ, parallel to the ground in EL-1 and EL-2. The commutated source velocity vector points in the direction $\theta = +90°$ on the upper sideband scan and $\theta = -90°$ on the lower. Therefore, the angle frequency observed at coordinate θ is

$$(\omega_r \pm \omega_{off})(1 \pm \frac{V_s}{c} \sin \theta) \quad , \tag{4-37}$$

the + or - sign depending upon the scan direction.

The proportionality constant in the angle-to-frequency mapping is called the <u>coding factor</u> and is denoted by K; from (4-35) it is evident that

$$K = \frac{\omega_r V_s}{c} \text{ (rad/sec)/rad}$$

(to within $\pm$ 2 ppm). A more readily understandable expression for K can be given in terms of the scan duration and the aperture size in wavelengths, or simpler yet, the antenna beamwidth in degrees (θ_{BW}), defined by the aperture in wavelengths in the familiar way:

$$K = \frac{\pi}{180\ T_s}\left(\frac{L}{\lambda}\right) = \frac{1}{\theta_{BW}T_s}\ \text{Hz/deg}$$

4.3.1.2 Received Signal

The received signal models for angle and sideband consist of a super-position of the direct path component and the multipath propogation components. Each component of the sideband signal is characterized by 6 parameters (see Section 4.2.1.2 for details). A similar set of 6 parameters characterize the reference signal; these are designated by primes (e.g., ρ_i' = i-th reference multipath amplitude). The values of the 12 parameters are calculated for each reflector in the scattering portion of the program. For the initial runs it was assumed that the reference and angle antennas are colocated, and in the case of AZ, have identical antenna patterns. In those cases for which the patterns are identical, the multipath parameters will be identical as well (the received frequencies ω_i and ω_i' will not of course be equal due to the difference in transmitted frequency and the commutated source Doppler, but their A/C-dependent Dopplers will be the same). More recently the simulation program has been rewritten to accommodate non-colocated reference and sideband antennas and to perform a separate multipath computation for each.

The received frequencies are a function of the angle between the aircraft velocity vector and the arrival direction of the incoming component. For the angle signal they also depend upon the angle between the commutated source velocity vector and the vector from the transmitter to the specular point on the reflector. These two situations are shown in Figs. 4-10 and 4-11. In the multipath signal case, the geometry is given in terms of an image transmitter and image source velocity vector. For the direct components, the refelctors are absent and the propagation path is rectilinear. Doppler information is computed in terms of the fractional frequency changes $(v_a \cos \beta_i)/c$ and $(v_s \cos \gamma_i)/c$.

In order to complete the received signal calculation, the time dependent delays along each of the paths must be evaluated. For the angle signal, τ_i represents the path delay at the beginning of the frame (t=0). The time dependent delay for the first scan is

$$\tau_i(t) = \tau_i - \left(\frac{v_a \cos \beta_i}{c}\right) t - \left(\frac{v_s \cos \gamma_i}{c}\right) t \qquad (4\text{-}38)$$

It is assumed that $\cos \beta_i > 0$, i.e., that the aircraft is approaching the transmitter. Since the sense of the source velocity vector reverses at each scan transition, $\cos \gamma_i$ will take on both signs. Equation (4-30) can be modified to yield the delay for the n-th scan by accommodating the changes in scan direction and updating the delay corresponding to the aircraft position at the beginning of the n-th scan. This is done in such a way that the time reference is reset to t=0 at the beginning of each scan:
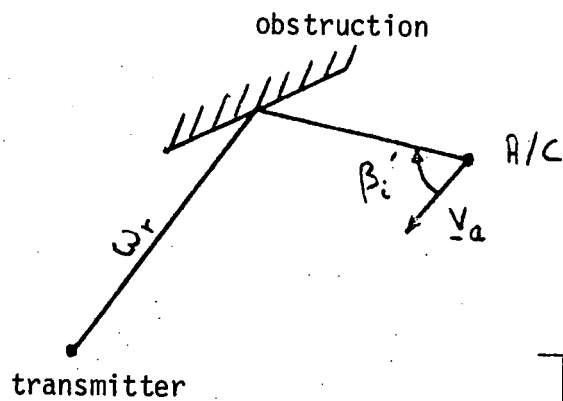
Fig. 4-10.   Geometry for received reference frequency calculation.
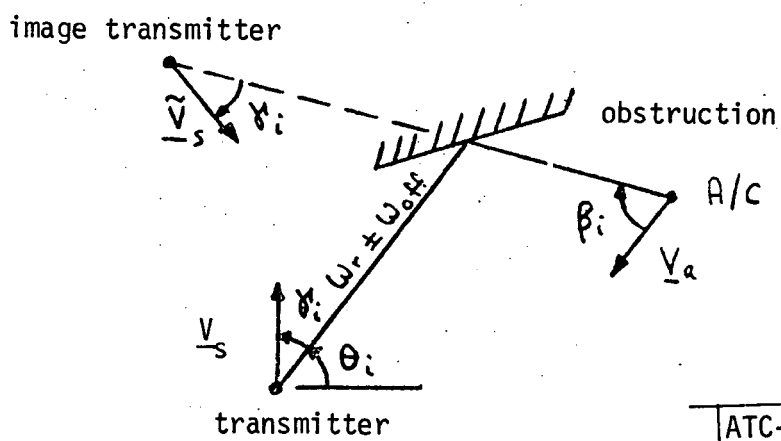
Fig. 4-11.   Geometry for received angle frequency calculation.

$$\tau_{in}(t) = \tau_i - \left(\frac{v_a \cos \beta_i}{c}\right) [t + (n-1)T_s] - \frac{v_s \cos \gamma_i}{c} \begin{cases} t & ; \ n=\text{odd} \\ (T_s-t); & n=\text{even} \end{cases}$$

(4-39)

In (4-39), γ_i is assumed to retain the value it takes on at the first scan (n=1). The delay formula for the reference signal is simpler since there is no source Doppler component:

$$\tau'_{in}(t) = \tau'_i - \left(\frac{v_a \cos \beta'_i}{c}\right)[t + (n-1)T_s]$$

(4-40)

The total received signal can be written in terms of the parameters defined above. The i-th angle component of the n-th scan is $\rho_i y_{in}(t)$, where[*]

$$y_{in}(t) = \exp j\left\{[\omega_r - (-1)^n \omega_{off}] [t - \tau_{in}(t)] + \phi_i\right\}$$

(4-41)

The corresponding reference component is $\rho'_i y'_{in}(t)$:

$$y'_{in}(t) = \exp j\left\{\omega_r[t - \tau'_{in}(t) + \phi'_i\right\}$$

(4-42)

Since the commutated and reference signals are transmitted simultaneously, the n-th scan received signal is the sum $r_n(t)$:

$$r_n(t) = \sum_{i=0}^{M} [\rho_i y_{in}(t) + \rho'_i y'_{in}(t)]$$

(4-43)

---

[*]The right-hand side of (4-41) should also contain a term equal to $\omega_{off}T_s$ on the even scans (see Eq. (4-35), but it is dropped under the assumption that it is a multiple of 2π.

From (4-39)-(4-42) we can identify the n-th scan frequencies ω_{in} and ω'_{in} of the received angle and reference signals, respectively:

$$\omega_{in} = [\omega_r - (-1)^n \omega_{off}] \left[1 + \frac{v_a \cos \beta_i}{c} - (-1)^n \frac{v_s \cos \gamma_i}{c} \right] \qquad (4-44)$$

$$\omega'_{in} = \omega_r \left[1 + \frac{v_a \cos \beta'_i}{c} \right] \qquad (4-45)$$

4.3.1.3 Receiver Processing

Figure 4-12 shows a block diagram of the ITT/G angle processor[18,31]. The input sum signal is translated through two IF stages. The second IF output is applied to the final square-law detector. The video output of this signal contains a term proportional to the product of the angle and reference signals centered in the vicinity of ω_r, and this is essentially the signal upon which the angle measurement is based.

Prior to angle measurement, the signal is subjected to multipath rejection filtering. The rejection filter is embedded in a tracking loop which attempts to VCO the direct component of the signal to a fixed frequency where the filtering takes place. After the filtering, the signal is returned to the original frequency band using the same VCO, eliminating the possibility of residual frequency offset in the angle signal. Following the rejection filter loop is a scan gate generator which blanks out the initial segment of each scan. The gate generator controls the operation of the zero-crossing counter (ZCC) and time interval counter (TIC) which follow. These count both the number of zero crossings within the scan gate and the elapsed time between
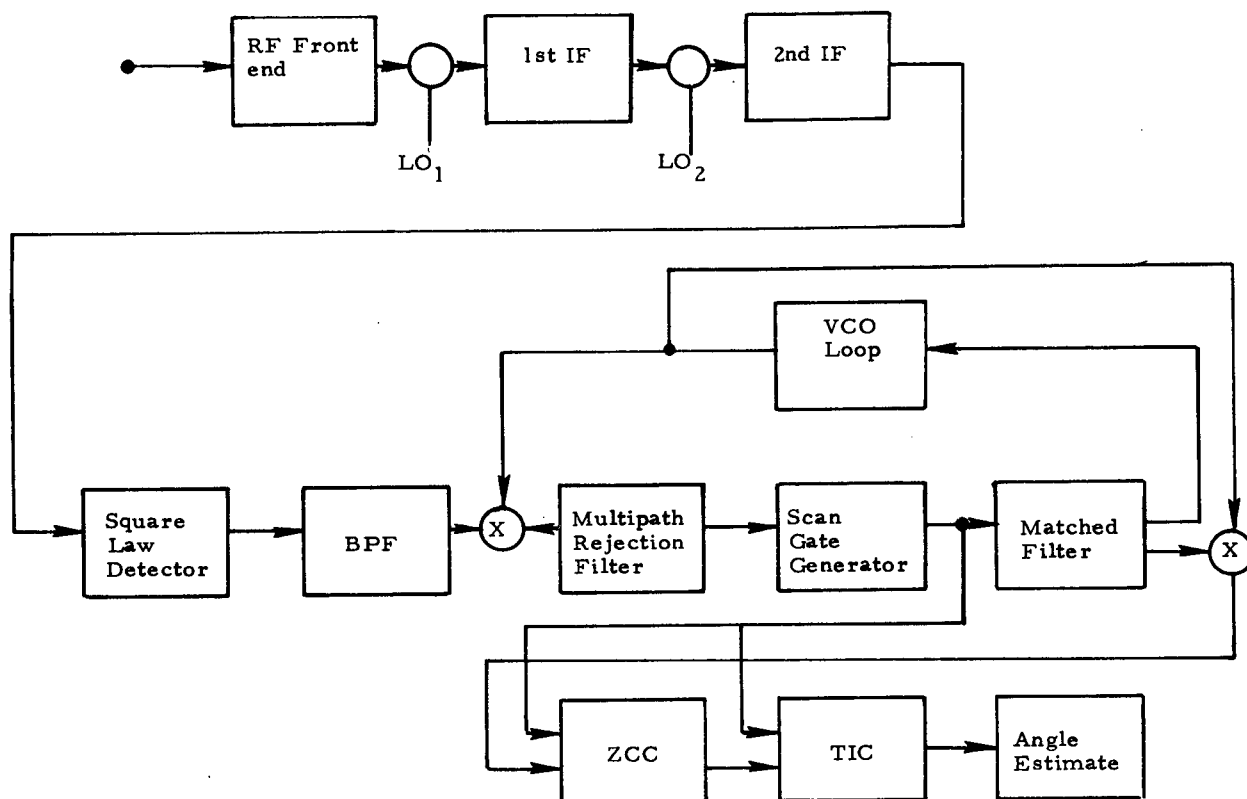
Fig. 4-12. ITT/G angle processing receiver.

the first and last crossings. This occurs on all 2N scans and the angle estimate is essentially proportional to the ratio of total number of crossings to the total elapsed time measured by the TIC. The length of the scan gate, T_c, is chosen by a compromise between blanking the filter transients due to the scan reversals and eliminating large portions of the signal.*

The analog multipath rejection filters employed by ITT/G during the Phase II tests were narrowband and hence have transients which can persist longer than a scan duration. The sharp rolloff of such a filter character-istic will permit it to achieve good multipath rejection when properly centered; this feature is useful in rejecting multipath returns from reflec-tors at in-beam or nearly in-beam angles which are illuminated with angle code only slightly different from that of the direct path. However, a large portion of the received signal must be scan-gated out for transient suppres-sion.

The filters employed by Hazeltine[30,33] during the Phase II trials were wideband and have fairly shallow rolloff. Their transient response is short relative to the scan time, which permits a large portion of the scan to be used for frequency measurement. On the other hand, significant multi-path suppression at the receiver is achieved only at far-out-of-beam separa-tion angles. Of course, it must be emphasized that Hazeltine employed this receiver configuration in conjunction with ground system antennas which are

---

*Roughly, the error in a Doppler scan system is proportional to T_s/T_c, the ratio of scan duration to scan gate duration. Obviously then, this should be as large as possible while eliminating most of the rejection filter trans-sients.

designed, for example, to have a sharp horizon rolloff in elevation which would suppress ground reflection multipath at the transmitter end of the system.

The angle processor model described below incorporates the following features which were deemed necessary to achieve representative error models:

1. All the modulation products between the angle and reference signals are retained. Thus effects due to multipath on both signals should emerge.

2. Scalloping of both the angle and reference signals is included by representing the scan-to-scan phase coherence of each received component.

3. An amplitude check for reference signal fading is included.

4. An elementary model of the tracker dynamics is included. By tracking on the previous angle estimate rather than the true A/C position, the "pulling" effect of in-beam multipath will be observed. This effect tends to give higher and more realistic errors than would otherwise be predicted using fixed gate tracking.

In the simulation, a steady state model for the filter output is assumed; that is, rather than characterize the filtering in the time domain where the output would be computed by convolving the input with an impulse response, we look only at the steady state residual of the filtering. This is obtained by multiplying each term of the complex signal by the filter transfer function evaluated at the appropriate frequency.

This type of model is most appropriate to scan-gated delay line processors, a type of processor which is thought by many to give the best Doppler performance. Transversal delay line filters (feed-forward only) have finite duration impulse responses, so that, with proper scan gating, no performance degradation due to scan turnaround transients need occur. In this case the steady state model is rigorously accurate. Because of the finite duration

of the impulse response, the frequency response of the filter will exhibit a sidelobe structure which allows some "out of beam" components through with less than the desired rejection.

We recognize that many of the rejection filters implemented to date are analog. Experiments by the U.K.[39] and others indicate that if the actual analog filter transfer function is used in a model such as ours, the errors which are predicted tend to be too small, especially as the multipath separation angle increases beyond a beamwidth. This is attributable to the transient effects which are not accurately modeled by the steady state approach. In order to properly account for filter effects in a steady state model, one needs a transfer function which has sidelobe structure of the sort that naturally occurs in a finite impulse response (FIR) filter. This suggests that an appropriate first order model for the analog filter may be an FIR with approximately the same in-band response as the analog filter and sidelobe structure which arises from truncating the impulse response to a duration equal to the scan gate.

The square-law detector output contains a term proportional to the angle-reference crossproduct:

$$y_n(t) \, y_n'^{*}(t) = \sum_{i=0}^{M} \sum_{j=0}^{M} \rho_i \rho_j' \, y_{in}(t) \, y_{jn}'^{*}(t) \qquad (4\text{-}46)$$

This signal can be written as

$$y_n(t) \, y_n'^{*}(t) = \sum_{i=0}^{M} \sum_{j=0}^{M} \rho_i \rho_j' \, \cos(\omega_{ijn} t + \alpha_{ijn}) \qquad (4\text{-}47)$$

where the frequency and phase of the (i,j) component are given by

$$\omega_{ijn} = \omega_{in} - \omega'_{jn} = \omega_r \left[\frac{v_a(\cos\beta_i - \cos\beta'_j)}{c} + (-1)^{n-1} \frac{v_s \cos\gamma_i}{c} \right]$$
$$+ (-1)^{n-1} \omega_{off} \left[1 + \frac{v_a \cos\beta_i}{e} + (-1)^n \frac{v_s \cos\beta_i}{c} \right] \qquad (4\text{-}48)$$

$$\alpha_{ijn} = \omega_r \left[\tau'_j - \tau_i + \frac{v_a(\cos\beta_i - \cos\beta'_j)}{c}(n-1)T_s \right]$$
$$+ (-1)^n \omega_{off} \left[-\tau_i \frac{v_a \cos\beta_i}{c}(n-1)T_s \right] + \phi_i - \phi_j + \delta_{in} \qquad (4\text{-}49)$$

$$\delta_{in} = \begin{cases} 0 & ; \text{ odd } n \\[2ex] \frac{\omega_r v_s \cos\gamma_i}{c} T_s + \omega_{off}\left(1 - \frac{v_s \cos\gamma_i}{c}\right) T_s & ; \text{ even } n \end{cases} \qquad (4\text{-}50)$$

Let $H(\omega)$ be the rejection filter characteristic. The function is centered at $\omega=0$. Assume that the tracking loop centers the filter on the frequency measured during the previous frame, $\hat{\omega}_{old}$. Then the signal out of the rejection filter loop is modeled as

$$\sum_{i=0}^{M} \sum_{j=0}^{M} H(\omega_{ijn} - \hat{\omega}_{old}) \rho_i \rho'_j y_{in}(t) \, y'^{*}_{jn}(t) \qquad (4\text{-}51)$$

on the n-th scan. The scan gate removes a leading and trailing segment of the scan, allowing zero-crossing counting to be done only over the interval $t \, [\frac{1}{2}(T_s - T_c), \frac{1}{2}(T_s + T_c)].$[†]

[†]The centered scan gate is employed because the filter model as posed is unrealizable. For a realizable filter only the leading segment contains transient behavior which must be deleted. In the simulation, the gate location is of no consequence other than to systematically shift the phase relationships among the multipath components.

The data obtained by an actual receiver on the n-th scan consists of the number of zero-crossings k_n and the intervals T_n'' between the first and last zero-crossings within the gate. The angle estimate is obtained as follows:

$$\hat{\omega} = \frac{\displaystyle\sum_{n=1}^{2N} (k_n - 1)}{\displaystyle\sum_{n=1}^{2N} T_n''} \tag{4-52}$$

which is nothing more than the ratio of the phase accumulated across the dwell gates to the total time measured by the TIC.

The intervals T_n'' are determined by the phase perturbation method described in the scanning beam, Section 4.2. The method is more readily justified here because the sinewave bursts are not amplitude modulated.

It should be noted that the phase perturbation method of analysis is not new; it can be traced to the NATO-NIAG simulation by ELAB[40], and has been used by both U.S. Doppler contractors as well.[18,30,31,33]. The mathematical support for the angle estimation model is detailed below.

Three separate cases can be considered in developing the mathematical models for the procedure just described. In the first of these (Case A), it is assumed that the direct component is sufficiently strong to capture the zero crossing counter; in the second (Case B), a multipath component is larger than the direct and captures the counter. A third (Case C) includes those intermediate situations in which, although one component has amplitude greater than all others, it may not be sufficiently large to guarantee that

its frequency dominates the zero crossing process.[*] The treatment of Case C involves direct zero crossing counting of the angle waveform and has not been included in the present version of the simulation.

Cases A and B are treated together, as A is really just a special instance of B. Sufficient conditions for dominance of the IJ component are

$$\rho_{INn} \geq \rho_{ijn}, \quad i \neq I, \, j \neq J \tag{4-53}$$

and

$$\rho_{IJn} > \sum_{i=0}^{M} \sum_{j=0}^{M} \rho_{ijn} \atop i,j \neq I,J \tag{4-54}$$

where

$$\rho_{ijn} = \frac{\rho_i \rho_j H(|\omega_{ijn} - \hat{\omega}_{old}|)}{\rho_0 \rho_0 H(|\omega_{oon} - \hat{\omega}_{old}|)} \tag{4-55}$$

Condition (4-54) states that the amplitude of the dominant component exceeds the sum of the remaining $M^2 + 2M$ amplitudes. This is a rather stringent condition, especially since at low scalloping frequencies the reference frequency

---

[*]Certain Doppler contractors claimed that the direct component would always capture the zero crossing counter if it were larger than the other components. However, it has been shown [41] that in the simplest case of a single multipath component, one needs the condition

$$\rho_0 \, \omega_0 > \rho_1 \, \omega_1$$

as well as $\rho_0 > \rho_1$ to insure that no false zero crossings are generated. The practical impact of this condition is that reliance on capture effect for wide-band Doppler signals to accomplish signal acquisition may be unreliable when the direct signal Doppler is substantially less than that of multipath even though the direct signal has a larger amplitude.

terms could be combined into a single term. If no (i,j) pair satisfies (4-54), then the receiver should be in Case C. For the present, the default option is to assign I,J to the component with the maximum value of ρ_{ijn}. In either event, the test(s) need only be done for one even and one odd scan (e.g., n=1,2), since the multipath environment is constant over the frame (aircraft motion causes the post-filtered amplitudes to differ on the even and odd scans). Thus Case A corresponds to $(I,J) = (0,0)$.

The net phase accumulated by the dominant component across the n-th scan gate is

$$\omega_{IJn}(t_2 - t_1) = \omega_{IJn} T_c \tag{4-56}$$

where

$$t_1 = \frac{1}{2}(T_s - T_c)$$

$$t_2 = \frac{1}{2}(T_s + T_c)$$

are the scan gate edges (the gate picks up the middle T_c sec of each scan). The greatest number of full half cycles represented by the phase increment (4-56) is

$$C_n = \text{Integer Part} \left(\frac{\omega_{IJn} T_c}{\pi} \right) \tag{4-57}$$

The number of crossings k_n is either C_n or C_{n+1} and is determined using the rule given in Table 4-1, Section 4.2.1.3; in this case the argument function is simply

$$\text{arg}(t) = w_{IJn} t + \alpha_{IJn}$$

4-50

Having determined the number of zero crossings caused by the dominant wave, the instants of the first and last crossings of the wave within the scan gate must be computed. Define q_{1n} and q_{2n} as follows:

$$q_{1n} = (\omega_{IJn}t_1 + \alpha_{IJn}) \pmod{\pi}$$

$$q_{2n} = (\omega_{IJn}t_2 + \alpha_{IJn}) \pmod{\pi}$$

(4-58)

These parameters represent the phase excess over π of the dominant wave phasor at the two ends of the scan gate. The endpoint zero crossings t'_{1n} and t'_{2n} are found by extrapolating time to the next zero crossing. At the leading edge of the gate, time is extrapolated forward - at the trailing edge backward. Due to the sideband alternation of the commutated signal, the phasor rotates counterclockwise on the first scan and reverses direction at each new scan. Hence separate projection formulas are needed, depending on the parity of n.

$$t'_{1n} = \begin{cases} t_1 + \dfrac{\pi - q_{1n}}{|\omega_{IJn}|} & ; \quad \text{odd } n \\[2em] t_1 + \dfrac{q_{1n}}{|\omega_{IJn}|} & ; \quad \text{even } n \end{cases}$$

(4-59)

$$t'_{2n} = \begin{cases} t_2 - \dfrac{q_{2n}}{|\omega_{IJn}|} & ; \quad \text{odd } n \\[2em] t_2 - \dfrac{\pi - q_2}{|\omega_{IJn}|} & ; \quad \text{even } n \end{cases}$$

(4-60)

By definition, the phase of the dominant component is zero at times t'_{1n}, t'_{2n}. However, this is not necessarily true of the total angle signal in the presence of multipath. That signal has nearest zero-crossings at times t''_{1n} and t''_{2n} which can be approximated by computing the phase angle of the net signal phasor referenced to the dominant component phase and projecting the times of the nearest zero crossings. The n-th scan phase function described above is

$$\phi_n(t) = \tan^{-1} \left\{ \frac{\displaystyle\sum_{i=0}^{M} \sum_{j=0}^{M} \rho_{ijn} \sin[(\omega_{ijn} - \omega_{IJn})t + \alpha_{ijn} - \alpha_{IJn}]}{\displaystyle\sum_{i=0}^{M} \sum_{j=0}^{M} \rho_{ijn} \cos[(\omega_{ijn} - \omega_{IJn})t + \alpha_{ijn} - \alpha_{IJn}]} \right\} \tag{4-61}$$

and the zero crossing projections are

$$t''_{1n} = t'_{1n} - \frac{\phi_n(t'_{1n})}{\omega_{IJn}} \tag{4-62}$$

$$t''_{2n} = t'_{2n} - \frac{\phi_n(t'_{2n})}{\omega_{IJn}} \tag{4-63}$$

The alteration in direction of rotation of the dominant phasor is taken into account by the sign of ω_{IJn}.

The values of k_n and T'_n, where

$$T''_n = t''_{2n} - t''_{1n} \tag{4-64}$$

are substituted into (4-52) to derive the frequency estimate $\hat{\omega}$. This value is stored as $\hat{\omega}_{old}$ to be used in the next frame tracking filter loop. The corresponding angle estimate is easily found in terms of $\hat{\omega}$, ω_{off} and the coding factor K, Eq. (4-37):

$$\hat{\theta} = \sin^{-1}\left[\frac{\hat{\omega} - \omega_{off}}{K}\right] \tag{4-65}$$

The angle error is simply

$$err = \hat{\theta} - \theta_0$$

4.3.1.4 Reference Signal Fading

One condition which can cause significant error in Doppler MLS is fading of the reference signal. The received reference components have only the small frequency differences induced by aircraft motion, and hence can combine into a slowly fading reference signal. We have already discussed the necessity for reference strength equal to or greater than the angle signal strength with regard to operation of a linear detector, so it is important to flag those instances in which the net amplitude sinks below some threshold value. This is simply accomplished by a check on the reference amplitude at a single point, the midscan point.

The composite reference signal is

$$\sum_{j=0}^{M} \rho_j' \, \exp j\left[\omega_r(1 + \frac{v_a}{c} \cos \gamma_j')t + \phi_j'\right] \tag{4-66}$$

with amplitude

$$A(t) = \left| \sum_{j=0}^{M} \rho'_j \, \text{expj}(\omega_r \frac{v}{c} \cos \gamma'_j t + \phi'_j) \right| \qquad (4\text{-}67)$$

$A(NT_s)$ is evaluated and compared to a threshold which is a parameter of the simulation model. If the amplitude is below threshold, no angle measurement is taken for the corresponding frame.

4.3.2 Alternative Doppler Antennas

4.3.2.1 The Circular Array

The Doppler azimuth antenna implemented by Hazeltine during Phase II of the MLS program consists of a circular array of radiating elements. The structure naturally produces a planar beam because of its circular symmetry. The surfaces of constant Doppler are vertical planes in contrast to the conical surfaces formed by the linear array. The circular array provides an advantageous implementation when wide angle or full 360° coverage is desired.

Due to the unusual design of this antenna, its properties were not well understood by the MLS community. Explanations of its behavior were offered from various points of view, but none was satisfactory. Since a treatment of the circular array by conventional antenna theory had not appeared, such an analysis was undertaken to gain further insight on the properties of the antenna design. The mathematical derivations are reported in Appendix E and will not be repeated here.

Starting from fundamental principles, the antenna far field was derived for the array angle-dependent aperture element excitation. The field was

shown to have the desired average Doppler shift as a function of the azimuth angle to the observation point. The field is modulated by a time varying frequency or chirp independent of azimuth angle. The derivation for the chirp confirmed the formula derived earlier by less direct methods. An explicit expression for the elevation angle dependence of the chirp was also obtained. It was shown that the "moving bright spot" on the aperture could not serve as the heuristic basis of the average Doppler. However, a moving bright spot could be used to explain the chirp phenomenon.

The analysis yields an expression for an incidental amplitude modulation as a function of scan time which causes the radiated signal to depart from a constant envelope. Due to the effect of finite aperture cutoff, the amplitude is dependent on the observation angle as well. Both amplitude variations had been observed in simulations by Hazeltine and are now substantiated by a well-founded theory.

4.3.2.2 Beamport Antenna

The Doppler elevation antennas implemented by Hazeltine during Phase II of the MLS program consist of multiple feed beamport reflectors. These antennas can generate planar beams with any desired angle encoding, for example, the linear encoding actually employed. In addition, the beamport reflector can be shaped to provide rapid elevation rolloff near the horizon for suppression of ground reflection multipath. This feature was found to be of particular importance in the Ku-band flare guidance system.

A single RF source is divided into several feed lines, each containing a digital or analog phase shifter. The composite phase shifter characteristics (deg/sec) determine the angle encoding function. The feed outputs are a set of coherently related frequencies which simultaneously illuminate the reflector. Because of the coherence, one can envision a "spot" on the reflector surface at which all the feed outputs are in phase; this spot will migrate across the reflector during the scan, thus providing a moving source analogy to the commutated array implementation. The horizon rolloff achieved with the Hazeltine array (up to 23 dB/deg) is much steeper than that achieved by a typical commutated array element (5 dB/deg) which has little vertical aperture.

In terms of system modeling, the antenna pattern of the beamport array is incorporated by weighting the received signal amplitude by an appropriate antenna weighting factor $P_1(\theta)$. The remainder of the model then proceeds as in the case of the ITT/G model described earlier.

4.3.3   Thinned Arrays

One of the key changes proposed by the U.K. to the basic Doppler scan concept is a "thinning out" of the azimuthal sideband array coupled with a commutated finely spaced reference array. By doing this, a quite significant reduction in the number of radiating elements and switches, etc. can be achieved without introducing any grating lobes (i.e., false courses) in the absence of multipath.

In this section, we show that the transform of the received Doppler signal with a periodically thinned sideband (offset) array and commutated reference differs significantly from the spectrum of a full sideband array

with fixed reference when there is a multipath component present. Thus, the test results for a full array (e.g., ITT Gilfillan at NAFEC[31]) cannot simply be applied to the case of a thinned array (e.g., USAF azimuth at WPAFB[42] and U.K. azimuth by RAE[27]) and vice versa. Some general observations regarding the result are made at the end.

The "thinned" Doppler array shown in Fig. 4-13 operates as follows: initially the "coarse" array element nearest the reference array and the reference array element nearest the coarse array are radiating. Next, successive reference array elements are excited in turn while the radiating coarse element does not change. When the last reference array element has finished radiating, the next coarse array element and the initial reference array element commence radiating. This pattern is repeated until the end of the coarse array is reached, at which point the scan pattern is usually reversed (to give a bidirectional scan).

Since the distance between the reference element and coarse array element radiating increases with time in the same manner as is achieved with a full sideband array and fixed reference, it is not surprising that in the absence of multipath, the two systems are equivalent. What is not so obvious is the impact on multipath performance of jumping around in effective antenna phase center during the scan progression. Regrettably, a clear statement of this impact has only been achieved by the mathematical derivation outlined below.

Taking the zero-th coarse element as reference for the "thinned" array shown in Fig. 4-13, the signal at the receiver from the k-th coarse element can be written

Reference (fine) array   ·   Main (coarse) array
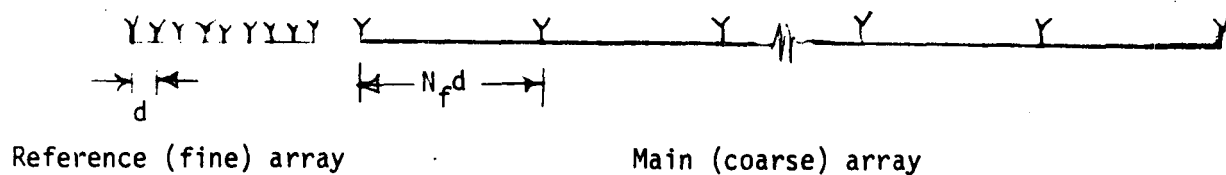
d = fine element spacing = 0.236λ for system at WPAFB [42]

                                = 0.232λ for UK system [27]

$N_f d$ = coarse element spacing = 1.89λ for system at WPAFB

                               = 1.86λ for UK system

N_c = number of coarse elements = 64 for system at WPAFB and UK system

ATC-63 VI 4-13

Fig. 4-13. "Thinned" Doppler array.

4-58

$$a_k e^{j(2\pi f_i t)} [e^{j\phi_c} + \rho e^{j\tilde{\phi}_c}] e^{j(2\pi f_0 t)} \qquad (4\text{-}68)$$

while the signal at receiver from the n-th fine element is

$$a_f a_n [e^{j\phi_f} + \rho e^{j\tilde{\phi}_f}] e^{j(2\pi f_0 t)} \qquad (4\text{-}69)$$

where:

f_i = offset frequency between coarse and fine (i.e., reference and sideband) arrays

a_n = magnitude of fine element direct signal before mixer

a_k = magnitude of coarse element direct signal before mixer

a_f = excitation shape for a single fine element

ρ = multipath magnitude/direct magnitude

ϕ_c = phase of direct signal at coarse element

$\tilde{\phi}_c$ = phase of multipath signal at coarse element

ϕ_f = phase of direct signal at fine element

$\tilde{\phi}_f$ = phase of multipath signal at fine element

By simple calculation:

$$\phi_f = -2\pi(n+1) \, d \sin \theta_d/\lambda + \varepsilon = -(n+1) \, B + \varepsilon$$

$$\phi_c = 2\pi k \, N_f \, d \sin \theta_d/\lambda + \varepsilon = kN_f \, B + \varepsilon$$

$$\tilde{\phi}_f = 2\pi(n+1) \, d \sin \theta_m/\lambda + \varepsilon_m = -(n+1) \, B_m + \varepsilon_m$$

$$\tilde{\phi}_c = 2k\pi N_f \, d \sin \theta_m/\lambda + \varepsilon_m = kN_f \, B_m + \varepsilon_m$$

when:

d = separation between fine elements

ε = initial phase of direct component at coarse element 0

4-59

ε_m = initial phase of multipath component at coarse element 0

θ_d = direct component arrival angle

θ_m = multipath component arrival angle

Modeling the mixer as a multiplication of the k-th coarse element signal x n-th fine element signal followed by low pass filtering, the mixer output is

$$s_{nk}(t) = a_f a_n a_k \, e^{j2\pi f_i t}\left[e^{j(\phi_c - \phi_f)} + \rho\, e^{j(\phi_c - \tilde{\phi}_f)} + e^{j(\tilde{\phi}_c - \phi_f)} + \rho^2 e^{j(\tilde{\phi}_c - \tilde{\phi}_f)}\right]$$

(4-70)

where

$$\phi_c - \phi_f = (N_f k + n + 1)B$$

$$\phi_c - \tilde{\phi}_f = N_f k\, B + (n+1)B_n + \varepsilon - \varepsilon_m$$

$$\tilde{\phi}_c - \phi_m = N_f k\, B_m + (n+1)B + \varepsilon_m - \varepsilon$$

$$\tilde{\phi}_c - \phi_f = (N_f k + n + 1)B_m$$

We now want to compute the Fourier transform of the signal into the zero crossings counter assuming a_n and a_k are constant:

$$H(f) = \int_0^{N_c N_f} \left[\sum_{k=1}^{N_c} \sum_{n=1}^{N_f} s_{nk}(t)\right] e^{-j2\pi ft}\, dt$$

(4-71)

$$= c[H_{dd} + \rho(H_{dm} + H_{md}) + \rho^2 H_{mm}]$$

Each of the terms H_{dd}, H_{dm}, H_{md} can be readily determined by straightforward calculation. The amplitudes are as follows:

$$H_{dd} = \frac{\sin[N_c N_f (B-A)/2]}{\sin (B-A)/2} \cdot P_f$$

$$H_{md} = \frac{\sin[N_c N_f (B_m-A)/2]}{\sin[N_f (B_m-A)/2]} \cdot \frac{\sin N_f(B-A)/2}{\sin (B-A)/2} \cdot P_f$$

$$H_{dm} = \frac{\sin[N_c N_f (B-A)/2]}{\sin[N_f (B-A)/2]} \cdot \frac{\sin[N_f (B_m-A)/2]}{\sin[(B_m-A)/2]} \cdot P_f$$

$$H_{mm} = \frac{\sin[N_c N_f (B_m-A)/2]}{\sin[(B_m-A)/2]} \cdot P_f$$

where

$$A = 2\pi \tau(f-f_1)$$

τ = 1/rate at which fine elements are switched

P_f = transform of the fine element excitation waveform a_f

$\quad$ = 2[sin A/2]/A for "hard switching"

Next, we compute the transform of the input to the zero crossing counter of a full sideband array and fixed reference for the same multipath environment. In doing so, it is convenient to take the zero-th sideband element as reference and have $N_c N_f$ "fine" elements. For this case.

$$\phi_c = \epsilon$$

$$\tilde{\phi}_c = \epsilon_m$$

$$\phi_f = -kB + \epsilon \qquad k = 1,2,\ldots, N_f N_c$$

$$\tilde{\phi}_f = -kB_m + \epsilon_m \qquad k = 1,2,\ldots, N_f N_c$$

The mixer output for the k-th element is then

$$s_k(t) = a_f \, a_k \, a_0 \, e^{j2\pi f_i t + \varepsilon} [1 + e^{j(\varepsilon_m - \varepsilon)}][e^{jkB} + \rho \, e^{j(kB_m + \varepsilon - \varepsilon_m)}]$$

with transform:

$$H(f) = \int_0^{N_c N_f} \sum_{k=1}^{N_c N_f} s_k(t) \, e^{-j2\pi ft} \, dt = a_k \, a_0 \, e^{j\varepsilon}[1 + e^{j(\varepsilon_m - \varepsilon)}][H_d + \rho \, H_m] \tag{4-72}$$

Proceeding as before, it is trivial to show that the amplitudes are

$$H_d = \frac{\sin[N_c N_f \, (B-A)/2]}{\sin[(B-A)/2]} \cdot P_f$$

$$H_m = \frac{\sin[N_c N_f \, (B_m - A)/2]}{\sin(B_m - A)/2} \cdot P_f$$

Comparing (4-71) with (4-72), we see that the thinned array output has two terms (H_{md} and H_{dm}) in addition to those obtained with the full array.

These additional terms represent multipath generated by the grating lobes of the main (coarse) array, and are analogous to a 0 dB sidelobe in a scanning beam array. To illustrate, when $\sin \theta_m = \sin \theta d \pm \lambda/d \, N_f$ corresponding to an "out of beam" condition, H_{md} peaks at the same frequency as H_{dd} and thus is equivalent to "inbeam" multipath.

The deficiencies of this scheme have been recognized by the U.K., and more recent proposals have suggested randomized thinning of the main array[38]. No concrete proposals have yet been made, so it has not been possible to perform an analysis of the type above to determine the improvement by such

schemes. It is hypothesized on the basis of general estimation theoretic considerations that the performance of such a system can be upper bounded by considering the beam pattern of the total Doppler array (i.e., reference and main arrays treated as a single array).

This pattern is of the form

$$G_{thin}(\theta) = |V_r(\theta) + e^{j\phi(\theta)} V_m(\theta)|^2 \tag{4-73}$$

where

$V_r(\theta)$ = reference array (voltage) pattern = $\sin(N_f \eta)/\sin \eta$ assuming equal amplitude weighting

$V_m(\theta)$ = (voltage) pattern of main array

η = $\pi(d/\lambda) \sin \theta$

If the main array has N_c equally weighted elements, then standard antenna theory arguments (see Chapter 6 of ref. [43]) suggest that

1. the beam pattern near boresight drops off initially as a filled-in array of the same length and then flares out to follow $V_r(\theta)$ at a level approximately $-20 \log_{10}(1 + N_c/N_f)$ down from the main lobe.

and

2. on the average, the sidelobes are approximately $(1-r)/(N_c+N_f)$

    = $(\frac{1}{r} - 1)/N_f$ down in power from the main beam peak where r is the thinning ratio (= number of elements in the thinned array/ number of elements in full array of the same length) and N_f = number of elements in a full array.

For a 60λ full array, $N_f \sim 120$, so that a thinning factor of 0.5 would suggest -20 dB sidelobes. Since contemporary MLS designs typically try to achieve sidelobes better than -20 dB; it seems unlikely that large

thinning factors can be realized by the scheme above without generating un-
acceptable sidelobe performance.

Two caveats should be noted regarding the above conclusions. First, it
is not clear that practical Doppler processors can achieve the performance
suggested by estimation theory considerations due to the nonoptimal process-
ing in the receivers. On the other hand, by very clever synthesis and/or
exhaustive search, it may be possible to find a thinning pattern which is
substantially better than the "average" thinning.

4.4 Distance Measuring Equipment Models

The distance measuring equipment (DME) systems operate on the principle
of round-trip time delay measurement. An airborne interrogator transmits a
pulse coded waveform which is received at a transponder on the airport sur-
face. The transponder estimates the arrival time of the interrogation and
after a known fixed delay transmits a reply signal. The airborne interro-
gator, upon receipt of this signal, estimates its arrival time and computes
the range on the basis of an adjusted round-trip delay.

In the systems which have been modeled, time of arrival estimation is
based upon detection of the leading edge of the first pulse (the usual pulse
code consists of a pulse pair). The intent is to sense the leading edge
arrival as early as possible in order to minimize the effect of multipath
echoes which have small differential delay.

Each one-way DME link model consists of (i) a pulse waveform and
(ii) a processor algorithm. These can be chosen independently; the com-
binations which constitute the downlink and uplink may differ. Three wave-
form models (trapezoidal, Gaussian, and chirp) and three processor models

(fixed threshold, real time threshold, and delay and compare) are available. Others can be prepared with ease. The downlink and uplink DME's are specified separately.

4.4.1   Waveforms and Transmitted Signal

4.4.1.1   Trapezoidal Pulse

The trapezoidal pulse waveform is defined as

$$P(t) = \begin{cases} \dfrac{t}{t_r} & ; \quad 0 \leq t \leq t_r \\ 1 & ; \quad t_r \leq t \leq T-t_r \\ \dfrac{T-t}{t_r} & ; \quad T-t_r \leq t \leq T \\ 0 & ; \quad \text{otherwise} \end{cases}$$

where T is the pulse duration and t_r the 0% - 100% risetime.

4.4.1.2   Gaussian Pulse

The Gaussian pulse waveform is

$$P(t) = e^{-\beta\left(\frac{t}{t_r}\right)^2}$$

where β is a scaling constant which allows for various definitions of risetime. Much of the literature dealing with DME, e.g., ICAO Annex 10[44], uses 10%-90% definition of t_r, in which case $\beta = 1.423$.

4.4.1.3   Chirp Pulse

The chirp DME model is somewhat more complicated than the other two in that what the simulation model requires is a representation of the pulse at the range processor, and that waveform is not proportional to the transmitted one. The difference is the matched filtering which occurs in the receiver.

The transmitted pulse has a rectangular envelope and a quadratic phase (linear FM) characteristic:

$$P(t) = \begin{cases} e^{j\frac{\mu}{2}(t-\frac{T}{2})^2} & ; \quad 0 \leq t \leq T \\ 0 & ; \quad \text{otherwise} \end{cases} \qquad (4\text{-}74)$$

In Eq. (4-74), μ is the chirp parameter (rad/sec). After matched filtering the pulse has amplitude proportional to

$$P(t) = \left| \frac{\sin\left[\frac{1}{2}\mu t(T-|t|)\right]}{\frac{1}{2}\mu t\, T} \right| \quad ; \quad |t| \leq T \qquad (4\text{-}75)$$

and zero phase. Because of the time-frequency coupling in the linear FM pulse, a Doppler shift ω_d affects the amplitude of the filter output and introduces a linear phase term as well. The amplitude and phase terms are

$$P(t,\omega_d) = \left| \frac{\sin \frac{1}{2}(\mu t + \omega_d)(T - |t|)}{\frac{1}{2}(\mu t + \omega_d)T} \right|$$

$$\phi(t,\omega_d) = \frac{1}{2}\omega_d t$$

4.4.2   Received Signal

As in the angle systems, the DME multipath calculation is finalized in the DME routine itself. For each multipath component, a normalized amplitude is computed by weighting the M/D ratio by the ratio of the ground antenna azimuth and elevation patterns:

$$\rho_i = \frac{A_i \, P_1(\theta_i)P_2(\Phi_i)}{A_0 \, P_1(\theta_0)P_2(\Phi_0)} \tag{4-76}$$

The DME data rate is 40 Hz, and eight uniformly spaced returns are averaged to obtain 5 Hz range data. A phase retardation term of the sort described for the multiscan angle systems is introduced on each scan for this purpose. Other multipath parameters are used as before. The n-th scan received envelope is

$$e_n(t) = \left| \sum_{i=0}^{M} \rho_i p(t - \tau_i, \, \omega_i - \omega_0) \, \text{expj} \left\{ (\omega_i - \omega_0)t - \omega_i \tau_i \right. \right.$$
$$\left. \left. - \frac{\omega_i \, V_a \, \cos\beta_i}{c} \, (n-1) \, T_d + \phi(t - \tau_i, \, \omega_i - \omega_c) + \phi_i \right\} \right| \tag{4-77}$$

where T_d is the delay between pulses. For the trapezoidal and Gaussian pulses, assume that $p(t, \omega_d) = s(t)$, $\phi(t, \omega_d) = 0$.

The chirp DME was proposed and bench tested by Texas Instruments. In the actual receiver a hard limiter is used in front of the matched filter for AGC; the resultant loss of amplitude information is not especially critical to the matched filtering. The introduction of the hard limiter considerably complicates analytic modeling of the total multipath signal, however, and was omitted from the simulation effort.

4.4.3   Receiver Processing

The three processor types which have been modeled encompass all the processing techniques used by the Phase II contractors. Two of these are threshold processors; the threshold level is either <u>fixed</u> at a constant level

of set at a constant <u>percentage</u> of the peak amplitude of the received pulse (the latter is called real time thresholding). The former was used by Hazeltine, and the latter serves as a model for at least one link of each of the remaining systems. Both Bendix/Bell and ITT/G used the third type, <u>delay-and-compare</u>, on one link.

4.4.3.1   Threshold Processors

The receiver routine computes the time at which the received envelope crosses a threshold level. This is done by a straightforward search procedure over a set of stored envelope samples. For a fixed threshold processor the equation to be solved on the n-th scan is

$$e_n(\hat{t}_n) = \alpha$$

In the real time processor the peak value $e_n|_{max}$ is found by searching the envelope samples, and the crossing occurs at the solution of

$$e_n(\hat{t}_n) = \alpha e_n|_{max}$$

In order to find the errors, the time at which the crossings would have occurred in the absence of multipath must be found. Call this time $\tilde{t}$ (independent of n):

$$p(\tilde{t},o) = \alpha \qquad : \text{ fixed}$$
$$p(\tilde{t},o) = \alpha p_n|_{max} : \text{ real time}$$

For the trapezoidal and Gaussian pulses, $\tilde{t}$ can be determined analytically. For chirp, the crossing is found by search.

The n-th scan arrival time error is

$$\varepsilon_n = \hat{t}_n - \tilde{t}$$

4.4.3.2 Delay-and-Compare Processor

The delay-and-compare processor is shown in Fig. 4-14. Arrival time is estimated by detecting coincidence of the received envelope and a delayed, amplified replica. It is a self-AGC'ed processor since no absolute levels are involved. By adjusting the value of gain (G) and comparator delay (τ_d), one can adjust the crossing point anywhere from low on the undelayed pulse leading edge to a point on the peak, or plateau, region of the pulse.

The processor equations are

$$p(\tilde{t}) = G\, p(\tilde{t}-\tau_d) \qquad : \text{ perturbed crossing}$$

$$e_n(\hat{t}_n) = G\, e_n(\hat{t}_n - {}_d) \qquad : \text{ nominal crossing}$$

Once again, for the trapezoid and Gaussian pulses, expressions for $\tilde{t}$ can be derived. The remaining combination, chirp pulse with delay-and-compare receiver has not been implemented; if it were, the value of $\tilde{t}$ would be found by search or table lookup.

4.4.4 Range Error

Individual TOA errors are computed for each link by averaging N uniformly spaced errors (N = 8 for 40 Hz → 5 Hz conversion). Denote these by ε_d and ε_u (downlink and uplink, respectively):

$$\varepsilon_d = \frac{1}{N} \sum_{n=1}^{N} \varepsilon_{dn}$$
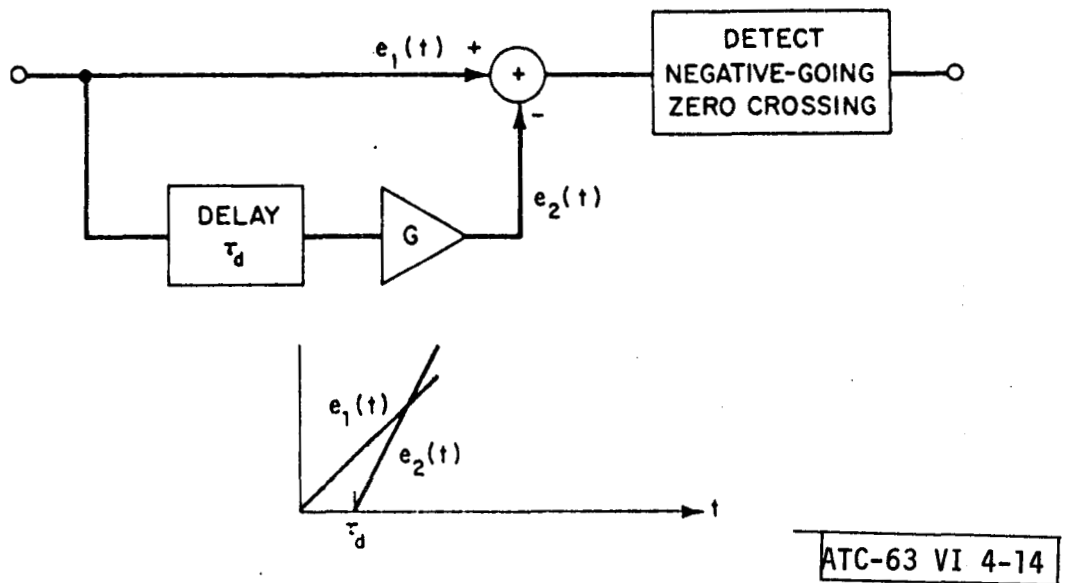
Fig. 4-14. Delay and compare thresholding.

$$\varepsilon_u = \frac{1}{N} \sum_{n=1}^{N} \varepsilon_{un}$$

The two way range error in feet is found by averaging ε_d and ε_u and multiplying by the speed of light in air (ft/sec):

$$\varepsilon = \frac{c}{2} (\varepsilon_{dn} + \varepsilon_{un})$$

This concludes the DME system model description.

V. MOTION AVERAGING

The MLS achieves high accuracy and data rates over a wide coverage by use of two narrow fan beams, one for azimuth and another for elevation. Multipath problems are avoided by not illuminating the aircraft and potential reflectors "simultaneously" (e.g., in time for scanning beam and in frequency for Doppler). When this is achieved, multipath errors should, in most cases of practical significance, be very low for a system if appropriate receiver processing is employed.

However, cases may arise where "simultaneous" illumination occurs. Examples of this include:

(a) the fan beam is not narrow enough in the coordinate system being transmitter (e.g., taxiing aircraft too near the approach end of a long runway, rising terrain in front of an elevation array).

(b) a scattering object lies within the fan beam in its wide plane (e.g., hangars or aircraft tails within the elevation system coverage, the ground in front of azimuth systems).

For a considerably period of time, it was not fully appreciated in the MLS community that problem (b) above could be a significant problem for any MLS providing elevation information over a wide azimuth coverage sector. However, studies of existing airports have shown that hangars and aircraft would be present in the contemplated coverage sectors. Thus, it is important to see if the resulting errors could be reduced by means other than coverage reduction.

We have seen that on a single measurement, the resulting error is a function of several multipath characteristics.

(a) multipath level relative to direct signal level

(b) multipath angle coordinate relative to direct path angle (i.e., the "separation angle")

(c) multipath path delay, rf phase relative to direct signal

(d) rate of change of path delay in (c) due to aircraft motion.

The last item leads to the possibility of motion averaging which is the central topic of this section. Systems having a signal format which yield measurements more rapidly than the required data rate may take advantage of motion averaging to reduce the degradation due to inbeam multipath.[*] Since the signal format is generally a fairly flexible feature of most MLS systems, motion averaging represents an attractive means of substantially reducing the errors. The primary objective of the initial motion averaging studies was to determine under what circumstances motion averaging would be effective in reducing multipath error.

In the next section, the improvement in accuracy due to averaging a sequence of samples is derived by means of correlation analysis on the measurement time series. The analysis also leads to a general expression for the beam noise spectrum of the output data samples as a function of the spectrum or correlation function of the individual measurements and the averaging

---

[*]It should be emphasized that the treatment here makes no distinction as to air derived systems versus ground derived systems. Thus, the basic results may be applied to all ground derived systems whose signal format yields a measurement sequence of the type considered here.

parameters. These results are then specialized to the usual case where the error is a sinusoidal function of the RF phase between direct and multipath, and the improvement due to averaging is dependent on the rate-of-change of RF phase, the so-called scalloping frequency, f_s.

The average improvement factor for a fixed scalloping frequency f_s has "grating lobes" where the improvement reverts to the value unity it had at $f_s=0$. Section 5.2 assesses the importance of grating lobes by determining the time required to fly through these regions of poor motion averaging as a function of f_s and reflector/flight path geometry. In section 5.4, the theory used in sections 5.1 and 5.3 is refined to consider items such as motion averaging between to-and-fro TRSB scans as well as jittered time formats.

The remainder of the chapter deals with the existence of multipath and its scalloping frequency in relation to aircraft position and velocity and the location, height and orientation of reflecting surfaces. In-beam multipath for elevation systems due to buildings is treated explicitly.

5.1 Motion Averaging Improvement

In this section a general formulation is presented of the effects of averaging individual measurements on the error at the output of the MLS system where it interfaces with the flight control system. The measurement errors will be represented by a sequence of samples $\{e_i\}$. Each sample pertains to a periodic measurement event such as a pair of up-down Doppler scans or a to-fro scanning beam sweep.[†]

[†] Focusing on the measurement events is done here to obtain basic characteristics of motion averaging improvement. In a later section, we consider some refinements such as motion averaging between to and fro sweeps and the effect of time jittered measurement formats.

The samples occur at a uniform rate with spacing T as shown in Fig. 5-1. A contiguous sequence of M of the high rate samples is averaged. The averaging process is repeated every N high rate samples resulting in a new sample sequence with spacing NT. The averaged samples are denoted E_k where the indices are related by $i=Nk$, i.e.,

$$E_k = \frac{1}{M} \sum_{j=0}^{M-1} e_{kN+j} \tag{5-1}$$

This model retains the time relationship of all the sample instants and encompasses situations where averaging is applied over part of a TDM frame.

The correlation function of the basic time series is defined as the statistical or time average of the product of two samples separated by j sampling instants:

$$\overline{e_i \, e_{i+j}} = R(j)$$

Stationarity has been assumed in that the average is independent of the index i.

The correlation function of the averaged time series is

$$\overline{E_k \, E_{k+m}} = \frac{1}{M^2} \left[MR(mN) + \sum_{p=1}^{M-1} (M-p)[R(mN+p) + R(mN-p)] \right] \tag{5-2}$$
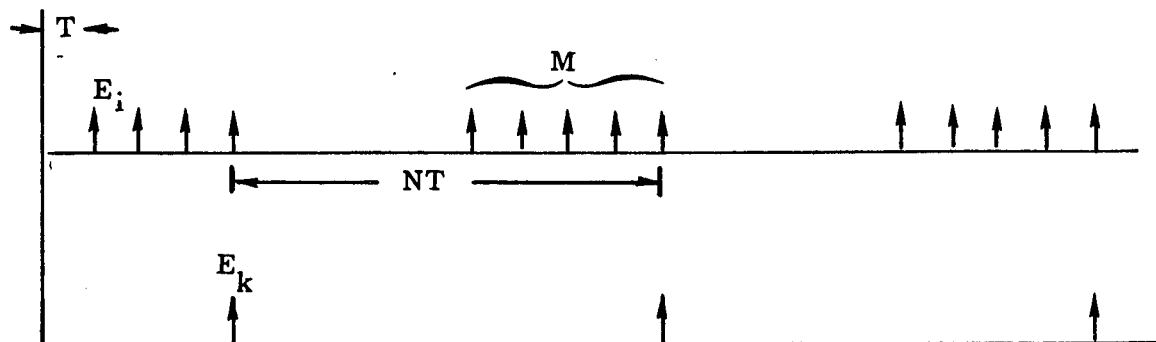
Fig. 5-1. Time sequence of measurement samples.

This expression may be evaluated for any correlation function of the basic process. Especially interesting is the periodic correlation associated with a scalloping frequency ω_s:

$$R(i) = R(0) \cos(\omega_s Ti)$$

Inserting the periodic correlation function into Eq. (5.2) gives

$$\overline{E_k E_{k+m}} = R(mN) \frac{\sin^2(M\omega_s T/2)}{M^2 \sin^2(\omega_s T/2)} \tag{5-3}$$

We observe that the correlation function of the averaged process is proportional to the correlation function of the basic process. The proportionality factor is the square of the averaging improvement.

It is instructive also to examine the beam-noise spectrum $S_B(\omega)$ defined as the discrete Fourier transform of the output sampled-data correlation function. It can be shown that

$$S_B(\omega) = \sum_m S\left(\omega - \frac{2\pi m}{NT}\right) \frac{\sin^2\left[MT\left(\omega - \frac{2\pi m}{NT}\right)\right] / 2]}{M^2 \sin^2\left[T\left(\omega - \frac{2\pi m}{T}\right)/2\right]} \tag{5-4}$$

where $S(\omega)$ is the noise power density spectrum of the continuous noise process underlying the basic measurement time series before averaging. The last expression shows the sampling spectral sidebands at multiples of the output sampling frequency 1/NT. Each spectral zone consists of the measurement error spectrum filtered through the averaging filter. When the significant bandwidth of $S(\omega)$ extends beyond π/NT, spectral foldover or aliasing will occur.

For example, if $1/T$ = 40 Hz, error components at all multiples of 40 Hz will be aliased down to zero frequency. It should be emphasized that this aliasing is a property of sampled data systems which did not occur with ILS because ILS furnishes data continuously in time. Thus, high frequency error signals which could be filtered out with a cw system such as ILS may be aliased down to a frequency within the aircraft flight control system passband.

The periodic correlation function discussed above leads to a δ function at the scalloping frequency

$$S(\omega) = \delta(\omega - \omega_s)$$

In the beam noise spectrum, each sampling sideband is then attenuated by a common improvement factor

$$A^2(\omega_s) = \frac{\sin^2(M\omega_s T/2)}{M^2 \sin^2(\omega_s T/2)} \tag{5-5}$$

i.e., $A(\omega_s)$ is the rms reduction in error at the frequency ω_s.

This expression places into clear focus all the parametric relationships of motion averaging with a fixed scalloping frequency $\omega_s = 2\pi f_s$. For very low scalloping frequency, the improvement factor goes to one as expected. The factor goes to zero, resulting in no errors, when the scalloping frequency goes through one or more complete cycles in the averaging time MT. The factor returns to unity whenever f_s is an integer multiple of $1/T$. These points, hereinafter called grating lobes, are the aliasing frequencies of the basic sampling rate.

The averaging improvement factor is shown in Fig. 5-2 for M=4, 16 and 25 as a function of the product $f_s T$. It is evident that an increase in the basic sampling interval T has the disadvantage of bringing the aliasing frequencies closer together in terms of f_s, but has the beneficial effect of narrowing the lobes of the function around each aliasing point.

5.2 Persistence of Grating Lobes

Statistical considerations suggest that the average motion averaging improvement should be $M^{-1/2}$.* However, we have seen that the "average" improvement is not obtained for error frequencies near the grating lobes. This lack of improvement is quite important in system design and comparison. Thus, it is necessary to examine in greater detail the practical significance of the grating lobes. A key issue here is how long in time the poor motion averaging condition will persist.

Following the lead of the U.K. Doppler studies[27,45], we consider the persistence P

$$P = \left[d\, f_s/dt \right]^{-1} \qquad \text{sec/Hz}$$

Given P, one then has the estimate

$$\Delta T = P\Delta f$$

as the time required to fly through a grating lobe whose frequency width is Δf Hz.

---

*This follows by considering E_k to be the sum of M independent random variables with zero mean and identical distributions.
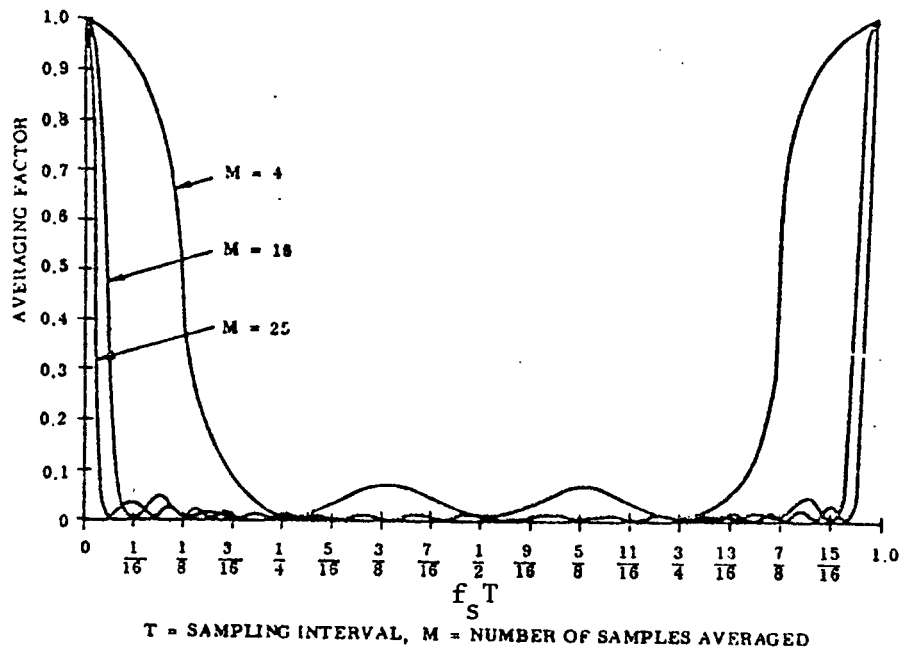
Fig. 5-2. Averaging factor versus normalized scalloping frequency.

We now want to relate P to the geometry of a multipath situation. A convenient way to do this is to obtain a power series in t for the path length difference between direct and multipath assuming a constant aircraft velocity vector. The pertinent geometry is shown in Fig. 5-3.

Taking derivatives, we find

$$f_s = \frac{v}{\lambda} (\cos \theta_{VT} - \cos \theta_{IV}) \tag{5-6}$$

$$\dot{f}_s = \frac{df_s}{dt} = -\frac{v^2}{\lambda} \left(\frac{\sin^2 \theta_{VT}}{R_T} - \frac{\sin^2 \theta_{IV}}{R_I} \right) \tag{5-7}$$

The distance R_I to the image is not a very meaningful quantity since it depends on the reflector location and its rotation with respect to the direct line of sight. An upper bound on persistence in terms of more useful parameters has been derived, viz.

$$\dot{f}_s > \frac{v^2}{\lambda R_T} \left[\sin^2 \theta_{IV} \cos(\theta_{IV} + \theta_{VT}) - \sin^2 \theta_{VT} \right] = (\bar{P})^{-1} \tag{5-8}$$

where $\bar{P}$ denotes upper bound on persistence.

Multiplying the persistence by the width of a grating lobe of the averaging factor, determines the length of time, T_p, required to pass through the lobe. The width is approximately 2/MT where M is the number of samples being averaged and T is the interval between them.

By eliminating θ_{IV} between f_s and $\bar{P}$, one obtains a relation between scalloping frequency and the bound on persistence with v, λ, R_T and θ_{VT} as parameters. This relation can be expressed as a normalized curve of
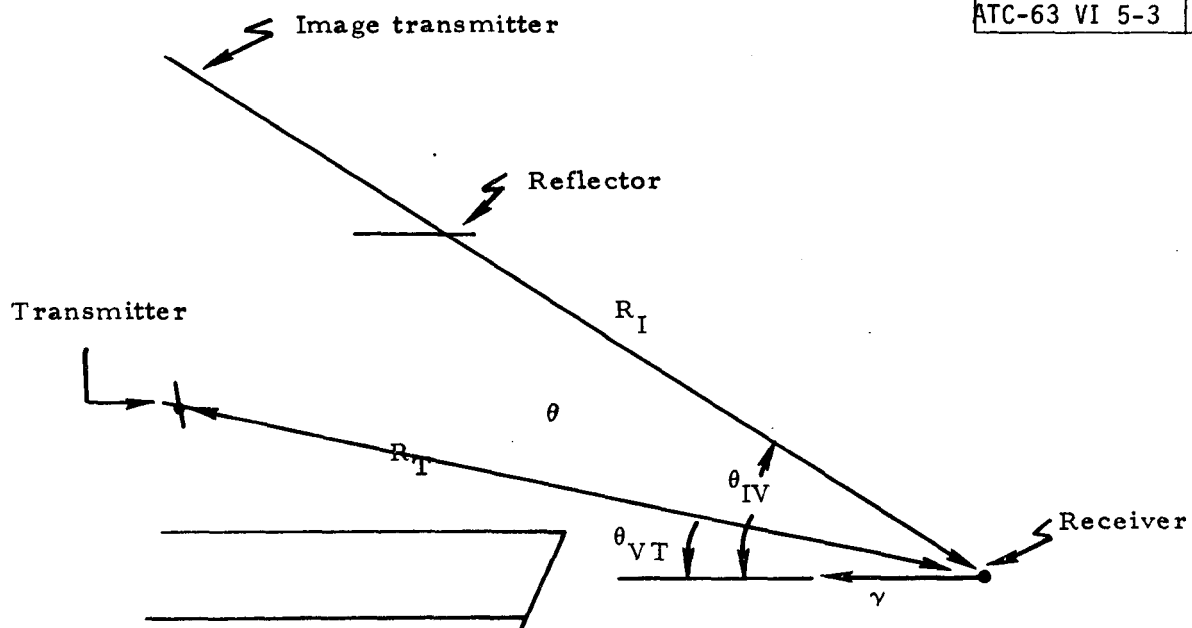
Fig. 5-3. Geometry for scalloping frequency calculations.

$$\bar{P} \left(\frac{v}{\lambda}\right)\left(\frac{v}{R_T}\right) \quad vs \quad f_s \frac{\lambda}{v}$$

It is plotted in Fig. 5-4 for several values of θ_{VT}.

The above analysis may be used to determine the persistence bound for the grating lobes applicable to the contending signal formats. Typical values are:

Scanning Beam Dual Subchannel

    EL-1 primary   10 Hz

        Flare, EL-1 primary and secondary   20 Hz

Time Reference Scanning Beam

    EL-1, EL-2   40 Hz

FDM Doppler [38]   80 Hz

TDM Doppler [38]   500 Hz

Except for the TDM Doppler each format has a single 5 Hz sampling sideband associated with each grating lobe. A TDM Doppler frame of 200 msec has an averaging time of 44 msec per function and hence a grating lobe width of 46 Hz comprising 9 sampling sidebands.

For those formats with only a single sampling sideband within a grating lobe, the critical frequencies of the flight control system determine the time to pass through a grating lobe. This band of frequencies is $\pm$ 1.6 Hz around each sampling sideband. Therefore, the persistence (sec/Hz) is multiplied by 3.2 Hz to obtain the time of passage T_p through the band of critical frequencies around each sampling sideband.

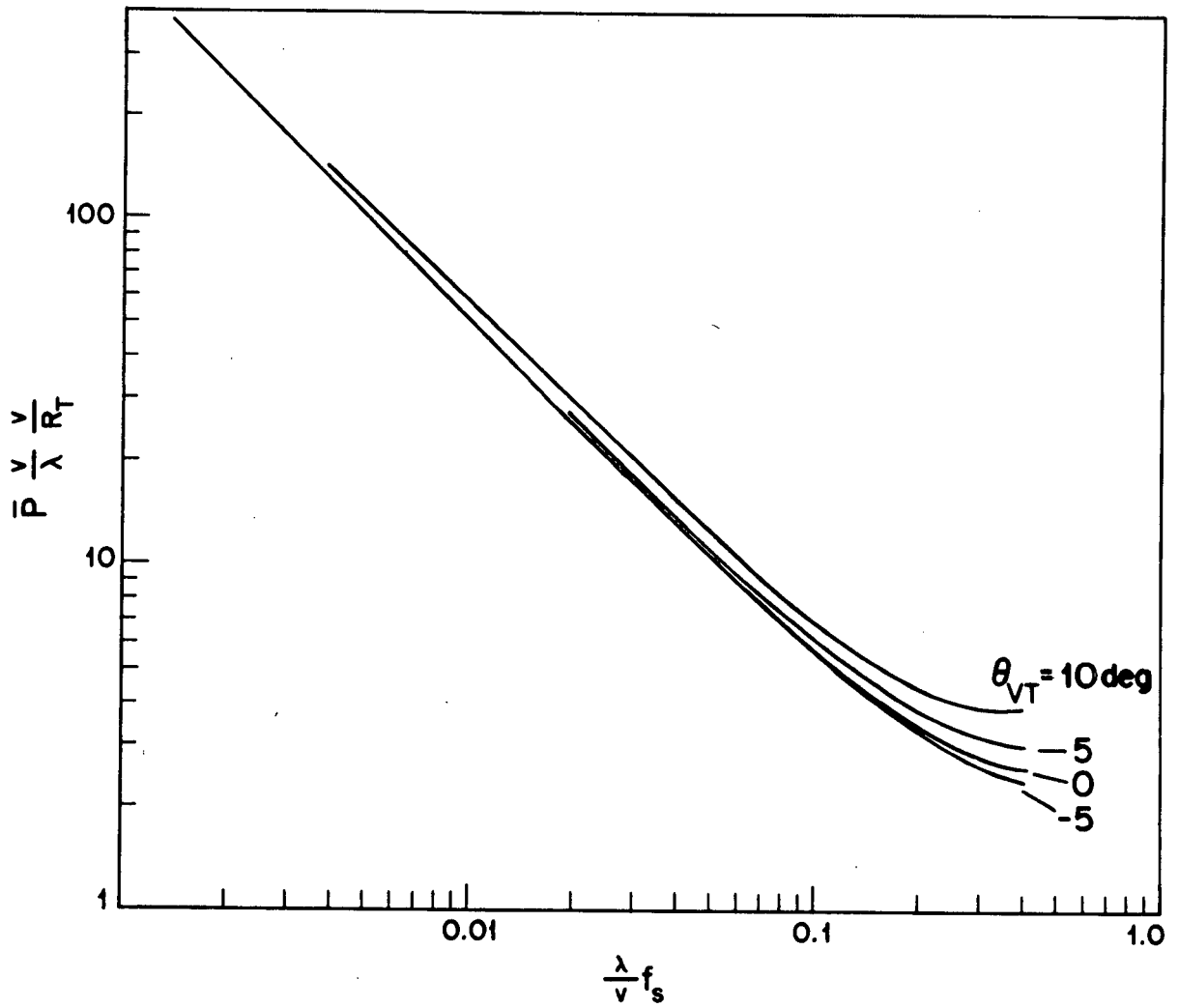Fig. 5-4.   Upper bound $\overline{P}$ on persistence vs scalloping frequency.

Table 5-1 lists T_p for the first few grating lobe frequencies at several different ranges R_T to the transmitter. Also indicated are the maximum offset angles θ_{VT} appropriate to the ranges from the elevation transmitter.

The persistence is nearly proportional to v^{-1}, so that a reduction in velocity by a factor of two will approximately double the persistence. For example, at $v = 100$ ft/sec $\lambda = 0.02$; the persistence at the 40 Hz grating lobe at 5000 ft is 2.24 sec compared to 1.1 sec in Table 5-1.

TABLE 5-1

TIME T_p (sec) TO PASS THROUGH CRITICAL FREQUENCY BAND

OF 3.2 Hz, $v = 200$ ft/sec, $\lambda = 0.2$ ft

R_T (feet)	θ_{VT}	GRATING LOBE FREQUENCY (Hz)							
		10	20	30	40	60	80	120	160
2500	10°	2.32	1.2	.8	0.61	0.42	0.34	0.24	0.2
5000	5°	7.6	2.12	1.44	1.1	0.76	0.6	0.43	0.35
10000	10°	9.28	4.8	3.2	2.44	1.68	1.34	0.96	0.8

5.3 Refinements to Simple Motion Averaging Model for TRSB

In this section, we present some refinements to the first order model presented above for the time reference scanning beam signal format.

1. Averaging Between the To-and-Fro Scans[†]

Since the rf phase between direct and reflected signals is changing over the time T_s between to-and-fro scans, motion averaging can occur within a scan. This effect can be incorporated into the earlier development by writing the averaged error in Eq. (5.1) as

$$E_k = \frac{1}{2M} \sum_{j=0}^{M-1} \sum_{i=1}^{2} e_{kNL+jL+i} \qquad (5\text{-}9)$$

where $L = T/T_s$.

Following through the development, it can be shown that improvement factor becomes

$$A(\omega_s) = \frac{\sin M\pi f_s T}{M \sin\pi f_s T} \cdot |\cos \pi f_s T_s| \qquad (5\text{-}10)$$

The cosine term represents to-fro averaging. For the TRS EL-1 system, $T_s \sim 0.3$ msec in which case the cosine term is ≤ 0.9 (= 1 dB reduction) only when $f_s > 480$ Hz. We shall see that such rates are geometrically fairly unlikely. On the other hand, for the TRS azimuth system, $T_s \sim 6.0$ msec, and

---

[†]Similar motion averaging effects occur between the to-and-fro scans of a typical Doppler systems. However, additional error terms also appear in such cases such that one ends up with an error expression more closely akin to that of section 5.1.

the cosine term becomes $\leq$ .707 (3 dB reduction) when f_s = 41 Hz. Such rates do occur in certain practical cases (e.g., scattering aircraft near the end of a runway as the landing aircraft nears threshold).

2.   Time Jittering

The grating lobes arise from the synchronous nature of the signal format in Fig. 5-1.[†] To avoid the possibility of long-term data loss due to propeller blockage, the TRSB signal format has been modified to introduce a time jitter between successive data frames; such was shown in Fig. 4-4.

For a jittered time sequence, the improvement depends on the starting point within the jitter sequence. Figure 5-5 presents a statistical summary of the TRSB EL-1 averaging factors where the averaging is over jitter starting point, e.g.:

$$\overline{A(\omega)} = \frac{1}{24} \sum_{i=1}^{24} A_i(\omega)$$

$$A_{rms}(\omega) = \sqrt{\frac{1}{24} \sum_{i=1}^{24} A_i^2(\omega)}$$

$A_i(\omega)$ = averaging factor for starting at the ith point in the sequence.

In Fig. 5-6, we compare the rms improvement for jittered TRSB signal format with the improvement factor for a non-jittered format and with the results of

---

[†]A similar problem arises in MTI detectors for skin tracking radars, where a similar solution (staggered prf) is employed to avoid "blind velocities."
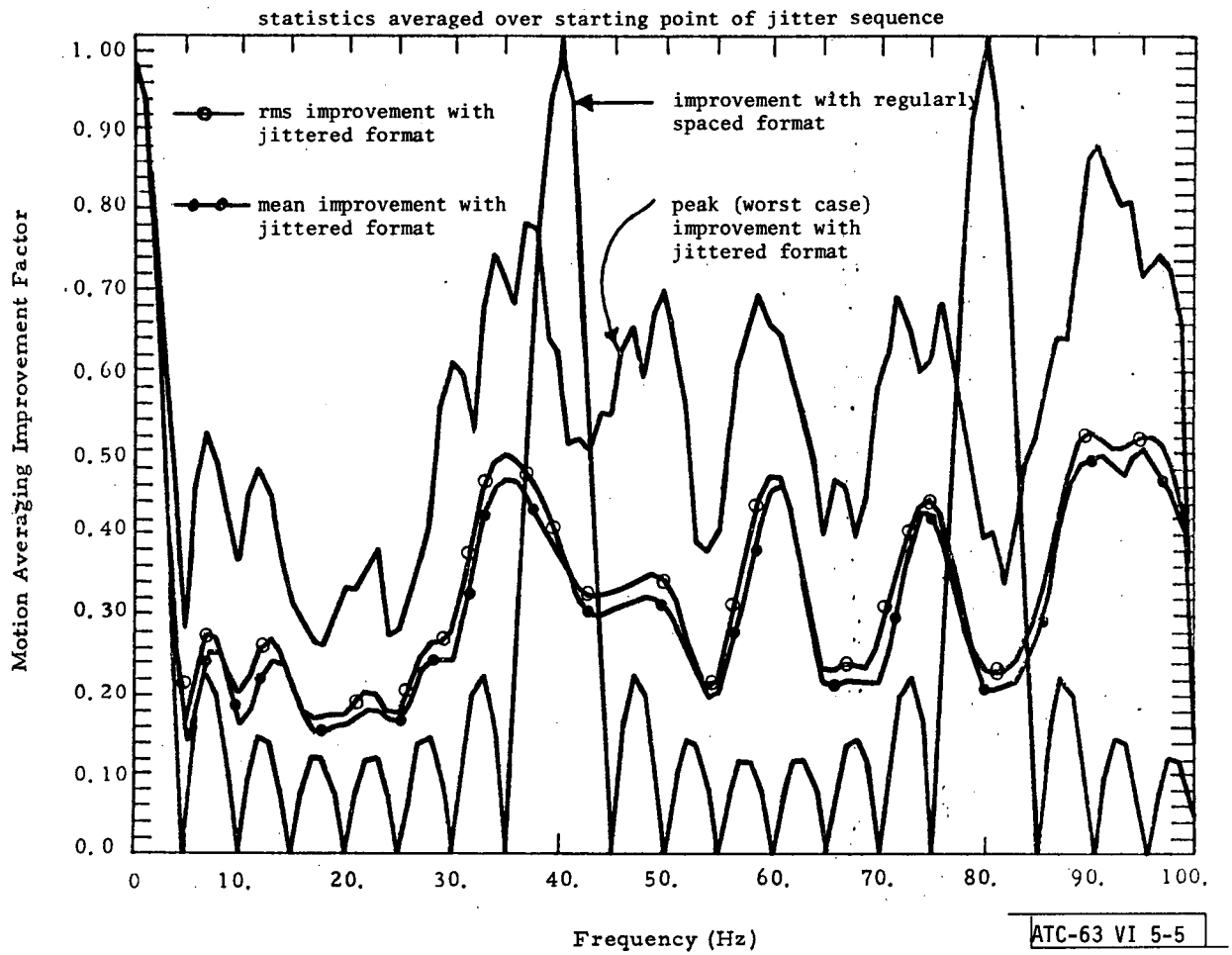
Fig. 5-5. TRSB motion averaging improvement with jittered format.

bench tests by Calspan on a Bendix airborne receiver[25]. Also shown in Fig. 5-6 is the rms improvement for purely random errors of $M^{-1/2}$.

We conclude that the proposed jitter sequence has a significant beneficial effect in reducing the grating lobes of the averaging improvement. The EL-1 40 Hz and 80 Hz grating lobes have been reduced to the random error level and no significant new grating lobes have been generated. The large values shown in Fig. 5-5 for the peak averaging factor are similar to what would be expected from averaging eight samples of a white noise process. Finally, the good agreement between the bench tests and theoretical analyses suggest that the TRSB dynamic error phenomena can be adequately characterized by the relatively simple models used in this section.

5.4   Reflector Geometry for Elevation Multipath from Buildings

The objective of this section is to incorporate geometric constraints such as aircraft position and obstacle restrictions to the existence of multipath errors and their scalloping frequency. The problem is difficult due to the many variables. Hence, the results will be presented in several steps:

(i) can substantial multipath exist, i.e., is a specular reflection from the buildings possible?

(ii) is the multipath in-beam for the angular coordinate system used?

(iii) will an appreciable motion averaging improvement be obtained?
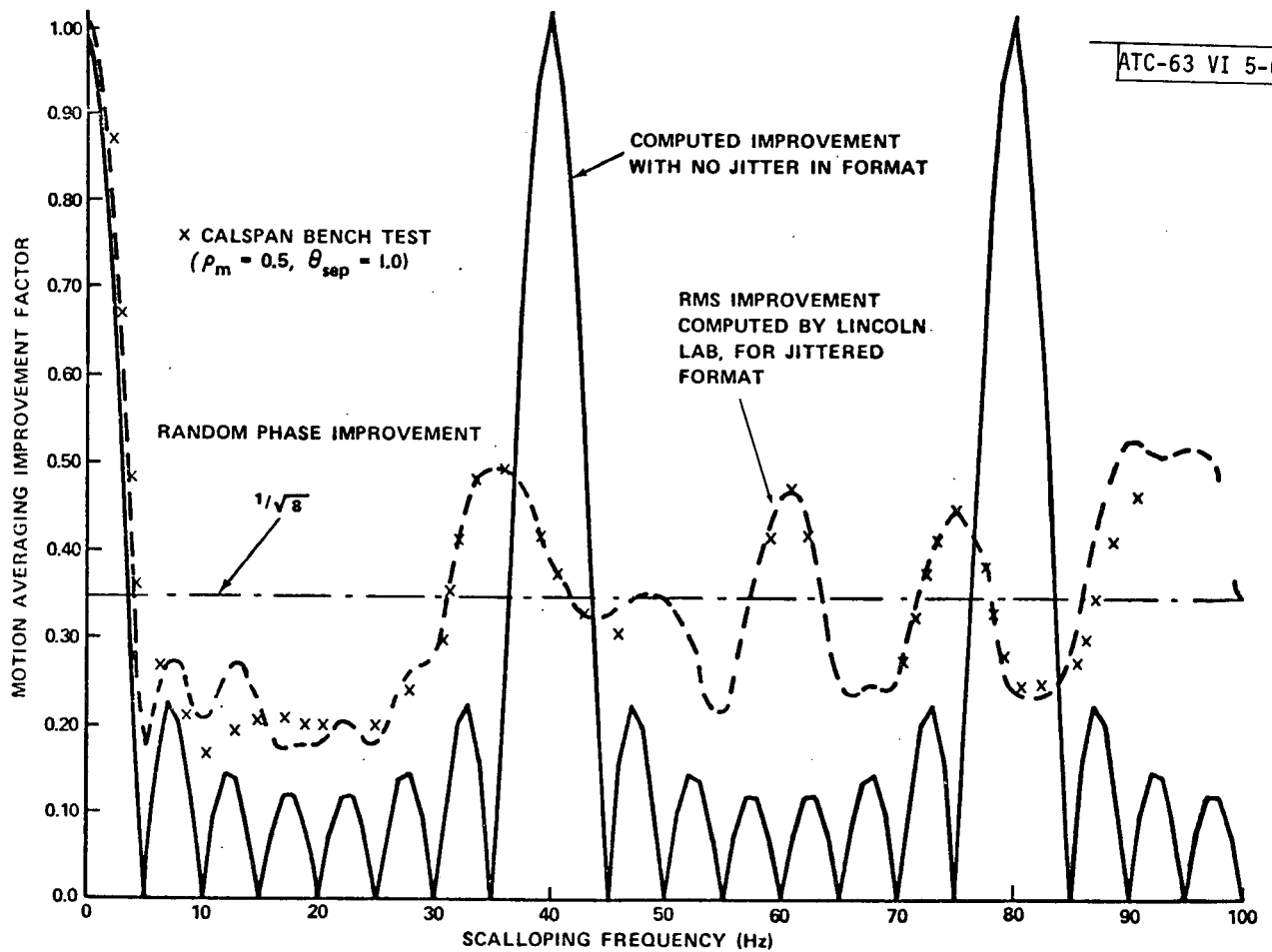
Fig. 5-6. Motion averaging improvement for jittered TRSB signal format (elevation and flare functions).

(a) <u>Location of Specular Point</u>

Consider a vertical reflector surface rotated an angle δ from being parallel to the L.O.S. between transmitter and receiver. The geometry in the plane of reflection is shown in Fig. 5-7. The projections onto the two vertical planes through the L.O.S. and perpendicular to it are also shown. The specular reflection point is indicated by S. An arrowhead denotes the normal to the reflecting surface which projects as a horizontal line in each vertical plane. We define ξ as the angle of tilt away from horizontal of the line from the specular point perpendicular to the L.O.S. Upon examination of the projections it follows that

$$\tan \delta \sin \alpha = \sin \xi \tag{5-11}$$

The height h_R and planar elevation angle α_R of the specular point may now be found using the coordinates (X_R, Y_R) of the point in the horizontal plane

$$h_R = Y_R \tan \alpha_R = Y_R \tan \alpha + X_R \tan \xi \tag{5-12}$$

$$\tan \alpha_R = \tan \alpha + \frac{X_R}{Y_R} \tan \xi \tag{5-13}$$

For given values of α, δ, Eqs. (5.11) and (5.12) may be used to delineate the regions where the specular point lies below the obstruction limits. A family of such boundaries is given in Fig. 5-8 for the special case $\alpha = 3°$ and the transmitter located on centerline.

The critical regions tend to grow with decreasing δ above C.L. and with increasing δ below. However, other limitations come into play to reduce the threat. In particular, in the plane of reflection (Fig. 5-7)
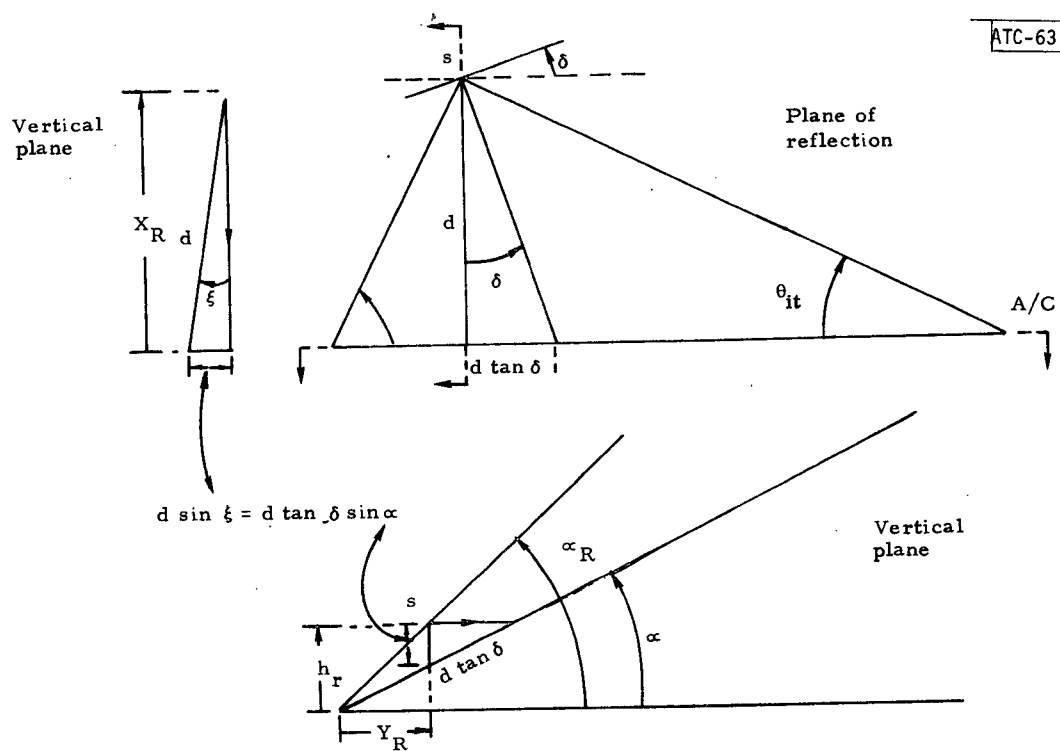
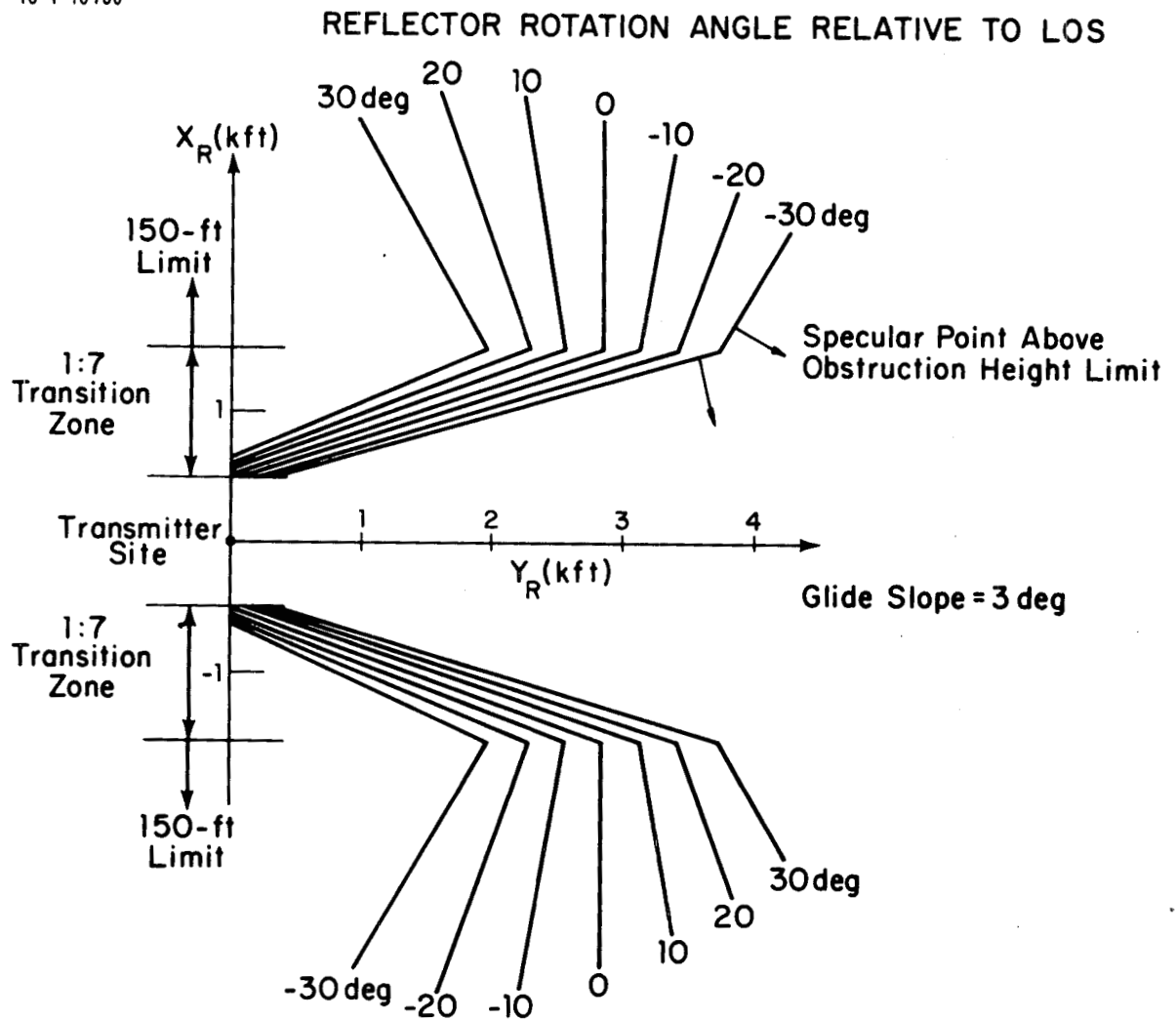**Fig. 5-7. Geometry for rotated reflector.**

18-4-16790

REFLECTOR ROTATION ANGLE RELATIVE TO LOS

REFLECTOR LOCATIONS FOR SPECULAR POINT
AT OBSTRUCTION HEIGHT LIMIT

Fig. 5-8. Reflector locations for specular point at obstruction height limit.

$$\psi = \theta_{IT} + 2\delta \qquad\qquad (5.14)$$

which implies $\theta_{IT} > -2\delta$. When $\delta = -15°$ we have $\theta_{IT} > 30°$, a value for which the scalloping frequencies are generally high enough to produce adequate motion averaging. In the specific cases to follow, $\delta = -15°$ has been used to determine the bounds on height limitation. Although this is not the worst possible rotation, it is a conservative choice for making system comparisons.

(b) Angular Separation of Multipath

We turn next to the question of in- or out-of-beam multipath. Toward that end the previously derived expression for the elevation angle α_R of the reflector will be evaluated. It should be recalled that α and α_R are planar elevation angles in a coordinate system aligned with the L.O.S. rather than the runway C.L. What follows is approximately correct for planar beams hinged perpendicular to the C.L. to the extent that the cosine of the angle between L.O.S. and C.L. is approximately one. Substituting Eq. (5.11) and (5.14) in (5.12) and using the small angle approximation $\tan \xi = \sin \xi$ gives

$$\tan \alpha_R = \tan \alpha + \tan(\theta_{IT} + 2\delta) \tan \delta \sin \alpha \qquad (5.15)$$

This equation is plotted in Fig. 5-9 as a family of curves of α_R vs δ with $\alpha = 3.0°$ and θ_{IT} as a parameter. If we select a separation of 1.5° as the boundary between in-beam and out-of-beam, we find the multipath is in-beam for all but extreme values of θ_{IT} and/or large positive rotation angles. Since neither of these conditions can be counted upon, the multipath must in general be regarded as in-beam.
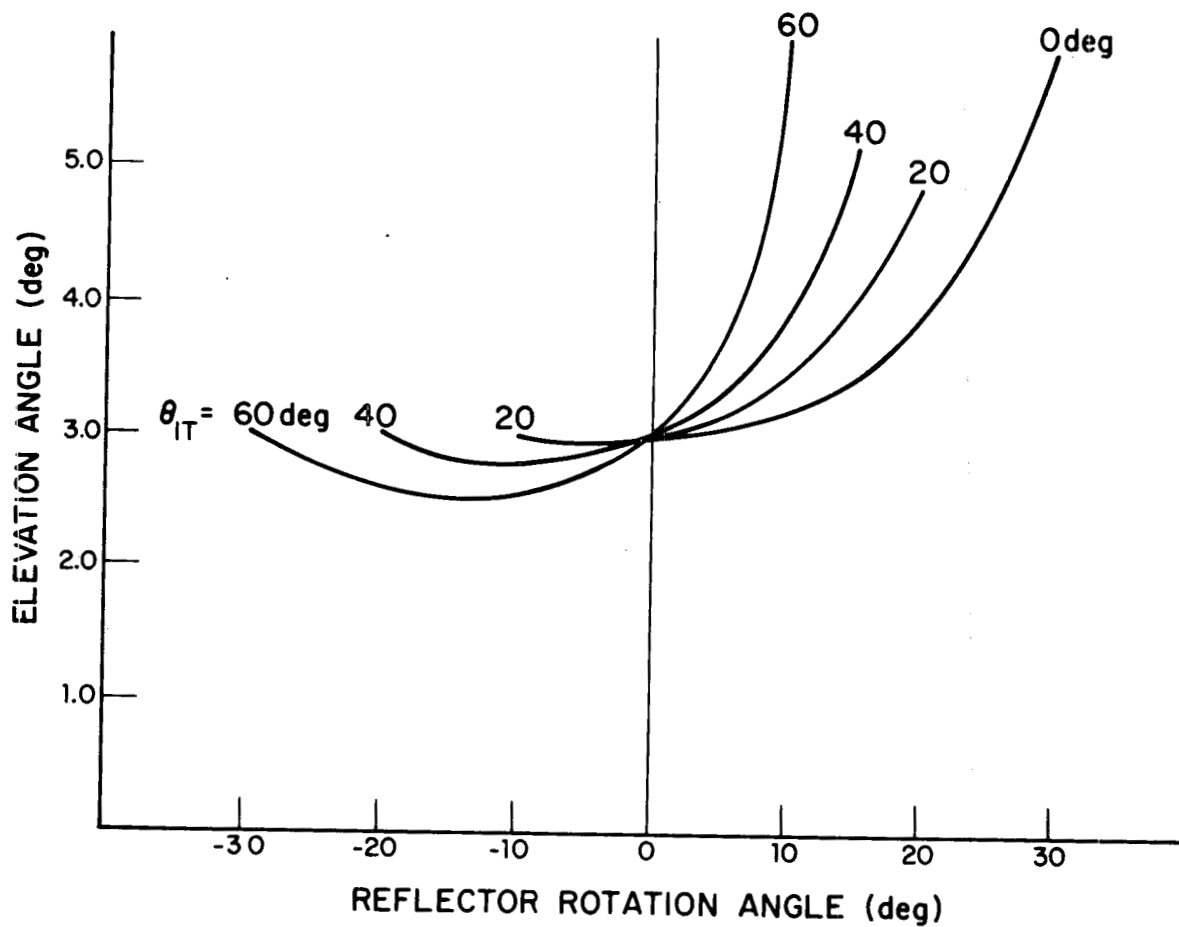
PLANAR ELEVATION ANGLE OF SPECULAR POINT
3-deg GLIDE SLOPE

Fig. 5-9. Planar elevation angle of specular point 3-deg glideslope.

The α_R above was defined as a planar elevation angle and hence in-beam applies to planar beams. Using the same approximations that gave Eq. (5.15), the conical elevation angle α_{RC} of the specular point is given by

$$\frac{Y_R \tan \alpha_{RC}}{\cos(\theta_{IT} + 2\delta)} = Y_R \tan \alpha_R$$

whence

$$\tan \alpha_{RC} = \cos(\theta_{IT} + 2\delta) \tan \alpha + \sin(\theta_{IT} + 2\delta)\tan \delta \sin \alpha$$

Using $\tan \alpha \approx \sin \alpha$ this can be simplified to

$$\tan \alpha_{RC} = \tan [\cos \theta_{IT} - \sin \theta_{IT} \tan \delta] \qquad (5.16)$$

Equation (5.16) is plotted in Fig. 5-10. Comparing with Fig. 5-9 shows that the dependence on reflector rotation is quite dissimilar. But neither for planar nor conical beams does the specular reflection move substantially out-of-beam until δ and/or θ_{IT} reach large values. In making comparisons as to the relative merits of planar and conical beams, it is important to include the coverage limits. From Eq. (5.14) the azimuth-coverage angle ψ_C must satisfy

$$\psi_C > \theta_{IT} + 2\delta$$

This limit is drawn on Figs. 5-9 and 5-10 for $\psi_C = 20°$ and $60°$. One observes that planar beams have a somewhat greater potential for creating out-of-beam multipath.
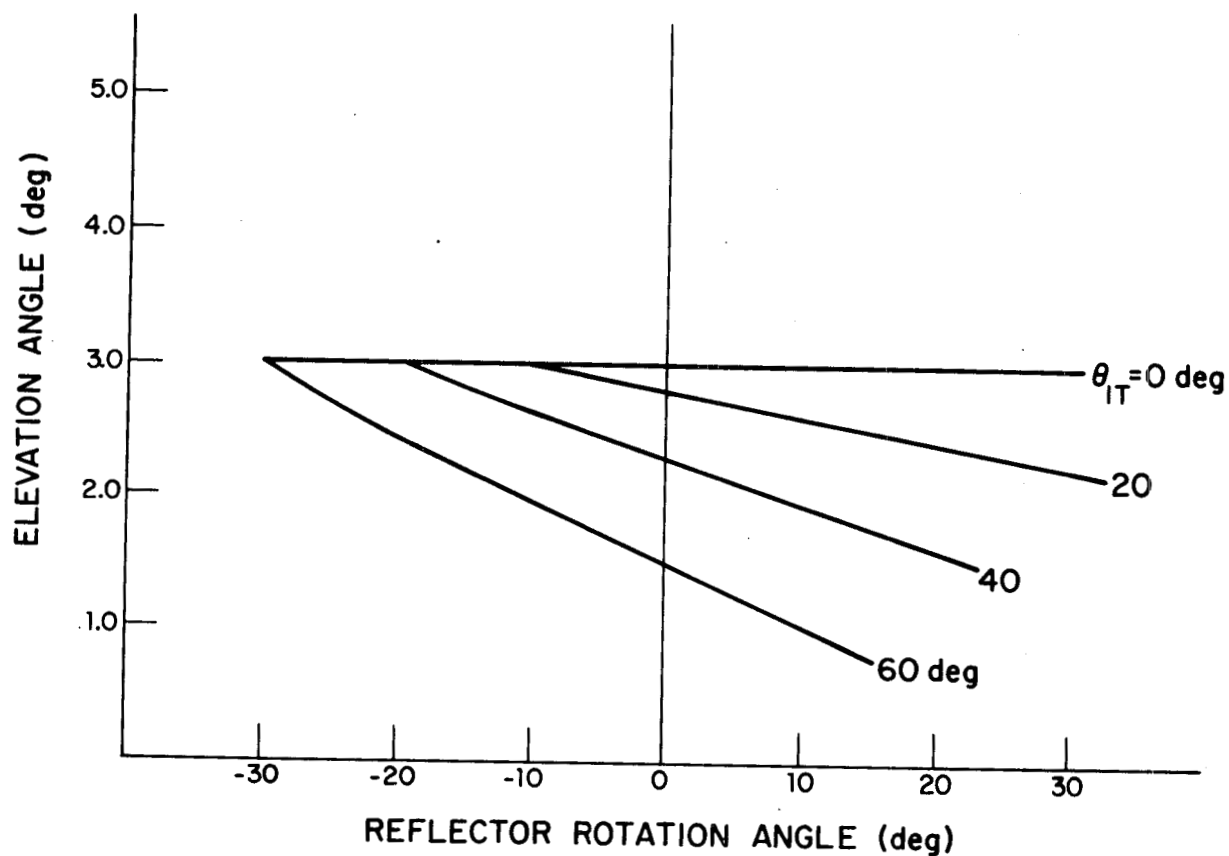
CONICAL ELEVATION ANGLE OF SPECULAR POINT
3-deg GLIDE SLOPE

Fig. 5-10. Conical elevation angle of specular point 3-deg glideslope.

One other factor should be noted. Planar beam multipath goes out-of-beam upward, which may confuse elevation processors that treat the higher coded signal as the valid one.

(c) Evaluation of Motion Averaging Based on Reflector Threat Locations

The results of the preceding two sections will now be combined to assess the benefits of motion averaging for the two competing systems in relation to the obstruction height limits and coverage areas. In Figs. 5-11 to 5-14, different scenarios are depicted for EL-1 sites offset 400 ft from runway centerline. In each case the aircraft is located on the extended C.L. on a 3° glide slope with respect to EL-1 and at a specific distance from the transmitter.

The angle of the velocity vector is varied according to the angle between L.O.S. and C.L. with an additional perturbation due to course deviation from a C.L. approach. The extreme values of θ_{VT} are used to compute a corresponding θ_{IT} for each of two scalloping frequencies: 5 Hz and 25 Hz. The 5 Hz pertains to the 0'th grating lobe of the TRSB system, and 25 Hz applies to one version of TDM Doppler. The θ_{IT} angles define the direction, referenced to the aircraft position and L.O.S., in which an appropriately oriented reflector would produce the indicated scalloping frequencies. The 5 Hz and 25 Hz directions are bounds that limit the region of potential reflector threats where motion averaging is ineffective.

The diagrams show the θ_{IT} limits for the selected situations. Also indicated in each figure are two sets of boundaries where the specular point passes through the obstruction height limits. One set is derived from the height
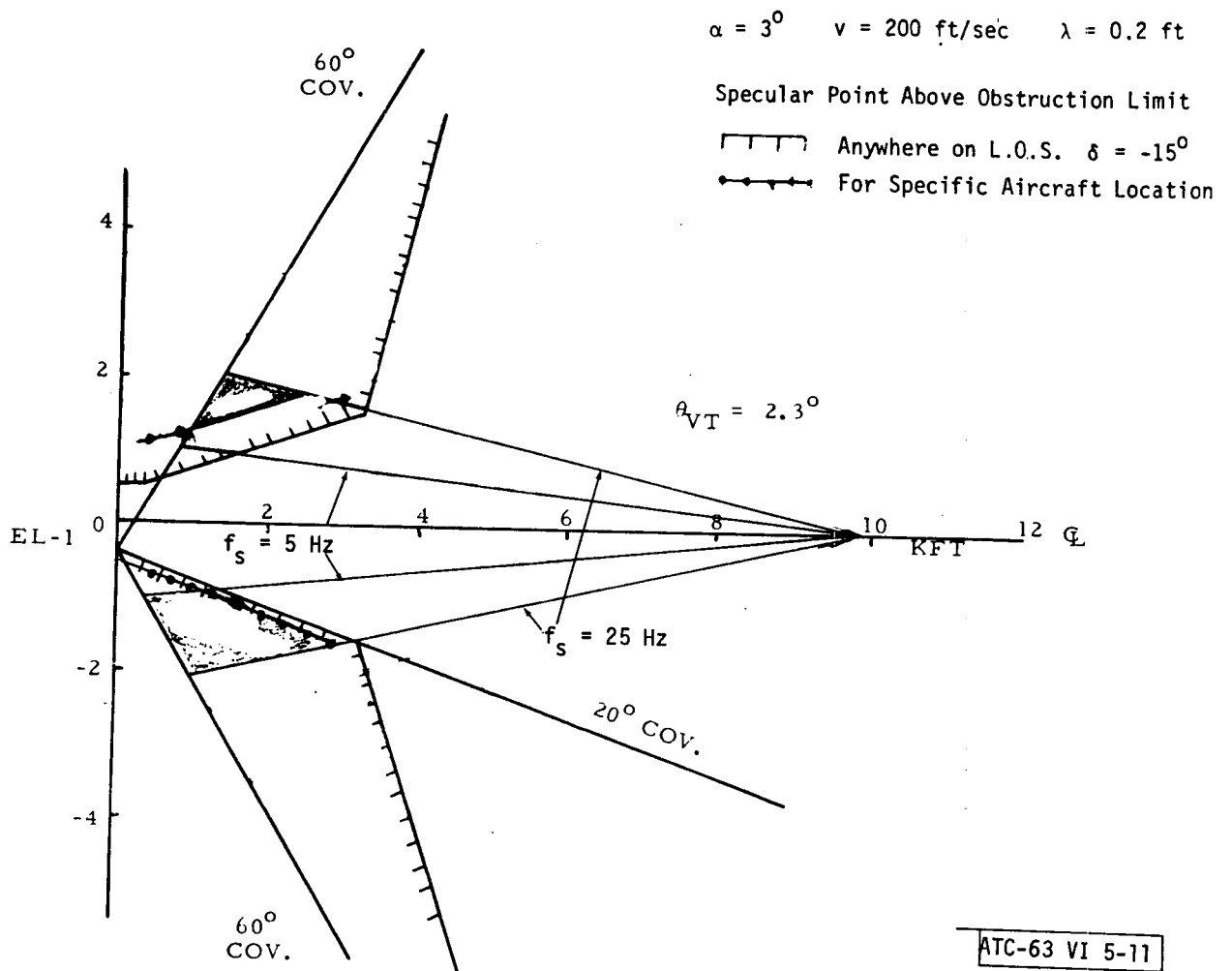
$\alpha = 3^{o}$ $v = 200$ ft/sec $\lambda = 0.2$ ft

Specular Point Above Obstruction Limit

Anywhere on L.O.S. $\delta = -15^{o}$
For Specific Aircraft Location

$\theta_{VT} = 2.3^{o}$

$f_s = 5$ Hz

$f_s = 25$ Hz

60° COV.

60° COV.

20° COV.

EL-1

KFT

ATC-63 VI 5-11

Fig. 5-11. Reflector location diagram.

5-28

$\alpha = 3^{\circ}$ $v = 200$ ft/sec $\lambda = 0.2$ ft

Specular Point Above Obstruction Limit

⌐|||⌐ Anywhere on L.O.S. $\delta = -15^{\circ}$

•—•—• For Specific Aircraft Location

$\theta_{VT} = 2.3^{\circ} \pm 7.7^{\circ}$

↑ > 25 Hz

↑ > 5 Hz

↓ > 5 Hz
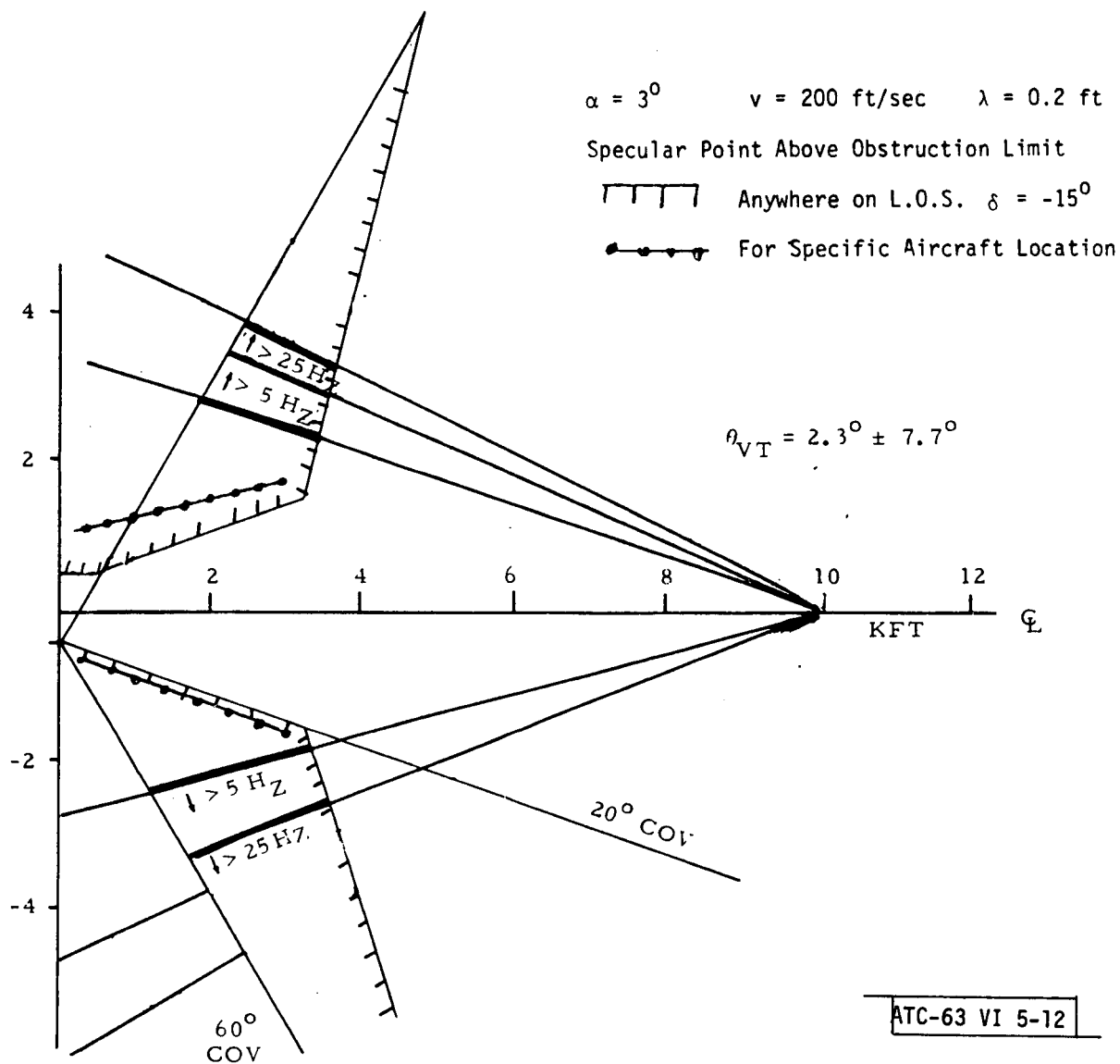
↓ > 25 Hz

20° COV

60° COV

KFT

ATC-63 VI 5-12

Fig. 5-12.   Reflector location diagram.
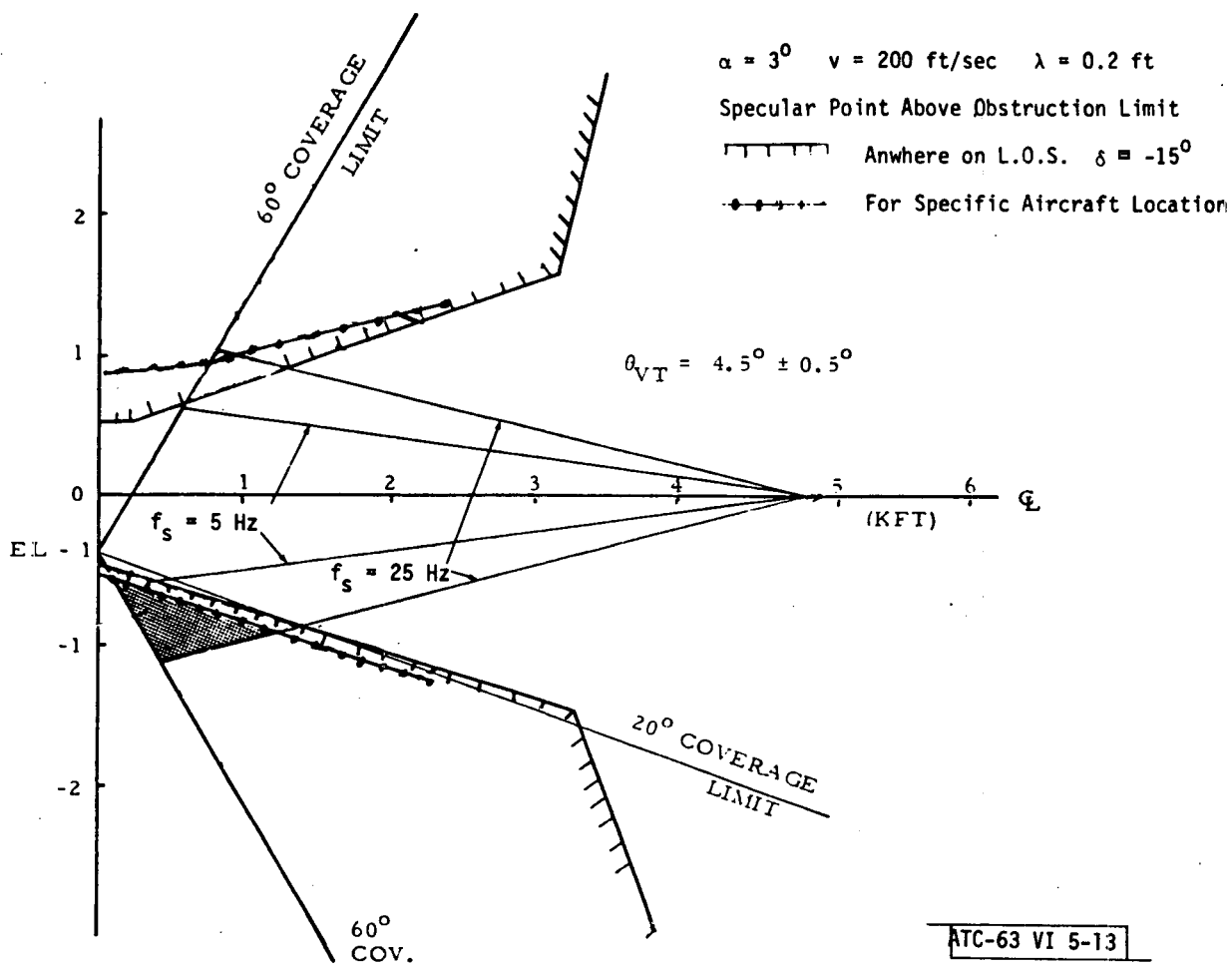
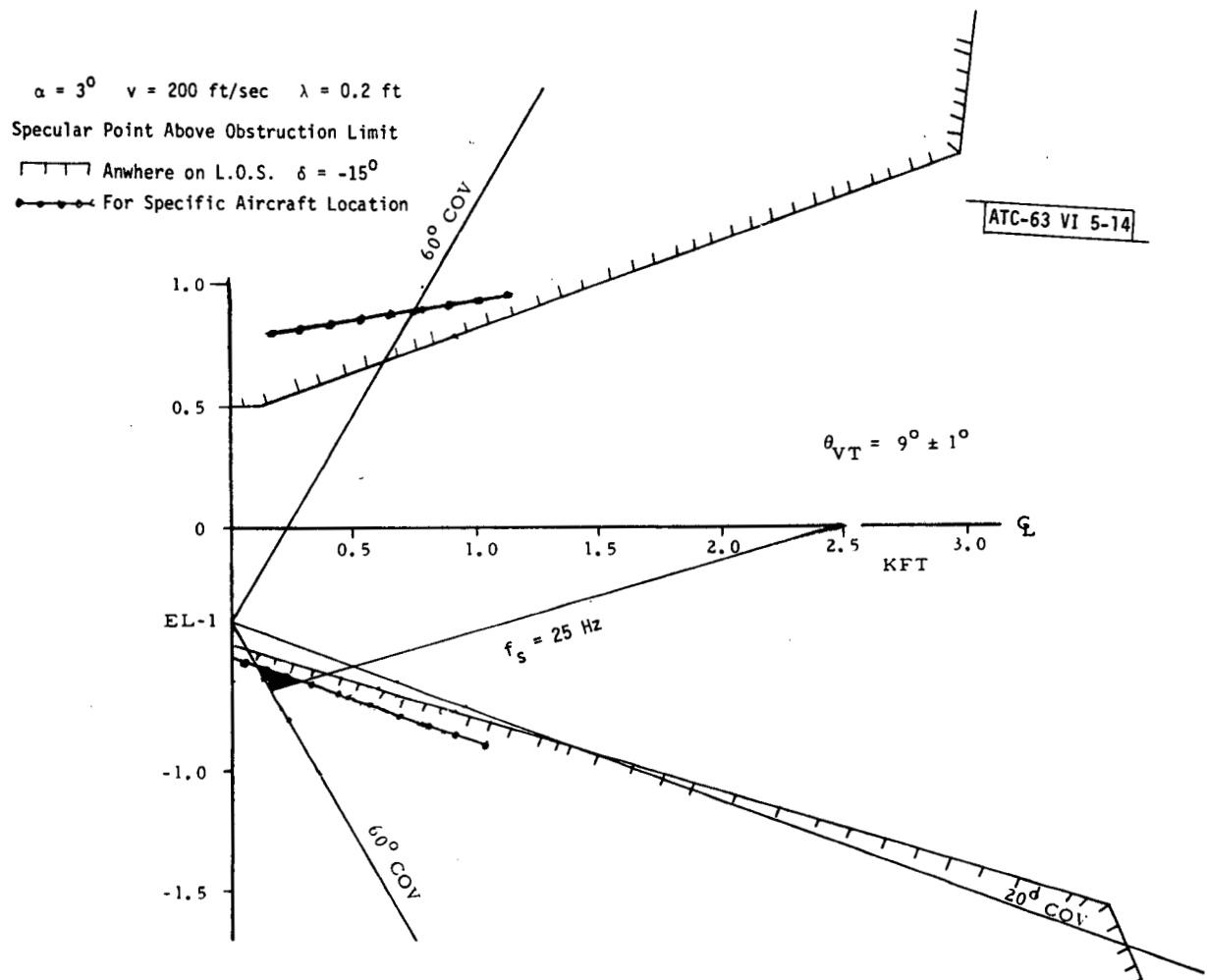Fig. 5-13.   Reflector location diagram.

Fig. 5-14. Reflector rotation diagram.

bounds computed above, taking into account the rotation of the L.O.S. with respect to runway C.L. These bounds apply for an aircraft anywhere along the L.O.S. independent of its distance from the transmitter. For the specific choice of aircraft location, a somewhat tighter bound can be obtained by finding the specular height from the ratio of distances multiplied by the aircraft height h_{ac}, i.e.

$$h_R = \frac{R_1}{R_1 + R_2} h_{ac}$$

where R_1 is distance from transmitter to reflector and R_2 the distance from reflector to aircraft. When h_R is equated to the obstruction height limits in the transitional surface, the dotted-line bounds are formed. The $\pm$ 20° and $\pm$ 60° coverage limits for EL-1 are indicated. It is interesting to note that illumination coverage less than 20° nearly excludes all reflectors that meet the obstruction height limits.

In comparing the two contending systems one must examine the size of the angular sector between the 5 Hz and 25 Hz lines. Reflectors located between the two lines would be suppressed by motion averaging for the TR system. We observe that this sector is largest for small θ_{VT} and tends to decrease as the velocity vector deviates in angle from the L.O.S. The region of definite advantage for TRS has almost disappeared entirely $\theta_{VT} = 9° \pm 1°$ in Fig. 5-13.

VI. SYSTEM MODEL VALIDATION

In order to provide some measure of confidence in the results obtained from the receiver simulations and the conclusions drawn from them, it was necessary to accomplish a program of model validation. Validation is a checkout procedure which begins with verification that the computer code properly represents the mathematical models of the systems and ends only when it is evident that the model outputs are in some sense "correct." This section summarizes the receiver model validation process.

6.1 Methods of Validation

Validation is accomplished by comparing the model output to data from other sources which should yield equivalent or similar results. From among these, theoretical studies based on idealized models of the transmitters and receivers and bench test experiments on hardware receivers have been incorporated into the validation process. These sources represent reasonably well controller situations that can rather easily be replicated by the computer simulation.

Figure 6-1 shows the scope of the angle system validation effort. The three basic inputs to the comparison process are the Calspan bench tests, simulation data (from both test programs and full simulations), and theoretical multipath performance calculations. The emphasis in this report will be on the scanning beam validation effort. Besides TRSB, some results for the two Phase II FRSB systems are included in cases where their behavior is envelope-only dependent and essentially identical to that of TRSB. Both static and dynamic validation tests have been conducted. Static tests are those for which
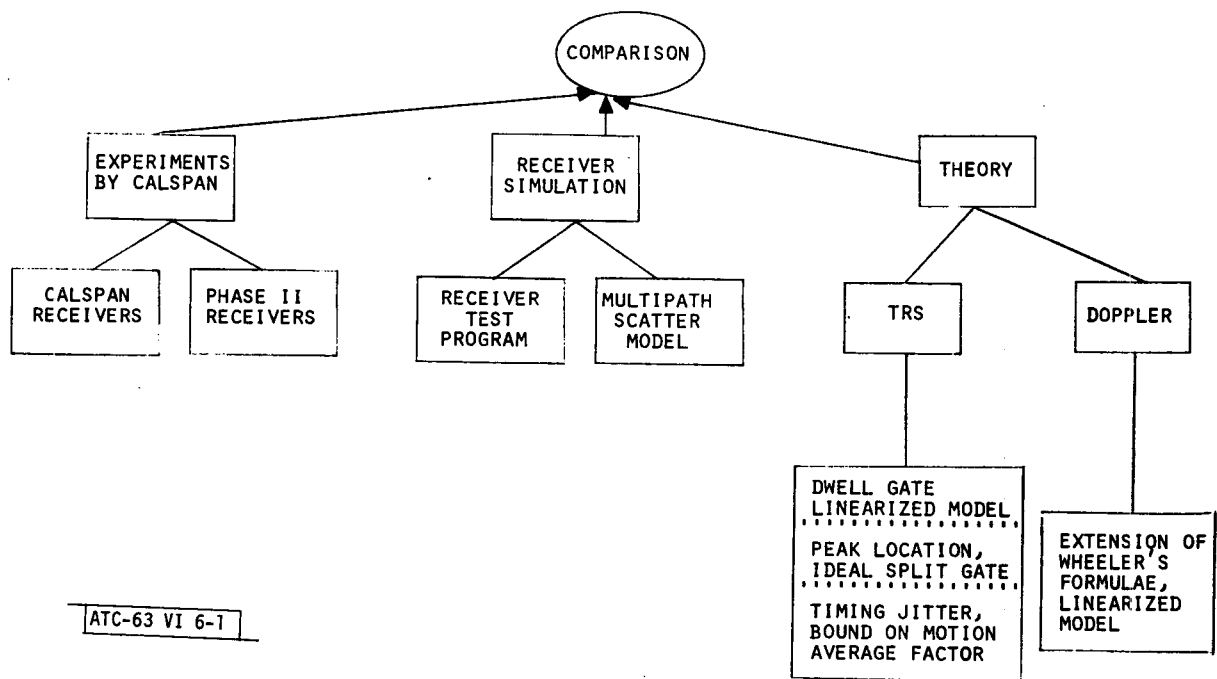
Fig. 6-1. Elements of angle receiver validation process.

the receiver position is fixed. Dynamic tests are those in which the receiver is assumed to be in motion with respect to the transmitter and the multipath environment. In the latter, the phase relationships among the received multipath components are time-varying and are of interest in those multiscan systems which can potentially benefit from motion averaging. In all cases the validation data consists of graphs of angle error vs some multipath parameter (e.g., relative phase, separation angle, etc.). In some tests, mean, peak, and rms error (with respect to RF phase) are presented.

The DME validation follows a similar pattern, except that comparisons are made solely against theory due to lack of adequate experimental data.

In those cases for which noticeable disagreement among the results is evident, an attempt to ascertain cause has been made. Occasionally, the discrepancies are attributable to differences in receiver processing techniques or parameters. Especially for the experimental data, there are sporadic anomalies for which no explanation can be found. Despite some areas of disagreement or uncertainty, the receiver validation results generally show good agreement with pertinent theory and experiment.

Sections 6.2, 6.3 and 6.4 deal with TRSB, Doppler, and DME, respectively. Each section begins with a summary of the theoretical results used in the comparisons. Derivations are relegated to appendices. Following that, curves of static error vs multipath phase or separation angle are presented. Next, dynamic simulation results are compared to both theory and bench tests. The bench tests were conducted by Calspan employing an MLS signal simulator and hardware receivers of their own design. At a later date, Calspan coupled their signal simulator with actual contractor receivers used in the MLS Phase

II feasibility test program. The Lincoln simulation was used to conduct parallel tests and the comparative results are reported. In the final set of tests, Section 6.5, the full simulation program was run for two airport configurations and the outputs analyzed using the program's multipath diagnostics and the theoretically predicted performance.

6.2 Time Reference Scanning Beam

6.2.1 Theory

It is assumed that the transmitting antenna has a Gaussian beamshape $P(x)$, where x stands for angular displacement in units of 3 dB beamwidths:

$$P(x) = e^{-kx^2} \quad : \quad k = 2 \ln 2 \tag{6-1}$$

In the absence of multipath, the leading and trailing edge crossings in a dwell gate processor will occur symmetrically on either side of the beam peak (center), at displacement $\pm v$ beamwidths. The value of v is selectable; for example, if the threshold setting is -3 dB with respect to the nominal peak value, $v = 0.5$.[*] Multipath of relative amplitude ρ perturbs the crossings from nominal. If ρ is not too large, the true crossing points can be approximated by linearly expanding the combined envelope about the nominal crossings. The dwell gate displacement is the average of the two threshold crossing errors. The indicated computation is carried out in Appendix D; in terms of notation given in Table 6-1, the single scan pair angle error which results is

---

[*]For the Gaussian beam, v is proportional to the square root of the threshold in dB: $v = \sqrt{-V_{dB}/12}$.

TABLE 6-1

NOTATION

Symbol	Units	Definition
ρ		Ratio of multipath to direct amplitude
V		Ratio of scanning beam threshold to envelope peak
V_{dB}		V in decibel units
T_s	sec	Scan duration
T_g	"	Doppler scan gate duration (counting interval)
T, T_d	"	Spacing between bidirectional scan pairs
T_z	"	Elapsed time between 0° boresight for bi-directional scan pair
T_k	"	Spacing between first and k-th scan pair
f_s	Hz	Scalloping frequency
ω_s	rad/sec	$2\pi f_s$
ω_c	"	Carrier frequency
ω_0	"	Subcarrier (or offset) frequency
r		$(\omega_0 + \omega_s)/\omega_c$
BW	deg	Beamwidth
θ_m	deg/BW	Separation between multipath and direct in scan coordinate (fractional beamwidths)
v	BW	Beam displacement at threshold crossing
$\dot{\theta}$	BW/sec	TRS antenna scan rate
ϕ_c	deg	Doppler midscan relative phase (direct and multi-path reference) for $f_s=0$
ϕ_m	"	Doppler midscan relative phase (direct and multi-path sideband) for $f_s=0$
ϕ'	"	TRS relative phase (direct and multipath) for $f_s=0$
η_m	"	Arbitrary phase between sampling instants and periodic scalloping error
n		Scan index
M		Number of scans per averaging interval
E_m	BW	Angle error for m-th scan pair

6-5

$$E_n = \rho \, \theta_m \, e^{-k\theta_m^2} \cos\left[\phi' + \frac{\omega_s T_z}{2}\right]$$

$$\cdot \left\{ \frac{\sinh(2k\theta_m v)}{2k\theta_m v} \cos\left(\frac{\omega_s v}{\dot\theta}\right) \cos\left(\frac{\omega_s T_z}{2}\right) + \frac{\cosh(2k\theta_m v)}{2k\theta_m v} \sin\left(\frac{\omega_s v}{\dot\theta}\right) \sin\left(\frac{\omega_s T_z}{2}\right) \right\} \cdot$$

$$\text{(6-2)}$$

In nearly all cases of interest, the term $\omega_s v/\dot\theta$, which corresponds to scalloping across the dwell gate of a single pulse, is small enough to be neglected ($\omega_s v/\dot\theta \approx 0$), thus yielding a simple formula which relates all the key TRSB multipath parameters to the error after motion averaging of M successive scan pairs:

$$E \approx \underbrace{\rho}_{\substack{\text{multipath} \\ \text{level}}} \underbrace{\theta_m \, e^{-k\theta_m^2}}_{\substack{\text{separation} \\ \text{angle and} \\ \text{xmtr beamwidth}}} \underbrace{\frac{\sinh(2kv\theta_m)}{2kv\theta_m}}_{\substack{\text{choice of} \\ \text{threshold}}} \underbrace{\frac{\cos\left(\frac{\omega_s T_z}{2}\right)}{2M} \sum_{k=1}^{M-1} \cos(\phi_s + \omega_s T_k)}_{\substack{\text{motion averaging and} \\ \text{rf phase}}}$$

$$\text{(6-3)}$$

The analytical model of the dwell gate processor provides considerable insight into the performance of scanning beam systems, but fails to predict the bias error resulting from the asymmetry of multipath error vs RF phase. An alternative model is a beam peak locator. Although more appropriate as an idealization of a split-gate discriminator, the model corresponds closely to a dwell gate processor for small separation angles and moderate multipath levels.

Appendix C derives the multipath error of a beam peak locator. No closed

form expression can be extracted, and one must resort to numerical methods to

obtain an answer. The method is applied in Section 6.2.2 to generate graphs

of error vs multipath phase for comparison with simulation data.

6.2.2 Static Tests

In the tests of the receiver routines conducted under static conditions,

i.e., in the absence of receiver motion, the RF phase between direct and multi-

path signal was varied in steps over a full cycle. Data was taken for various

multipath amplitudes, separation angles, and RF phase shifts. For the scan-

ning beam tests, experimental results from Calspan[23,24] were available,

and the simulation was run under the same conditions. Figure 6-2 shows ex-

perimental data, simulation results and theoretical results for error versus

separation angle for the time reference system. The experimental data at

0.5° and 1.0° separation angles are in reasonable agreement with the simula-

tion.

The theoretical error formula (6-3) also agrees well at the -10 dB level;

however, at the -6 dB level, there is a noticeable deviation near 90° which

arises from the fact that terms in ρ^2 were ignored in obtaining (6-3). When

the multipath amplitude exceeds the threshold level, the error is a markedly

non-sinusoidal function of rf phase which, although it can be explained (see

Fig. 4-8), does not emerge from the first order theory used to obtain Eq.

(6-3).

Figures 6-3 and 6-4 compare the experimental, simulation and theoretical

results as a function of separation angle at fixed rf phase. The experimental

results were obtained in the initial Calspan tests[23] in which thresholding
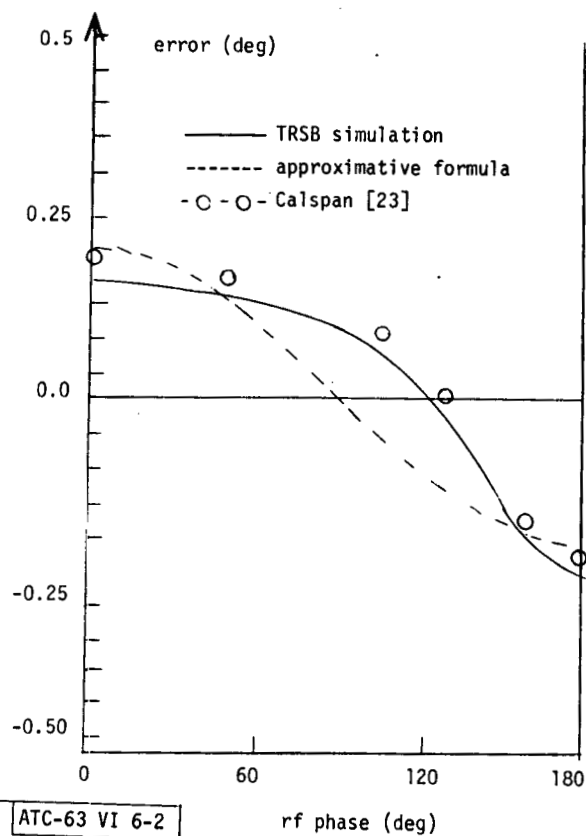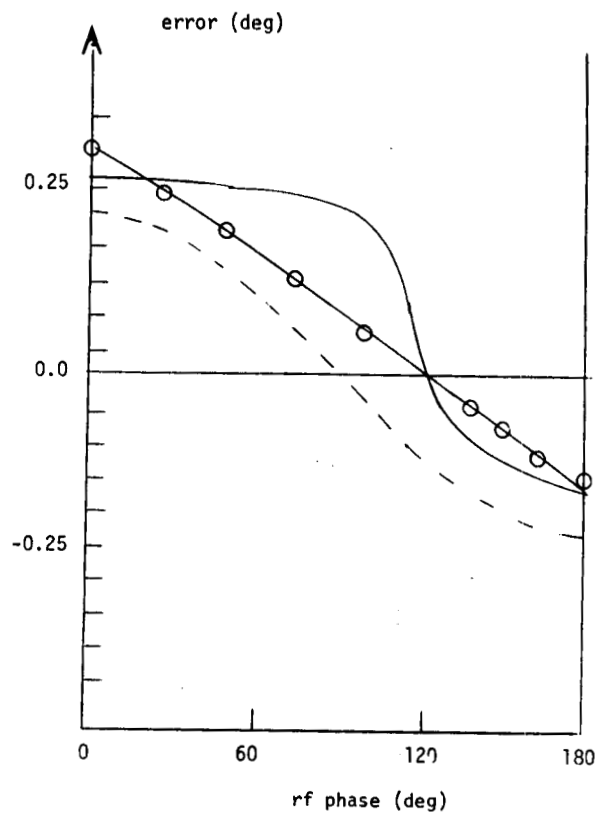
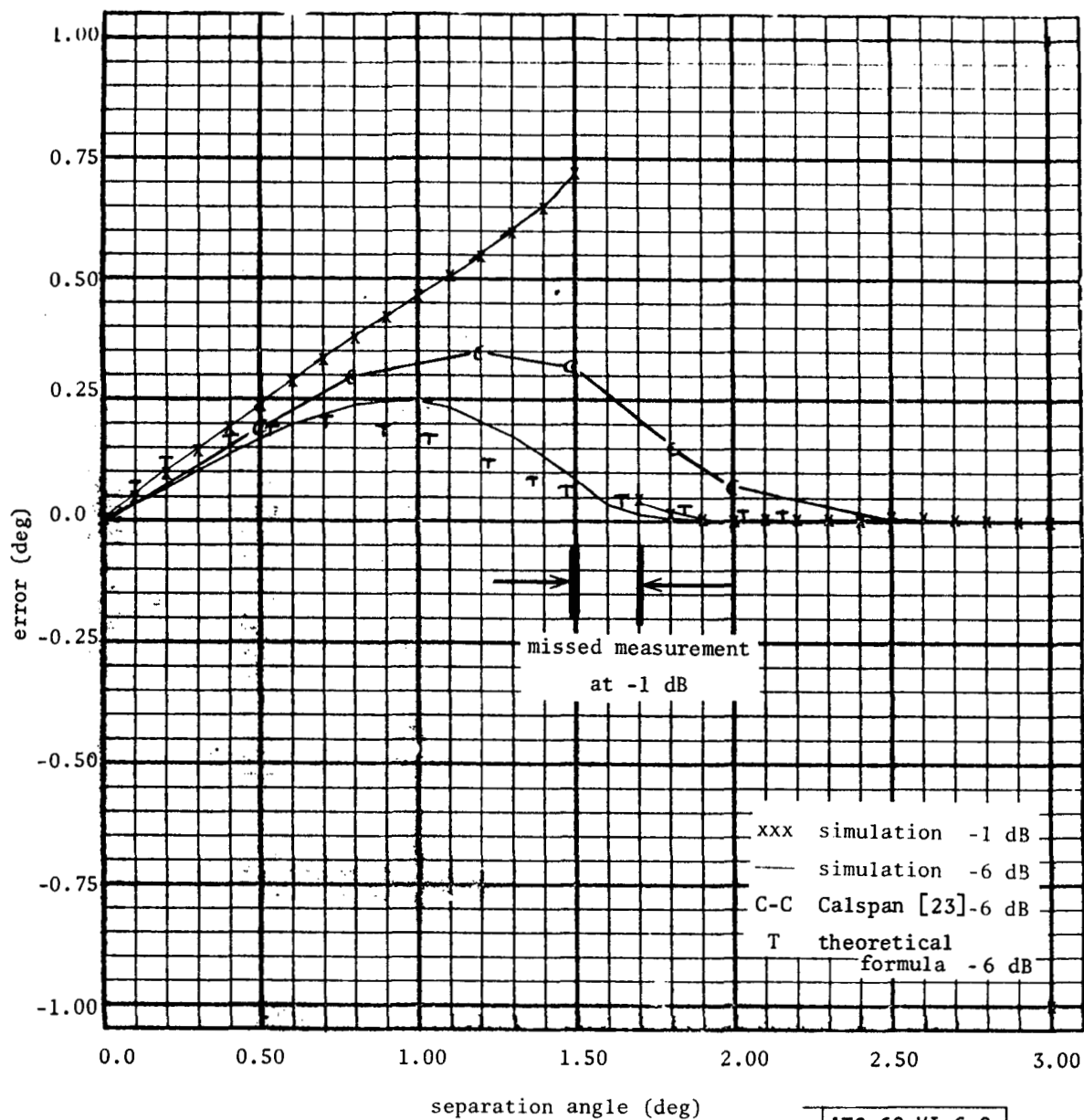Fig. 6-2. Error vs RF phase, TI scanning beam system, multipath = -6 dB

Fig. 6-3. Error vs separation angle, Bendix scanning beam system, multipath phase 0°.
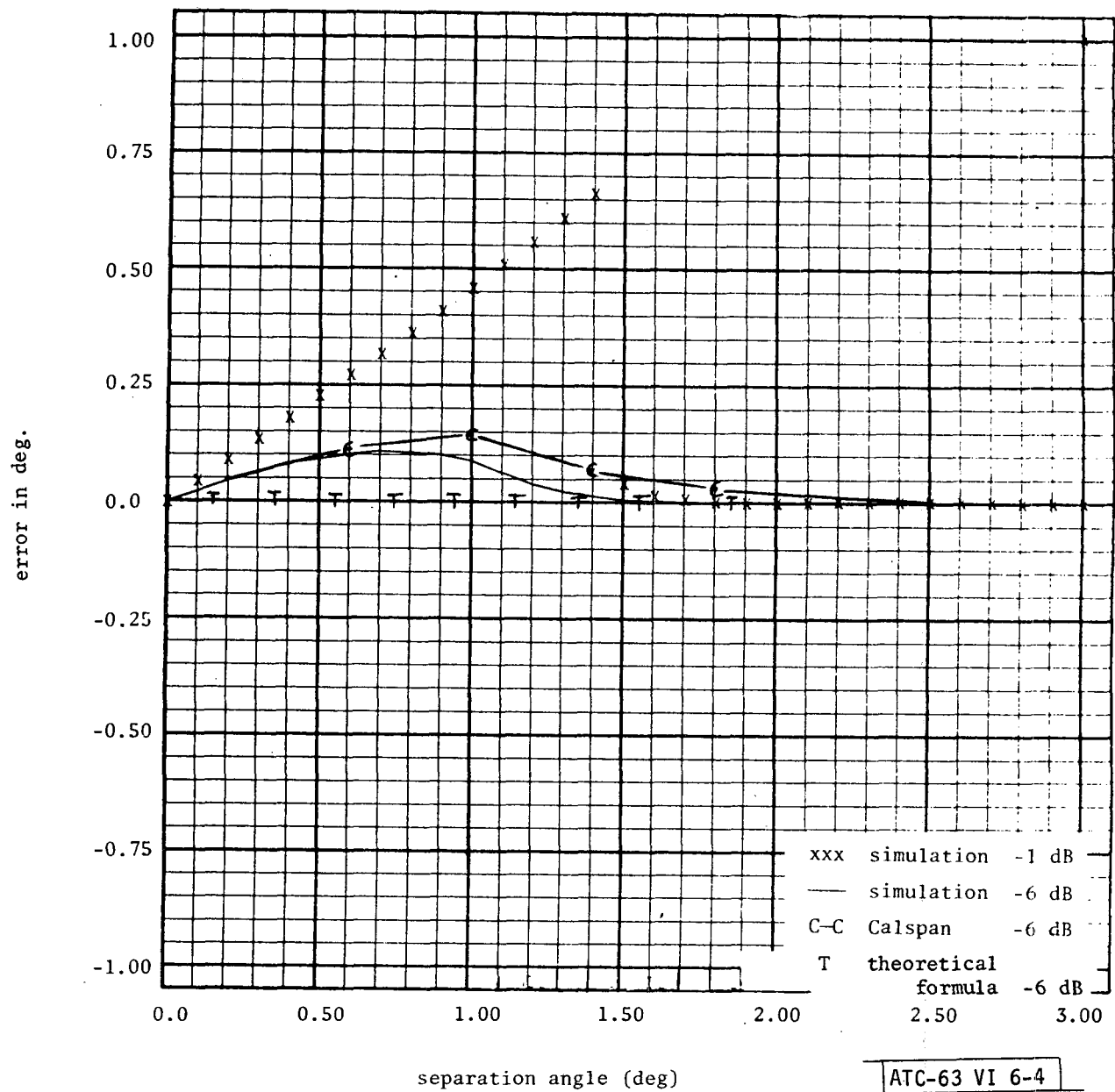
Fig. 6-4. Error vs separation angle, TI scanning beam system, multipath phase 90°.

may not have been as tightly controlled as in later tests. The data at -1 dB multipath level shows the very sharp changes in error performance that occur when the multipath level is comparable to or above the threshold level.

A comparison was also made between the dwell gate processor and the split gate processors described in Chapter IV. The results are shown in Table 6-2. We see that the more nearly "optimal" processing afforded by the split gate systems yields a substantial improvement against high level multipath.

Figure 6-5 compares the error statistics as averaged over rf phase for the scanning beam system as a function of separation angle for several multipath levels. The experimental data yields errors somewhat smaller than those for the computer simulation. It is believed that these differences arise because the actual receiver has several features (e.g., dwell gate qualification circuits) which limit the widening of the dwell gate associated with multipath[*], but are not incorporated in the first phase computer model. It is planned to incorporate these features into a more refined model to be developed during the next phase.

As expected, the theoretical error formula (6-3) gives results that compare favorably with the experimental and computer simulation results for small multipath levels and/or separation angles.

6.2.3 Dynamic Tests

Comparisons between the computer simulation, theory, and Calspan bench tests of the Bendix Phase II receiver for dynamic situations (i.e., $f_s \neq 0$) are reported in this section. Comparisons were also made between the computer model and earlier Calspan bench tests; however, it was subsequently

---

[*]For example, Calspan has shown [25] that varying the reset times can yield a 50% reduction in error.

TABLE 6-2

PEAK ERROR COMPARISON FOR RF PHASE 0°

MULTIPATH AMPLITUDE	DWELL-GATE (simulation)	SPLIT GATE (theoretical)	
		OFF-CENTER	ZERO CROSSING
-10 dB	0.15	0.11	0.13
-6 dB	0.24	0.16	0.21
-3 dB	0.60	0.21	0.32
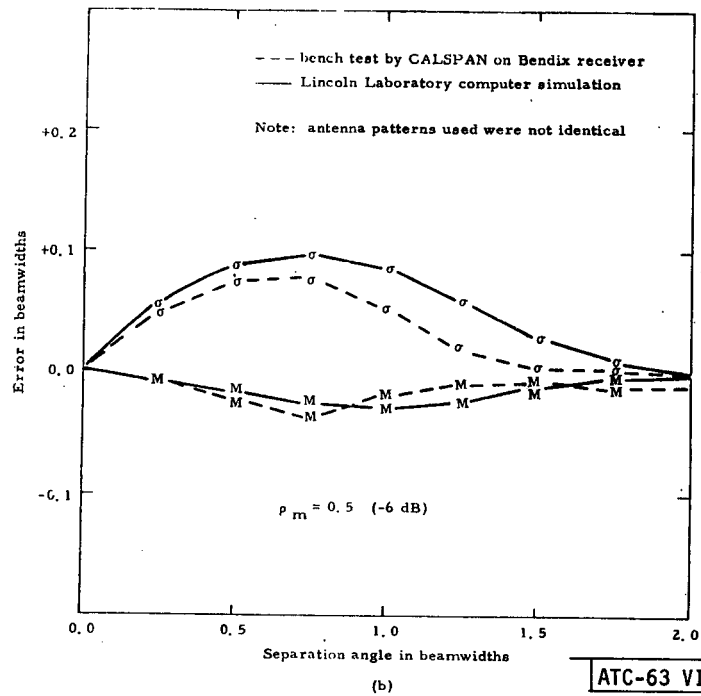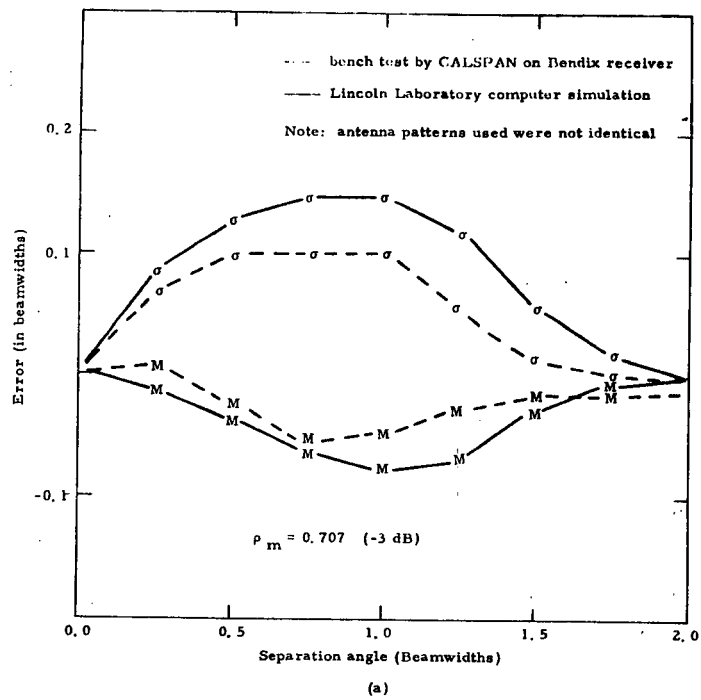
Fig. 6-5. TRSB static error vs separation angle.

learned that the receivers used for the initial bench tests had a number of hardware errors which were corrected in the later versions.

Figures 6-6 and 6-7 compare the EL-1 error as a function of separation angle for scalloping frequencies of 20.32 Hz and 40.32 Hz, respectively. The experimental data and computer simulation agree reasonably well. Again, the differences are felt to arise from certain dwell gate features of the Bendix receiver which were not in the initial TRSB model.

The final EL-1 plot (Fig. 6-8) is of error versus scalloping at fixed separation angle. Here we see quite good agreement as to the characteristic averaging factor. It should also be noted that Fig. 6-8 agrees quite well with the theoretical predictions of averaging factor (cf Fig. 5-6).

A similar set of tests were carried out for the AZ system and these had results comparable to those found for EL-1.

6.3 Doppler Scan

6.3.1 Theory

A theoretical analysis of Doppler error due to a single multipath component is given in Appendix A. Assumptions underlying the analysis are: small to moderate multipath amplitude, no multipath rejection filter, and scan gate centered on midscan. The error in fractional beamwidths averaged over M bidirectional scans is
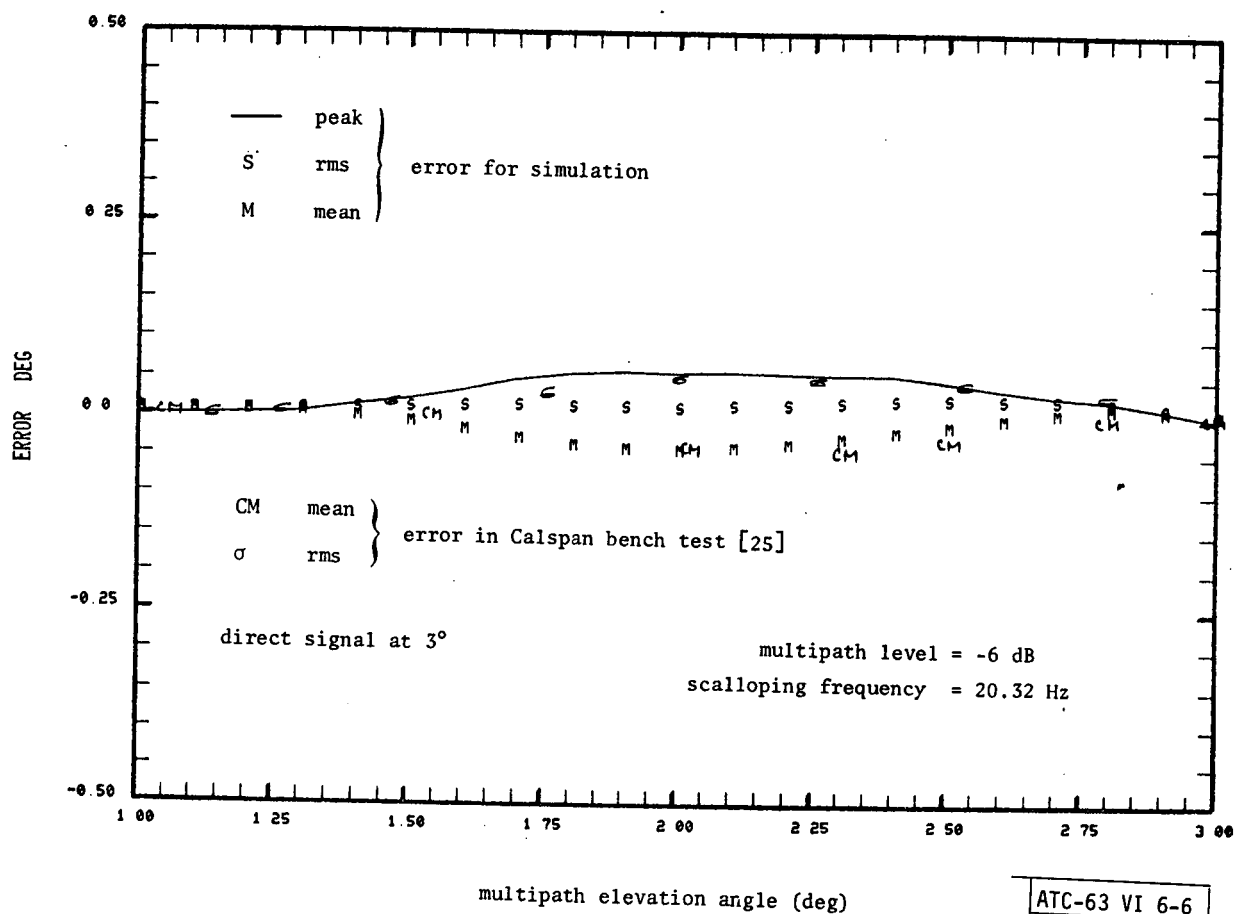
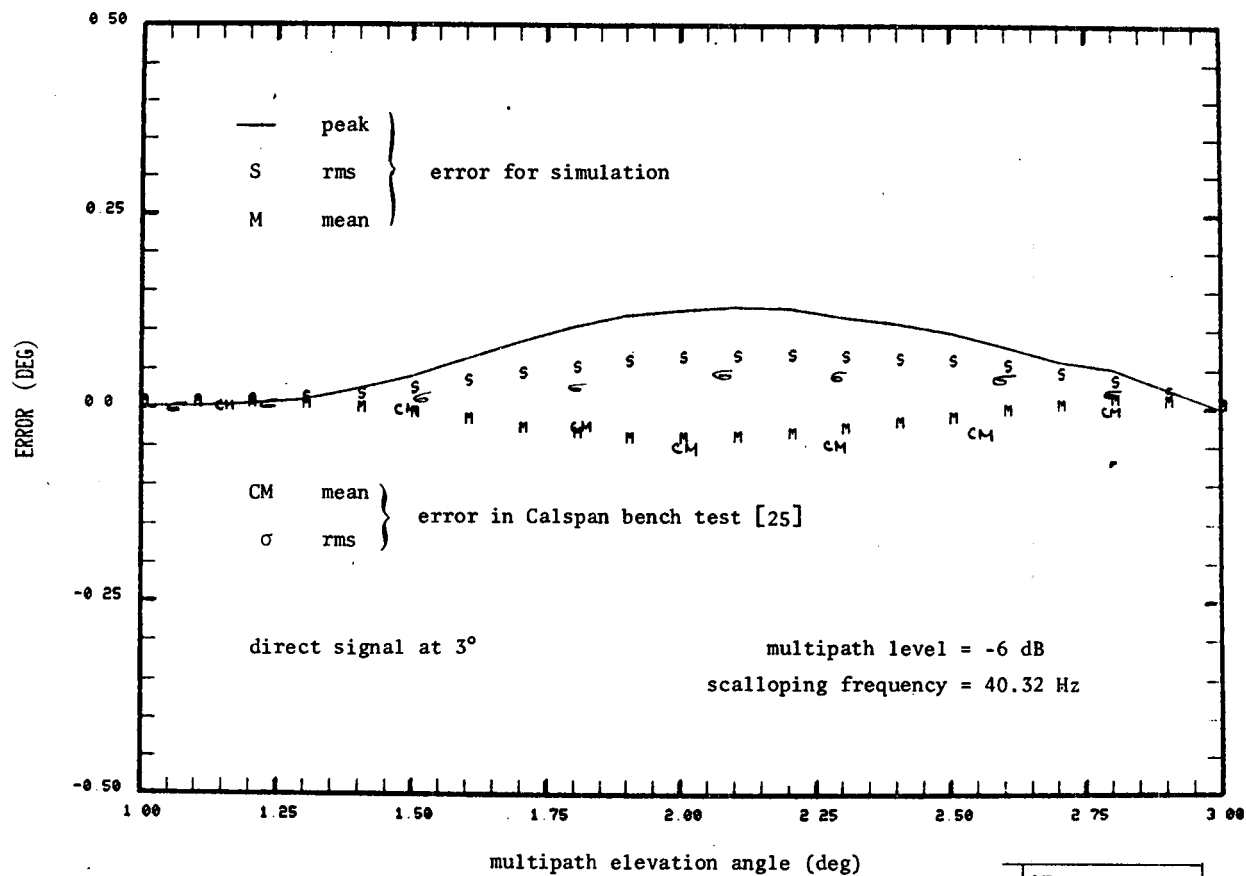Fig. 6-6. TRSB dynamic EL1 error vs separation angle.

ATC-63 VI 6-6

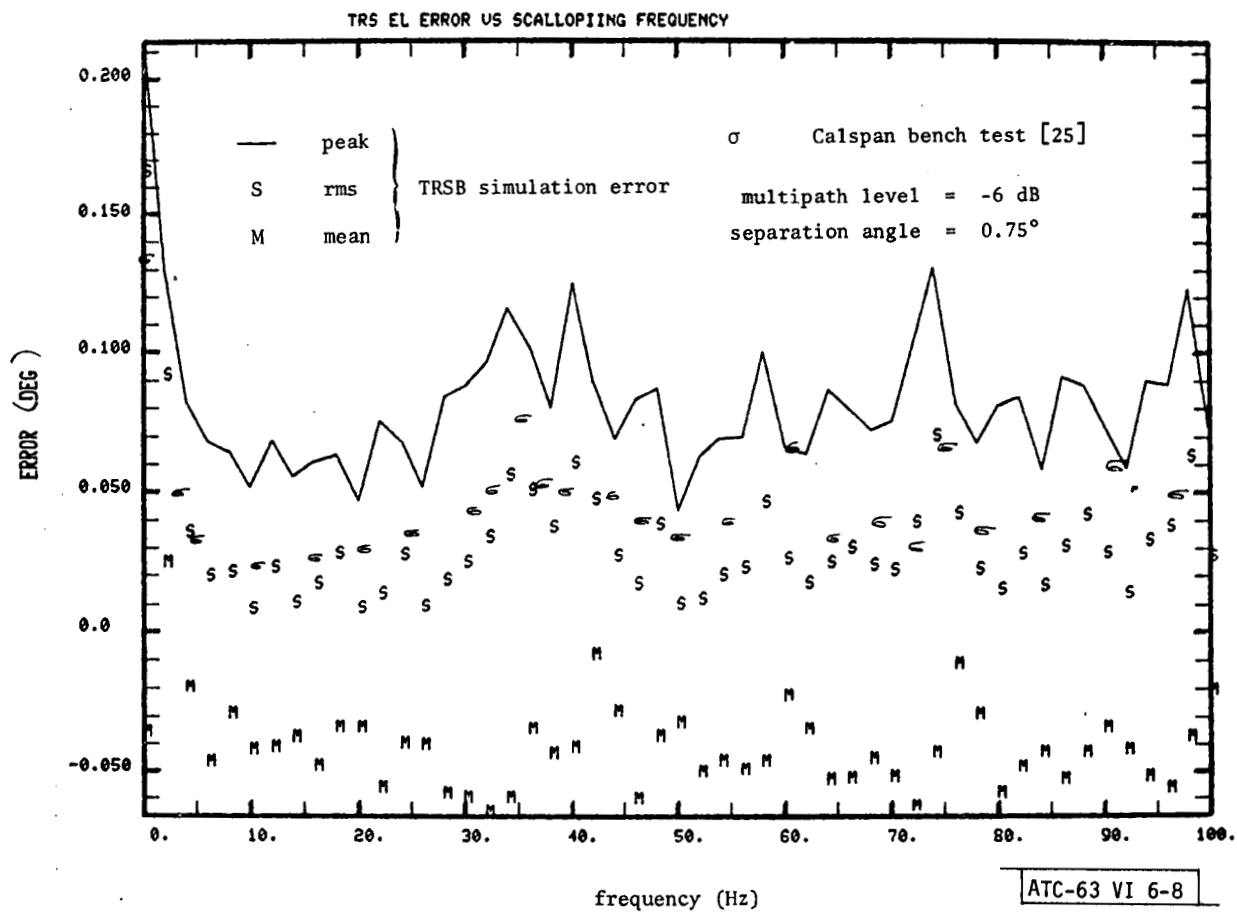Fig. 6-7. TRSB dynamic EL1 error vs separation angle.

Fig. 6-8. TRSB elevation error vs scalloping frequency.

$$\overline{E_m} = \frac{\rho T_s}{\pi T_g} \frac{\sin(M\omega_s T_s)}{2M} \left[\frac{\sin(\pi\theta_m T_g/T_s)\cos(\omega_s T_g/2)\cos\eta_m}{\sin(\omega_s T_s/2)} \right.$$

$$\left. - \frac{[1-\cos(\pi\theta_m T_g/T_s)]\sin(\omega_s T_g/2)\sin\eta_m}{\cos(\omega_s T_s/2)} \right] \qquad (6-4)$$

The notation was defined in Table 6-1.

For the special case of 100% scan gate $(T_g = T_s)$, the last expression is equivalent to Wheeler's multipath error formula[30].

We observe that $\overline{E_m} = 0$ when the multipath angle code equals that of the direct. Furthermore, for small separation angles the error is independent of the ratio T_s/T_g. The peak error is then

$$E_{mp} = \rho\theta_m \quad ; \quad \theta_m \ll 1 \qquad (6-5)$$

which interestingly is identical to that for TRSB in the same situation.

At the grating lobes of the averaging factor, where $\omega_s T_s = m\pi$, m an integer, motion averaging is generally ineffective. However, a special situation arises when the scan gate is 50% of the scan interval. For future reference we note that when $T_g = T_s/2$, the error at the grating lobes is

$$\overline{E_m} = \begin{cases} \dfrac{2\rho}{\pi} \sin(\pi\theta_m/2)\cos(m\pi/4)\cos\eta_m & \text{, m even} \\[3em] -\dfrac{2\rho}{\pi}[\cos(\pi\theta_m/2)-1]\sin(m\pi/4)\sin\eta_m, & \text{m odd} \end{cases} \qquad (6-6)$$

In particular $\overline{E_m} = 0$ at $\omega_s T_s = 2\pi$.

6.3.2 Static Tests

Using the ITT/G version of the Doppler system simulation, a plot (Fig. 6-9) of error vs multipath phase was generated for three multipath amplitudes at a fixed separation angle of 1.5°. The theoretical behavior from Eq. 6-4 ($\omega_s=0$) is a simple sinewave E_m vs ϕ_m, the midscan phase:

$$\phi_m = \phi_i + \pi\theta_m \qquad (6-7)$$

The figure shows simulation results for a value $\theta_m = 0.5°$ and amplitudes -3 dB, -6 dB and -10 dB without multipath rejection filter. A theoretical curve is given for -10 dB only. Deviation from a sinewave is more pronounced at higher amplitudes due to the decreasing validity of the linearized theory. Although the simulation curves become progressively more asymmetrical as the amplitude increases, the mean value remains zero. Figure 6-10 shows error vs phase when the multipath rejection filter whose characteristics are depicted in Fig. 6-11 is used; again, the separation angle is 1.5°.

A series of computer simulations were run to duplicate the conditions of Calspan tests on a Doppler receiver. The appropriate theoretical curve of error vs separation angle was calculated from Eq. 6-4 and plotted along with the simulation error and the experimental results. The three sets of data in Figs. 6-12 and 6-13 are in excellent agreement, considering the potential sources of discrepancy, such as experimental error and model inaccuracies.

Figure 6-14 illustrates the EL-1 error vs separation angle for separations up to 3°. The direct signal is at 3° elevation and the multipath is between 0° and 3°. Peak, mean, and standard deviation error for the simulation are
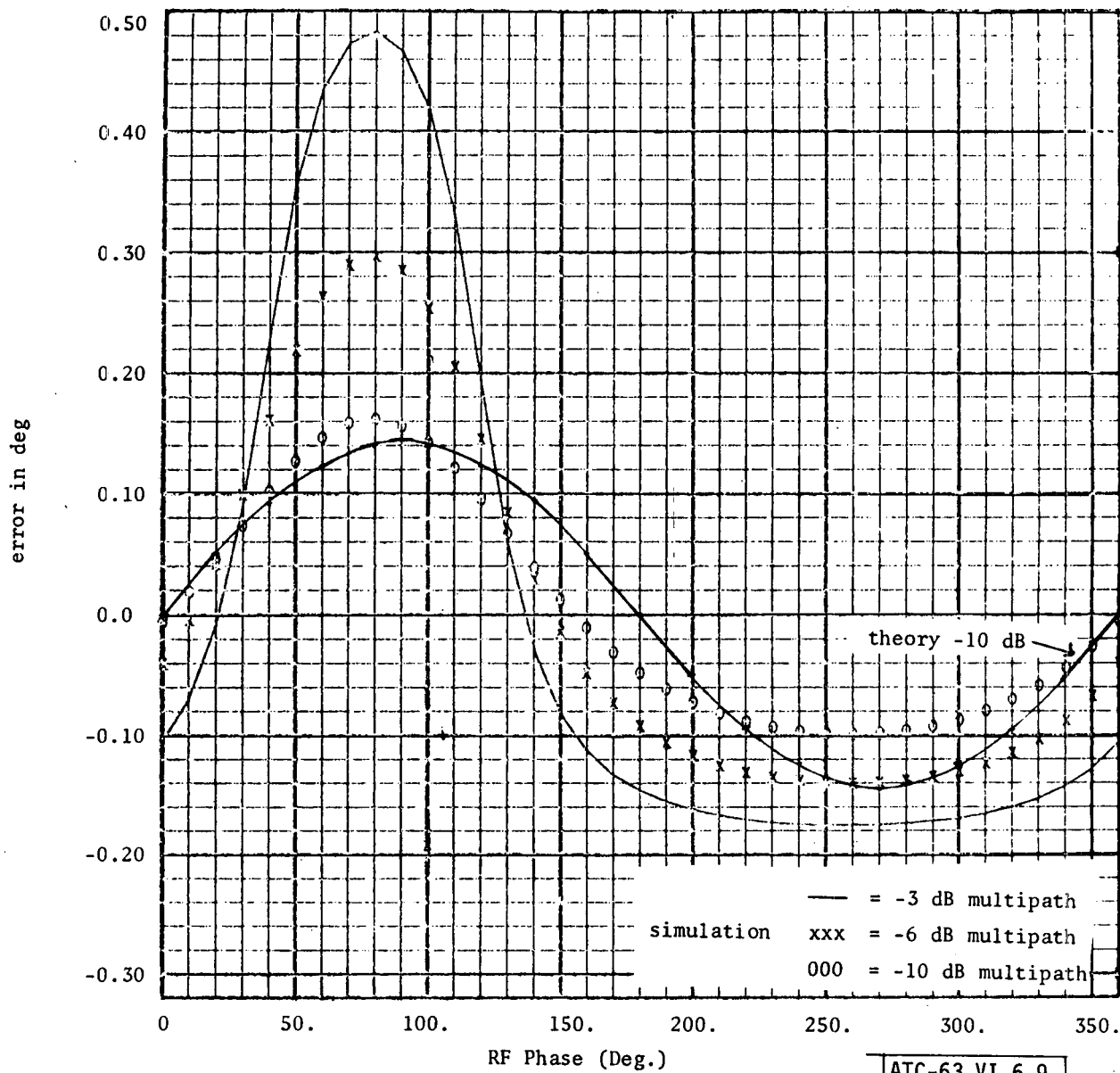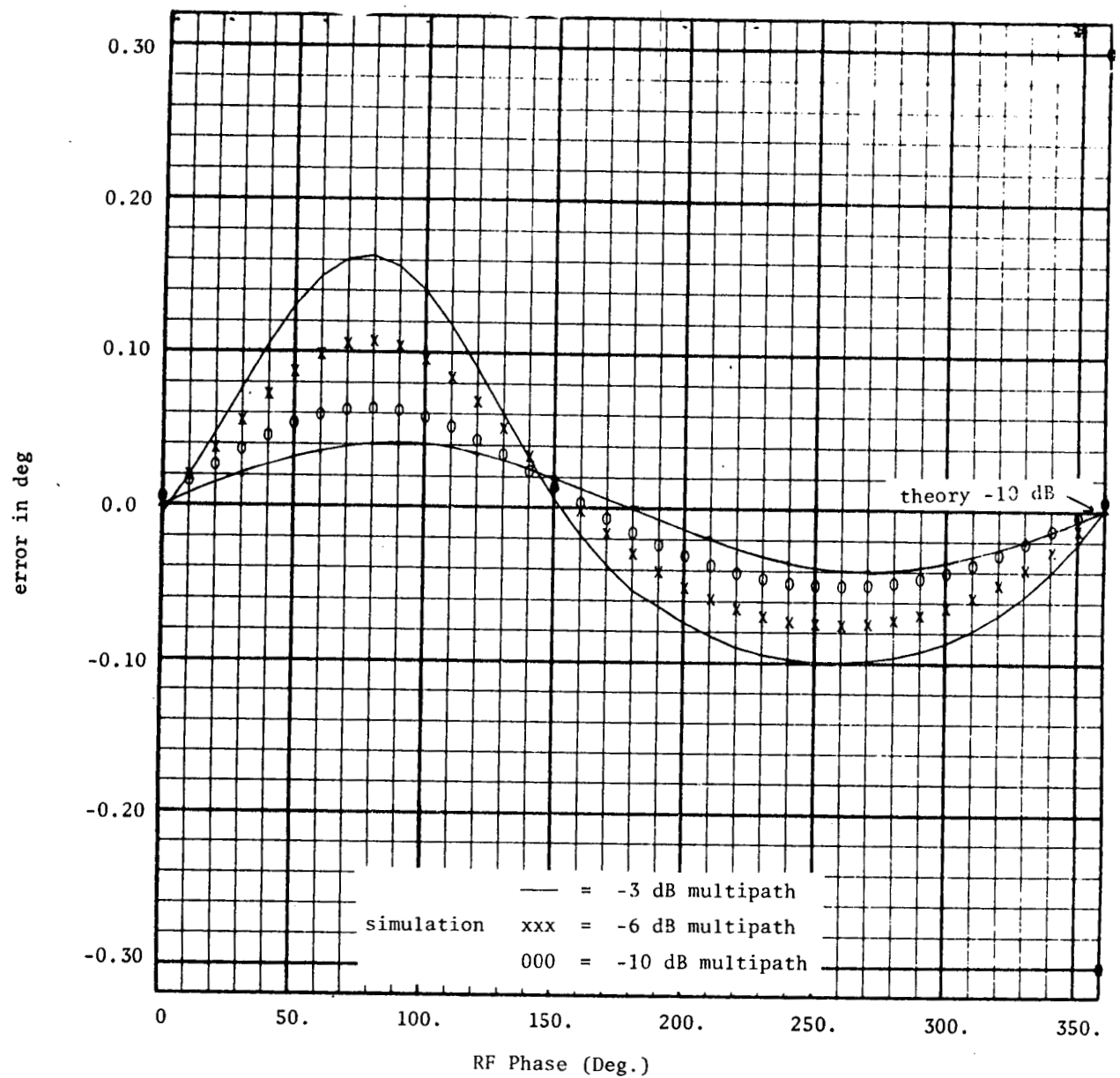
Fig. 6-9. Error vs RF phase, Doppler system without filter, separation angle = 1.5°.

Fig. 6-10. Error vs RF phase, Doppler system with elevation filter, separation angle = 1.5°.
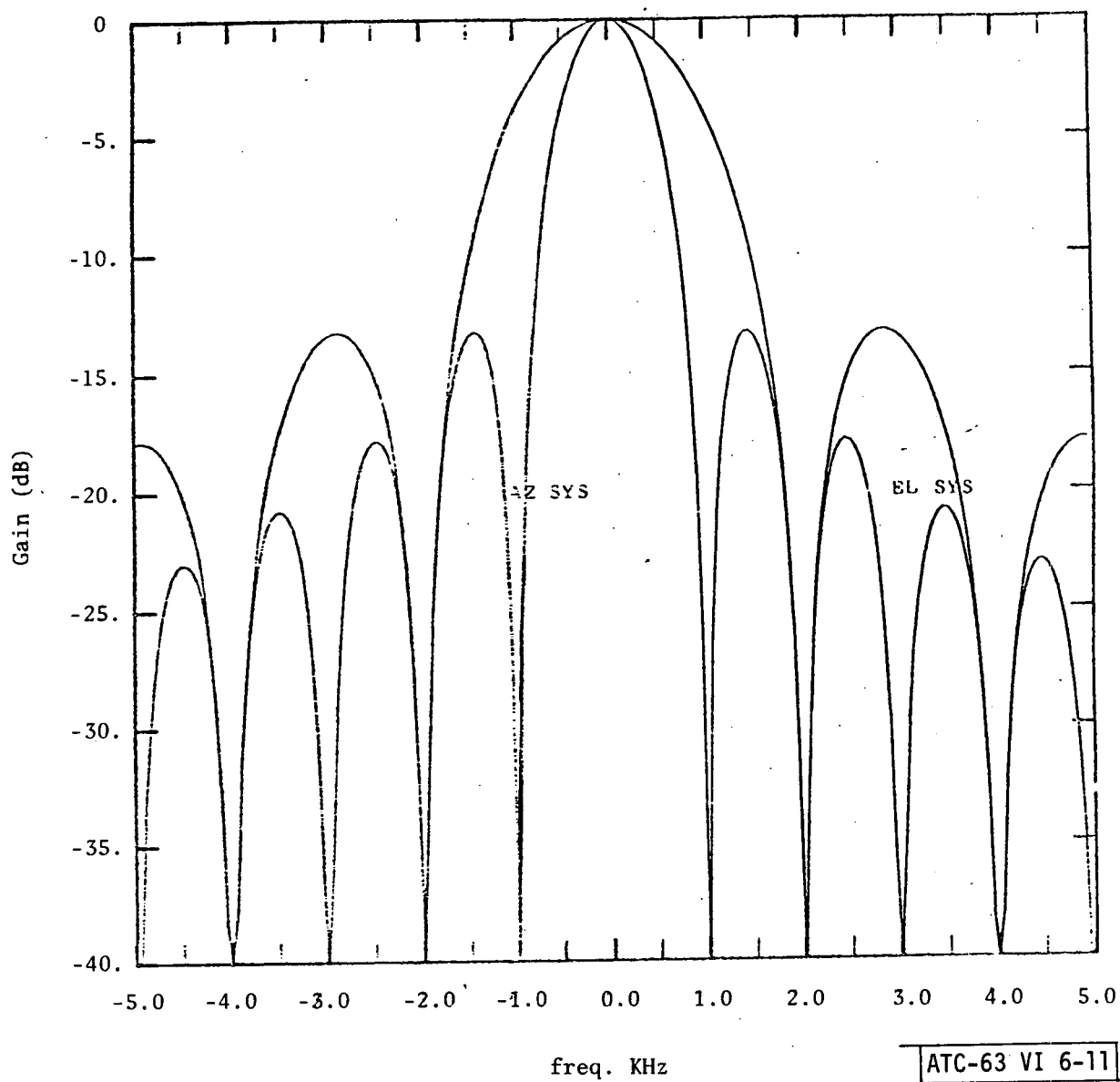
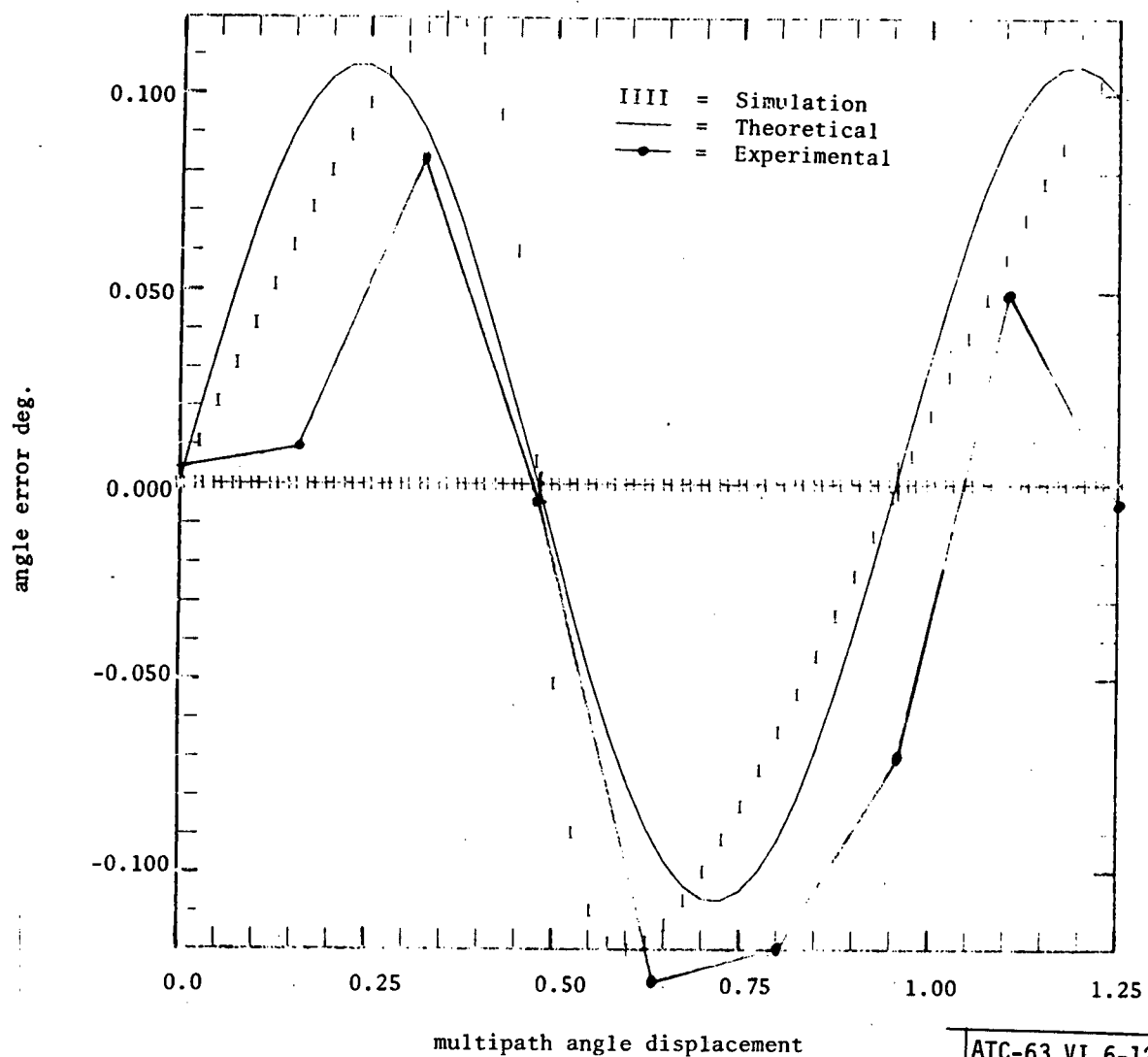Fig. 6-11. ITT/G angle system multipath rejection filter characteristics.

Fig. 6-12. Error vs separation angle, Doppler system without filter, multipath amplitude -6 dB. Initial phase = 0°.
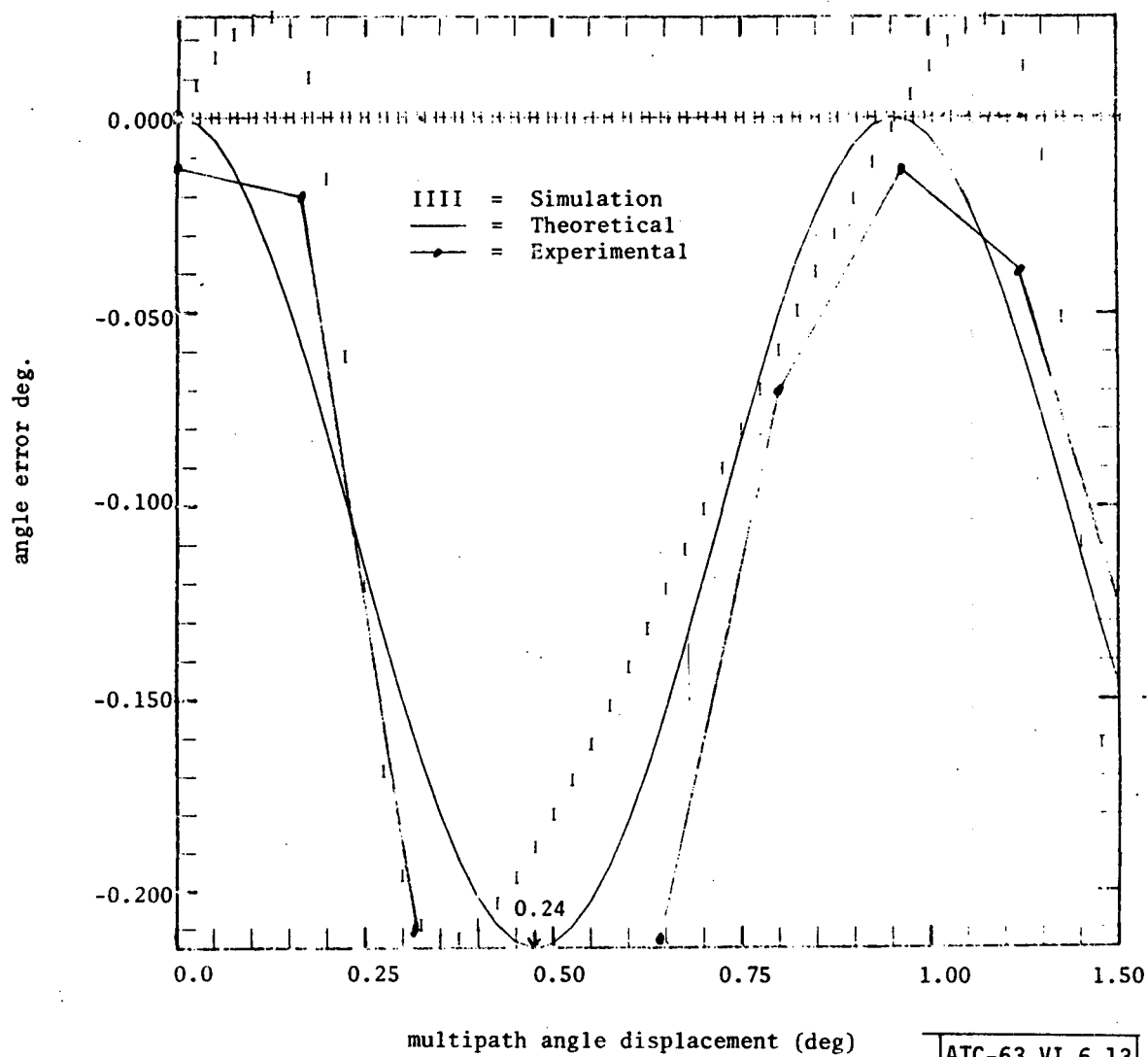
Fig. 6-13. Error vs separation angle, Doppler system without filter, multipath amplitude -6 dB. Initial phase = 90°.
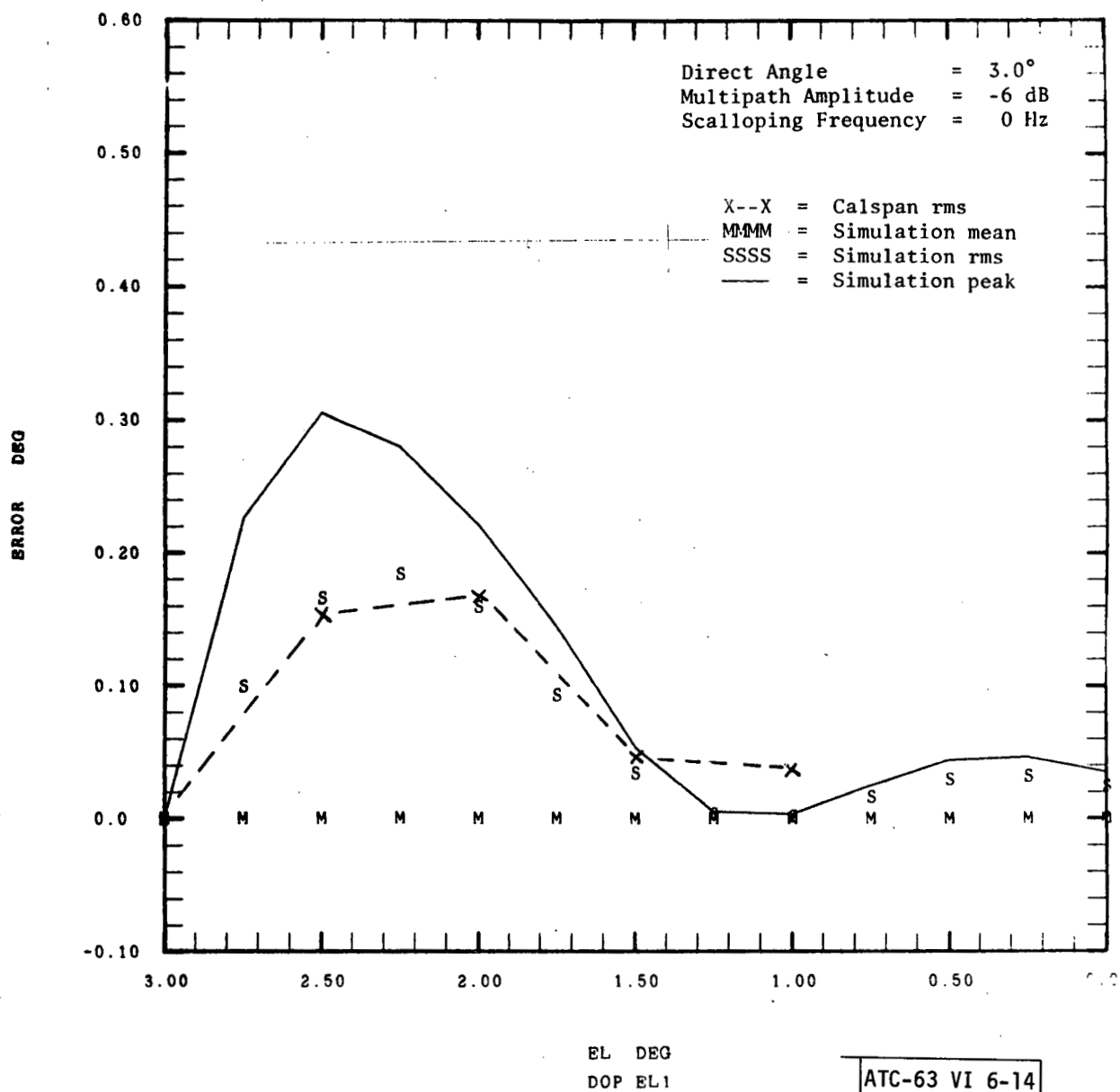
ATC-63 VI 6-13

Fig. 6-14. ITT/G EL1 error vs multipath elevation with multipath rejection filter.

shown. The Calspan measurements are rms error. The agreement is quite good, except for the unexplained slight discrepancy at 2° separation. The small multipath theory indicates that the 50% scan gating used in the simulation should drive the error to zero at 2 (i.e., T_s/T_g) beamwidths, which is what is observed. The Calspan data, which is also stated to have 50% scan gating, is small but nonzero at 2° separation.

6.3.3 Dynamic Tests

Two types of tests were run for the Doppler system. One is simply measurement error vs scalloping frequency for a given set of conditions specified by amplitude, separation angle, and multipath phase. Two sets of this type are shown in Figs. 6-15 and 6-16. The theoretical (solid) line is from Eq. (6-4) with $\eta_m=0$ and $\cos(\omega_s T_s/2) \approx 1$. The parameters were chosen to resemble corresponding Calspan tests, but direct comparison is not possible because the scan timings are not equivalent. Nevertheless, the peak values at the grating lobes, including 0 Hz, may be compared. These are summarized in Table 6-3.

TABLE 6-3
PEAK DOPPLER ERROR VS SCALLOPING FREQUENCY

Scalloping Freq. (Hz)	Simulation	Theory	Calspan
0	±0.145	±0.132	-0.15, +0.17
250		±0.276	-0.27, +0.25
500	±0.145	±0.132	-0.16, +0.17
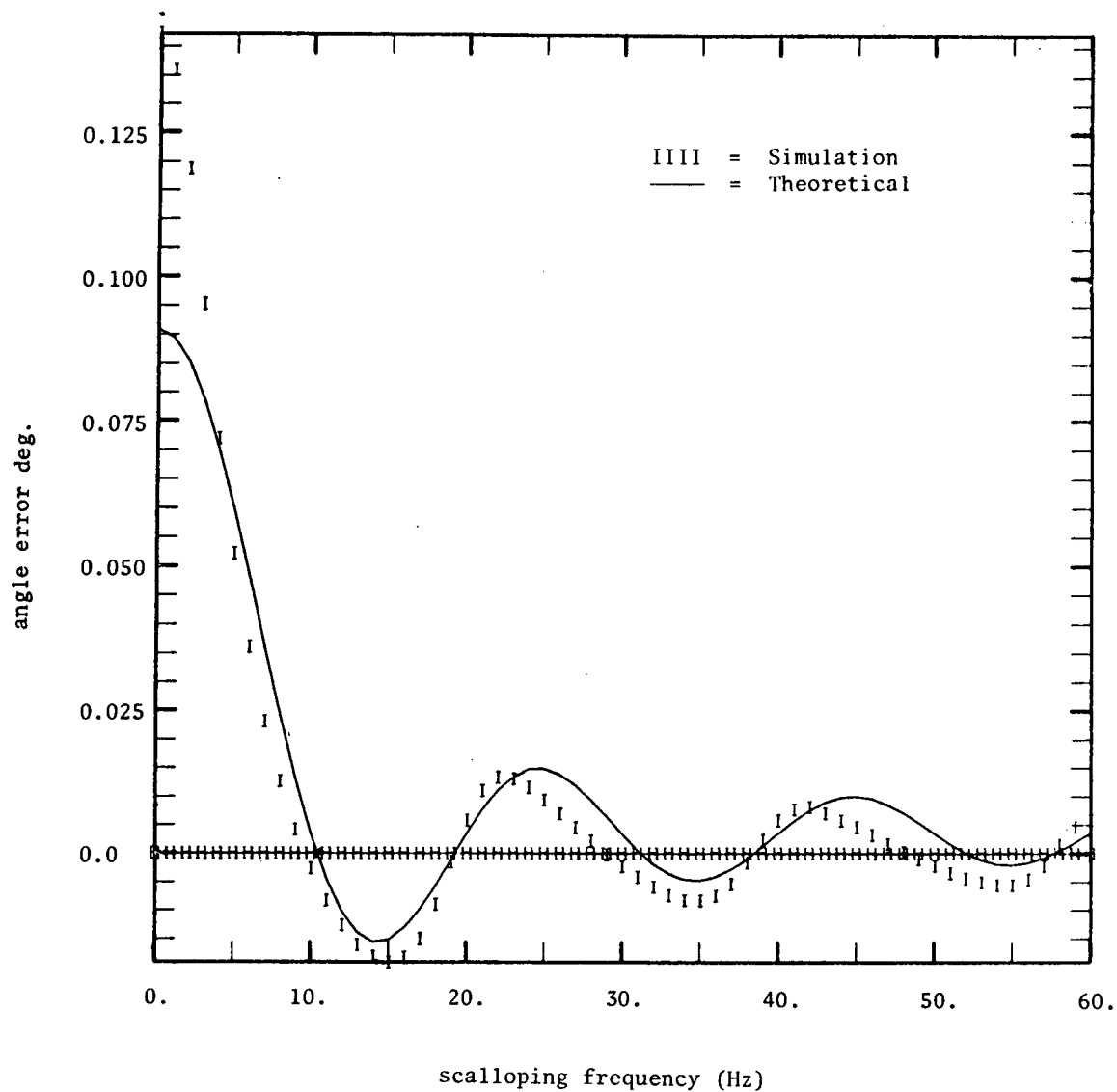
Fig. 6-15. Error vs scalloping frequency, Doppler system without filter, multipath amplitude -6 dB, separation angle 0.76°, phase -143.3°.
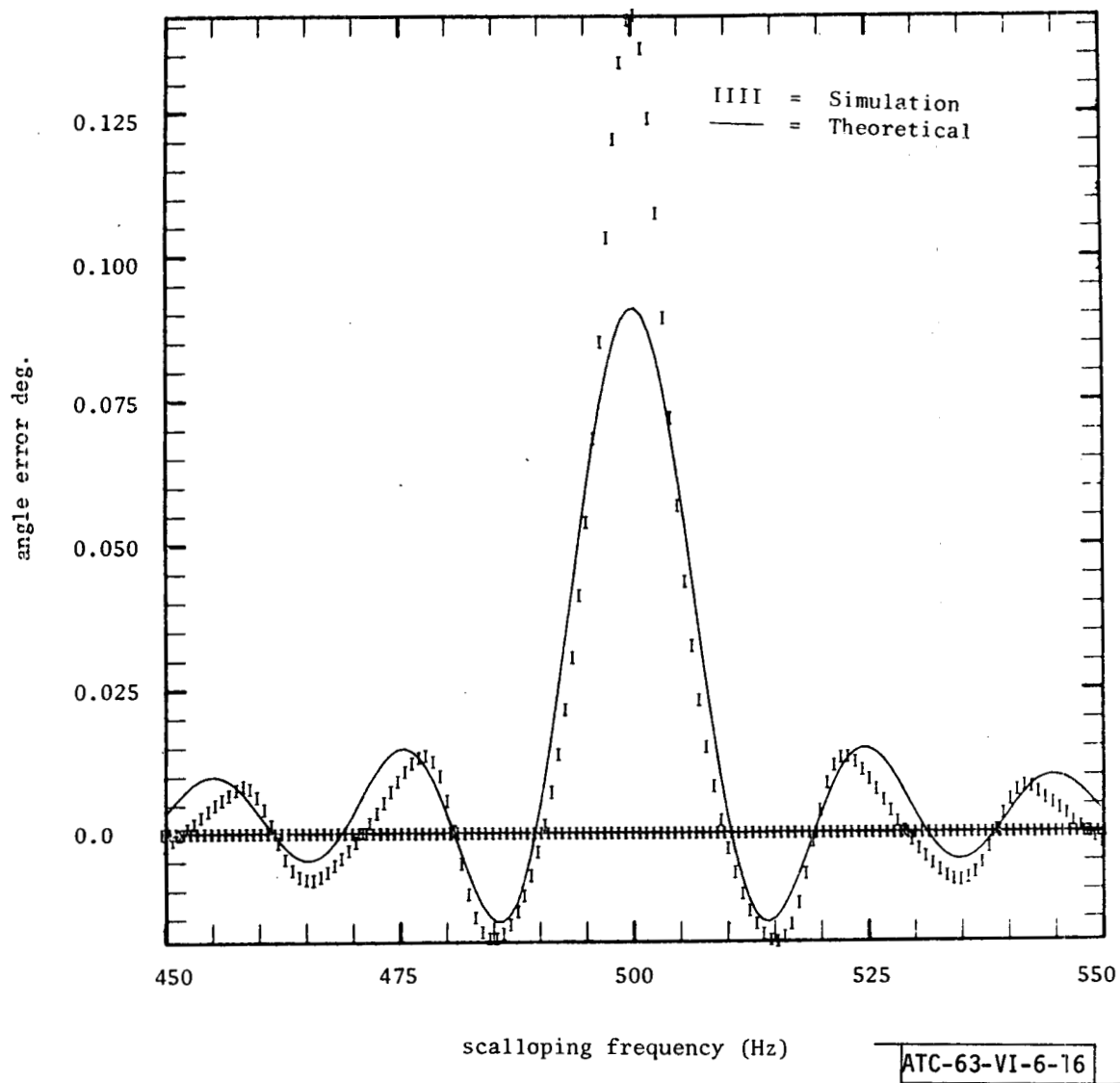
Fig. 6-16. Error vs scalloping frequency, Doppler system without filter, multipath amplitude -6 dB, separation angle 0.76°, phase -143.3°.

The agreement between simulation, theory, and bench tests is considered quite good.

Figure 6-17 shows the results of a dynamic test at a scalloping frequency of 103 Hz. This frequency is not near any grating lobe of the averaging factor and is, therefore, a case in which motion averaging should be effective. The graph shows that it is, with error reduction by at least a factor of 10. The actual improvement depends on the fine structure of the averaging factor near 103 Hz. The Calspan data exceeds the simulation data by about a factor of two, but the dependence on separation angle is qualitatively similar. No explanation has been found for why Calspan shows non-zero rms error at 0° separation.

The next dynamic test (Fig. 6-18) is at 480 Hz, which is the first grating lobe of the averaging factor ($1/2T_s$, where T_s = 1.04 msec). Again, good agreement is found, except at 0° separation. Both experimental and simulation data exhibit a bimodal error curve in which there are two local maxima. No particular reason for this behavior is known, but the correspondence is quite close. The error levels are similar to the static results, indicating little motion averaging.

Elevation error vs scalloping frequency is shown in Fig. 6-19 for 1° separation and -3 dB multipath. In this case, the Calspan data is one half the peak-to-peak error, which corresponds to the simulation peak error curve. The agreement at the Calspan data points is excellent. Simulation shows a minor lobe centered at the grating lobe subharmonic of 240 Hz, but unfortunately Calspan took no corresponding data.
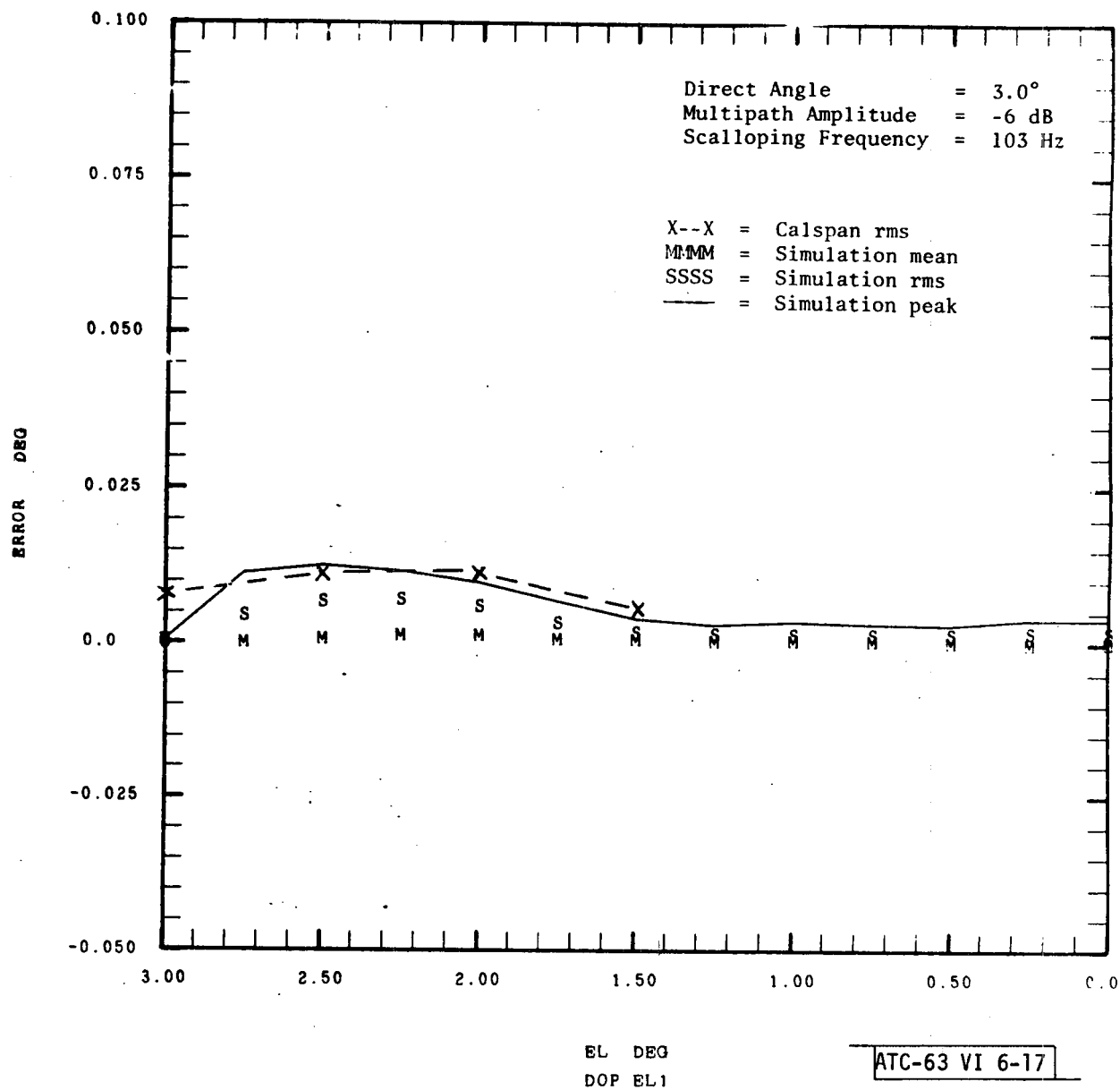
6-29

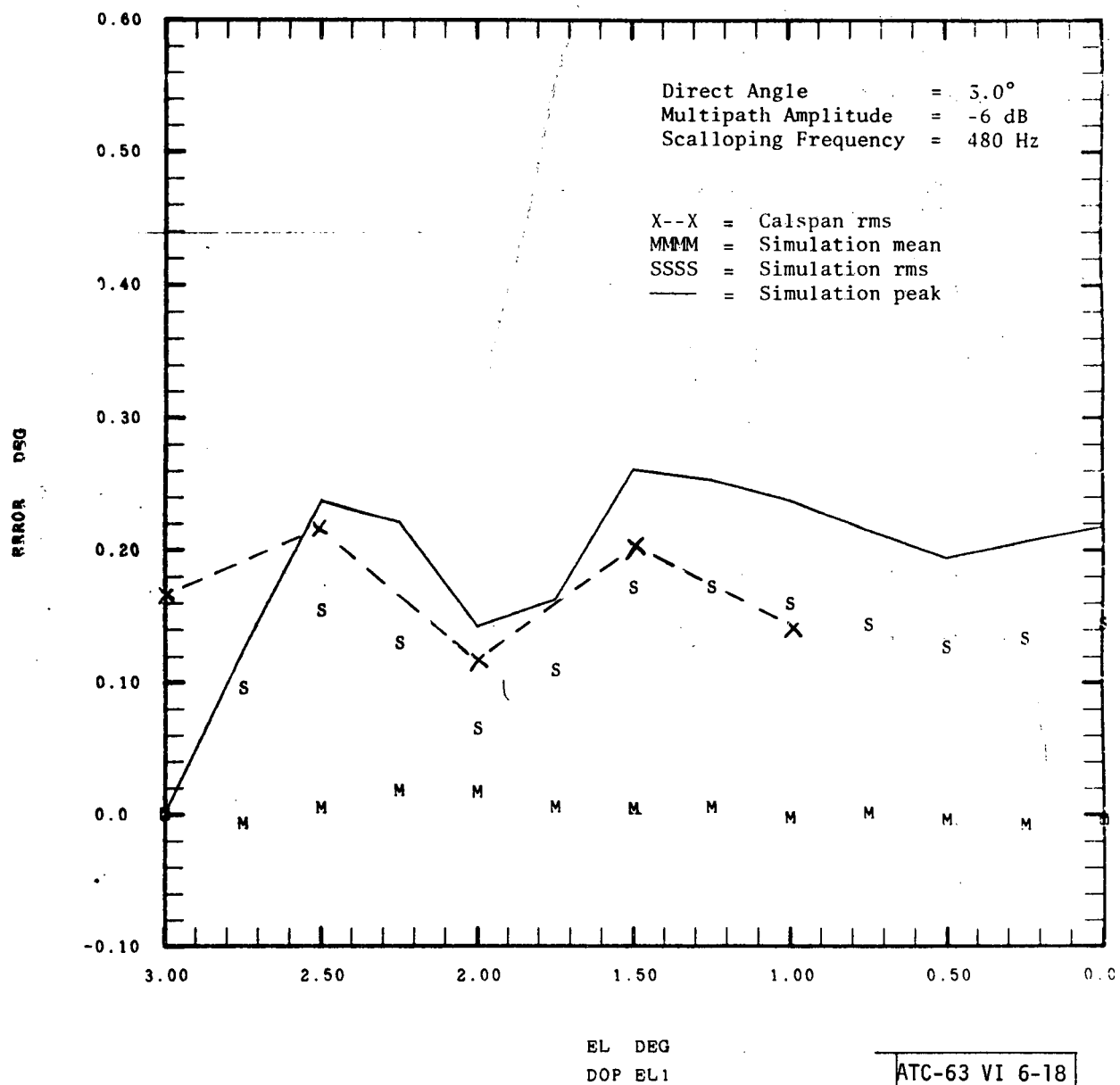Fig. 6-17. ITT/G EL1 error vs multipath elevation.

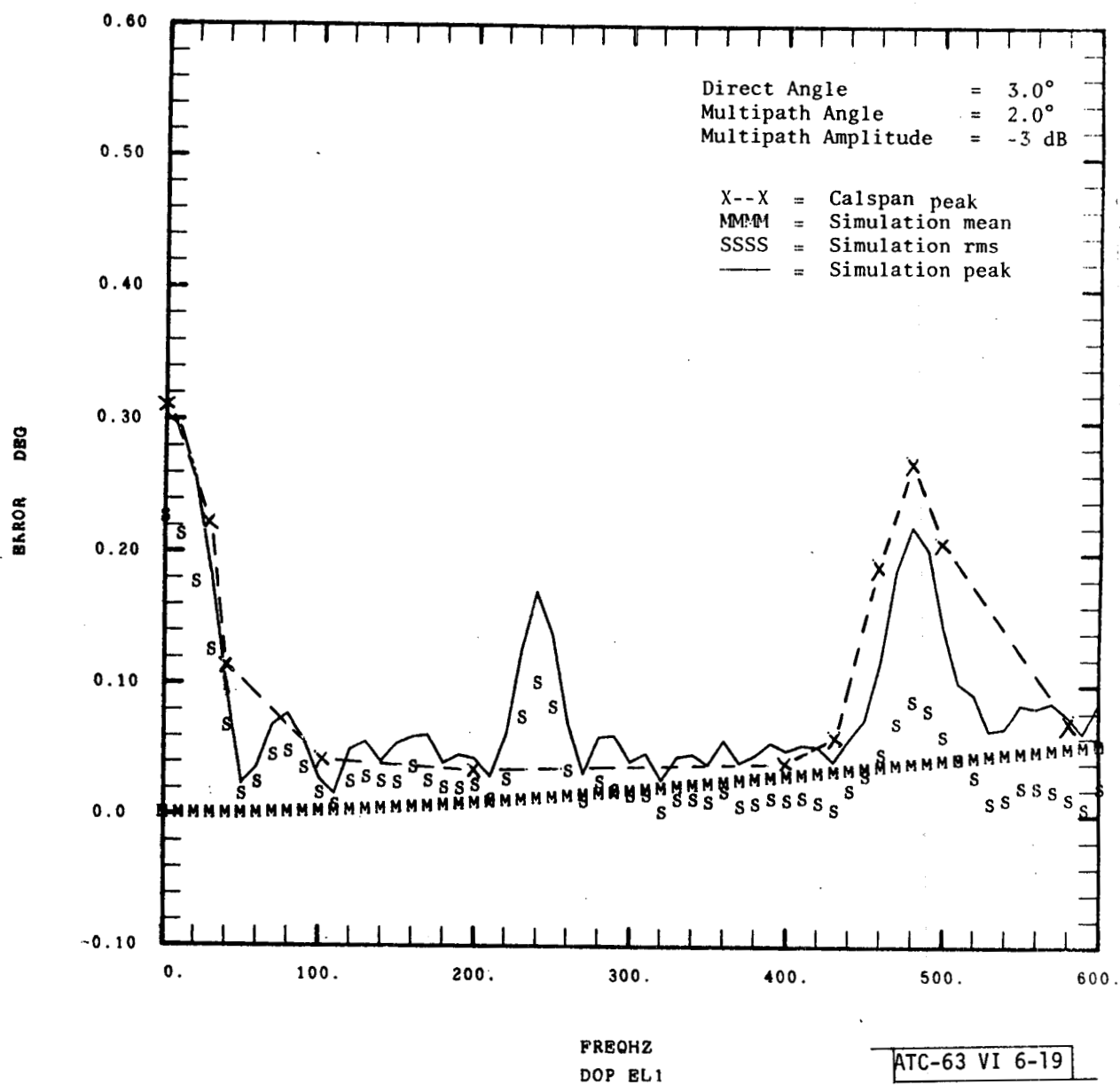Fig. 6-18. ITT/G EL1 error vs multipath elevation.

Fig. 6-19. ITT/G EL1 error vs multipath scalloping frequency.

Similar tests were run for the ITT/G AZ system and the Hazeltine EL-1 and AZ, resulting in data of comparable validity.

6.4 DME Validation

Validation of the DME models is a more difficult task than is angle receiver validation. The major difficulty is the lack of an experimental data base against which to compare model outputs. During Phase II, the MLS contractors performed tests of their C-band DME units, but the results are largely inconclusive because the scenarios were designed for AZ system multipath, not DME. Additionally, there is the more recent complication arising from the intent to propose L-band DME to ICAO. This decision has generated interest in new signal formats and processing techniques.

In view of the deficit in experimental data, the validation must be accomplished by comparing the model outputs to theoretical calculations. As was done for the angle systems, approximate formulas have been derived for the single multipath component performance of various DME's. Results are shown in this section for Gaussian and trapezoidal pulses and the three processors described in Section 4.4.

6.4.1 Multipath Error Formulas

The following formulas have been derived for the single multipath component performance of the indicated DME's. They are approximations which are valid for small-to-moderate multipath levels ($\rho \leq$ -10 dB). The pulse and processor parameters appearing in them are all defined in Sections 4.4.1 and 4.4.3. These formulas are used in any of the subsequent comparisons.

Gaussian Pulse:

Fixed Threshold:

$$\varepsilon_{fix} = -\frac{\rho t_r}{2\beta v}\, e^{-\beta(\frac{\tau}{t_r})(\frac{\tau}{t_r} + 2v)} \cos\phi$$

Real Time Threshold:

$$\varepsilon_{rt} = \rho\,\tau\, e^{-\beta(\frac{\tau}{t_r})(\frac{\tau}{t_r} + v)} \left[\frac{\sinh(\frac{\beta v\tau}{t_r})}{\frac{\beta v\tau}{t_r}}\right] \cos\phi$$

Delay and Compare:

$$\varepsilon_{dc} = \rho\,\tau\, e^{-\beta(\frac{\tau}{t_r})(\frac{\tau}{t_r} + 2v + \frac{\tau_d}{t_r})} \left[\frac{\sinh(\frac{\beta\tau_d\tau}{t_r^2})}{\frac{\beta\tau_d\tau}{t_r^2}}\right] \cos\phi$$

Trapezoidal Pulse:

Fixed Threshold:

$$\varepsilon_{fix} = \begin{cases} -\rho(\alpha t_r - \tau)\cos\phi : & \tau \le \alpha\, t_r \\[2ex] 0 & : \tau > \alpha\, t_r \end{cases}$$
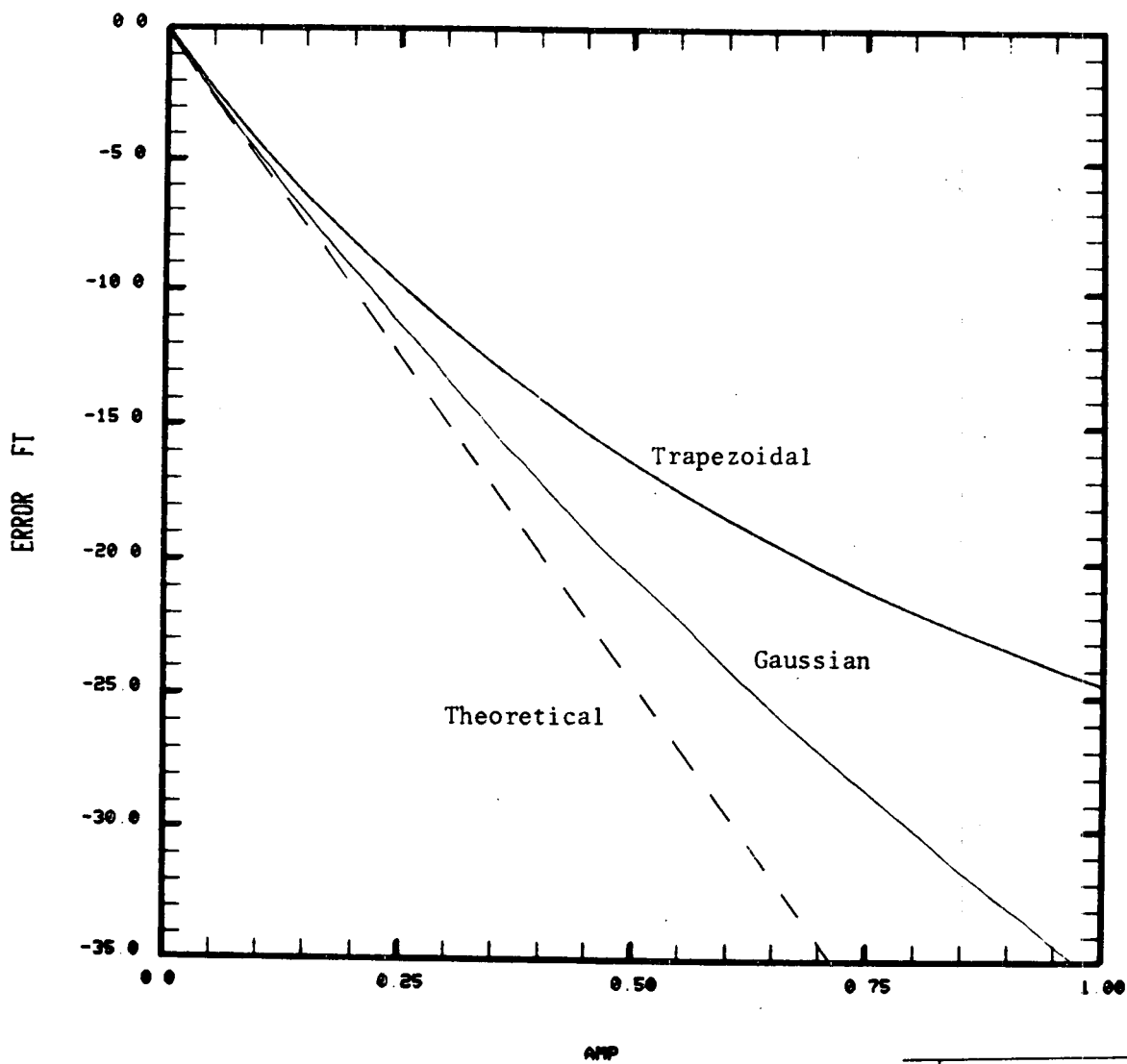
Real Time Threshold:

$$
\varepsilon_{rt} = \begin{cases} \rho\,\tau\,\cos\phi \; ; & \tau \le \alpha\,t_r \\[2em] \rho\,\alpha\,t_r\,\cos\phi \; ; & \tau > \alpha\,t_r \end{cases}
$$

Delay and Compare:

$$
\varepsilon_{dc} = \begin{cases} \rho\,\tau\,\cos\phi & ; \; 0 \le \tau \le \alpha t_r - \tau_d \\[1.5em] \rho\left(\dfrac{\alpha\,t_r}{\tau_d} - 1\right)\left(\alpha\,t_r - \tau\right)\cos\phi & ; \; \alpha t_r - \tau_d \le \tau \le \alpha t_r \\[1.5em] 0 & ; \; \tau > \alpha t_r \end{cases}
$$

6.4.2 Error vs Amplitude

Each of the preceding error formulas shows error directly proportional to multipath amplitude (ρ). The computed errors when plotted against ρ generally have the same slope at $\rho = 0$ as the error formula, but then the error increases slightly slower than linearly. Figures 6-20, 6-21 and 6-22 show comparisons of theoretical and computed errors, each for a different processor. For this comparison the parameters have been chosen to make the initial error slope identical (except for algebraic sign) in all cases; near $\rho = 0$, the error magnitude varies as 50ρ nsec. As ρ approaches 1, the linear approximation overestimates the error by about a factor of 2.

6-35

Fig. 6-20. DME error vs multipath amplitude-fixed thresholding.
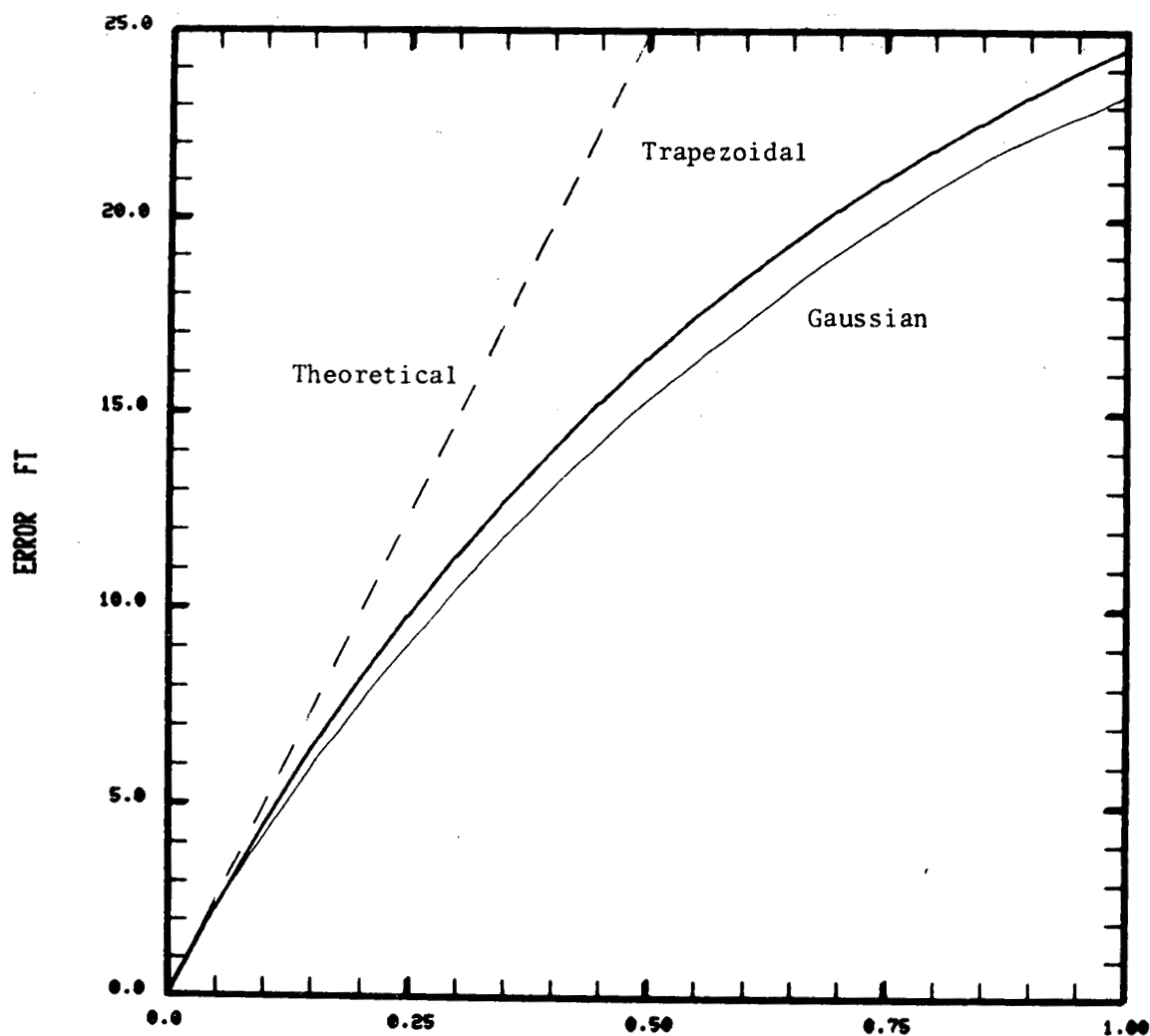
Fig. 6-21. DME error vs multipath amplitude - real time thresholding.
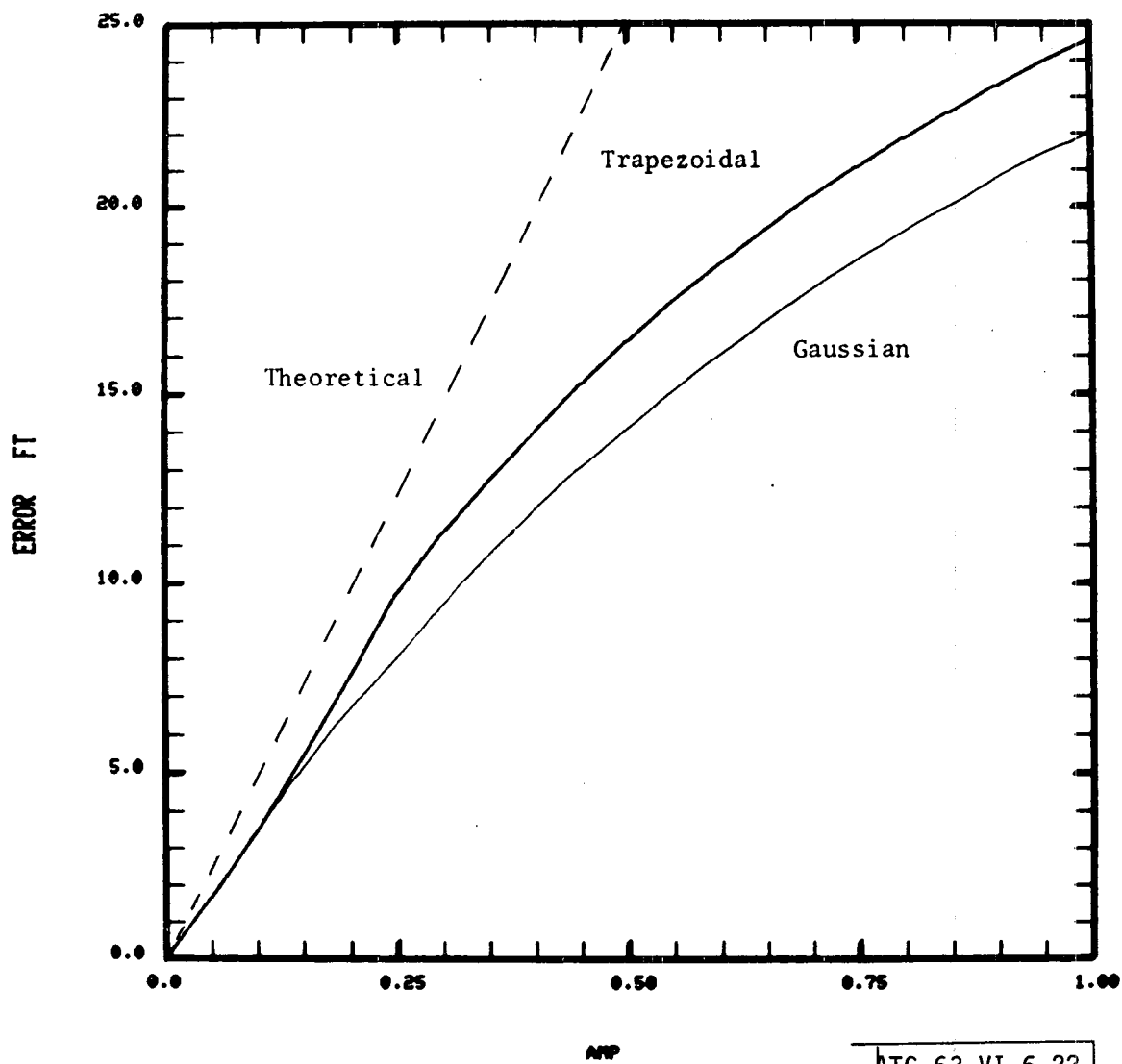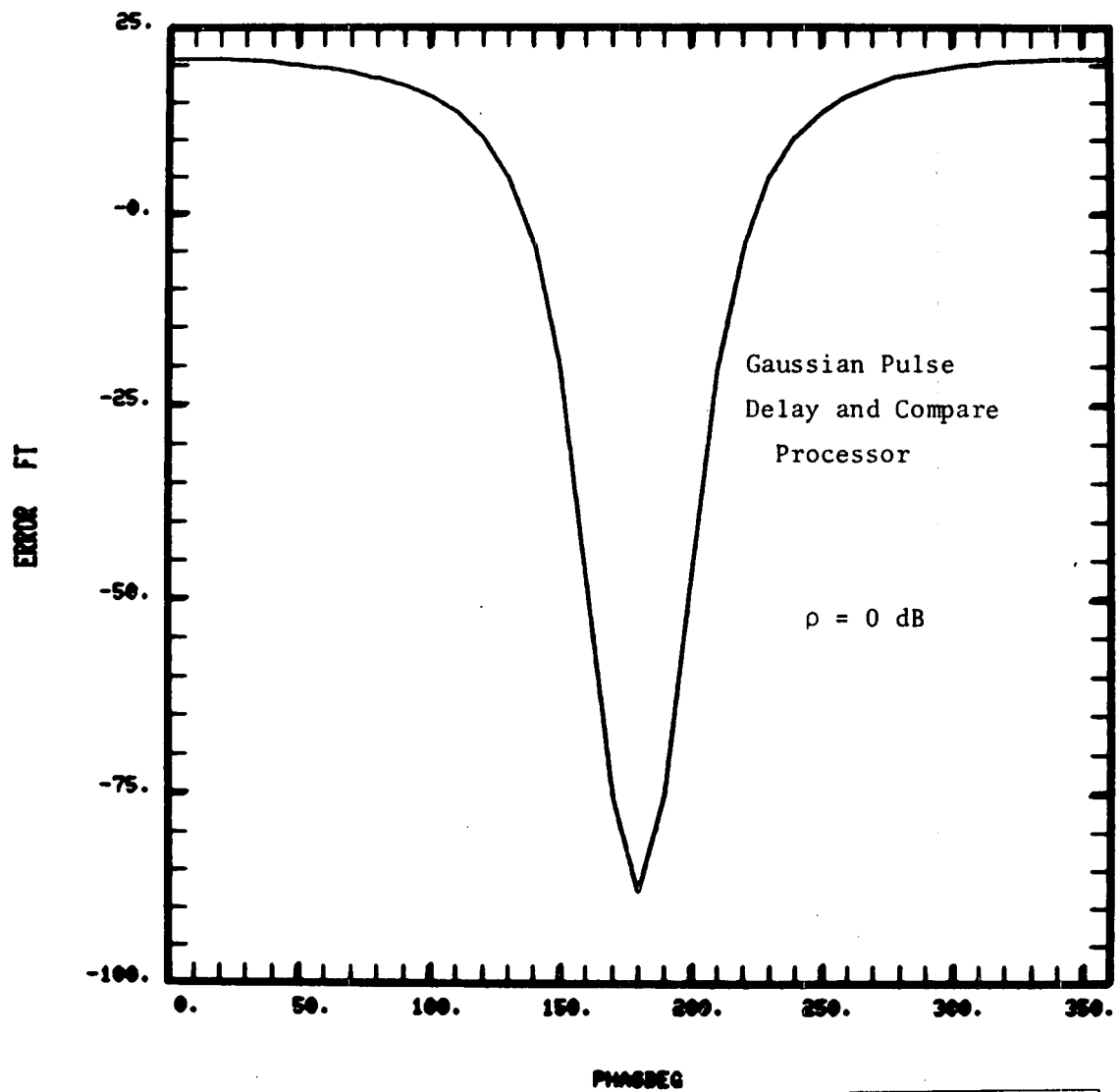
Fig. 6-22. DME error vs multipath amplitude - delay and compare.

6.4.3 Error vs Phase

The error formulas predict that the DME error should vary cosinusoidally with rf phase difference. At small enough multipath levels this is nearly true, but for larger values of ρ the behavior is quite different, as Fig. 6-23 shows. It contains a plot of error vs phase for real time thresholding of a Gaussian pulse and 0 dB multipath level. The largest error magnitude occurs at 180° phase. For phase angles more than 30° away from 180°, the error reaches a plateau. Figure 6-24 shows similar curves for smaller values of ρ. In all cases, however, averaged over 360° there is little bias in the error (theory shows that bias varies in proportion to ρ^2). This situation is analogous to error vs phase in Doppler scan angle systems. Figure 6-25 shows the corresponding data for a trapezoidal pulse.

6.4.4 Error vs Delay

Figures 6-26 and 6-27 contain curves of error vs time delay for Gaussian and trapezoidal pulses, respectively. Each graph contains three curves -- simulated mean error, simulated standard deviation error, and theoretical standard deviation error. The simulation data is obtained by averaging the error over 24 uniformly spaced values of relative phase (15° increments). The theoretical standard deviation is the error formula evaluated at $\cos \phi = 1/\sqrt{2}$, the rms value of the sinusoidal phase term. In each case the multipath level is -10 dB, and the agreement in the standard deviation curves is good. The simple theory generally predicts unbiased estimates, which is what the computed means indicate.

Fig. 6-23. DME error vs multipath phase - large amplitude.
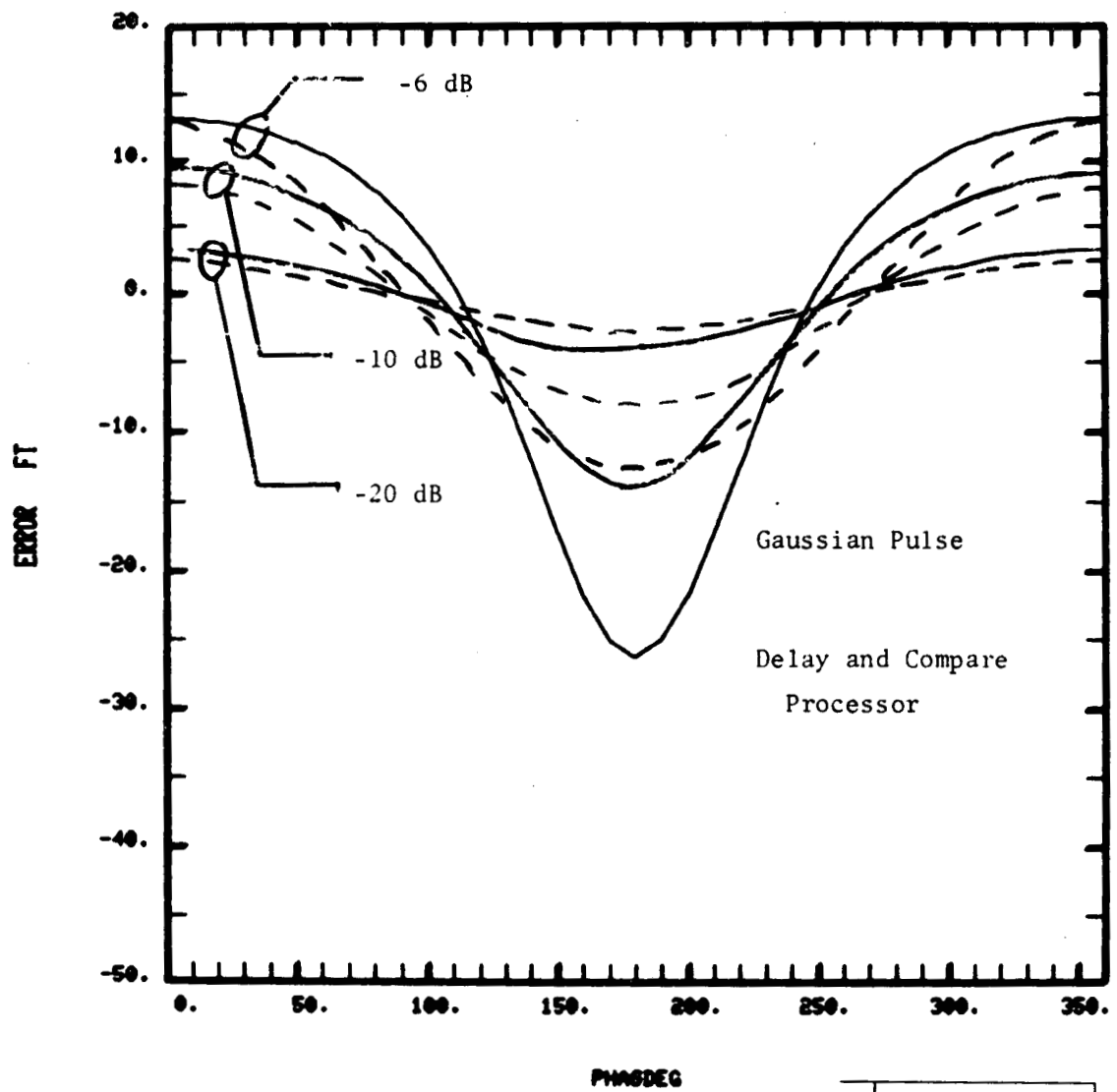
Fig. 6-24. DME error vs multipath phase - small amplitude.

Fig. 6-25.   DME error vs multipath phase.

Fig. 6-26. DME error vs multipath time delay: comparison of simulation and theory for Gaussian pulse.

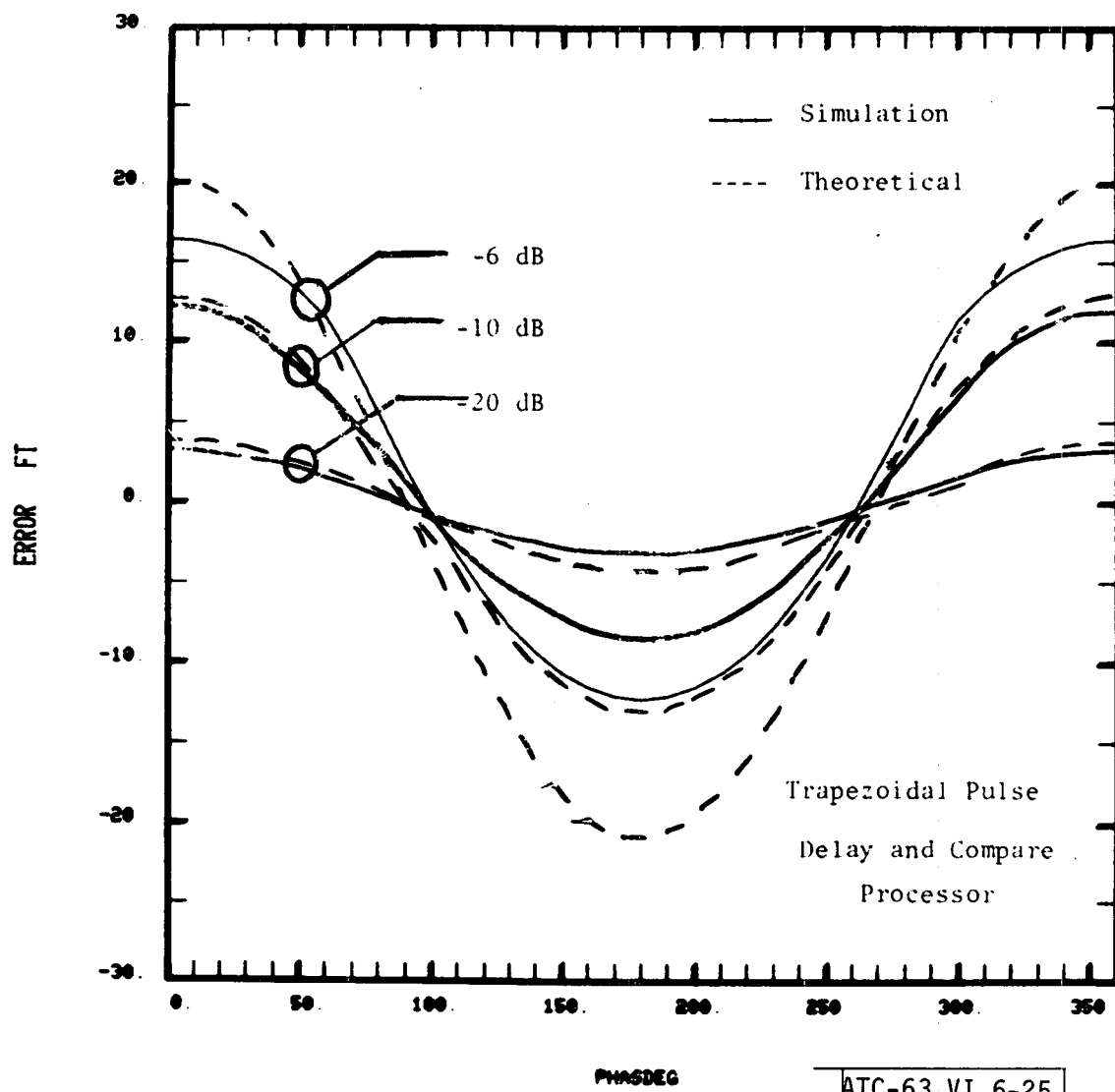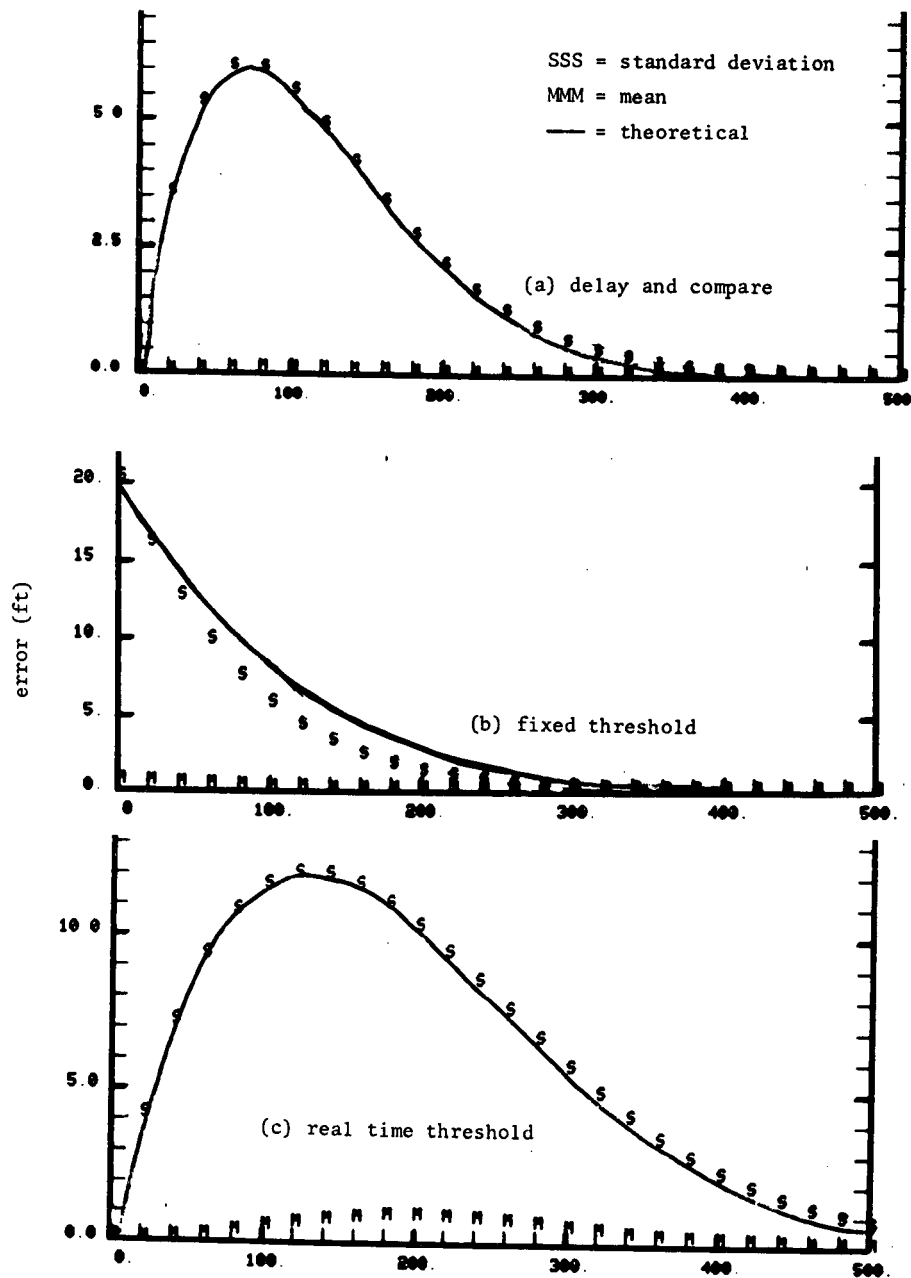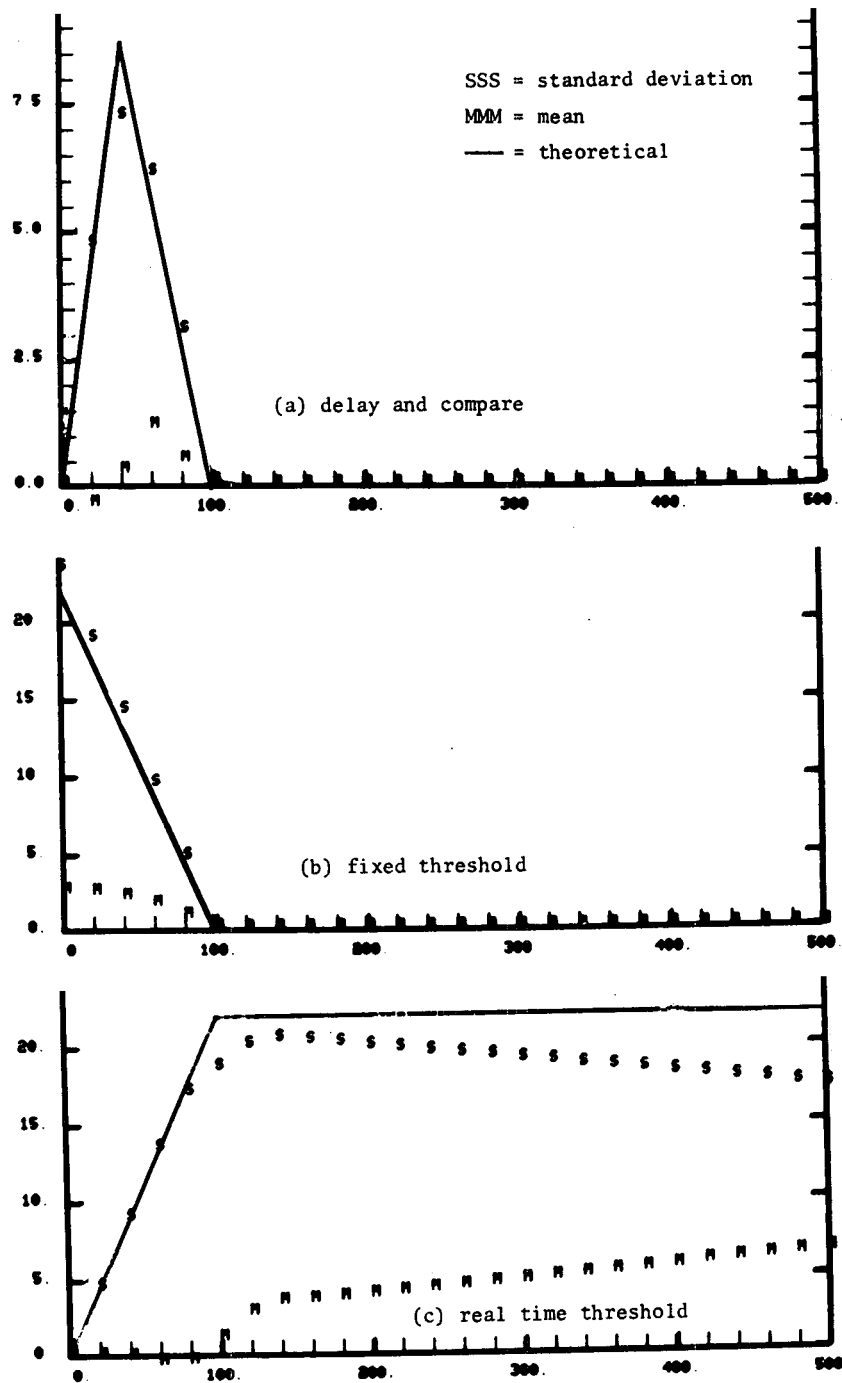Fig. 6-27. DME error vs multipath time delay: comparison of simulation and theory for trapezoidal pulse.

6.5   Complete Simulation Runs

The simulation data presented in the preceding sections was derived from special test programs that exercised the receiver routines. In order to validate the angle receivers while imbedded in the complete simulation program, simple scenarios were run using the multipath scattering model applied to selected airport configurations. The results of two such scenarios are described.

6.5.1   EL-1 and Logan International Terminal

In this configuration the EL-1 site is placed between two taxiways on the side of runway 15R opposite the present location of the ILS glideslope as shown in Fig. 6-28.[*] Such a placement is not unreasonable since the two systems may co-exist for a period of time. The major source of reflection for EL-1 signals is the International Terminal situated beside the runway.

The simulation flew an aircraft down the extended runway centerline on a 1:20 (2.86°) glideslope. To account for the 10-ft high phase center of the EL-1 array, the antenna is located 200 ft in front of the GPIP.[†] As a function of altitude along the flight path, a computer output plot gives the amplitude of the building reflection and the multipath separation angle as shown in Fig. 6-29.

Two points along the flight path are of particular interest. One is the point of maximum amplitude (-6 dB) which occurs at altitude 176 ft. The scalloping frequency at this point is 91 Hz assuming an aircraft speed of 200 ft/sec.

---

[*]A map of Logan Airport was shown in Fig. 3-2.

[†]Glide Path Intercept Point.
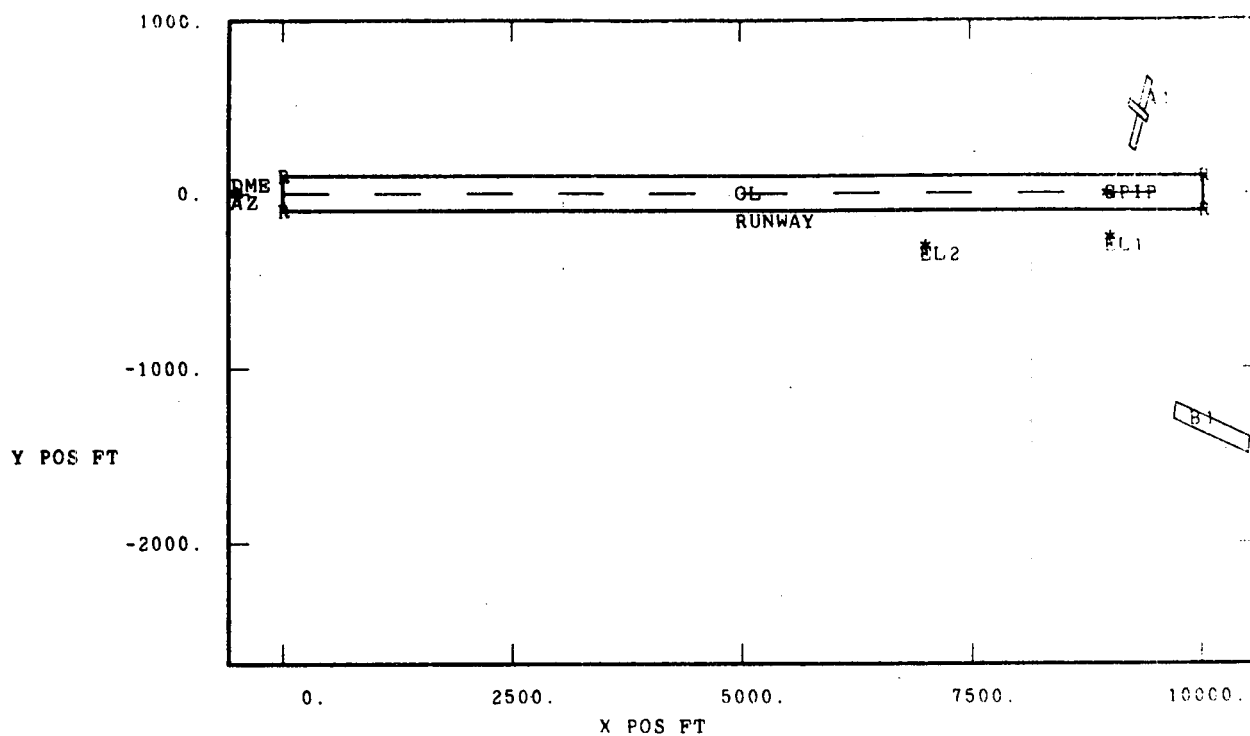
A1 = Aircraft 1
B1 = Building 1
*DME = DME site
*AZ = AZ site
*EL1 = EL1 site
*EL2 = EL2 site
*GPIP = Glide path intercept point
CL = Centerline

ATC-63 VI 6-28

Fig. 6-28. Airport map, Logan scenario.

Fig. 6-29. Relative amplitude and separation angle of multipath signals for Logan scenario.

The other point produces a scalloping frequency of 40 Hz, a TRSB grating lobe,[*] at an altitude of 280 ft. The amplitude of this reflection is -15 dB.
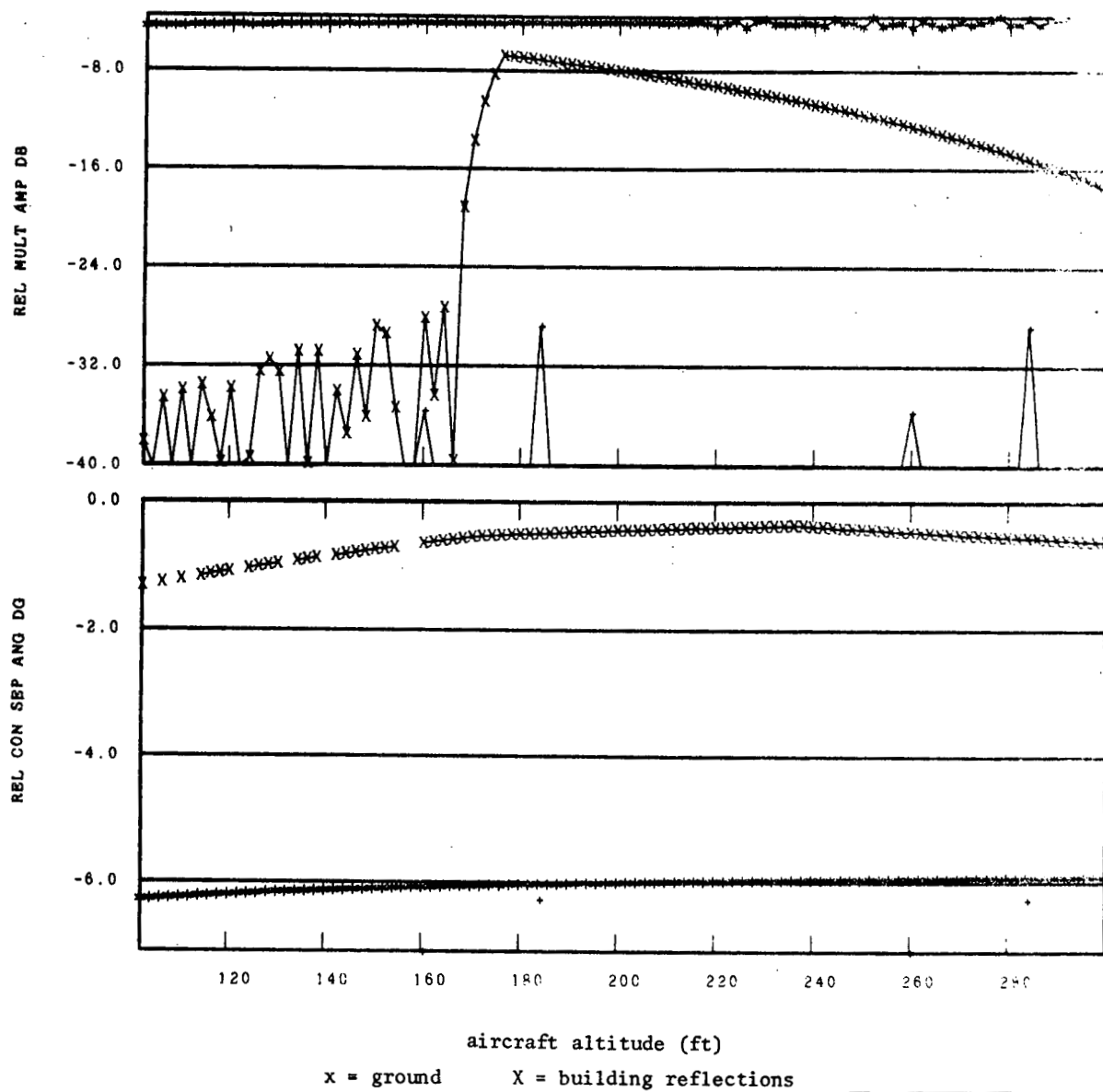
A plot of peak error along the flight path is given in Fig. 6-30 for the TRSB system and Fig. 6-31 for the Doppler System. In the former, the grating lobe error regions are clearly evident at 190 ft and 280 ft. The simulation error entries in Table 6-4 are taken from these plots. The "Static Error" pertains to motion at zero velocity along the flight path, and "Dynamic Error" is for a speed of 200 ft/sec.

The theoretical static errors are taken from Eq. (6-4) for Doppler and from Eq. (6-3) for TRSB. The theoretical dynamic error and averaging factor for Doppler also come from Eq. (6-4). However, the scalloping frequencies and separation angles are sufficiently small that the Doppler error components that vanish at $\omega_s=0$ may be ignored. The simulated TRSB system had a jittered signal format whose averaging factor is always less than unity, even at a grating lobe. The theoretical dynamic error is obtained by multiplying the static error by the appropriate averaging factor.

The agreement between theory and simulation for TRSB is excellent. Regarding the Doppler system where the simulation error is somewhat smaller than than theory predicts, we recall that the theoretical model does not incorporate the effect of a multipath rejection filter, whereas the simulation does. At a separation of over a half degree, the filter has a noticeable influence on the error.

---

[*]This particular simulation was conducted with the TRSB signal format generated by the scanning beam working group [67]. With this format, the TRSB first grating lobe was not reduced as much as with the format shown in Fig. 4-4.
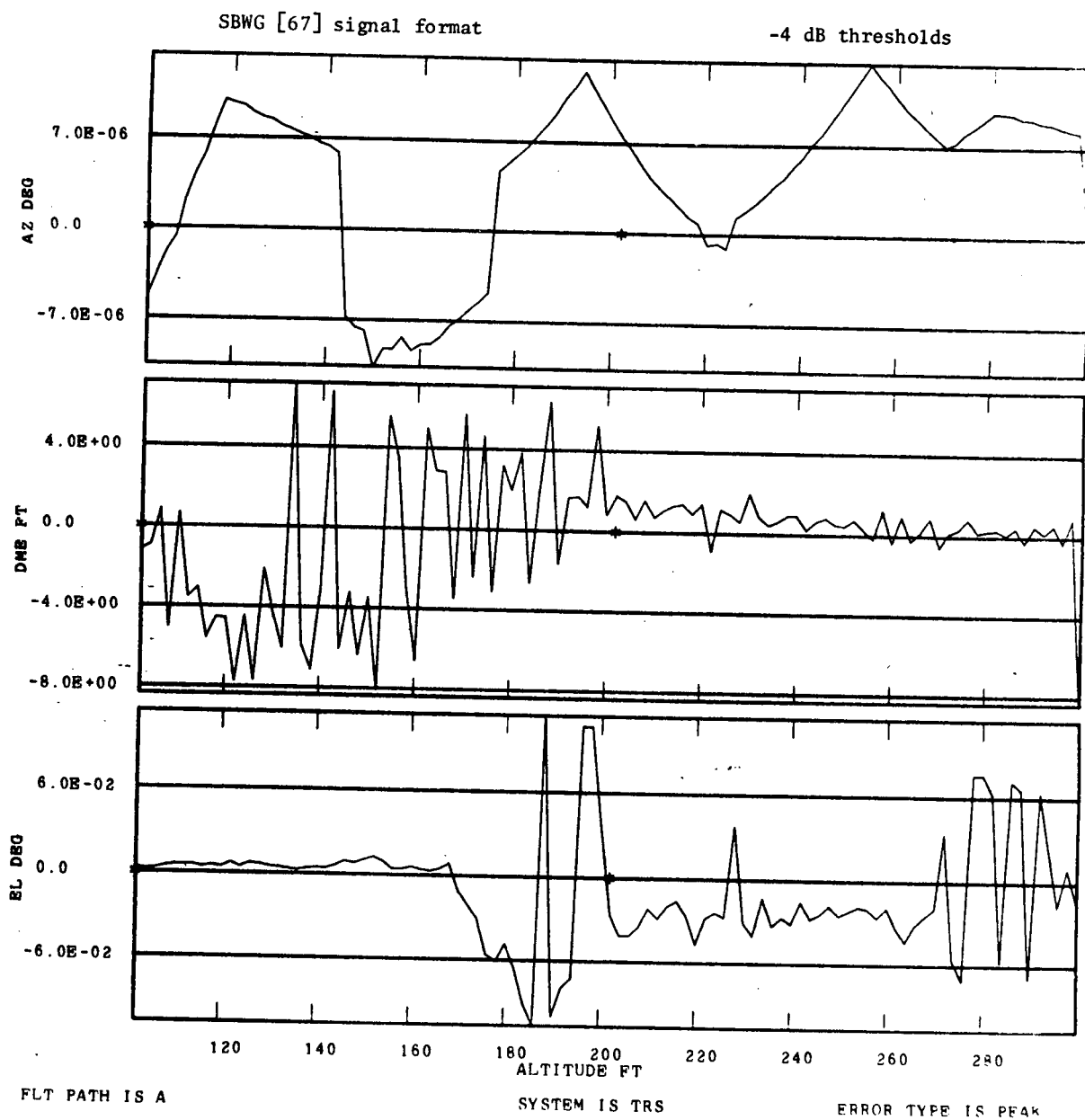
Fig. 6-30.   TRSB error vs altitude for Logan scenario.

ATC-63 VI 6-30

FLT PATH IS A   SYSTEM IS TRS   ERROR TYPE IS PEAK
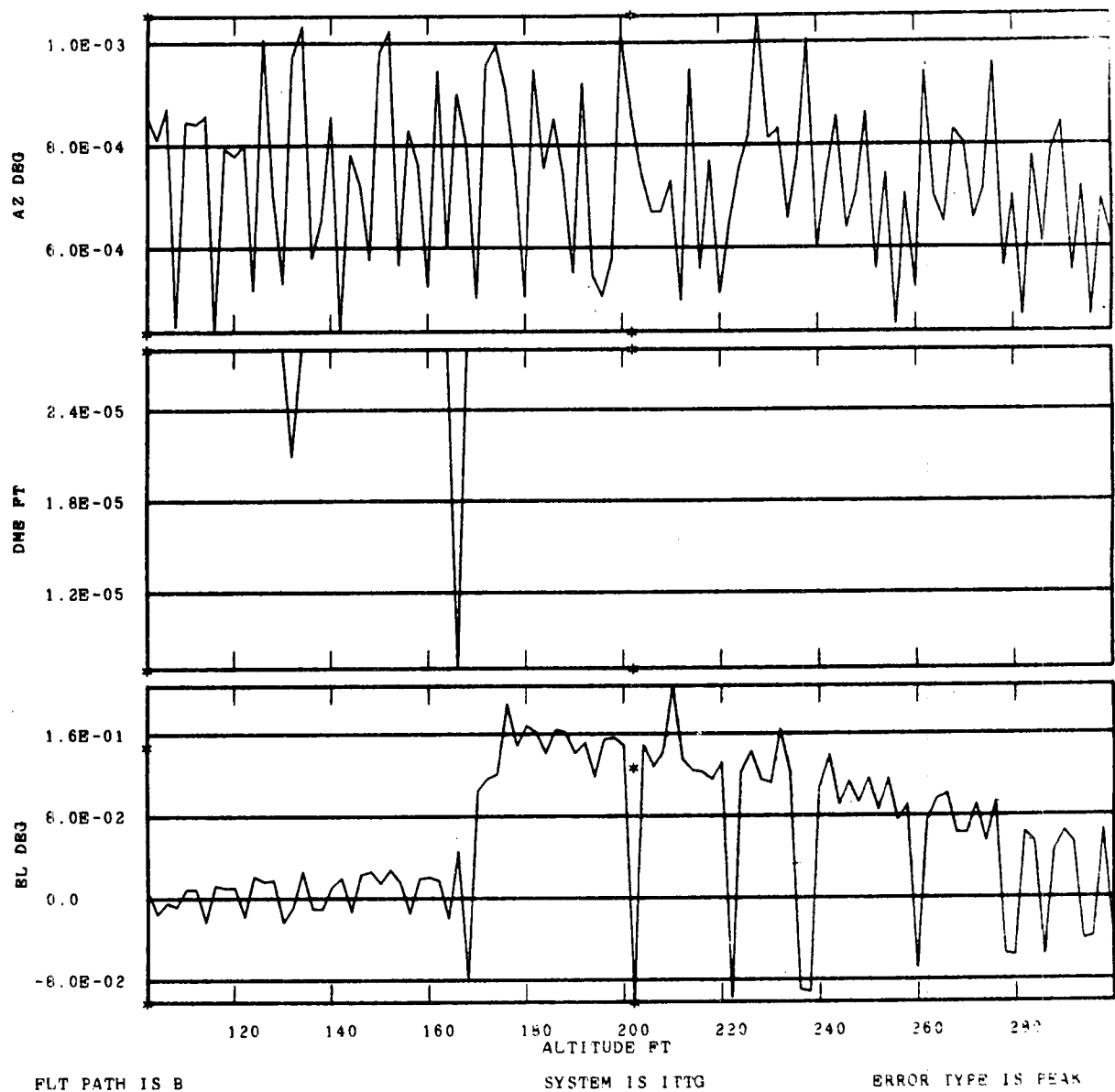
Fig. 6-31. Doppler scan error vs altitude before motion averaging.

TABLE 6-4

LOGAN AIRPORT INTERNATIONAL BUILDING

	Time Reference System				Doppler System			
	Simulation	Theory	Simulation	Theory	Simulation	Theory	Simulation	Theory
Aircraft Altitude	176 ft		280 ft		176 ft		280 ft	
Multipath Amplitude	-6 dB		-15 dB		-6 dB		-15 dB	
Separation Angle	0.6°		0.6°		0.6°		0.6°	
Static Error (peak)	0.14°	0.18°	0.01°	0.087°	0.17°	0.26°	0.06°	0.09°
Scalloping Frequency	91 Hz		40 Hz		91 Hz		40 Hz	
Dynamic Error (peak)	0.06°	0.045°	0.08°	0.07°	0.02°	0.023°	0.01°	0.018°
Averaging Factor		0.25	0.88	0.85	0.12	0.09	0.17	0.2

6.5.2 EL-1 and JFK with One Building Reflection

A second scenario, shown in Fig. 6-32, consists of a single building taken from the JFK environment in the vicinity of a hypothetical EL-1 site. The peak reflection amplitude from this building is -9 dB occurring at an altitude of 273.9 ft on a 2.86° glideslope. The reflection parameters calculated for this building are given in Table 6-5 along with the theoretical and simulated errors.

The agreement between theory and simulation is good for this scenario also. The maximum difference of 0.02° for static Doppler error in Table 6-4 is attributable to both differences between analytical model and simulation and to inaccuracies in determining parameters that enter in the theoretical calculations.
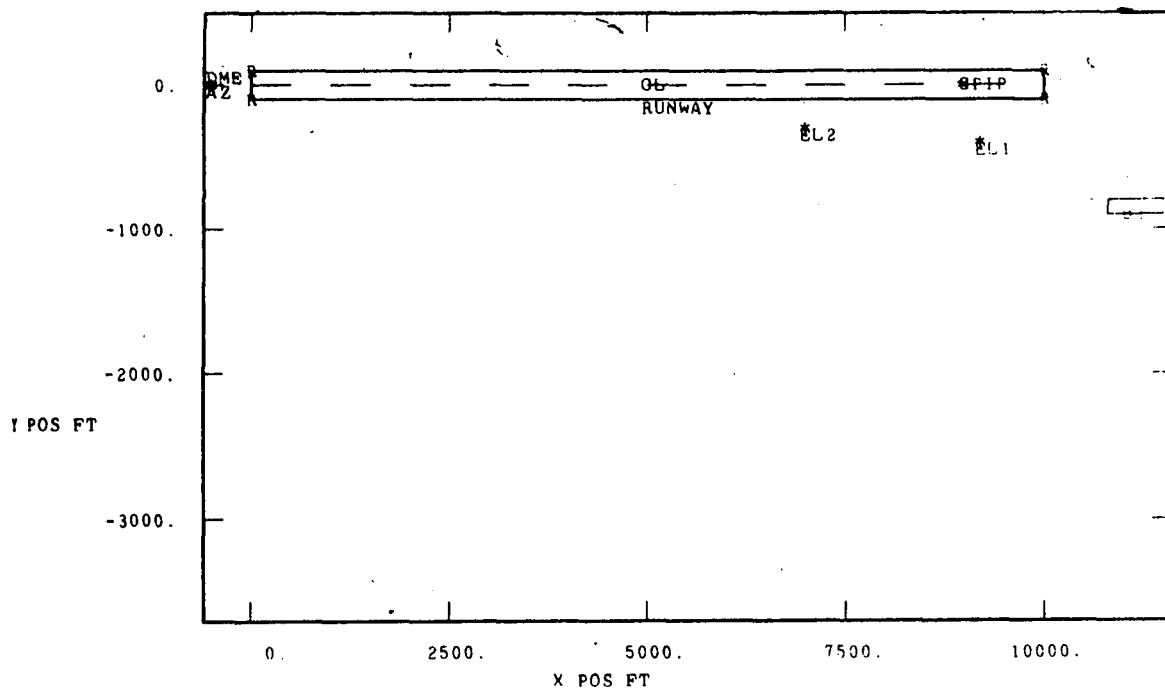
Fig. 6-32. Airport map, JFK scenario.

B1 = Building 1
*DME = DME site
*AZ = AZ site
*EL1 = EL1 site
*EL2 = EL2 site
*GPIP = Glide path intercept point
CL = Centerline

ATC-63 VI 6-32

TABLE 6-5

JFK AIRPORT SINGLE BUILDING

	TRS		Doppler	
	Simulation	Theory	Simulation	Theory
Aircraft Altitude	274 ft		274 ft	
Multipath Amplitude	-9 dB		-9 dB	
Separation Angle	0.07°		0.07°	
Static Error (peak)	0.035°	0.025°	0.045°	0.025°
Scalloping Frequency	23 Hz		23 Hz	
Dynamic Error (peak)	0.005°	0.003°	0.004°	0.0025°
Averaging Factor	0.14	0.13	0.09	0.1

VII. COMPUTER PROGRAM OPERATION

This section provides a brief summary of version 1.0 of the MLS simulation computer program. A more complete description of the programs is contained in the user's manual which will appear separately. The MLS simulation program is written in FORTRAN IV and has been successfully compiled on IBM 370 and SEL 86 machines. It has three major parts; multipath computations, receiver computations, and error plotting.

The multipath section takes an airport environment specified by the user (in a block data subroutine) and computes the multipath characteristics (level, separation angle, etc.). Two-segment linear flight paths are computed from waypoints supplied (in the block data subroutine), with the corresponding perturbation smoothing points. For a given flight path, a loop over all the evaluation points is established to calculate the receiver coordinates. At each evaluation point, the program loops through all transmitter locations, e.g., all angle functions such as azimuth, elevation, and DME. Reference transmitters, where appropriate, are included with their associated angle transmitter.

For a fixed transmitter-receiver geometry, a second loop is established to calculate the multipath parameters for each scattering object in the airport model. Multipath amplitude levels are determined as though the transmitter antenna pattern were omnidirectional. The multipath information to be passed to the receiver subroutines consists of the relative multipath amplitude, phase, time delay, azimuth and elevation planar angles specifying the direction of propagation for the multipath components, as well as the direction of propagation of the direct wave, and fractional Doppler shift.

Editing follows, so as to remove minor components. A digital tape with these multipath characteristics is then written. Multipath diagnostics are plotted along with an airport map showing the placement of obstacles. The multipath programs require 320k bytes of storage on the Lincoln 370 computer. The amount of computer time used depends on the number of obstacles and data points used; for a 'typical' 200 point run with 10 scatterers and no perturbation smoothing, 2 minutes of cpu (computer) time is required on the Lincoln 370 computer.

The receiver part of the simulation takes system parameters (initialized in the block data subroutine), reads in the multipath data from the tape generated by the multipath routines, and computes the resulting errors. If static errors are desired, the receiver routines are called again with zero-Doppler components. The program takes these errors and writes them out on a digital tape, along with scaling data, to be used by the third part. For a 'typical' run with 200 points, no perturbation smoothing or static errors, and 10 scatterers, it takes about three minutes of cpu time for the TRSB EL-1 system to be processed. This time is highly dependent on the number of multipath components. The TRSB azimuth system typically runs 25% faster than the EL-1 system. The DME systems tend to run about 25% slower than the TRSB EL-1 system. The receiver programs require about 176k bytes of storage on the Lincoln 370 computer.

The plotting program takes the error and scaling data generated by the receiver routines, asks which specific plots are desired, and plots them.

The plotting on a Stromberg Carlson 4060 plotter typically requires 30 seconds of cpu time.

The graphical routines used by the simulation are from the Integrated Graphics System of the Datagraphix Company with some modifications by the Lincoln Laboratory support staff. The simulation program generates these graphical outputs on either Tektronix storage scopes or on a Datagraphix 4060 microfilm plotter. The multipath part of the simulation produces a printout of the parameters used in the simulation run, an airport map locating the obstacles and transmitters, and multipath diagnostics. These diagnostics contain information about the multipath amplitude and separation angles along the flight path, indicating which obstacles generate significant multipath components. The receiver part of the simulation itself generates no plots. The plotting program writes out a title page identifying the run, and then plots for a specific system the azimuth, DME, and elevation errors along the flight path on one page, and the x, y, z positional errors for the corresponding system on the next page. Plots of the means, standard deviations, and peak errors can be obtained if perturbation smoothing was used. The static errors are plotted over the dynamic errors with a different symbol. Also, if desired, the error histories may be passed through digital filters to give the "path following" and "control motion" error characteristics.

These plotting routines exist in separate subroutines in all except a few cases. No multipath or receiver routine directly calls any plotting

routine. Thus the program may be readily adapted to other installations not having the Lincoln graphical routines.

The simulation routines involved with the computation of multipath receiver errors were written to be as independent as possible. That is, they essentially do not depend on the calling routine. In order for routines to work faster and more efficiently, especially when doing perturbation smoothing, some routines do have knowledge of the structure of the calling routine. However, the complexity this introduces is fairly small and, as a result, these routines can be used independently for a variety of other studies. For instance, the routines were used with very few changes for the critical areas studies described in Chapter VIII.

Similarly, test programs have been written which can check out the various multipath and receiver routines and/or be used as a tool in multipath measurement test design, system optimization, etc. Specific test programs include multipath from a single multipath obstacle (TESTMLT), performance of a specific receiver when a single multipath component is present (RCVTST), or received envelopes when a single multipath component is present (RCVENV). These routines are highly interactive and generate graphical output so specific cases can be examined easily and in great detail.

The multipath routines in version 1.0 of the program are "GREFC" (specular ground reflection), "DIFFUS" (diffuse ground reflection), "BREFC" (building reflection), "FREFC" (fuselage reflections), and "TREFC" (tail fin reflections). The receiver routines available are "TRSB" (time reference scanning beam) and "ITTG" (a Doppler routine based on the ITT/Gilfillan

zero-crossing counter processor). Routines using the Hazeltine Doppler processor and the TI frequency reference system were written, but are not being supported currently. A wide variety of DME's are available with many system options available. The pulse shapes available are Gaussian, trapezoidal, and chirped (as proposed by TI). Fixed thresholding, adaptive thresholding, or delay-and-compare processors can be applied to these pulse shapes, and different DME's can be used on down and up links. Beampatterns (both transmitter and receiver) are written in subprograms for easy changing. Since the wavelength is also user-specified (in the block data subprogram), DME systems at different frequencies may be easily compared with respect to multipath performance.

References

1. "Experimentation with REGAL Vertical Guidance Landing System," FAA Rep. RD-64-149 (Nov. 1964).

2. "Experimentation with FLARESCAN Vertical Guidance Landing System," FAA Rep. RD-64-150, Proj. 114-012-00X (Nov. 1964).

3. "Advanced Scanning Beam Guidance System for All Weather Landing," FAA Rep. RD-68-2, Proj. 320-01N (Feb. 1968).

4. L.N. Spinner and V.L. Bencivenga, "Advanced Scanning Beam Guidance System for All Weather Landing," FAA Syst. Res. Dev. Serv., Washington, D.C., RD 68-2 (Feb. 1968) AD 665 973.

5. E.J. Murphy, "Exploratory AILS Multipath Investigations" NAFEC Technical Note 1.

6. _____,"Modils Azimuth Investigations," NAFEC Technical Note 4.

7. _____,"Miscellaneous Tests on AILS and MODILS," NAFEC Technical Note 5.

8. _____,"Test and Evaluation of an Advanced Integrated Landing System for all Weather Landing," (Aug. 1970) FAA-RD-70-28.

9. V.L. Bencivenga, "Test and Evaluation of a Portable Scanning Beam Guidance System," (March 1972) FAA-RD-72-16.

10. J.D. Burlage, "AWCLS Take on Carrier Landings," U.S. Naval Aviation News (Nov. 1967).

11. "All Weather Landing System for Combat Aircraft," Interavia (March 1969).

12. "The STOL Navigation Package: 3-D Area Nav and MLS Provide Pinpoint Accuracy," Canadian Aviation (April 1974).

13. Woodward, J.E., "Post-1970 Scanning Beam Approach and Landing," AGARD Conf. Proc. No. 59 on Aircraft Landing Systems AGARD-CP-59-70 (May 1969).

14. "Test of the FLARESCAN Flareout System in Caravelle Number 02." Ministere des Armees (AIR), Direction Technique et Industrielle, Centre D'Essais en Vol. (April 1964).

15. F.X. Kelly, "Tests of Scanning-Beam Microwave Landing Systems at Difficult Sites," presented at technical seminar "Aviation - A Tool for Economic Development," First International Aerospace Show, Sao Paulo, Brazil (Sept. 1973).

16. R.J. Kelly, "Time Reference Microwave Landing System Multipath Control Techniques," Institute of Navigation 31st Annual Meeting (June 1975).

17. P. Fombonne, "Position Errors in Microwave Landing Systems," Electronics and Civil Aviation Intl. Conf., Paris, France (June 1972).

18. ITT/Gilfillan, "Microwave Landing System (MLS) Development Plan as Proposed by ITT/Gilfillan During the Technique Analysis and Contract Definition Phase," FAA-RD-74-118.

19. L. Sanders, "Multipath Challenge for MLS," Electronics and Civil Aviation International Conf., Paris, France (June 1972).

20. S.A. Meer, "Microwave Landing System Siting Case Studies at Kennedy, LaGuardia and Newark Airports," MITRE Corp. MTR-6958 (August 1975).

21 G. Ploussious, "Low Angle Guidance for Scanning Beam Systems," report to CALSPAN by Meyer Assoc. (21 Jan. 1975).

22. Bendix Corp., "Refined Microwave Landing System (MLS) Program Development Plan (Phase III)," (1 Oct. 1974).

23. C.W. Wightman, et al, "Dynamic Multipath Effects on MLS Scanning Beam and Doppler Scan Techniques," Cornell Aero. Lab., Inc., (Sept. 1972) FAA-RD-72-124.

24. _____,"Dynamic Multipath Performance of Airborne Processors," Report TN-3, Calspan Corp. (3 Dec. 1974).

25. _____,"Performance Characteristics of MLS Phase II Receiver-Processors," TN-4, Calspan Corp. (Dec. 1975).

26. "Microwave Landing System (MLS) Development Plan as Proposed by Texas Instruments,Inc., During the Technique Analysis and Contract Definition Phase of the National MLS Development Program," (1 Sept. 1972) FAA-RD-74-170.

27. J. Benjamin, and G.E.J. Peake, "Contributions to the U.K. Microwave Landing System Study (Phase I)," Royal Aircraft Establishment, Tech Memo 1021 (May 1973).

28. A.E. Brindley, L.C. Calhoun, and T.N. Patton, (IITRI) "Multipath Environment Evaluation," Air Force Flight Dynamics Laboratory (Nov. 1974) AFFDL-TR-74-150.

29. D.A. Shnidman, "The Logan MLS Multipath Experiment," Project Report ATC-55, Lincoln Laboratory, M.I.T. (23 Oct. 1975) FAA-RD-75-130.

30. Hazeltine Corp., "Refined Microwave Landing System (MLS) Development Program Plan Feasibility Demonstration Phase II," Report 11009 (1 Oct. 1974).

31. ITT/Gilfillan, "Five Year MLS Development Program Plan (updated) Microwave Landing System," MLS-0420 (1 October 1974).

32. Texas Instruments, Inc., "Refined Microwave Landing System (MLS) Development Program Plan," DM74-03-04 (1 Oct. 1974).

33. Hazeltine Corp., "Microwave Landing System (MLS) Development Plan as Proposed by Hazeltine Corp. During the Technique Analysis and Contract Definition Phase of the National MLS Development Program," (27 Sept. 1973) FAA-RD-73-185.

34. Bendix Corp., "Microwave Landing System (MLS) Development Plan as Proposed by Bendix Corp. During the Technique Analysis and Contract Definition Phase of the National MLS Development Program," (Sept. 1972) FAA-RD-74-152.

35. S.A. Meer, "Estimate of MLS Shadowing, Critical Areas and Airport Building Restrictions," MITRE Corp., MTR-6847 (May 1975).

36. D.A. Shnidman, "Airport Survey for MLS Multipath Issues," Project Report ATC-58, Lincoln Laboratory, M.I.T. (Nov. 1975) FAA-RD-75-195.

37. P.S. Demko, "Polarization/Multipath Study," U.S. Army Electrom. Command Rep. VL-5-72 (Aug. 1971/June 1972).

38. R.A. Rondini and R.H. McFarland, "Experimental Validation of Boeing 747 ILS Signal Scattering Calculations for Critical Area Determination," FAA SRDS (Jan. 1974) FAA-RD-74-57.

39. Microwave Landing System Technique Assessment Doppler Working Group, "Final Report of the Doppler Working Group" (Dec. 1974).

40. C.S. Smith and P. Barton, "Experiments with Narrow Band Information Filters," in UK Phase II Progress Report to FAA MLS Assessment (Sept. 1974).

41. Final Report to NATO: Performance of Advanced Approach and Landing Systems (AALS), Vol. 4, Appendix 1, Electronics Research Laboratory, Univ. of Trondheim, Norwegian Inst. of Tech. (March 1973).

42. N. Blachman, "Zero-Crossing Rate for the Sum of Two Sinuesoids or a Signal Plus Noise," IEEE Trans. on Info. Theory, Vol. IT-21 (Nov. 1975) pp. 671-675.

43. A.E. Brindley, L.E. Calhoun, T.N. Patton and L. Valcik, "Analysis, Test and Evaluation Support to the USAF Advanced Landing System Program," USAF Flight Dynamics Lab. (Aug. 1974) AFFDL-TR-74-62.

44. R. Collin and F. Zucker, Antenna Theory: Part I, McGraw-Hill, New York (1969).

45. "Aeronautical Telecommunications," Annex 10 to the Convention on International Civil Aviation, 2nd Ed., Vol. 2, International Civil Aviation Organization (April 1968).

46. F.G. Overbury, "The Effects of Scalloping and a Further Discussion of Scalloping," in Study of the Doppler Landing Guidance System - Second Report," Standard Telecommunications Laboratories (Oct. 1972).

47. P. Beckman, "Scattering by Composite Rough Surfaces," Proc. IEEE, (Aug. 1965), pp. 1012-1015.

48. D.E. Kerr, Propagation of Short Radio Waves, McGraw-Hill Book Co.,N.Y. (1951).

49. P. Beckmann, and A. Spizzichino, The Scattering of Electromagnetic Waves from Rough Surfaces, Pergamon Press, N.Y. (1963).

50. J.W. Goodman, Introduction to Fourier Optics, McGraw-Hill Book Co., N.Y. (1968).

51. K.M. Mitzner, "Change in Polarization on Reflection from a Tilted Plane," Radio Science, Vol. 1, no. 1 (Jan. 1966). pp. 27-29.

52. S. Silver, Microwave Antenna Theory and Design, McGraw-Hill Book Co., N.Y. (1949).

53. H.J. Riblet and C.B. Barker, "A General Divergence Formula," J. of Applied Physics, Vol. 19 (Jan. 1948). pp. 63-70.

54. R.E. Kell, "On the Derivation of Bistatic RCS from Monostatic Measurements," Proc. IEEE, (Aug. 1965), pp. 983-988.

55. R.D. Kodis, "A Note on the Theory of Scattering from an Irregular Surface," IEEE Trans. Ant. Prop., Vol. AP-14, no. 1 (January 1966), pp. 77-82.

56. D.E. Barrick, "Rough Surface Scattering Based on the Specular Point Theory," IEEE Trans. Ant. Prop., Vol. AP-16, no. 4 (July 1968), pp. 449-454.

57. T.P. McGarty, "Models of Multipath Propagation Effects in a Ground-to-Air Surveillance System," Technical Note 1974-7, Lincoln Laboratory, M.I.T. (25 February 1974).

58. E.C. Jordan and K.G. Balmain, Electromagnetic Waves and Radiating Systems, Prentice-Hall, Inc., N.J. (1968).

59. S.O. Rice, "Diffraction of Plane Radio Waves by a Parabolic Cylinder: Calculation of Shadows Behind Hills," Bell System Tech. Jour., Vol. 33 (March 1954), pp. 417-504.

60. G.T. Ruck, D.E. Barrick, W.D. Stuart and C.K. Krichbaum, Radar Cross Section Handbook, Vol. 1, 2, Plenum Press, N.Y. (1970).

61. J.W. Crispin, and K.M. Siegel, Methods of Radar Cross-Section Analysis, Academic Press, N.Y. (1968).

62. R. Horonjeff, Planning and Design of Airports, McGraw-Hill, N.Y. (1962).

63. J.B. Keller, "Geometrical Theory of Diffraction," J. of the Optical Society of America, Vol. 52, No. 2 (February 1962), pp. 116-130.

64. A. Sommerfeld, Optics, Academic Press, New York (1954).

65. A Spiridon, "Impact of Obstacle Shadows on Monopulse Azimuth Estimate," Project Report ATC-50, Lincoln Laboratory, M.I.T., FAA-RD-75-91..

66. "Test Requirements and Coordination Plan, National Microwave Landing System Phase II Test Program," FAA MLS Division (7 Sept. 1973).

67. C.J. Hirsch, "Experimentation for the Use of L-band DME with the MLS," Final Report to FAA SRDS (Feb. 1974).

68. "Final Report of the MLS Scanning Beam Working Group to the MLS Technique Assessment," MLS Scanning Beam Working Group (Dec. 1974).

69. G. Ploussious, "Circular Polarization Analysis Interim Report #2: Aircraft Reflections," Meyer Assoc., Inc., U.S. Army Contract #DAAB07-75-C-0801 (31 Jan. 1975).

70. _____ "Circular Polarization Analysis Final Report," Meyer Assoc., Inc., U.S. Army Contract #DAAB07-75-0801 (Dec. 1975).

71. G. Litchford, "Study and Analysis of SC-117, National and USAF Plans for a New Landing System," Technical Report AFFDL-TR-72-76 Part II, U.S. Air Force Flight Dynamics Laboratory (May 1974).

72. G.J. Schlieckert, "An Analysis of Aicraft L-band Beacon Antenna Patterns," Project Report ATC-37, Lincoln Laboratory, M.I.T. (15 Jan. 1975), FAA-RD-74-144.

73. T.C.M. Tong and T.B.A. Senior, "Scattering of Electromagnetic Waves by a Periodic Surface with Arbitrary Profile," Scientific Rep. 13, Univ. of Michigan (April 1972) AFCRL-72-0258.

74. A. Hessel and J. Shmoys, "Computer Analysis of Propagation/Reflection Phenomena," Scientific Report Contract Number DAAB07-73-M-2716, Polytechnic Inst. of Brooklyn (Aug. 1973).

75. K.A. Zaki and A.R. Neureuther, "Scattering from a Perfectly Conducting Surface with a Sinusoidal Height Profile: TE-Polarization," IEEE Trans. Antennas Prop. AP-19, 208-214 (1971).

76. K.A. Zakai and A.R. Neureuther, "Scattering from a Perfectly Conducting Surface with a Sinusoidal Height Profile: TM-Polarization," IEEE Trans. Antennas Prop. AP-19, 747-751 (1971).

77. A. Papoulis, The Fourier Integral and its Applications, McGraw-Hill, N.Y. (1962), pp. 134-143.